Tools for Improved Quantum Metrology on Atomic Platforms

by

Athreya Shankar

B.Tech. (Hons), Indian Institute of Technology Madras, 2014

M.S., University of Colorado Boulder, 2017

A thesis submitted to the

Faculty of the Graduate School of the

University of Colorado in partial fulfillment

of the requirements for the degree of

Doctor of Philosophy

Department of Physics

2020

This thesis entitled:
Tools for Improved Quantum Metrology on Atomic Platforms
written by Athreya Shankar
has been approved for the Department of Physics

_____

Prof. Murray J. Holland

_____

Dr. John Bollinger

Date _____

The final copy of this thesis has been examined by the signatories, and we find that both the content and the form meet acceptable presentation standards of scholarly work in the above mentioned discipline.

Shankar, Athreya (Ph.D., Physics)

Tools for Improved Quantum Metrology on Atomic Platforms

Thesis directed by Prof. Murray J. Holland

The last three decades have witnessed the rapid rise of technologies based on quantum mechanical principles. In particular, quantum systems are expected to revolutionize the way we sense and measure properties of our universe. The ongoing transition from fundamental studies of quantum systems to a quantum technology revolution is being powered by significant advancements in laser cooling and trapping of atoms, and in the manipulation and readout of quantum degrees of freedom. In this thesis, we contribute to this movement by presenting theoretical ideas of practical relevance, that will enable improved quantum metrology using atom-based platforms.

We advance capabilities in three areas of relevance to quantum metrology. First, under the theme of sub-Doppler cooling of large quantums systems, we describe the numerical modeling of a successful experiment for near ground-state cooling of trapped ion crystals with more than 100 ions in a Penning trap. Second, we propose a new readout technique using atom-cavity interactions to continuously and precisely track the relative phase of a spin superposition. Third, we propose a scheme to engineer squeezing on a platform where controllable atom-atom interactions have been hard to achieve, namely atomic Bragg interferometers. In this way, we introduce useful entanglement into a sensing platform traditionally relying on single-atom physics.

Dedication

To *Amma*, *Nanna*, Myka, Rajamma *aththa*, Jothi *avva* and Venkatesh *thatha*.

Acknowledgements

A wave of gratitude sweeps over me as I express my heartfelt thanks to the people who have helped me reach where I am today. Thank you, Murray, for giving me the freedom to explore physics as a graduate student. He has always allowed me to venture freely in any direction I wanted to, with the quiet assurance that a safety net was always in place in case things didn't work out. As an aspiring professor myself, I hope to be as supportive of my students' ideas as Murray has been of mine.

My mindset towards physics, research, scientific collaboration and mentoring has been shaped by some terrific scientists I have interacted with during grad school. Thank you, Jinx, for teaching me that the physics should dictate the math, and not the other way round. I am grateful to John Bollinger for always making me feel equal in any discussion, even though he has been in the field longer than I have been alive. Your humility has inspired me to stay grounded no matter what I may achieve. Thanks to James Thompson for all the enthusiastic physics discussions that would go on forever like a cricket Test match. I am sure that I will listen to my future students with the same level of patience and interest that you have displayed during our conversations. Thanks to Marilu Chiofalo and Nicola Poli for the fantastic hospitality in Pisa and Florence during my short trip to Italy. They have been very patient in collaborating with me and have always allowed me to work in my natural style. Thanks to Ana Maria Rey for several engaging discussions. I am very grateful to Dr. K. S. Balaji and Prof. Lakshmi Bala for kindling my early interest in physics.

I have always struggled with my thoughts and emotions. If not for my mother, I would never have been able to emerge successful from these struggles at various stages in my life; thank you,

Amma, for making it your life's mission to see me successful. Also, thanks to the amazing resources offered by the Counseling and Psychiatric Services at CU Boulder for helping me systematically overcome my mental health problems.

During high school, I still remember how my father used to wake up at 4.30 AM in the morning just to make tea for me, so that I could wake up at 5 AM and study for my exams; thank you, *Nanna*, for being the sturdy pillar on which I have always leaned on. Thanks to my sister, Mythreyi, for the long, random phone conversations that helped me to relax after work; *Myka*, you have played an enormous role in keeping loneliness and homesickness at bay. I am forever indebted to my great aunt Rajamma *atha* and my grandparents, Venkatesh *thatha* and Jothi *avva*, for taking care of me during my formative years and thereby supporting my working parents.

I am grateful to have been surrounded by an enthusiastic and approachable group of fellow students and postdocs. Thanks to John Bartolotta, Haonan Liu, Lilian Chih, Jarrod Reilly, Chris Langlett and Simon Jaeger for being collaborative and welcoming group mates. Thanks to David Tieri for early advice on life as a grad student. Baochen and Graham— I have enjoyed the countless discussions we have had on various physics ideas. Thanks to Elena, Arghavan and Kevin, who shared my excitement for modeling an experiment as it was being performed. I am thankful to Leo Salvi for all the Skype meetings from which I learned so much physics. I have also enjoyed discussing physics with Matt Affolter, Chen Tang, Yiheng Lin, Robert Lewis-Swan and Chengyi Luo.

Life away from home would have been hard if not for my friends who were as good as family for me. Kannan, Balaji and Harsha, it is not a stretch to say that you guys have been more than brothers to me. I will always remember the amazing badminton and cricket games I played with Harish, Mano and Nishant. Thanks to Prasanth and Akshay for being adjusting and extremely caring flat mates. Thanks to Suchit, Abhimanyu, Kiran and Sanni for all the get-togethers. Thanks to Ramesh, Karuna, Susheera, Jayson and all the AID Colorado members. Sungoh, Tyko and Ashik— thanks for always being there to help and to have a long conversation. I am indebted to Nithin Sivadas for some very valuable conversations at various stages of my PhD.

Contents

Chapter

Tables

Table

Figures

Figure

Chapter 1

Context

We are currently entering an era where quantum technologies are expected to revolutionize the way we communicate, compute, measure and understand our universe. Tremendous advancements in the theoretical understanding and experimental control of physics in the quantum regime has led to a 'There And Back Again' scenario: Early experiments in the 20th century typically worked with a large number of poorly controlled atoms or molecules, but greatly contributed to understanding central concepts in quantum physics. The late 20th and early 21st centuries witnessed significant advances in laser cooling and trapping [126], heralded by elegant theoretical schemes for the cooling of single atoms and unprecedented experiments with a single or a few atoms [29, 69, 109]. We are now ready to reconsider working with large quantum systems by asking the following two very exciting questions:

(1) Can we leverage the lessons learned with small systems and scale up these techniques to exquisitely control and manipulate large quantum systems?

(2) If we had such exquisite control, can we engineer and observe intrinsically many-body features predicted by quantum mechanics, such as entanglement, and exploit such features for novel practical applications?

Indeed, modern theory and experiments have answered both of these questions in the affirmative. The last decade has witnessed rapid advancements in studies and applications of quantum many-body systems. The demonstration of quantum computers claiming quantum supremacy over

known classical algorithms [3], quantum simulations of exotic states of matter such as discrete time crystals [135] and the operation of optical lattice clocks with record breaking precision [86] are important but nevertheless only representative examples of quantum many-body systems playing a central role in quantum computing, simulation and metrology.

In particular, quantum metrology with atoms stands to benefit immensely with the development of large, well controlled quantum systems. Typically, metrology with atoms involves preparing an initial quantum state with high accuracy, perturbing the state with a signal to be measured, and reading out the change in the state as a result of the applied signal. Working in the spirit of the questions raised above, we broadly identify three crucial themes in the context of quantum metrology, where advancements will lead to new and improved practical applications:

(1) Sub-Doppler laser cooling of large quantum systems,

(2) Novel techniques to read out changes in the prepared state, and

(3) Engineering entanglement to improve measurement precision in traditionally non-interacting quantum systems.

In this thesis, we present our contributions to advancing state-of-the-art capabilities in each of these three areas. We begin with an introduction in Chapter 2, where we establish the backdrop against which our work has been carried out. Subsequently, under the first theme, we report on the numerical modeling of an experiment to ground-state cool large two dimensional trapped ion crystals in a Penning trap. This work is detailed in Chapters 3 and 4. Under the second theme, in Chapters 5 and 6, we describe and numerically demonstrate a proposal for continuously and precisely tracking the relative phase of a spin superposition using atom-cavity interactions. As a paradigm for the third theme, we propose in Chapters 7 and 8 a scheme for entangling spins encoded in the center-of-mass motion of atoms, for use in a Bragg interferometer. For each of these projects, we comment on possible future directions at the end of the relevant chapters. We conclude with a brief summary in Chapter 9.

Chapter 2

Introduction

In the last chapter, we identified three central themes in quantum metrology that we will be exploring in this thesis. In this chapter, we provide an overview of concepts that are essential to understanding our work on these themes. Accordingly, we first review advancements in laser cooling from a trapped ion perspective. To warm up to our second and third themes, we introduce the notion of spin-1/2 systems and how such systems can be encoded in a variety of atomic degrees of freedom. Next, we describe the Ramsey sequence, a protocol that is currently the workhorse for quantum metrology with atomic systems. Despite its widespread application, we point out some situations where it is not effective and alternative protocols may be required. We show how the use of uncorrelated atoms in this sequence leads to limits on measurement precision. We discuss how precision beyond this limit can be achieved via the concept of spin squeezing. As examples, we describe a couple of mechanisms by which such squeezed spin states can be generated. Finally, we briefly describe the operation of an atomic Bragg interferometer, a platform where controllable atom-atom interactions are hard to engineer and spin squeezing has not been experimentally realized till date.

2.1 Laser cooling of trapped ions

To illustrate general features of laser cooling, we consider a toy model of a single trapped ion with two internal (electronic) states $|g\rangle, |e\rangle$ and with one external (motional) degree of freedom, say along the z direction. The harmonic trapping potential enables us to treat the ion's motion as

that of a quantum harmonic oscillator. The Hamiltonian for this isolated trapped ion is

$$\hat{H}_A = \frac{\hbar\omega_a}{2}\left(|e\rangle\langle e| - |g\rangle\langle g|\right) + \hbar\omega_0 \hat{b}^\dagger \hat{b}, \tag{2.1}$$

where $\hbar\omega_a$ is the energy difference between the ground ($|g\rangle$) and excited states ($|e\rangle$) and ω_0 is the trapping frequency. The external degree of freedom is described using bosonic creation and annihilation operators $\hat{b}^\dagger, \hat{b}$ satisfying $[\hat{b}, \hat{b}^\dagger] = 1$ from which a position operator $\hat{z}$ for the ion can be constructed.

2.1.1 The atom-laser interaction

The essential idea behind laser cooling is that the absorption and emission of photons in general simultaneously affects both the electronic and motional state of an ion. We assume that a traveling wave laser with frequency ω_l tuned close to ω_a and wavevector $\mathbf{k}_l = k_l\hat{z}$ drives the $|g\rangle \leftrightarrow |e\rangle$ transition. The electric field associated with this laser is given by $\mathbf{E}(z,t) = \mathbf{E}_0 \cos(k_l z - \omega_l t)$. Within the electric dipole approximation, the Hamiltonian for the interaction of the atom with the laser field is given by the expression $-\hat{\mathbf{d}}\cdot\mathbf{E}$, where the atomic dipole operator $\hat{\mathbf{d}} = \mathbf{d}\,|e\rangle\langle g| + \mathbf{d}^*\,|g\rangle\langle e|$ induces transitions from $|g\rangle$ to $|e\rangle$ and vice versa [41]. The transition dipole matrix element $\mathbf{d}$ is a vector and captures details about the spatial profile of the wavefunctions associated with the two electronic states. A subtle point to note is that only the center-of-mass coordinate of the entire ion is represented as a quantum harmonic oscillator. The valence electron that is making transitions between the two electronic states should be pictured as tagging along closely with the ion, thereby making the electric dipole approximation valid. In other words, the dipole formed by the valence electron and the ionic shell can still be regarded as a point dipole, but the location of the point dipole itself is captured by the center-of-mass coordinate $\hat{z}$ of the ion.

Except at very strong laser intensities, energy conservation can be imposed by assuming that the $|g\rangle \to |e\rangle$ ($|e\rangle \to |g\rangle$) transition is accompanied by the absorption (emission) of a laser photon. Rigorously, this assumption amounts to making the rotating wave approximation (RWA) [41]. Within the electric dipole and rotating wave approximations, the Hamiltonian for the atom-laser

interaction is given by

$$\hat{H}_{AF} = \frac{\hbar\Omega}{2} |e\rangle \langle g| e^{i(k_l \hat{z} - \omega_l t)} + \frac{\hbar\Omega^*}{2} |g\rangle \langle e| e^{-i(k_l \hat{z} - \omega_l t)}, \tag{2.2}$$

where $\Omega = -\hat{\mathbf{d}} \cdot \mathbf{E}_0/\hbar$ is called the Rabi frequency and captures the driving strength. Without loss of generality, we assume Ω to be real in the subsequent discussion as its complex phase can always be absorbed into an initial phase offset of the electric field. One way to understand the signs of the complex exponentials multiplying the atomic transition operators is to consider the case when the laser field is quantized and is described by bosonic creation and annihilation operators $\hat{a}^\dagger, \hat{a}$. The laser field is then governed by a Hamiltonian $\hat{H}_L = \hbar\omega_l \hat{a}^\dagger \hat{a}$. From $\hat{H}_L$, it is easy to see that the time evolution of the Heisenberg picture operators $\hat{a}(t), \hat{a}^\dagger(t)$ is given by $\hat{a}(t) = \hat{a}e^{-i\omega_l t}$ and $\hat{a}^\dagger(t) = \hat{a}^\dagger e^{i\omega_l t}$. Matching signs with the exponentials in Eq. (2.2), we see that the raising operator $|e\rangle \langle g|$ is accompanied by photon annihilation or absorption while the lowering operator $|g\rangle \langle e|$ is accompanied by photon creation or emission. Since the laser field is assumed to carry a large number of photons, the operators $\hat{a}, \hat{a}^\dagger$ which should have appeared in Eq. (2.2) have been replaced by a macroscopic c-number, that has been absorbed into the definition of the classical electric field $\mathbf{E}_0$.

Since the laser electric field is z dependent, the ion experiences a varying electric field as it oscillates along the z direction. This piece of physics is captured by the $e^{\pm ik_l \hat{z}}$ terms entering the atom-laser interaction in Eq. (2.2), where $\hat{z}$ is the position operator for the ion. Clearly, from the form of Eq. (2.2), the laser affects both the electronic and motional state of the ion and therefore we can envisage the possibility of cooling the ion using the laser.

Time dependent Hamiltonians such as Eq. (2.2) are harder to analyze, so we first transform to an interaction picture with free Hamiltonian $H_0 = \hbar\omega_l/2 \left(|e\rangle \langle e| - |g\rangle \langle g|\right)$. In this picture, the total Hamiltonian is time independent and is given by

$$\hat{H}_I = -\frac{\hbar\Delta}{2} \left(|e\rangle \langle e| - |g\rangle \langle g|\right) + \hbar\omega_0 \hat{b}^\dagger \hat{b} + \frac{\hbar\Omega}{2} \left(|e\rangle \langle g| e^{ik_l \hat{z}} + |g\rangle \langle e| e^{-ik_l \hat{z}}\right), \tag{2.3}$$

where $\Delta = \omega_l - \omega_a$ is the laser-atom detuning.

2.1.2 The Lamb-Dicke regime

When the typical displacement of the ion, as it oscillates, is small compared to the wavelength of the laser light, the exponentials $e^{\pm ik_l\hat{z}}$ can be expanded in a Taylor series. Mathematically, this condition translates to $k_l\sqrt{\langle\hat{z}^2\rangle} \ll 1$, and is called the Lamb-Dicke criterion [126]. Furthermore, expressing the position operator $\hat{z}$ in terms of the creation and annihilation operators, we can write

$$k_l\hat{z} = \eta\left(\hat{b} + \hat{b}^\dagger\right), \tag{2.4}$$

where $\eta = k_l\sqrt{\hbar/2M\omega_0}$ is called the Lamb-Dicke parameter. An important point is that a small Lamb-Dicke parameter, $\eta \ll 1$, is necessary but not sufficient to satisfy the more restrictive Lamb-Dicke criterion defined above [126]; from the definition of η, we see that it is the ratio of the RMS zero-point displacement to the laser wavelength. However, the Lamb-Dicke criterion also requires that the number of vibrational quanta in the harmonic oscillator remains small.

The atom-laser interaction in Eq. (2.3) can now be expanded in powers of η as

$$\frac{\hbar\Omega}{2}\left|e\right\rangle\left\langle g\right|\left(1 + i\eta\left(\hat{b} + \hat{b}^\dagger\right) - \frac{\eta^2}{2}\left(\hat{b} + \hat{b}^\dagger\right)^2 + \ldots\right) + \text{ H.c.} \tag{2.5}$$

2.1.3 Motional sidebands

Eq. (2.5) implies that the atom can be excited from $\left|e\right\rangle\left\langle g\right|$ not just by the absorption of a laser photon, but also by the simultaneous absorption and emission of vibrational quanta, or phonons [126, 36]. The $\mathcal{O}(\eta)$ term describes two processes where the excitation of an atom is accompanied by the absorption of a photon and a phonon or by the absorption of a photon and emission of a phonon. Similarly, the $\mathcal{O}(\eta^n)$ term describes various processes involving n phonons and a single laser photon. To understand what these terms entail from an energy perspective, let us consider the $\mathcal{O}(\eta)$ term as an example. The energy required to excite the atom is $\hbar\omega_a$. The laser photon supplies $\hbar\omega_l$, while the absorption (emission) of a phonon supplies (demands) $\hbar\omega_0$, leading to a net excitation energy of $\hbar\left(\omega_l + \omega_0\right)$ ($\hbar\left(\omega_l - \omega_0\right)$). If the laser is appropriately detuned from the atomic transition frequency, one of these two processes can be tuned closer to resonance than the other. From a cooling perspective, we would prefer to make the phonon absorption process more

resonant, as this would ensure that every atomic excitation is more likely to remove, rather than add, one quantum of motional energy. From the atom's perspective, the laser now appears to have sidebands at frequencies $\omega_l \pm \omega_0$. Almost all laser cooling schemes rely on strongly enhancing atomic excitation via the motion removing sideband at $\omega_l + \omega_0$ while simultaneously suppressing excitations via the motion adding sideband at $\omega_l - \omega_0$.

2.1.4 Spontaneous emission

A purely Hamiltonian process cannot irreversibly remove energy from the system, as the reverse process (the Hermitian conjugate term) is also energetically equally favorable. Instead, such irreversible removal of energy occurs through spontaneous emission from the excited state $|e\rangle$ that resets the atom to the ground state $|g\rangle$, thereby completing one absorption-emission cycle. As an example for a single cooling cycle, an atom in an n-phonon state $|g, n\rangle$ is likely to be excited to the state $|e, n-1\rangle$, from where spontaneous emission brings the state to $|g, n-1\rangle$. In this way, laser cooling can be pictured as a sequence of absorption-emission cycles, with each cycle more likely to remove a phonon rather than add one. For this picture to be accurate, spontaneous emission itself should not change the vibrational quantum number. To see the effect of spontaneous emission on the motion, we consider the Lindblad dissipator associated with this process, given by

$$\mathcal{D}\rho = \Gamma \left\{ |g\rangle\langle e| \left(\int_{-1}^{1} du \mathcal{N}_\mu(u) e^{-ik_{\rm sc}\hat{z}u} \rho e^{ik_{\rm sc}\hat{z}u} \right) |e\rangle\langle g| - \frac{1}{2}|e\rangle\langle e|\rho - \frac{1}{2}\rho|e\rangle\langle e| \right\}. \tag{2.6}$$

Here, the density matrix ρ describes the joint electronic and motional state of the ion, Γ is the spontaneous decay rate of $|e\rangle \to |g\rangle$, $\mathbf{k}_{\rm sc}$ is the wavevector associated with the spontaneously emitted photon, $u = \cos\theta_{\rm sc}$, with $\theta_{\rm sc}$ the angle between $\mathbf{k}_{\rm sc}$ and the z axis, and $\mathcal{N}(u)$ is the normalized dipole radiation pattern associated with the emission. Assuming $k_{\rm sc} \approx k_l$, we can expand the complex exponentials in Eq. (2.6) to $\mathcal{O}(\eta^2)$ to write $\mathcal{D}\rho \approx \mathcal{D}_0\rho + \mathcal{K}_2\rho$, where

$$\mathcal{D}_0\rho = \Gamma \left\{ |g\rangle\langle e|\rho|e\rangle\langle g| - \frac{1}{2}|e\rangle\langle e|\rho - \frac{1}{2}\rho|e\rangle\langle e| \right\}, \tag{2.7}$$

is the familiar Lindblad dissipator for spontaneous emission that neglects effects on the motion, and

$$\mathcal{K}_2\rho = \frac{\eta^2\Gamma\langle u^2\rangle}{2}\,|g\rangle\langle e|\left(2\hat{X}\rho\hat{X} - \hat{X}^2\rho - \rho\hat{X}^2\right)|e\rangle\langle g|\,, \tag{2.8}$$

is a term that accounts for changes in motional state at $\mathcal{O}(\eta^2)$. The $\mathcal{O}(\eta)$ term vanishes because $\mathcal{N}(u)$ is an even function. Therefore, at $\mathcal{O}(\eta^0)$, spontaneous emission predominantly does not change the motional state, thereby providing support to the cooling cycle picture described above.

Yet another interpretation of η helps understand the associated physics [126]. Upon spontaneously emitting a photon, the kinetic energy of the atom is reduced by $\sim \hbar\omega_r$, where $\omega_r = \hbar k_1^2/2M$ ($k_{\rm sc} \approx k_l$) is the recoil frequency. The energy required to change the harmonic oscillator state by one quantum is $\hbar\omega_0$. The ratio of the two frequencies is

$$\frac{\omega_r}{\omega_0} = \frac{\hbar k_l^2}{2M\omega_0} = \eta^2. \tag{2.9}$$

Therefore, $\eta \ll 1$ is also equivalent to assuming that the recoil energy of the scattered photon is too small to cause significant changes in the motional state.

2.1.5 Laser cooling with two electronic states

The toy model we developed using just two electronic states forms the basis for the two most popular laser cooling techniques, Doppler cooling and sideband cooling, which are closely related. The absorption spectrum of the two level system is a useful tool for understanding the cooling mechanism [36]. This spectrum is obtained by addressing the $|g\rangle \leftrightarrow |e\rangle$ transition with a laser and measuring the scattered intensity as the laser frequency is varied across the atomic resonance. Essentially, this measurement is equivalent to probing the excited state population ρ_{ee}. For a laser detuning Δ, decay rate Γ and Rabi frequency $\Omega \ll \Gamma$, the steady state excited population takes the form of a Lorentzian given by

$$\rho_{\rm ee} \approx \frac{\Omega^2/4}{\frac{\Gamma^2}{4} + \Delta^2}. \tag{2.10}$$

From Eq. (2.5), the action of the first motion removing sideband on the state $|g, n\rangle$ is

$$\frac{i\hbar\Omega\eta}{2}\,|e\rangle\langle g|\,\hat{b}\,|g, n\rangle = \frac{i\hbar\Omega\eta}{2}\sqrt{n}\,|e, n-1\rangle\,, \tag{2.11}$$

suggesting that the Rabi frequency associated with this sideband drive is $\Omega_n^- = i\Omega\eta\sqrt{n}$. Similarly, for the motion adding sideband, the associated Rabi frequency is $\Omega_n^+ = i\Omega\eta\sqrt{n+1}$. Combined with Eq. (2.10), the rates for cooling and heating cycles are respectively given by $R_n^- = n\eta^2 A^-$ and $R_n^+ = (n+1)\eta^2 A^+$, where

$$A^- = \Gamma \frac{\Omega^2/4}{\frac{\Gamma^2}{4} + (\Delta + \omega_0)^2},\ A^+ = \Gamma \frac{\Omega^2/4}{\frac{\Gamma^2}{4} + (\Delta - \omega_0)^2}, \tag{2.12}$$

where the modified detunings now account for the respective sideband frequencies. These rates are linear in n, therefore we can immediately write down a rate equation for the average occupation $\bar{n}$ of the harmonic oscillator as

$$\begin{aligned} \frac{d}{dt}\bar{n} &= -R_{\bar{n}}^- + R_{\bar{n}}^+ \\ &= -W\bar{n} + \eta^2 A^+, \end{aligned} \tag{2.13}$$

where $W = \eta^2(A^- - A^+)$ is the cooling rate provided that $A^- > A^+$. The steady-state occupation $\bar{n}_{\mathrm{SS}}$ is given by

$$\bar{n}_{\mathrm{SS}} = \frac{A^+}{A^- - A^+}. \tag{2.14}$$

In addition to these cooling and heating cycles, there is a third diffusive cycle that first involves absorbing just a laser photon (the 'carrier' transition, $\mathcal{O}(\eta^0)$ term in Eq. (2.5)) and leaving the motional state unaffected, and then changing the motional state via the spontaneously emitted photon. As the $\mathcal{K}_2$ term, Eq. (2.8) shows, this process is also $\mathcal{O}(\eta^2)$. However, such a process has equal probability for heating and cooling, and therefore leaves the net cooling rate W unaffected. However, $\bar{n}_{\mathrm{SS}}$ depends additionally on A^+ which is modified because of this cycle. Therefore, $\bar{n}_{\mathrm{SS}}$ increases by a small numerical factor of $O(1)$.

2.1.5.1 Doppler cooling

When $\Gamma \gg \omega_0$, the Lorentzian absorption spectrum with width $\sim \Gamma$ is so broad that several motional sidebands can fit within the broad peak. The sidebands are said to be unresolved and cooling in this regime is traditionally called Doppler cooling. The maximum ratio of A^-/A^+, and

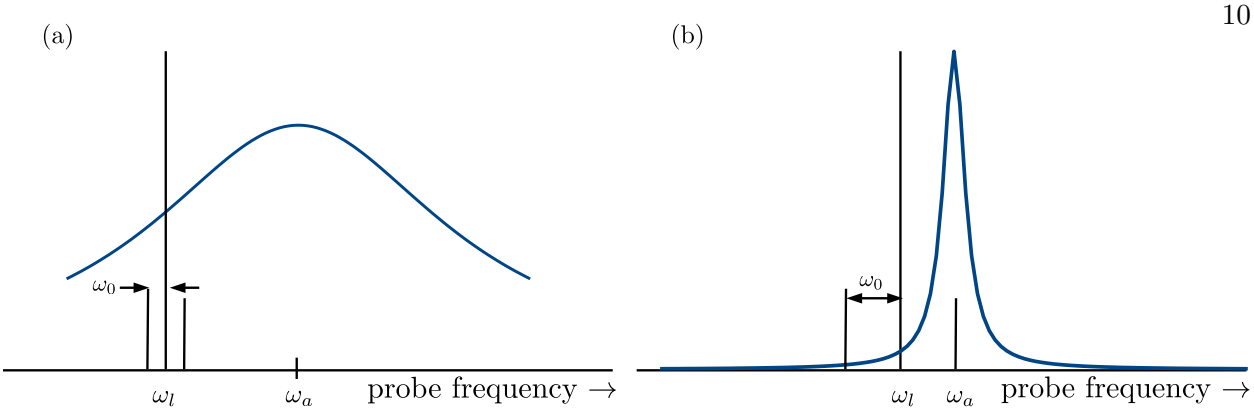

Figure 2.1: Sketch of absorption spectrum and locations of the carrier, motion adding and motion removing sidebands in (a) Doppler cooling and (b) Sideband cooling.

correspondingly, the lowest $\bar{n}_{\rm SS}$ is obtained for the optimum value $\Delta = -\Gamma/2$ [36]. Intuitively, this optimum value can be understood by noting that for a Lorentzian function $f(x) = 1/(1+x^2)$, the maximum fractional change between two points $x \pm \delta x$, characterized by $2\delta x f'(x)/f(x)$, occurs at the the half maximum point corresponding to $x = \pm 1$ and takes the simple value $2\delta x$. Identifying $x = 2\Delta/\Gamma$ and $\delta x = \pm 2\omega_0/\Gamma$, this result can directly be applied to the absorption spectrum, Eq. (2.10), in the regime where $\Gamma \gg \omega_0$. The minimum value of $\bar{n}_{\rm SS}$ is then simply given by

$$\bar{n}_{\rm SS}^{\rm min} \sim \frac{\Gamma}{2\omega_0} \gg 1. \tag{2.15}$$

We avoid writing a strict equality since a rigorous derivation must also account for the previously discussed diffusion cycles. Therefore, in Doppler cooling, the mean occupation, or equivalently, the temperature $k_{\rm B}T = \bar{n}\hbar\omega_0 \sim \hbar\Gamma$, is limited by the lifetime of the excited state.

2.1.5.2 Sideband cooling

In the opposite limit when $\Gamma \ll \omega_0$, the absorption spectrum is so narrow that with the choice of $\Delta = -\omega_0$, the motion removing sideband is exactly on resonance, while the carrier and motion adding sideband are strongly suppressed [36]. The sidebands are now said to be resolved and cooling in this regime is called resolved sideband cooling. At this value of Δ, clearly $A^- \sim \Omega^2/\Gamma$

whereas $A^+ \sim A^-\Gamma^2/\omega_0^2 \ll A^-$. Therefore, the minimum occupation is given by

$$\bar{n}_{\rm SS} \approx \frac{A^+}{A^-} \sim \frac{\Gamma^2}{\omega_0^2} \ll 1. \tag{2.16}$$

Therefore, sideband cooling is an attractive choice for cooling the ion to near ground state occupancies. We note that a popular technique to implement sideband cooling involves creating an artifical narrow line transition using stimulated Raman transitions on a three-level system. However, the general features from the two-level model still apply in that case [126].

2.1.6 Engineering the absorption spectrum using quantum interference

An attractive question to ask is the following. Is it possible to somehow engineer the absorption spectrum so that the asymmetry between the motion removing and motion adding sidebands is greatly enhanced? Furthermore, can the diffusion arising from the carrier transition be completely suppressed? It turns out that these features can be engineered by coupling the state $|e\rangle$ to a third long-lived state $|r\rangle$ as shown in Fig. 2.2(a) [84]. A strong coupling laser with Rabi frequency Ω_c couples the $|r\rangle \leftrightarrow |e\rangle$ transition and is blue detuned so that $\Delta_c > 0$. To obtain the absorption spectrum, a weak probe laser with Rabi frequency $\Omega_p \ll \Omega_c$ couples the $|g\rangle \leftrightarrow |e\rangle$ transition and the excitation probability is studied as its detuning Δ_p is swept across Δ_c. The excited state is assumed to decay with rates Γ_g and Γ_r respectively to the two long-lived states, and its total lifetime is $\Gamma = \Gamma_g + \Gamma_r$. An analytic expression for the steady state value of ρ_{ee} is tedious to derive, but has been done, for example in Refs. [57, 73]. For $\Omega_p \ll \Omega_c$, the expression can be compactly written as

$$\rho_{ee} \approx \frac{1}{\Gamma_g} \frac{4\delta^2\Omega_p^2\Gamma}{4\delta^2\Gamma^2 + \left[\Omega_c^2 - 4\delta(\Delta_c + \delta)\right]^2}, \tag{2.17}$$

where $\delta = \Delta_p - \Delta_c$ is the two-photon detuning from Raman resonance. Figure 2.2(b) shows the absorption spectrum as a function of Δ_p for a specific choice of parameters. The spectrum features a broad resonance, around $\Delta_p \approx 0$ when $\Omega_c \ll \Delta_c$, and a narrow resonance for Δ_p slightly greater than Δ_c. Remarkably, the absorption completely vanishes at Raman resonance, when $\Delta_p = \Delta_c$. The vanishing of the absorption probability from a probe laser when the excited state is coupled to an auxiliary state by a second laser is called electromagnetically induced transparency (EIT).

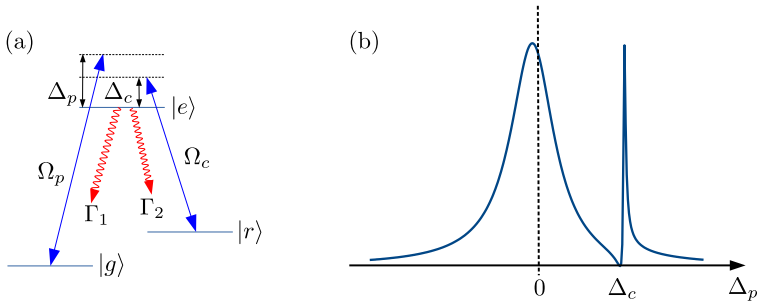

Figure 2.2: Engineering the absorption spectrum using quantum interference. (a) A weak probe laser is scanned across the $|g\rangle \leftrightarrow |e\rangle$ transition as the state $|e\rangle$ is dressed by a strong coupling laser driving the $|r\rangle \leftrightarrow |e\rangle$ transition in a blue detuned regime ($\Delta_c > 0$). (b) The corresponding absorption spectrum displays a Fano profile close to $\Delta_p \approx \Delta_c$.

In the bare basis, the transparency point can be understood as arising from destructive interference between two pathways [73]. In the first pathway, a probe photon is absorbed from $|g\rangle$ and immediately scattered into free space via $|e\rangle$, returning the atom to $|g\rangle$. In the second, a probe photon absorption from $|g\rangle$ is followed by the emission and absorption of a coupling laser photon, before free space scattering from $|e\rangle$ returns the atom to $|g\rangle$. These pathways are depicted in Fig. 2.3.

The two resonances can be understood by considering the dressed states $|\psi_\pm\rangle$ of the system comprising the atom and the coupling laser [84]. With the zero energy reference chosen to be the excited state $|e\rangle$, the energies of the two dressed states are given by

$$E_\pm = \hbar \frac{\Delta_c \mp \sqrt{\Delta_c^2 + \Omega_c^2}}{2}. \tag{2.18}$$

With $\hbar\Delta_c$ the bare energy of the state $|r\rangle$, $|\psi_+\rangle$ ($|\psi_-\rangle$) can be identified with the broad (narrow) resonance in the absorption spectrum shown in Fig. 2.2(b). Further confirmation can be obtained from the form of $|\psi_\pm\rangle$, which for $\Omega_c \ll \Delta_c$ simplify to

$$|\psi_+\rangle = \frac{1}{\sqrt{4\Delta_c^2 + \Omega_c^2}} \left(\Omega_c |r\rangle - 2\Delta_c |e\rangle\right), \; |\psi_-\rangle = \frac{1}{\sqrt{4\Delta_c^2 + \Omega_c^2}} \left(2\Delta_c |r\rangle + \Omega_c |e\rangle\right). \tag{2.19}$$

From the excited state coefficient, the lifetime of these states can be approximately identified as $\Gamma_+ \approx \Gamma$ and $\Gamma_- \approx \Gamma\Omega_c^2/4\Delta_c^2 \ll \Gamma_+$, corresponding respectively to the broad and narrow peaks in the spectrum.

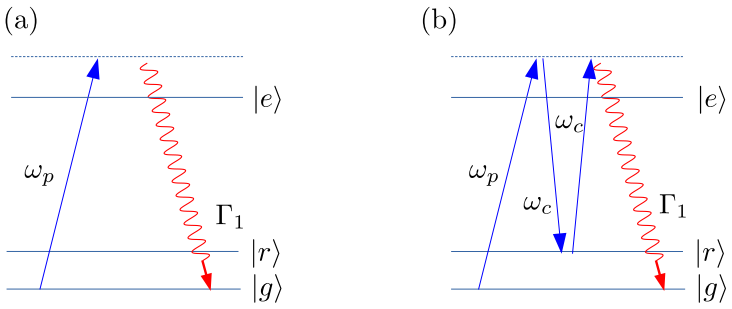

Figure 2.3: The two interfering pathways that transfer the atom from $|g\rangle$ to $|e\rangle$. Subsequent spontaneous emission returns the atom to $|g\rangle$.

2.1.6.1 EIT cooling

From the perspective of cooling, an important feature of the spectrum is that the energy difference between the transparency point and the sharp narrow peak can be tuned via the Rabi frequency Ω_c of the coupling laser [84]. Consider the case when the probe laser is fixed at the detuning $\Delta_p = \Delta_c$. Then, by arranging

$$\frac{\Delta_c + \sqrt{\Delta_c^2 + \Omega_c^2}}{2} - \Delta_c = \omega_0, \tag{2.20}$$

the motion removing sideband at $\Delta_p + \omega_0$ can be brought on resonance with the narrow peak and is therefore strongly enhanced. Simultaneously, the very low absorption probability at $\Delta_p - \omega_0$ strongly suppresses the motion adding sideband. Naturally, this cooling mechanism is called EIT cooling. Notably, diffusion from the carrier transition is nonexistent as the absorption vanishes exactly at $\Delta_p = \Delta_c$. This latter property ensures that for the same cooling rates, EIT cooling achieves lower $\bar{n}_{\mathrm{SS}}$ compared with resolved sideband cooling. Under the optimum condition Eq. (2.20), the minimum value of $\bar{n}_{\mathrm{SS}} = (\Gamma/4\Delta_c)^2$ is attained, indicating that the lowest occupations are obtained when the atom is dressed with a far detuned laser [84]. In contrast to Doppler and sideband cooling, EIT cooling works only for blue detuned probe and coupling lasers. When the coupling laser is red detuned, the absorption spectrum is a mirror image of the one shown in Fig. 2.2(b) (see Ref. [73]), and with $\Delta_c = \Delta_p$, the motion adding sideband is instead enhanced, leading to heating.

As in the case of Doppler and sideband cooling, analytic expressions for the $A^{\pm}$ rates and $\bar{n}_{\mathrm{SS}}$

have also been derived for EIT cooling. The rates can be motivated from the form of Eq. (2.17), although a formal derivation is tedious and involves projection operator techniques [84, 83]. An important feature of the corresponding rate equation is that the Lamb-Dicke parameter η dictating the cooling rate corresponds to the projection of an effective wavevector along the motional axis. Specifically,

$$\eta = |\mathbf{k}_p - \mathbf{k_c}| \cos\phi \sqrt{\frac{\hbar}{2M\omega_0}}, \tag{2.21}$$

where $\mathbf{k}_p, \mathbf{k}_c$ are respectively the wavevectors of the probe and coupling lasers, and ϕ is the angle of the difference wavevector along the motional axis. Furthermore, the results have been generalized to the case when $\Omega_p \approx \Omega_c$, an attractive parameter regime for rapid cooling since the cooling rate scales with the product $\Omega_c\Omega_p$ for a fixed value of $\Omega = \sqrt{\Omega_c^2 + \Omega_p^2}$ [83]. However, the physics is not as intuitive as in the $\Omega_p \ll \Omega_c$ limit presented here.

2.2 Quantum Metrology with pseudospin-1/2 systems

A two-level system such as the toy model we introduced in Section 2.1 can be conveniently mapped onto a spin-1/2 system by defining the following operators

$$\hat{\sigma}^x = (|e\rangle\langle g| + |g\rangle\langle e|)\,,\ \hat{\sigma}^y = -i\,(|e\rangle\langle g| - |g\rangle\langle e|)\,,\ \hat{\sigma}^z = (|e\rangle\langle e| - |g\rangle\langle g|)\,. \tag{2.22}$$

These operators are precisely the Pauli matrices that are ubiquituous in the description of spin-1/2 systems. Specifically, they satisfy the commutation relations $[\hat{\sigma}^j/2, \hat{\sigma}^k/2] = i\epsilon_{jkl}\hat{\sigma}^l$, implying that the vector $\hat{\sigma}/2 = (\hat{\sigma}^x/2)\hat{\mathbf{x}} + (\hat{\sigma}^y/2)\hat{\mathbf{y}} + (\hat{\sigma}^z/2)\hat{\mathbf{z}}$ is a legitimate angular momentum operator. Furthermore, since $\left(\hat{\sigma}^j\right)^2 = 1$, the quantity $\hat{\sigma}^2/4 \equiv S(S+1) = 3/4$, revealing that the total spin $S = 1/2$. We can also define ladder operators $\hat{\sigma}^{\pm} = \hat{\sigma}^x/2 \pm i\hat{\sigma}^y/2$ that correspond to exciting and de-exciting the atom. To connect with spin terminology, we will henceforth generically refer to the two states as $|\uparrow\rangle$ and $|\downarrow\rangle$ in this chapter.

Atoms and atom-like systems provide a variety of degrees of freedom in which spin-1/2 systems can be encoded. Such 'pseudospin-1/2' systems find applications throughout quantum computing, simulation and metrology. For example, optical atomic clocks based on ^{87}Sr atoms rely

on encoding a pseudospin-1/2 system in an ultranarrow linewidth optical transition with $|\downarrow\rangle \equiv {}^1S_0$ and $|\uparrow\rangle \equiv {}^3P_0$ [86]. As a second instance, quantum computing and simulations with trapped ions are often enabled by the ability to encode spins in atomic hyperfine levels [46, 10]. For example, in Chapter 4, we will encounter a motion sensing technique that relies on encoding a spin-1/2 system in the $2s^2S_{1/2}(m_J = -1/2)$ and $2s^2S_{1/2}(m_J = +1/2)$ hyperfine states of $^9Be^+$ ions trapped in a high magnetic field [105, 42, 58]. A very interesting spin encoding is utilized in the case of atomic Bragg interferometers, where a discrete spin-1/2 system is mapped on to a continuous variable, namely the center-of-mass momentum of the atom. Important applications of such interferometers include their use as gravimeters and gravity gradient sensors [1, 31, 27]. We will provide a brief introduction to Bragg interferometers in Section 2.4 as our work in Chapters 7 and 8 revolves around such momentum pseudospin based systems.

2.2.1 The Ramsey sequence

The Ramsey sequence is by far the most important and most common technique for metrology with spin-1/2 systems. The sequence is best illustrated by visualizing pure states of a spin-1/2 system as points on the surface of a Bloch sphere. For the purpose of this discussion, a pure state can be parameterized in spherical coordinates as

$$|\psi(\theta,\phi)\rangle = \cos\frac{\theta}{2}|\uparrow\rangle + e^{i\phi}\sin\frac{\theta}{2}|\downarrow\rangle, \tag{2.23}$$

where θ and ϕ represent polar and azimuthal angles respectively (see Fig. 2.4). In this representation, the south (north) pole corresponds to $|\downarrow\rangle$ ($|\uparrow\rangle$), while points on the equator correspond to equal superpositions of the form

$$|\psi(\theta=\pi/2,\phi)\rangle = \frac{|\downarrow\rangle + e^{i\phi}|\uparrow\rangle}{\sqrt{2}}. \tag{2.24}$$

Measurements with spin-1/2 systems rely on mapping the signal of interest on to the azimuthal phase ϕ. For example, let us suppose that the $|\downarrow\rangle$ and $|\uparrow\rangle$ are nominally separated in

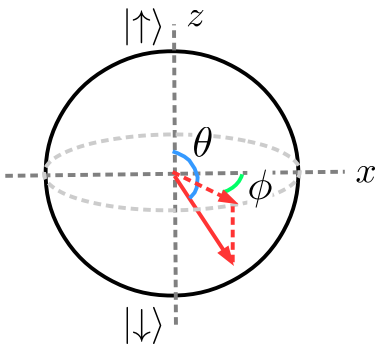

Figure 2.4: Bloch sphere representation of the pure state of a single spin-1/2 system

energy by $E_0 = \hbar\omega_0$. Then, the time evolution of a initial state with $\theta = \pi/2, \phi = 0$ is given by

$$|\psi(T)\rangle = \frac{|\downarrow\rangle + e^{i\omega_0 T}|\uparrow\rangle}{\sqrt{2}}. \tag{2.25}$$

Therefore, the spin transition frequency is mapped on to a total accumulated phase of $\phi(T) = \omega_0 T$. Extending this example further, let us suppose that the energy difference of the spin states increases linearly in the presence of a weak magnetic field. In a frame rotating at ω_0, the accumulated phase $\phi(T) = 0$ in the absence of a magnetic field and $\phi(t) \propto B \times T$ in the presence of an applied field. That is, the magnetic field strength is mapped on to the accumulated phase.

There still remains the question of how this accumulated phase can be measured. In the Ramsey sequence, the accumulated phase is converted into a difference in population between the two states $|\uparrow\rangle$ and $|\downarrow\rangle$. Mathematically, the angle ϕ is mapped on to θ. The sequence is illustrated in Fig. 2.5. The spin is initially prepared in $|\downarrow\rangle$. A $\pi/2$ rotation about the $-y$ axis prepares the spin in an equal superposition of the two spin states with $\phi = 0$. A signal field $\mu(t)$ interacts with the spin for a total time T, leading to a net accumulated phase

$$\phi(T) = G\int_0^T dt\mu(t), \tag{2.26}$$

where G is a proportionality constant. Finally, a second $\pi/2$ rotation about the $-y$ axis takes the state out of the equatorial plane. If $\phi(T) = 0$, the spin ends up in the north pole after the second rotation and the final polar angle $\theta_f = 0$. If $\phi(T) \neq 0$, $\theta_f > 0$ after the second rotation. The

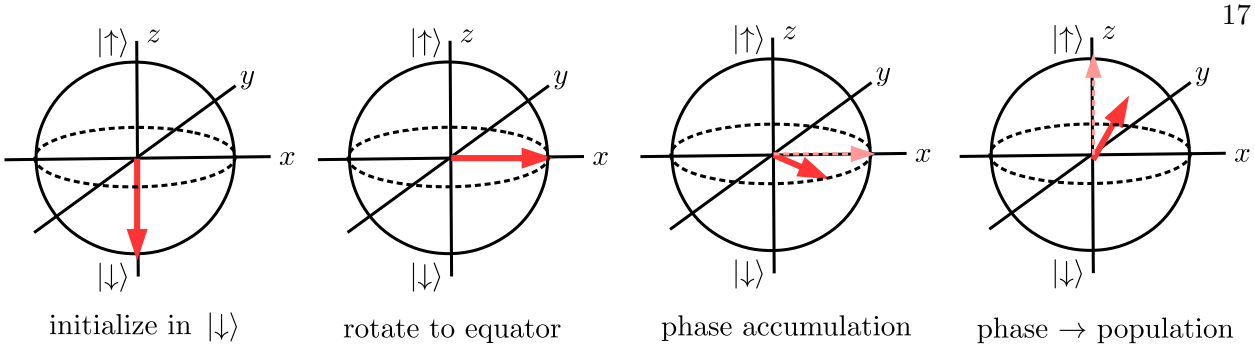

Figure 2.5: State of the spin at different points in the Ramsey sequence.

probability to find the spin in the state $|\uparrow\rangle$ at the end of the sequence is

$$P_\uparrow = \cos^2 \frac{\theta_f}{2} = \frac{1+\cos\theta_f}{2} = \frac{1+\cos\phi(T)}{2}. \tag{2.27}$$

If $\phi(T)$ is linear in the accumulation time T, $P_\uparrow$ oscillates between 0 and 1 as T increases, leading to the so called Ramsey fringes.

With just a single spin, one run of the Ramsey sequence will simply collapse the spin to $|\downarrow\rangle$ or $|\uparrow\rangle$. In order to measure the underlying probabilities, experiments typically employ a large number of spins in each run of the Ramsey sequence, and also repeat the sequence several times for each accumulation time T. The random collapse of each spin means that the measurement precision is limited by quantum noise. We will further discuss this notion of measurement precision, as well as how to improve it using entanglement, in Section 2.3.

2.2.2 Limitations of the Ramsey sequence

A big advantage of the Ramsey sequence is that, in the end, the experimenter has to only measure state populations. Such measurements are facilitated by well established techniques, for example, using fluorescence measurements on cycling transitions [126]. However, let us now analyze some features of the traditional Ramsey sequence, which makes it unsuitable for use in certain situations. Here, we assume that $N \gg 1$ spins are participating in each sequence.

In Section 2.2.1, we emphasized that the Ramsey sequence is designed to measure the net phase $\phi(T)$ accumulated up to some time T. In a single run of the sequence, the population

measurement collapses the state of individual spins, and the next run must begin with re-initializing all spins in the $|\downarrow\rangle$ state. In order to study the time variation of a signal field $\mu(t)$, the sequence has to be repeated at least once for several different accumulation times T so that the time series of $\phi(T)$ versus T can be constructed. The derivative of $\phi(T)$ then yields information about $\mu(t)$. This procedure seems straightforward, but it intrinsically assumes that the signal field is reproducible. If $\mu(t)$ is, for example, derived from a rare phenomenon, then we would like to have a protocol by which the entire time series of $\mu(t)$ can be measured in a single experimental run without re-initializing the spins at all.

A second problem with the Ramsey sequence concerns the variation of $P_\uparrow$ with $\phi(T)$. From Eq. (2.27), the mapping of $\phi(T)$ on to $P_\uparrow$ is one to one only for $\phi(T) \in [0, \pi]$. Phase excursions beyond such an unambiguous interval cannot be uniquely measured within the traditional Ramsey paradigm.

Recent work has attempted to increase the length of the unambiguous interval beyond π by a modification of the Ramsey sequence [112, 63]. First, a phase $\phi(T)$, within the unambiguous interval, is allowed to accumulate over time T. Next, an intermittent rotation converts the phase into a population difference. The subsequent population measurement, however, is coherence preserving in nature. This means that a measurement of the total population in $|\uparrow\rangle$ is performed without gaining knowledge about the state of each individual spin. After measurement, the state is rotated back on to the equatorial plane. The inferred phase is then fed back as an azimuthal rotation that returns the phase of the spins to zero. In this process, the time history of applied phase corrections can be tracked, and the net accumulated phase can be uniquely measured even when it is well outside the unambiguous interval. We note that this procedure also partially overcomes the first problem discussed above as several rotation-measurement-feedback sequences are possible before decoherence effects force re-initialization of the spins and restarting of the experiment.

While this workaround is elegant, it naturally begs the following question. Can we design a scheme where the phase can be continuously monitored even as it accumulates? That is, can we move beyond the Ramsey paradigm of converting the accumulated phase $\phi(T)$ into a population

difference, and attempt to directly measure the instantaneous phase $\phi(t)$? In Chapters 5 and 6, we present such a scheme for continuous real-time tracking of the instantaneous phase $\phi(t)$. Furthermore, it can potentially be combined with a feedback loop to extend the unambiguous interval for phase measurements while avoiding intermittent rotation-measurement-feedback sequences that interfere with the phase accumulation.

2.3 Measurement precision in the Ramsey sequence

Upon measurement, a single spin in a superposition state will collapse to either $|\uparrow\rangle$ or $|\downarrow\rangle$ with fixed probabilities. Because of this inherent randomness, measurements of the accumulated phase are always noisy and it is meaningful to define a measurement precision $\Delta\phi$.

To do so, we first introduce the concept of a collective spin associated with N spin-1/2 systems. The vector components of this collective spin are described by collective angular momentum operators $\hat{J}^j = \sum_{r=1}^{N} \hat{\sigma}_r^j/2, j = x, y, z$. These operators also satisfy the angular momentum commutation relations $[\hat{J}^j, \hat{J}^k] = i\epsilon_{jkl}\hat{J}^l$. Analogous to the spin-1/2 case, raising and lowering operators can be defined as $\hat{J}^{\pm} = \hat{J}^x \pm i\hat{J}^y$.

2.3.1 Coherent spin states

Let us suppose that all of the N spins are initialized in the state $|\psi(\theta = \pi/2, \phi = 0)\rangle$ (Eq. (2.23), that is, they are directed along the x axis. This state is an example of a coherent spin state (CSS) $|\Psi(\theta, \phi)\rangle$, where the collective spin is simply built as a direct product of N identical, uncorrelated spins. Classically, the collective spin can be visualized as the expectation value of the angular momentum vector, $\langle\hat{\mathbf{J}}\rangle = \langle\hat{J}^x\rangle\hat{\mathbf{x}} + \langle\hat{J}^y\rangle\hat{\mathbf{y}} + \langle\hat{J}^z\rangle\hat{\mathbf{z}} = (N/2)\hat{\mathbf{x}}$. Although the mean values of $\hat{J}^y, \hat{J}^z$ are zero, the quantum fluctuations in these quantities do not vanish. For the present state, we have that

$$\langle\left(\hat{J}^y\right)^2\rangle = \frac{1}{4}\left(\sum_{r=1}^{N}\langle(\hat{\sigma}_r^y)^2\rangle + \sum_{r\neq s}\langle\hat{\sigma}_r^y\hat{\sigma}_s^y\rangle\right) = \frac{N}{4}. \tag{2.28}$$

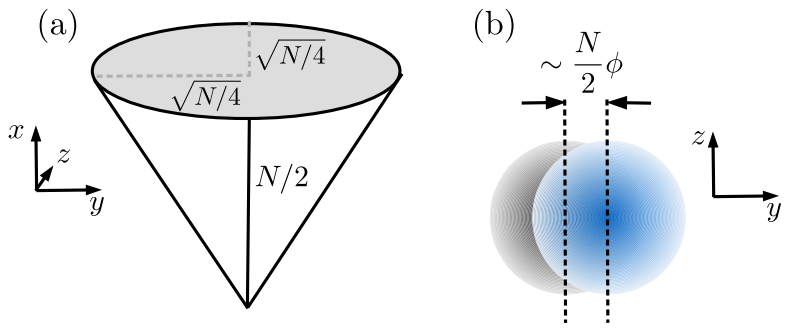

Figure 2.6: Coherent spin state (CSS). (a) Visualization of a CSS as a cone ending in an uncertainty circle. (b) Quantum fluctuations in the components orthogonal to the mean spin direction lead to limited resolution of small rotations.

In calculating the above variance, we have used the properties that $\left(\hat{\sigma}_r^j\right)^2 = 1$ and in this particular state, $\langle \hat{\sigma}_r^y \hat{\sigma}_s^y \rangle = \langle \hat{\sigma}_r^y \rangle \langle \hat{\sigma}_s^y \rangle = 0$. Similarly, we can compute $\langle \left(\hat{J}^z\right)^2 \rangle = N/4$.

Therefore, quantum mechanically, a CSS can be visualized as a cone as shown in Fig. 2.6, with the radius of the circular base representing the isotropic standard deviations in the directions perpendicular to the mean spin direction (MSD) [62]. Rigorously, such states can be represented on a collective Bloch sphere using quasiprobability distributions [76]. However, the notion of a mean spin and an uncertainty circle (or more generally, an uncertainty ellipse) is sufficient for our present discussion, especially since we generally consider $N \gg 1$ spins, in which case the curvature of the spherical phase space can be neglected.

The measurement precision of such a CSS can be determined by considering a rotation by a small angle ϕ about the z axis. Classically,

$$J^y = J^x \tan\phi \approx J^x \phi. \tag{2.29}$$

By the propagation of errors, we have that

$$\Delta\phi = \left| \frac{\Delta J^y}{\partial J^y / \partial \phi} \right|. \tag{2.30}$$

Using the quantum mechanical value of $(\Delta J^y)^2 = N/4$ and $\partial J^y / \partial \phi = J^x = N/2$, we get

$$\Delta\phi_{\mathrm{SQL}} = \frac{1}{\sqrt{N}}. \tag{2.31}$$

The measurement precision $\Delta\phi_{\mathrm{SQL}}$ associated with a coherent spin state is called the standard quantum limit (SQL) in the metrology community [76]. Going through the full sequence of state rotations involved in the Ramsey technique still leads to the very same measurement precision for an initial CSS pointing along the $\pm z$ axes.

2.3.2 Squeezed spin states

The Heisenberg uncertainty relation dictates that for a collective spin (assuming MSD along the x axis),

$$\left(\Delta\hat{J}^y\right)^2\left(\Delta\hat{J}^z\right)^2 \geq \frac{|\langle\hat{J}^x\rangle|^2}{4}. \tag{2.32}$$

States which satisfy the equality are called minimum uncertainty states. We restrict the subsequent discussion to such minimum uncertainty states. The CSS $|\Psi(\theta=\pi/2,\phi=0)\rangle$ is a trivial example of such a state.

The concept of squeezed spin states (SSS) arises with the realization that the equality in Eq. (2.32) only imposes a constraint on the product of the variances in the orthogonal components. This means that the variance in one of these components can be significantly reduced at the expense of increasing the variance in the other component. In other words, as shown in Fig. 2.7, the base of the cone can be 'squeezed' into an ellipse with vastly different lengths for the major and minor axes such that the area of the ellipse is still equal to that of the original circle [62].

Depending on the context, various types of spin squeezing parameters have been introduced to quantify the degree of squeezing. From a metrology perspective, the relevant parameter is the Wineland squeezing parameter ξ_{R} [76]. This parameter has a practical definition as the improvement in phase sensitivity of the prepared squeezed state, compared to a coherent spin state with the same number of spins. Mathematically,

$$\xi_{\mathrm{R}}^2 = \frac{(\Delta\phi)^2}{(\Delta\phi_{\mathrm{SQL}})^2}. \tag{2.33}$$

Values of $\xi_{\mathrm{R}} < 1 \implies \Delta\phi < \Delta\phi_{\mathrm{SQL}}$, signifying an improvement in measurement precision beyond the standard quantum limit.

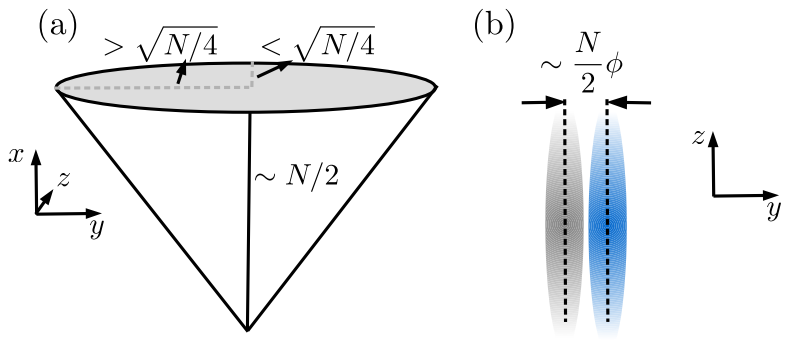

Figure 2.7: Squeezed spin state (SSS). (a) Visualization of an SSS as a cone ending in an uncertainty ellipse with unequal major and minor axes. (b) The minor axis can be oriented along the component accumulating phase in order to improve the resolution of small rotations.

For a collective spin state, the Wineland parameter can be written in terms of the angular momentum components as

$$\xi_{\mathrm{R}}^2 = \min_{\hat{\mathbf{n}} \perp \hat{\mathbf{n}}_{\mathrm{MSD}}} \frac{N \times \mathrm{Var}\left(\hat{\mathbf{J}} \cdot \hat{\mathbf{n}}\right)}{|\langle \hat{\mathbf{J}} \rangle|^2}, \tag{2.34}$$

where $\hat{\mathbf{n}}_{\mathrm{MSD}}$ is the mean spin direction. The factor of N is simply the inverse of the baseline value of $(\Delta\phi_{\mathrm{SQL}})^2$. The remaining fraction corresponds to the minimum possible value of $(\Delta\phi)^2$ given the present state.[1]

2.3.3 Mechanisms to prepare squeezed spin states

Taking the y component as an example, Eq. (2.28) implies that in order to reduce the variance below the $N/4$ level, spin-spin correlations have to be engineered so that $\sum_{r \neq s} \langle \hat{\sigma}_r^y \hat{\sigma}_s^y \rangle < 0$. While many methods to engineer spin-spin interactions have been proposed and demonstrated, a broad class of spin squeezing techniques rely on the availability of a common bosonic channel, such as a cavity mode [11] or a shared vibrational mode [12], which couples to all the constituent spin-1/2 particles.

[1] The formula assumes that the direction corresponding to the minimum variance can always be rotated to align with the spin component that accumulates phase. For example, consider a SSS with MSD along the x axis and with $\left(\Delta \hat{J}^z\right)^2 = N/20$, $\left(\Delta \hat{J}^y\right)^2 = 5N/4$ and $\langle \hat{J}^x \rangle \approx N/2$, so that $\xi_{\mathrm{R}}^2 = 1/5$. In the Ramsey sequence, phase accumulates in the $x - y$ plane. Therefore, the SSS must be first rotated by 90° about the MSD so that the minimum variance component aligns with the y axis and enhances the measurement precision.

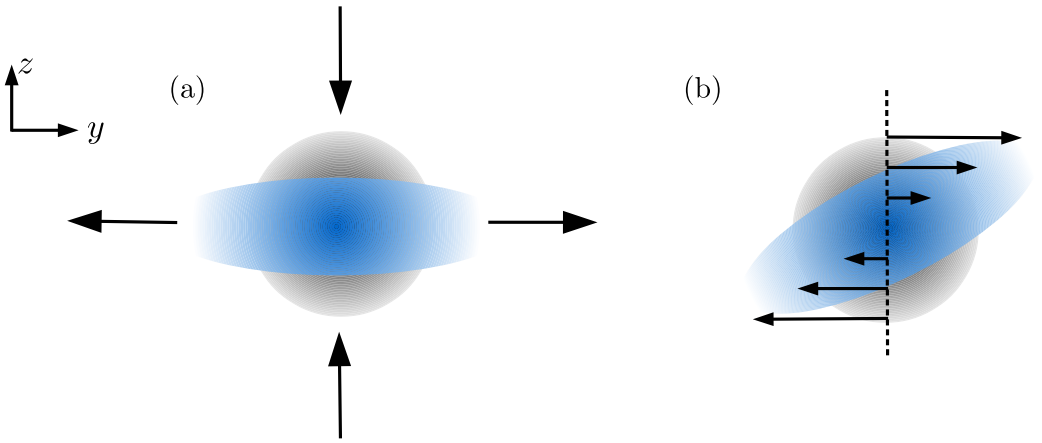

Figure 2.8: Two common mechanisms to generate squeezed spin states involve (a) Squishing the uncertainty ellipse, as happens during squeezing by quantum nondemolition measurements, and (b) Shearing the uncertainty ellipse, as happens during squeezing by one-axis twisting.

Two typical squeezing mechanisms enabled by such a channel are collective quantum non-demolition (QND) measurements [67, 51, 11, 26] and twisting protocols that work using a non-linear interaction [12, 71, 107].

2.3.3.1 Squeezing by quantum non-demolition measurements

Squeezing by QND measurements arises naturally in our proposal for real time phase tracking and we therefore extensively discuss this mechanism in Chapters 5 and 6. Briefly, such schemes involve coupling a Hermitian operator of the common channel with a spin component by engineering a QND Hamiltonian of the form

$$\hat{H}_{\mathrm{QND}} = \hbar g \hat{X} \hat{J}^z. \tag{2.35}$$

Here, $\hat{X}$ could be, for example, the amplitude quadrature, given by $\left(\hat{a} + \hat{a}^\dagger\right)/\sqrt{2}$. Measurement of the conjugate phase quadrature can then enable estimation of the collective spin component $\hat{J}^z$ below the $N/4$ level. In such schemes, the squeezing dynamics proceeds by continuously 'squishing' the measured component of the uncertainty ellipse while elongating the orthogonal component. For simple QND schemes, the variance in the squeezed component falls as $1/T$ with the measurement time T.

2.3.3.2 Squeezing by one-axis twisting

The one axis twisting (OAT) Hamiltonian is a common non-linear mechanism to generate spin squeezing [62]. Here, we will briefly describe the OAT mechanism in its simplest form. The Hamiltonian is of the form

$$\hat{H}_{\mathrm{OAT}} = \hbar\chi \left(\hat{J}^z\right)^2. \tag{2.36}$$

Let us consider an initial CSS along the x axis. The squeezing mechanism can be visualized by considering the dynamics of different points (j_y, j_z) within the uncertainty ellipse. A Hamiltonian of the form $\Omega\hat{J}^z$ leads to a rotation of the CSS around the z axis. Over a short time interval Δt, the transformation is $(j_y, j_z) \to (j_y + N\Omega\Delta t/2, j_z)$. Analogously, H_{OAT} can be visualized as a non-linear rotation where the rotation rate of a point depends on its j_z coordinate. The transformation in the OAT case is given by $(j_y, j_z) \to (j_y + N\chi j_z \Delta t, j_z)$. As a result, the uncertainty ellipse is 'sheared' or twisted over time, leading to reduced variance in one component at the expense of the orthogonal one. The minor axis of the ellipse rotates over time and gets closer to the z axis.

Simple calculations can reveal the rate of squeezing in this mechanism. For sufficiently short times, the state is accurately described by a mean spin, assumed along the x axis and of approximate length $N/2$, and a covariance matrix that captures the quantum fluctuations in the $y-z$ plane. The diagonal components of this covariance matrix evolve as

$$\frac{d}{dt}\langle(\hat{J}^y)^2\rangle = 2N\chi\langle\hat{J}^y\hat{J}^z\rangle_s,\ \frac{d}{dt}\langle(\hat{J}^z)^2\rangle = 0. \tag{2.37}$$

Here, $\langle\hat{A}\hat{B}\rangle_s = \left(\langle\hat{A}\hat{B}\rangle + \langle\hat{B}\hat{A}\rangle\right)/2$ is the symmetric combination of the second order moments. Clearly, all moments involving only $\hat{J}^z$ commute with $\hat{H}_{\mathrm{OAT}}$. The off-diagonal element $\langle\hat{J}^y\hat{J}^z\rangle_s$ evolves as

$$\frac{d}{dt}\langle\hat{J}^y\hat{J}^z\rangle_s = N\chi\langle(\hat{J}^z)^2\rangle. \tag{2.38}$$

In deriving these equations, we have substituted $\hat{J}^x \to N/2$ wherever it appears on the right hand side. The solution to these equations are given by

$$\langle(\hat{J}^z)^2\rangle(t) = \frac{N}{4},\ \langle\hat{J}^y\hat{J}^z\rangle_s(t) = \frac{N^2\chi t}{4},\ \langle(\hat{J}^y)^2\rangle(t) = \frac{N}{4} + \frac{N^3\chi^2t^2}{4}. \tag{2.39}$$

The squared lengths of the major and minor axes of the corresponding uncertainty ellipse are given by the eigenvalues of the covariance matrix

$$\Sigma = \begin{pmatrix} \langle (\hat{J}^y)^2 \rangle & \langle \hat{J}^y \hat{J}^z \rangle_s \\ \langle \hat{J}^y \hat{J}^z \rangle_s & \langle (\hat{J}^z)^2 \rangle \end{pmatrix}. \tag{2.40}$$

The eigenvalues are given by

$$\lambda_\pm = \frac{N}{4}\left[1 + \frac{N^2\chi^2 t^2}{2} \pm \frac{N^2\chi^2 t^2}{2}\left(1 + \frac{4}{N^2\chi^2 t^2}\right)^{1/2}\right]. \tag{2.41}$$

For $t \gg 1/N\chi$, $N\chi t \gg 1$ and the expression under the square root can be Taylor expanded to second order. The two eigenvalues are then respectively given by

$$\lambda_+ \approx \left(N^2\chi^2 t^2\right) \times N/4,\ \lambda_- \approx \frac{N/4}{N^2\chi^2 t^2}. \tag{2.42}$$

Therefore, the minor axis of the uncertainty ellipse shrinks as $1/t^2$ with interaction time t. Furthermore, we can identify $N\chi$ as a characteristic rate for the dynamics. The assumption that the dynamics in the $y-z$ plane can be decoupled from the x axis fails when the major axis becomes comparable to the mean spin length. Therefore, this analysis is valid for times such that

$$\frac{\lambda_+}{N^2/4} \ll 1 \implies N\chi^2 t^2 \ll 1. \tag{2.43}$$

In fact, the dynamics of an initial CSS under the action of $\hat{H}_{\mathrm{OAT}}$ can be computed exactly. Expressions for the minimum attainable variance and spin squeezing parameters that account for the curvature of the collective Bloch sphere can be found in Refs. [76, 62].

2.4 Momentum pseudospins and Bragg interferometers

In Chapters 7 and 8, we will engineer the OAT interaction between pseudospins encoded in the center-of-mass momentum of the atomic wavepackets. We will then study the efficiency of squeezing accounting for the complications arising from the setup and the nature of the spins themselves. Here, we introduce the notion of momentum pseudospins and explain how they form the basis of Bragg interferometers.

Atomic Bragg interferometers are so named because the basic working principle can be visualized as the diffraction of atomic matter waves from periodic potentials of light [27]. Compared to, say, X-ray diffraction from a crystal, where electromagnetic waves are diffracted from periodic arrays of atoms, here the roles of atoms and light are interchanged. Atomic Bragg interferometers are widely used for applications such as tests of fundamental physics [90, 64, 4, 134] and precision measurements of gravitational acceleration [1, 31]. These systems are attractive because of the unique encoding of the spin-1/2 system in two momentum states associated with the center-of-mass motion of the atomic wavepacket. They operate by splitting the wavepacket into two momentum states—that propagate along different spatial paths accumulating a relative phase—and finally recombining them to obtain interference fringes. Throughout the interferometer operation, the atom is confined to the same metastable electronic state, typically the ground state. Although an atom's momentum is a continuous variable, a pseudospin-1/2 system with two discrete states can be mapped on to the external motion in a Bragg interferometer. This mapping requires an initial atomic momentum distribution that is a sharp peak about a central value, so that the distribution serves as one of the pseudospin states. Subsequently, pulses of light resonantly couple this distribution to a second narrow peak that is shifted by an even multiple of the well-defined photon momentum. This shifted distribution serves as the other pseudospin state.

2.4.1 Coherent manipulation of momentum states

To understand how the momentum of the atom can be manipulated, let us consider a toy model of a two-level atom in free space. The initial state of the atom is assumed to be $|g, p\rangle$, where the variable p denotes the momentum of the atom along the z axis in the lab frame. By addressing the atom with two suitable counterpropagating lasers as shown in Fig. 2.9(a), the atom can be coherently transferred to the state $|g, p + 2\hbar k\rangle$. These lasers drive the $|g\rangle \rightarrow |e\rangle$ transition in a far detuned regime so that the state $|e\rangle$ is negligibly occupied. However, as Fig. 2.9(b) illustrates, the two-photon process involving the absorption of a photon from the upward propagating laser and emission into the other laser is arranged to be a resonant process: Momentum conservation dictates

that the atom has gained a momentum of $2\hbar k$ after such a two-photon process. Therefore, energy conservation requires that the two-photon process must also supply the associated excess energy for the atom to occupy the new momentum state. Therefore, the frequencies of the lasers, ω_1 and ω_2 must be arranged such that

$$\hbar\omega_1 - \hbar\omega_2 = \frac{(p+2\hbar k)^2}{2M} - \frac{p^2}{2M}. \tag{2.44}$$

Assuming that the Rabi frequency associated with either laser driving the $|g\rangle \leftrightarrow |e\rangle$ transition is Ω, and that the single photon detuning is Δ, the effective two-photon Rabi rate for the $|g,p\rangle \leftrightarrow |g,p+2\hbar k\rangle$ transition is $\Omega_{\text{eff}} \sim \Omega^2/\Delta$. The recoil frequency $\omega_r = \hbar k^2/2M$ characterizes the energy increase of a stationary atom as a result of absorbing or emitting a single photon. Provided $\Omega_{\text{eff}} \ll 8\omega_r$, the $|g,p\rangle \leftrightarrow |g,p-2\hbar k\rangle$ and $|g,p+2\hbar k\rangle \leftrightarrow |g,p+4\hbar k\rangle$ transitions are far off resonance and the $|g,p\rangle$, $|g,p+2\hbar k\rangle$ manifold can be considered a closed two-level system. A two-photon Bragg transition between these two states is then analogous to two-photon Raman transitions mediated by a far off resonant excited state.

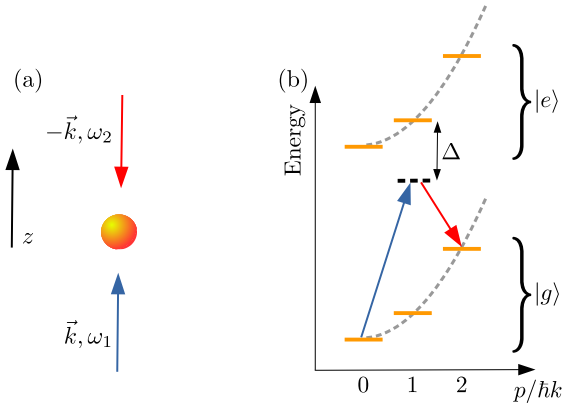

Figure 2.9: Bragg transitions. (a) Two counterpropagating lasers address an upward moving atom with frequencies arranged to satisfy Eq. (2.44). (b) The two lasers drive a resonant transition between two momentum states (taken to be $|0\hbar k\rangle$ and $|2\hbar k\rangle$ here) in the same electronic manifold. The process is reminiscent of a two-photon Raman transition.

Although the above example illustrates the basic concept, significant theoretical and experimental research has been devoted to the design of momentum transfer pulses [85, 118]. Furthermore, experiments are now using large momentum transfer pulses that use a succession of higher-order

multi-photon Bragg pulses [21, 93, 65]. Such pulses enable the spin-1/2 system to be encoded in states with a large momentum difference, greatly increasing the sensitivity to external fields such as gravity.

2.4.2 Phase accumulation in a gravitational field

We conclude this chapter with an illustration of how Bragg interferometers typically operate and how they are capable of sensing gravitation fields (see Fig. 2.10). The sequence of state manipulations is exactly as in a two-path Mach Zehnder interferometer. Here, the beam splitter and mirror operations are achieved using Bragg pulses that rotate the state of each atom by 90° or 180° in a Bloch sphere formed by the two states $|\downarrow\rangle \equiv |p\rangle$ and $|\uparrow\rangle \equiv |p + 2\hbar k\rangle$.

First, the atoms are prepared in a narrow momentum distribution about $|p\rangle$. We ignore the momentum spread in this simple discussion. Two counterpropagating lasers resonantly drive a Bragg transition and place all the atoms in an equal superposition of $|p\rangle$ and $|p + 2\hbar k\rangle$. In the presence of a gravitational field, the momentum of these states linearly decreases with time. Therefore, the energy difference between the two states at a time t is given by

$$\frac{E_\uparrow(t) - E_\downarrow(t)}{\hbar} = 4\omega_r \left(1 + \frac{p - Mgt}{\hbar k}\right), \tag{2.45}$$

where g is the gravitational acceleration and M is the atomic mass. Knowing the approximate value of g, the difference frequency of the two lasers is chirped at a rate α that roughly compensates for this changing transition frequency, thereby ensuring that the lasers always drive near resonant Bragg transitions [78]. The laser frequency difference therefore varies in time as

$$\omega_1(t) - \omega_2(t) = 4\omega_r \left(1 + \frac{p}{\hbar k}\right) - \alpha t. \tag{2.46}$$

The atoms are then allowed to freely evolve for time T. During this time, the two momentum states propagate along different spatial paths that we will denote as A and B as shown in Fig. 2.10.

From Eq. (2.45) and Eq. (2.46), the net phase accumulated relative to the two-photon drive is given by

$$\phi_{BA}^{(1)} = -\int_0^T \left(4\omega_r \frac{Mg}{\hbar k} - \alpha\right) t \, dt = -\frac{1}{2}\left(4\omega_r \frac{Mg}{\hbar k} - \alpha\right) T^2. \tag{2.47}$$

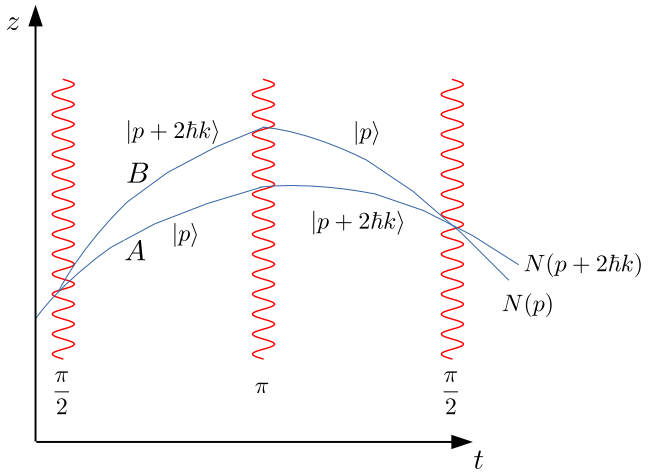

Figure 2.10: Schematic of a two-path Bragg interferometer. The two paths are respectively denoted by A and B. The momentum labels indicate the 'spin up' ($|\uparrow\rangle \equiv |p+2\hbar k\rangle$) and 'spin down' ($|\downarrow\rangle \equiv |p\rangle$) states at different points during the interferometer sequence. Gravitational acceleration causes the momenta of the two states to linearly vary over time.

At time T, a Bragg pulse is applied so that the momenta of the two paths are interchanged. The atoms are then allowed to freely evolve again for time T. The relative phase accumulated between the two paths in this arm is given by

$$\phi_{BA}^{(2)} = -\phi_{AB}^{(2)} = \int_{T}^{2T} \left(4\omega_r \frac{Mg}{\hbar k} - \alpha\right) t \, dt = \frac{3}{2}\left(4\omega_r \frac{Mg}{\hbar k} - \alpha\right) T^2. \tag{2.48}$$

The sign of the accumulated phase in the second arm is opposite to that in the first because the momenta of the two paths have been flipped. Therefore, the net phase accumulated up to time $2T$ is given by

$$\Phi = \phi_{BA}^{(1)} + \phi_{BA}^{(2)} = (2kg - \alpha)\, T^2. \tag{2.49}$$

The net phase accumulated depends on the precise value of g and scales with the square of the interferometer arm time T. Finally, a third Bragg pulse converts the accumulated phase into a population difference. In practice, the net phase accumulated also depends on the phases of the three Bragg pulses, leading to the formula [78]

$$\Phi = (2kg - \alpha)\, T^2 + \phi_1 - 2\phi_2 + \phi_3. \tag{2.50}$$

In a Bloch sphere picture, the phases $\phi_j, j = 1, 2, 3$ set the axis of rotation in the $x - y$ plane for

the three Bragg pulses. Ramsey-type fringes of the population in one of the momentum states are typically obtained by varying the phase of the final Bragg pulse while keeping other parameters fixed.

Finally, we note that the entire sequence can be viewed as a Ramsey sequence with an extra spin echo pulse halfway through the phase accumulation time. The spin echo pulse ensures that dephasing arising from a momentum width is reversed during the second half of the sequence. In real space, such a cancellation ensures that the two atomic wavepackets spatially overlap at the end of the sequence, thereby closing the interferometer.

In Chapters 7 and 8, we will discuss how to engineer squeezing on momentum pseudospins for use in such Bragg interferometers.

Chapter 3

Near ground-state cooling large trapped ion crystals: Theoretical modeling

3.1 Motivation: Why ground-state cooling?

Trapped ions have rapidly evolved to become a leading platform for quantum computing, quantum simulation and metrology [46, 10]. Specifically, ions stored in Penning traps have been demonstrated to be ideal for analog quantum simulation as well as quantum-enhanced sensing, in part because large ion crystals are routinely formed and controlled in this device [8, 77, 5]. For example, planar crystals of tens to hundreds of $^9Be^+$ ions have been used to simulate spin-spin as well as spin-boson models including the Ising [17, 12], transverse-field Ising, as well as Dicke models [101, 24]. Quantum information studies on the growth of entanglement [39] as well as investigations on preparing ground states of exotic Hamiltonians [101, 24] have shown that exciting many-body physics can be studied with this versatile quantum simulator. In addition, ions in Penning traps serve as excellent motion sensors capable of resolving, in a single experimental trial, motional amplitudes smaller than the zero-point fluctuations of the normal modes dictating the motion transverse to the crystal plane [42], thus enabling the detection of extremely weak forces and electric fields.

For implementing these protocols with the NIST Penning trap, the spin is encoded in two hyperfine ground states of $^9Be^+$ [8]. Spin-spin interactions are mediated by the motional drumhead modes, transverse to the crystal plane, that arise from the interplay of the trap potential and the inter-ion Coulomb repulsion, with the spin-motion coupling generated using suitable drive lasers [17]. As a result, excess thermal energy in these normal modes adversely affects the science protocol

being investigated, higlighting the need for sub-Doppler, near ground-state cooling. For example, the fidelity of preparing the ground state of the Dicke model is significantly reduced by the thermal occupation of $\bar{n} \approx 6$ of the center-of-mass (COM) mode, which is close to the Doppler cooling limit [101, 24]. Estimates show that the fidelity significantly improves if the COM mode is cooled down to $\bar{n} \approx 0$. From a metrology standpoint, near ground-state cooling should also greatly improve the motion sensing capability of this platform.

3.2 EIT cooling in a Penning trap: Expectation and challenges

Electromagnetically induced transparency (EIT) promises a path for cooling the entire bandwidth of drumhead modes close to their ground states. In contrast to sideband cooling where the modes are cooled one-by-one by sweeping the two-photon detuning across the bandwidth of modes, EIT cooling can potentially cool the full bandwidth of modes in a single experimental application with no time-varying parameters, allowing for simpler implementation and faster cooling. The naive expectation comes from the well understood physics of EIT cooling of a single trapped ion [83], which we now recall briefly. The ion is assumed to have a closed three-level electronic manifold consisting of two long-lived states, such as the hyperfine ground states of $^9Be^+$, and an excited state (see Fig. 3.1). Two strong dressing lasers couple the long-lived states to the excited state and are equally blue detuned from their respective transitions. EIT cooling can be understood by considering the absorption of a fictitious weak probe coupling one of the long-lived states to the excited state. As shown in Fig. 3.2, the steady-state absorption spectrum has a unique profile as the probe detuning Δ_P is swept, with the absorption exactly vanishing when the probe detuning equals the dressing detuning Δ_D. A sharp peak immediately follows this transparency point and the separation between this peak and the transparency point can be tuned using the dressing laser powers. For a trapped ion, the motion-adding and motion-removing sidebands of the dressing lasers serve as weak probes that sample this absorption spectrum. Tuning the separation between the sharp peak and the transparency point to match the motional frequency causes the motion-removing sideband to be strongly enhanced and the motion-adding sideband to be strongly

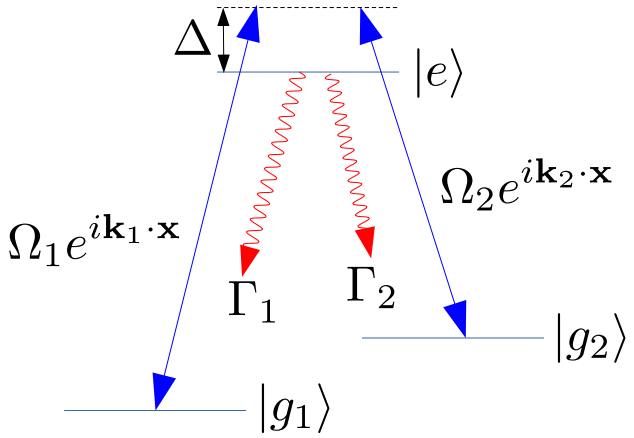

Figure 3.1: Two EIT lasers address the ion, with one driving the $|g_1\rangle \leftrightarrow |e\rangle$ transition and the other driving the $|g_2\rangle \leftrightarrow |e\rangle$ transition in a blue-detuned regime ($\Delta > 0$).

suppressed, leading to highly efficient cooling. In the Penning trap, by tuning this separation to coincide with the frequency of the COM mode, which is the highest frequency drumhead mode, all the drumhead modes have highly asymmetric motion-removing and motion-adding sidebands, which should produce efficient cooling over the full bandwidth of these modes. In this chapter, we theoretically investigate this idea under realistic experimental conditions employed in the NIST Penning trap.

The unique challenges confronted in implementing EIT cooling in a Penning trap further motivate our theoretical study of the prospects for its success. First, ions stored in a Penning trap are constantly revolving around the trap center and therefore, in general, experience time-varying Doppler shifts on the applied dressing lasers. Second, experimental constraints as well as a compromise between the speed of cooling and the final temperature dictate that the timescales for the electronic and motional degrees of freedom may not be sufficiently well separated to adiabatically eliminate the electronic degrees of freedom, as was done in the initial analysis of trapped-ion EIT cooling [83, 84]. Third, although EIT cooling has been used to cool all the radial modes of a linear chain of up to 18 ions [68], the dynamics of simultaneously EIT cooling several tens to hundreds of normal modes that can interact via the applied lasers is not well understood and could be very different from the single-ion case.

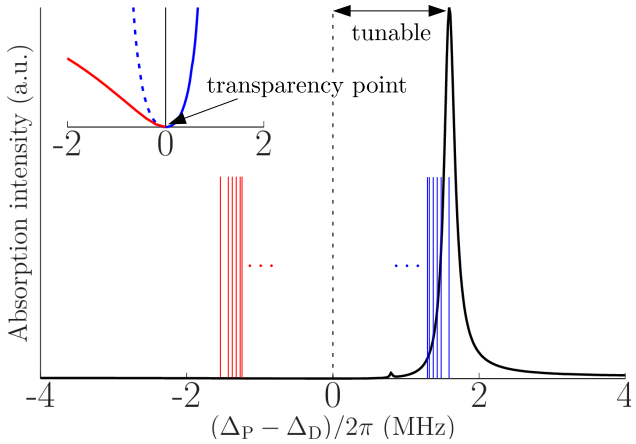

Figure 3.2: EIT absorption spectrum with laser parameters relevant to the NIST EIT cooling experiment. Two strong dressing lasers, with equal Rabi frequencies and equal detunings from their respective transitions, couple two long-lived states to an excited state in a closed three-level system. The absorption from a weak probe is plotted as the probe detuning Δ_P is scanned across the dressing detuning Δ_D. The motion-removing (blue impulses) and motion-adding (red impulses) sidebands can be interpreted as weak probes that sample this spectrum. Inset: Close-up near $(\Delta_P - \Delta_D)/2\pi = 0$, with a magnified y-axis, showing the zero at the transparency point as well as the asymmetry in the spectrum on either side of this point. The blue dashed line is a mirror image of the spectrum on the blue-detuned side, drawn on the red-detuned side to highlight the asymmetric growth of the absorption away from the transparency point. The dressing lasers have equal detuning $\Delta_D/2\pi \equiv \Delta^0/2\pi = 360$ MHz, and equal Rabi frequency $\Omega_{opt}(\Delta^0)/2\pi \approx 33.9$ MHz. The Rabi frequency of the weak probe is $\Omega_P = 0.05\ \Omega_{opt}(\Delta^0)$. The decay rates from the excited state to the two long-lived states are $\Gamma_1/2\pi = 6$ MHz, $\Gamma_2/2\pi = 12$ MHz. (See the discussion in Section 3.4 and Eq. (3.14) for a detailed explanation of the parameters.)

3.3 Summary of predictions

At the outset, we summarize the major predictions from our study. Under typical experimental conditions, EIT cooling leads to near ground-state occupancies for all the drumhead modes, spread over a bandwidth of hundreds of kilohertz, of large ion crystals in a Penning trap. The cooling of the COM mode has a time constant of few tens of μs. Further, under suitable experimental conditions, the cooling rate of the COM mode increases with the number of ions in the crystal. This latter result leads us to predict that the measured cooling of multi-ion crystals will be faster than the rate expected if the ions cooled independently. These predictions have been verified by the successful demonstration of EIT cooling with more than 100 ions [58], where significant sub-Doppler cooling, strongly suggestive of near-ground state cooling, has been observed over the full

bandwidth of drumhead modes. Quantitative measurements on the COM mode reveal occupations of $\bar{n} \approx 0.3 \pm 0.2$, and a measured cooling constant $\tau \approx 28\ \mu$s. The measured cooling rate is faster than the expected single-ion rate under the same experimental conditions.

The rest of this chapter is devoted to the modeling procedures and the numerical results. In Section 3.4, we describe the NIST Penning trap and proceed to set up the master equation for the EIT cooling of multiple ions. In Section 3.5, we use a toy model of a single revolving ion to illustrate the degrading effects of the time-varying Doppler shifts as well as demonstrate the invalidity of the adiabatic elimination procedure in our system. In Section 3.6, we first build a Gaussian model for approximately studying the cooling dynamics for multiple ions, and demonstrate the near-ground state cooling of the COM mode for crystals with up to $N = 37$ ions. By comparing the cooling transients from our Gaussian model to full density matrix calculations for a single ion, we show the build-up of beyond Gaussian correlations between the system degrees of freedom, which we are able to reproduce by systematically extending our approximate model beyond the Gaussian regime. Our improved model predicts a surprising enhancement in the cooling rate of the COM mode with increasing number of ions that is not captured by the Gaussian model. In Section 3.7, we show how EIT cooling works efficiently over the full bandwidth of drumhead modes of crystals with as many as 120 ions, resulting in near ground state occupancies for all these modes. In Section 3.8, we briefly demonstrate the expected robustness of EIT cooling to small misalignments of the dressing lasers. We conclude with a brief summary in Section 3.9, where we also discuss possible future extensions of our work.

3.4 Modeling the experiment

3.4.1 NIST Penning trap

The NIST Penning trap is used to routinely produce, control and manipulate planar ion crystals of tens to hundreds of $^9Be^+$ ions [8]. A static electric quadrupole field is used to achieve transverse confinement, while the addition of a strong transverse magnetic field ensures radial

confinement. Potentials applied to electrodes arranged symmetrically around the z-axis generate the required electric fields and a superconducting magnet produces a strong magnetic field of 4.46 T. The $\mathbf{E} \times \mathbf{B}$ drift of the ions arising from the combination of the magnetic field and the azimuthally symmetric electric fields causes the ions to revolve around the trap center. The frequency of the crystal rotation can be precisely controlled and stabilized by applying a weak rotating potential on the electrodes. Typically, this 'rotating wall' potential is used to stabilize the rotation frequency of the crystal to $\omega_r/2\pi = 180$ kHz. When the radial confinement is weak compared to the transverse confinement, the ions form a 2D planar crystal with an approximate triangular lattice (see Fig. 3.3 for an illustration). The strength of the transverse harmonic confinement is characterized by a trapping frequency that is also the frequency of the transverse center-of-mass (COM) mode, ω_{COM}, of the ion crystal. A planar ion crystal with N ions has $3N$ normal modes of motion, $2N$ of which are in-plane modes superposed on the crystal rotation, and N of which are drumhead modes transverse to the crystal plane. The COM mode is the highest-frequency drumhead mode. For the experiments we model here, $\omega_{\mathrm{COM}}/2\pi \approx 1.57 - 1.59$ MHz, tunable using trap parameters. The $2N$ in-plane modes consist of N high frequency cyclotron modes and N low frequency magnetron modes. Typical frequencies characterizing the three branches are summarized in Table 3.1. Further discussion of these modes is postponed to Chapter 4.

Branch	Displacement	Typical frequency
Drumhead	z axis	$1 - 1.59$ MHz
Cyclotron	$x - y$ plane	$7.2 - 7.3$ MHz
Magnetron	$x - y$ plane	$0 - 170$ kHz

Table 3.1: Summary of approximate characteristic frequencies for the three branches of modes for two dimensional crystals in the NIST Penning trap.

3.4.2 Master equation model

We consider singly-charged positive ions with a closed three-level electronic structure loaded in a Penning trap (see Fig. 3.1). The two hyperfine ground states of each ion are labeled $|g_1\rangle$ and

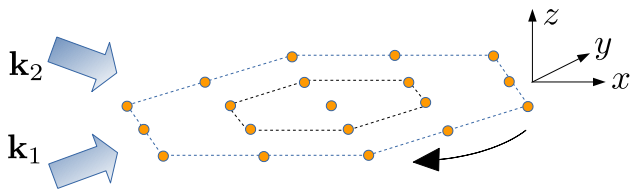

Figure 3.3: Experimental setup to cool ions in a Penning trap using electromagnetically induced transparency (EIT). Two EIT lasers address the ion crystal at angles $\pm\theta$ with respect to the x-axis. The curved arrow indicates the rotation direction in the x-y plane.

$|g_2\rangle$. Two EIT lasers are respectively blue-detuned from the $|g_1\rangle \leftrightarrow |e\rangle$ and $|g_2\rangle \leftrightarrow |e\rangle$ transitions, where $|e\rangle$ is an excited state separated from the two ground states by optical frequencies. The two EIT lasers are incident on the planar ion crystal at angles $\pm\theta$ with respect to the plane of the crystal, which we take to be the x-y plane. The $\{|e\rangle, |g_1\rangle, |g_2\rangle\}$ manifold is a closed system, with decay rates of Γ_1 and Γ_2 for the $|e\rangle \to |g_1\rangle$ and $|e\rangle \to |g_2\rangle$ pathways respectively. We will adopt the shorthand notation $\sigma_{\alpha\beta}$ to denote the internal state operator $|\alpha\rangle\langle\beta|$.

In the Schrödinger picture, the Hamiltonian for the interaction of the EIT lasers with a single ion is $H^{\mathrm{S}} = H_0^{\mathrm{S}} + H_1^{\mathrm{S}}(t)$, where

$$H_0^{\mathrm{S}} = -\sum_{\mu} \left(\omega_e - \omega_{g_\mu}\right) \sigma_{g_\mu g_\mu} \tag{3.1}$$

and

$$H_1^{\mathrm{S}}(t) = \sum_{\mu} \frac{\Omega_\mu}{2} \left(e^{i(\mathbf{k}_\mu \cdot \mathbf{r}(t) - \omega_\mu t)} \sigma_{e g_\mu} + \mathrm{H.c.} \right), \tag{3.2}$$

where the index $\mu = 1, 2$ accounts for the two ground states and the two EIT lasers coupling them to $|e\rangle$. Here, $\omega_e - \omega_{g_\mu}$ are the $|g_\mu\rangle \leftrightarrow |e\rangle$ transition frequencies, Ω_μ are the Rabi frequencies for the laser-ion interaction, and ω_μ and $\mathbf{k}_\mu$ are the angular frequencies and propagation vectors for the two EIT lasers. Eventually, we will describe the motion along the z-direction using a set of quantized normal modes, and add the self-energy terms associated with these quantum harmonic oscillators to the interaction Hamiltonian. Throughout this Chapter, we have set $\hbar = 1$, unless we explicitly specify otherwise. For brevity, we have also dropped hats on the operators in this Chapter.

Since any given ion in the Penning trap is undergoing a coherent rotation in the x-y plane,

its position $\mathbf{r}(t)$ is

$$\mathbf{r}(t) = \left(x(0) + \int_0^t dt' v_x(t')\right)\hat{\mathbf{x}} + \left(y(0) + \int_0^t dt' v_y(t')\right)\hat{\mathbf{y}} + z(t)\hat{\mathbf{z}}, \tag{3.3}$$

Here we are neglecting any thermal motion in the plane of the ion crystal and assume $v_x(t')$ and $v_y(t')$ arise from the coherent circular motion caused by the $\mathbf{E}\times\mathbf{B}$ drift, which is the dominant in-plane motion. We assume that the laser beams are propagating in the x-z plane, so that $\mathbf{k}_1 = k_{1,x}\hat{\mathbf{x}} + k_{1,z}\hat{\mathbf{z}}$ and $\mathbf{k}_2 = k_{2,x}\hat{\mathbf{x}} + k_{2,z}\hat{\mathbf{z}}$.

We then transform to an interaction picture with a time-dependent 'free evolution' Hamiltonian $H_f^{\mathrm{S}}(t)$ given by

$$H_f^{\mathrm{S}}(t) = \quad -\sum_\mu \left\{\omega_\mu - k_{\mu,x} v_x(t)\right\} \sigma_{g_\mu g_\mu}. \tag{3.4}$$

The interaction picture transformation is very similar to the usual case with a time-independent free evolution Hamiltonian because $H_f^{\mathrm{S}}(t)$, $H_f^{\mathrm{S}}(t')$ commute at all times t, t'. The interaction Hamiltonian in this frame, given by the transformation $H^{\mathrm{I}}(t) = e^{i\int_0^t dt' H_f^{\mathrm{S}}(t')}(H_0^{\mathrm{S}} + H_1^{\mathrm{S}}(t) - H_f^{\mathrm{S}}(t))e^{-i\int_0^t dt' H_f^{\mathrm{S}}(t')}$, is

$$H^{\mathrm{I}}(t) = \sum_\mu \Delta_\mu(t)\sigma_{g_\mu g_\mu} + \sum_\mu \frac{\Omega_\mu}{2}\left\{e^{ik_{\mu,x}x(0)}e^{ik_{\mu,z}z(t)}\sigma_{eg_\mu} + \mathrm{H.c.}\right\}, \tag{3.5}$$

where $\Delta_\mu(t) = \Delta_\mu^0 - k_{\mu,x}v_x(t)$ are the effective detunings of the EIT lasers as seen by the ion, with $\Delta_\mu^0 = \omega_\mu - (\omega_e - \omega_{g_\mu})$. For an ion with initial position $\{x(0), y(0)\}$, the x-component of the velocity is $v_x(t) = \omega_r(y(0)\cos\omega_r t - x(0)\sin\omega_r t)$, where ω_r is the angular frequency of the rotating wall potential.

To perform EIT cooling, we tune the EIT lasers to satisfy the two-photon resonance on the blue-detuned side [83], i.e. $\Delta_1^0 = \Delta_2^0 \equiv \Delta^0 > 0$. Further, the lasers are aligned such that their difference wavevector lies along the z-axis. This implies $k_{2,x} = k_{1,x}$ and $k_{2,z} \approx -k_{1,z}$. However, we will develop the theory without these two simplifications, and only apply these conditions numerically. For N ions in the Penning trap, the interaction Hamiltonian generalizes straightforwardly as a sum over all ions.

The equilibrium crystal configuration results from the balance of the trap potential and the inter-ion Coulomb repulsion. The transverse motion of the N ions about their equilibrium positions are not independent, instead being described by a set of N collective normal modes with frequencies ω_n, $n = 1, 2, \ldots, N$ and amplitudes $\mathcal{M}_{jn}$ at each ion j. The frequencies ω_n and the column vectors of the matrix $\mathcal{M}$ are respectively obtained as the eigenvalues and eigenvectors of the potential energy matrix associated with the coupled transverse harmonic motion of the ions [124]. The transverse displacement of any ion j can be expressed in terms of the N quantized drumhead modes of the ion crystal as

$$z_j(t) = \sum_{n=1}^{N} \sqrt{\frac{\hbar}{2M\omega_n}} \mathcal{M}_{jn} \left(b_n e^{-i\omega_n t} + b_n^\dagger e^{i\omega_n t} \right), \tag{3.6}$$

where $b_n^\dagger, b_n$ are the creation and annihilation operators for the normal mode n.

The time-dependent exponentials in Eq. (3.6) can be recast as self-energy terms, leading to the total interaction Hamiltonian

$$H^{\mathrm{I}}(t) = \sum_n \omega_n b_n^\dagger b_n + \sum_{j,\mu} \Delta_{\mu,j}(t) \sigma^j_{g_\mu g_\mu} + \sum_{j,\mu} \frac{1}{2} \left\{ \Omega_{\mu,j} e^{i k_{\mu,z} z_j} \sigma^j_{e g_\mu} + \mathrm{H.c.} \right\}, \tag{3.7}$$

where the displacement operators z_j are now simply $z_j = \sum_n \sqrt{\hbar/2M\omega_n} \mathcal{M}_{jn} \left(b_n + b_n^\dagger \right)$.

Here, the instantaneous detunings experienced by each ion is different, depending on the x-component of the ion's velocity at that time point. In writing Eq. (3.7), the complex phase factors associated with the initial positions of the ions have been absorbed into the (now complex) Rabi frequencies. Further, for large ion crystals, the spatial profile of the EIT lasers over the extent of the crystal may be important, and therefore $\Omega_{1(2),j} \equiv \Omega^0_{1(2)}\left(x_j(t), y_j(t)\right) e^{i k_{1(2),x} x_j(0)}$, i.e. the amplitude of the Rabi frequency is in general a function of the instantaneous in-plane position of the rotating ion.

Spontaneous emission from the excited level $|e\rangle$ to the two ground states is accounted for using dissipation terms written in Lindblad form, i.e. for any jump operator O, the dissipation term takes the form $\mathcal{D}[O]\rho = O\rho O^\dagger - \frac{1}{2} O^\dagger O \rho - \frac{1}{2} \rho O^\dagger O$, where ρ is the density matrix of the system at hand. Since we are interested in the effect on the motion along the z-direction, the dissipation terms must account for the recoil momentum along the z-axis due to spontaneous emission [28].

Therefore, the Lindblad term for ion j, including recoil associated with spontaneous decay of $|e\rangle$ to $|g_\mu\rangle$, is

$$\mathcal{D}_{\mu,j}\rho = \Gamma_\mu \left\{ \int_{-1}^{1} du \mathcal{N}_\mu(u) \sigma^j_{g_\mu e} e^{-ik_{\rm sc} z_j u} \rho e^{ik_{\rm sc} z_j u} \sigma^j_{e g_\mu} - \frac{1}{2}\sigma^j_{ee}\rho - \frac{1}{2}\rho\sigma^j_{ee} \right\}, \tag{3.8}$$

where Γ_μ is the spontaneous decay rate of $|e\rangle \to |g_\mu\rangle$, $\mathbf{k}_{\rm sc}$ is the wavevector associated with the spontaneously emitted photon, $u = \cos\theta_{\rm sc}$, with $\theta_{\rm sc}$ the angle between $\mathbf{k}_{\rm sc}$ and the z-axis, and $\mathcal{N}_\mu(u)$ is the normalized dipole radiation pattern associated with the transition. Finally, the master equation for EIT cooling of N ions in a Penning trap is given by

$$\dot{\rho} = -i[H^{\rm I}(t), \rho] + \sum_{j,\mu} D_{\mu,j}\rho, \tag{3.9}$$

where $H^{\rm I}(t)$ and $D_{\mu,j}\rho$ are as in Eq. (3.7) and Eq. (3.8) respectively.

3.4.2.1 Lamb-Dicke regime

When the condition $\langle (k_{\mu,z} z_j)^2 \rangle^{1/2} \ll 1$ is satisfied for every ion, the motion is in the Lamb-Dicke regime [126] and the master equation can be expanded in a series expansion in $k_{\mu,z} z_j$ [83]. In our setup, the angles $\pm\theta$ are such that the z-components $k_{\mu,z}$ are (a) not too large to cause beyond Lamb-Dicke regime dynamics, and (b) not too small that the cooling is weak. For any wavevector, it is useful to recast its coupling to the z-motion in terms of the Lamb-Dicke parameters associated with the drumhead modes as

$$k_z z_j = \sum_{i=1}^{N} \eta_n^{k_z} \mathcal{M}_{jn} (b_n + b_n^\dagger), \tag{3.10}$$

where $\eta_n^{k_z} = k_z \sqrt{\frac{\hbar}{2M\omega_n}}$ is the Lamb-Dicke parameter [126] for mode n, associated with a wavevector whose z-component is k_z. Expanding the master equation Eq. (3.9) up to second-order in the Lamb-Dicke parameters results in

$$\dot{\rho} = \mathcal{L}_0\rho + \mathcal{L}_1\rho + \mathcal{L}_2\rho. \tag{3.11}$$

Here,

$$\begin{aligned}\mathcal{L}_0\rho &= -i[H_0(t),\rho] + \sum_{\mu,j}\Gamma_\mu \mathcal{D}[\sigma^j_{g_\mu e}]\rho,\\ \mathcal{L}_1\rho &= -i[H_1,\rho],\\ \mathcal{L}_2\rho &= -i[H_2,\rho] + \mathcal{K}_2\rho,\end{aligned} \tag{3.12}$$

with

$$\begin{aligned}H_0(t) &= \sum_n \omega_n b_n^\dagger b_n + \sum_{j,\mu}\Delta_{\mu,j}(t)\sigma^j_{g_\mu g_\mu} + \sum_{j,\mu}\frac{\Omega_{\mu,j}}{2}\sigma^j_{eg_\mu} + \text{H.c.},\\ H_1 &= \sum_{j,n,\mu}\frac{i\lambda^\mu_{jn}\Omega_{\mu,j}}{2}X_n\sigma^j_{eg_\mu} + \text{H.c.},\\ H_2 &= -\sum_{j,n,k,\mu}\frac{\lambda^\mu_{jn}\lambda^\mu_{jk}\Omega_{\mu,j}}{4}X_nX_k\sigma^j_{eg_\mu} + \text{H.c.},\\ \mathcal{K}_2\rho &= \sum_{j,n,k,\mu}\frac{\Gamma_\mu}{2}\langle u^2\rangle_{eg_\mu}\lambda^{\text{sc}}_{jn}\lambda^{\text{sc}}_{jk}\mathcal{K}_2\rho\sigma^j_{g_\mu e}\left(2X_n\rho X_k - X_nX_k\rho - \rho X_nX_k\right)\sigma^j_{eg_\mu},\end{aligned} \tag{3.13}$$

where $X_n = b_n + b_n^\dagger$ and $\lambda^\mu_{jn} = \eta_n^{k_{\mu,z}}\mathcal{M}_{jn}$, $\lambda^{\text{sc}}_{jn} = \eta_n^{k_{\text{sc}}}\mathcal{M}_{jn}$ are dimensionless electronic-motional coupling strengths. The quantity $\langle u^2\rangle_{eg_\mu}$ is the variance of $u = \cos\theta_{\text{sc}}$ taken with respect to the dipole radiation pattern $\mathcal{N}_{eg_\mu}(u)$ associated with the $|e\rangle \to |g_\mu\rangle$ decay. The master equation, Eq. (3.11), is the starting point for our analysis of EIT cooling of ions in the Penning trap.

3.4.3 Parameters from the NIST EIT cooling experiment

In the NIST EIT cooling experiment with $^9\text{Be}^+$ ions, the transverse magnetic field of $B = 4.46$ T leads to a splitting of 124 GHz between the $2s^2S_{1/2}(m_J = -1/2)$ and $2s^2S_{1/2}(m_J = +1/2)$ levels [8], labeled as $|g_1\rangle$ and $|g_2\rangle$ respectively. The $|g_1\rangle \leftrightarrow |e\rangle$ transition frequency is $\omega_{g_1e}/2\pi \approx 957$ THz. The two EIT lasers, with σ^+ and π polarizations are oriented at $\pm 10^\circ$ with respect to the x-axis and respectively couple the $|g_1\rangle$ and $|g_2\rangle$ levels to the excited level $2p^2P_{3/2}(m_J = +1/2)$, labeled as $|e\rangle$. They are blue detuned with equal detuning Δ^0 from their respective transitions by hundreds of megahertz. These lasers generate sufficient power to give Rabi frequencies of tens of megahertz. The beam diameters (≈ 1 mm) of the EIT lasers are large compared to the diameters

of the ion crystals ($\leq$ 300 μm) so that we can assume constant laser intensities over the spatial extent of the crystal. The decay rates out of $|e\rangle$ are $\Gamma_1/2\pi \approx 6$ MHz and $\Gamma_2/2\pi \approx 12$ MHz, with $\langle u^2\rangle_{eg_1} = 2/5$ and $\langle u^2\rangle_{eg_2} = 1/5$.

For all the results in this chapter, we operate at the expected optimum EIT cooling condition for the COM mode of a stationary ion [83] given by $\Omega_1^2 + \Omega_2^2 = 4\omega_{\mathrm{COM}}(\omega_{\mathrm{COM}} + \Delta^0)$, and assume equal Rabi frequencies, i.e. $\Omega_1 = \Omega_2 = \Omega_{\mathrm{opt}}$, so that

$$\Omega_{\mathrm{opt}}(\Delta^0) = \sqrt{2\omega_{\mathrm{COM}}(\omega_{\mathrm{COM}} + \Delta^0)}, \tag{3.14}$$

where we use the value $\omega_{\mathrm{COM}}/2\pi = 1.59$ MHz. Further, we assume the rotation frequency of the crystal is $\omega_r/2\pi = 180$ kHz.

3.5 A single revolving ion

3.5.1 Time-varying Doppler shifts

A toy model of a single ion revolving around the trap center in the x-y plane can shed light on the impact of the in-plane motion on the cooling of the transverse motion. We recall that the circular in-plane motion of the ion causes a sinusoidally modulated Doppler shift, with the precise form of the modulation detailed in the paragraph immediately following Eq. (3.5). For a single ion, we are able to perform full density matrix computations using the master equation, Eq. (3.11).

We set the detuning $\Delta^0/2\pi \approx 180$ MHz, and operate with equal Rabi frequencies $\Omega_{\mathrm{opt}}(\Delta^0)$ given by Eq. (3.14). We assume that a preceding Doppler cooling stage initializes the transverse motion of the ion to a thermal state with $\bar{n} = 5$. Typically, EIT cooling is applied after initializing the ion(s) in $|g_1\rangle$ by optical pumping. Figure 3.4 shows the decrease in the thermal occupation $\bar{n}$ with time as the EIT lasers address a single revolving ion, for different distances of the ion from the trap center. For a detuning ~ 180 MHz, the ion experiences effective red detunings for parts of its trajectory for a radius $r \gtrsim 50$ μm. Consequently, the ion undergoes heating in these regions, leading to slower cooling and higher final occupancies at larger radii (see inset of Fig. 3.4).

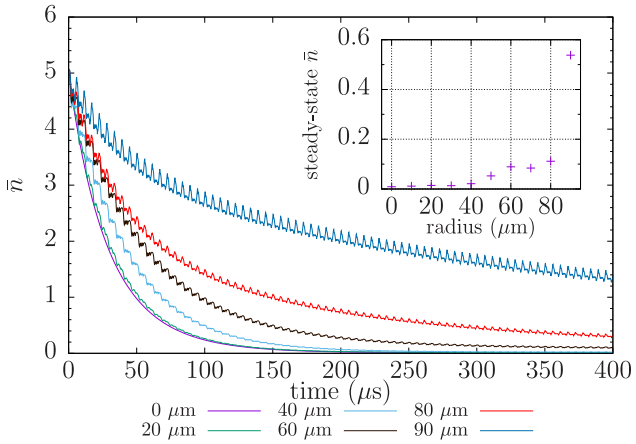

Figure 3.4: Cooling of the transverse motion over time, for a single ion revolving around the trap center at different radii. The cooling is slower at larger radii because of time-varying Doppler shifts modulating the detunings of the EIT lasers as seen by the ion. Inset: The steady-state occupation also increases with distance from the trap center. Here, $\Delta^0/2\pi = 180$ MHz, $\Omega_1/2\pi = \Omega_2/2\pi = \Omega_{\rm opt}(\Delta^0)/2\pi \approx 24$ MHz.

Therefore, sufficiently large detunings have to be used, so that ions at the outer boundary of large crystals still experience an effective blue detuning of the EIT lasers.

3.5.2 Timescale for internal dynamics

An ion located at the trap center experiences no Doppler shifts, and hence, we could argue that analytical expressions derived elsewhere [83] for EIT cooling of a single ion might be valid in such a situation. With the EIT wavevectors making an angle of $\pm 10^\circ$ with the x-axis, the Lamb-Dicke parameters are $\eta^{k_{1,z}} \approx -\eta^{k_{2,z}} \approx 0.066$. Combined with the typical Rabi frequencies used in the experiment, in the range of tens of megahertz, the wide separation of electronic and motion timescales demanded by an adiabatic elimination procedure is not satisfied in our system [83]. Figure 3.5 shows the disagreement between the cooling curves obtained with (black dashed line) and without (red solid line) adiabatic elimination of the electronic degrees of freedom (DOF) for an ion at the trap center. The insufficient separation of timescales can also be seen qualitatively by simultaneously examining the transient dynamics of the population, in say, $|g_1\rangle$, on a common time axis, as shown in Fig. 3.5.

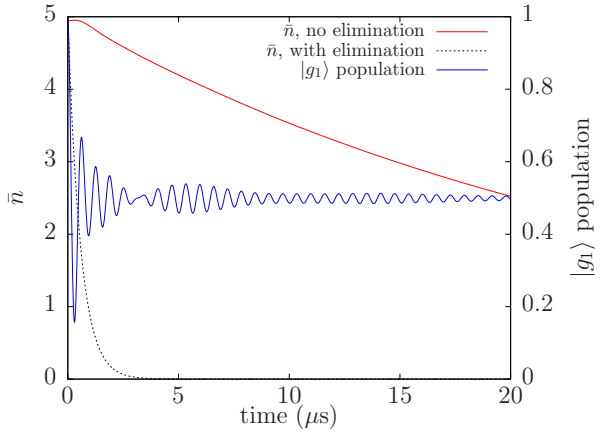

Figure 3.5: Cooling curve for an ion at the trap center that experiences no Doppler shifts. The separation of the timescales for the electronic and motional degrees of freedom is not large enough to validate the adiabatic elimination of the electronic degrees of freedom. The cooling is therefore much slower than the result predicted from such an elimination procedure [83]. Here, $\Delta^0/2\pi = 180$ MHz, $\Omega_1/2\pi = \Omega_2/2\pi = \Omega_{\rm opt}(\Delta^0)/2\pi \approx 24$ MHz.

3.6 EIT cooling of multiple ions

The NIST Penning trap routinely stores and manipulates tens to hundreds of ions. Since the density matrix, now consisting of the electronic degrees of freedom of all the ions and their drumhead modes, scales exponentially in the ion number, full density matrix solutions are impossible, and we are forced to resort to approximate techniques.

From the master equation, Eq. (3.11), we write down the equations of motion for the means of all the system operators (first order moments) and the products of operator pairs (second order moments). In general, these equations will couple to higher order moments, for example, means of products of triplets of operators, and so on. We truncate the hierarchy at second order by neglecting all cumulants higher than means and covariances, and close the set of equations by approximating higher order moments using sums of products of first and second order moments [80, 132]. As an example, for a product of three operators this would imply

$$\langle ABC\rangle \approx \langle AB\rangle\langle C\rangle + \langle AC\rangle\langle B\rangle + \langle BC\rangle\langle A\rangle - 2\langle A\rangle\langle B\rangle\langle C\rangle. \tag{3.15}$$

Here $\langle \ldots \rangle$ denotes the mean value of an operator or product of operators. We will refer to

Type	Moments
Internal	$\langle\sigma^j_{g_1g_1}\rangle$, $\langle\sigma^j_{g_1g_2}\rangle$, $\langle\sigma^j_{g_1e}\rangle$, $\langle\sigma^j_{g_2g_2}\rangle^{\#}$, $\langle\sigma^j_{g_2e}\rangle^{\#}$
External	$\langle b_n\rangle$, $\langle b_n b_k\rangle$, $\langle b_n^\dagger b_k\rangle$
Hybrid	$\langle b_n\sigma^j_{g_1g_1}\rangle$, $\langle b_n\sigma^j_{g_1g_2}\rangle$, $\langle b_n\sigma^j_{g_1e}\rangle$ $\langle b_n\sigma^j_{g_2g_1}\rangle^{\#}$, $\langle b_n\sigma^j_{g_2g_2}\rangle^{\#}$, $\langle b_n\sigma^j_{g_2e}\rangle^{\#}$, $\langle b_n\sigma^j_{eg_1}\rangle$, $\langle b_n\sigma^j_{eg_2}\rangle^{\#}$

Table 3.2: List of moments classified according to the nature of the operators involved. The equations for the moments marked with a # can be derived trivially by exchanging $g_1 \leftrightarrow g_2$ in the appropriate equations of motion for the other moments.

the equations obtained for the first and second order moments using this truncation scheme as the Gaussian model (GM), since the scheme neglects third and higher order cumulants. We note, however, that we factorize second order moments involving the electronic degrees of freedom of different ions of the type $\langle\sigma^j_{\alpha\beta}\sigma^k_{\gamma\delta}\rangle$ as $\langle\sigma^j_{\alpha\beta}\rangle\langle\sigma^k_{\gamma\delta}\rangle$ for $j \neq k$. We classify the remaining moments into three categories: internal, external and hybrid moments. These are listed in Table 3.2. In Appendix A.1, we write down the equations of motion (EOM) for the moments not marked with a # in Table 3.2, from which the remaining EOM can be obtained by appropriately exchanging $g_1 \leftrightarrow g_2$.

3.6.1 Results from the Gaussian model

We set the detuning $\Delta^0/2\pi = 360$ MHz, which ensures that the cooling rate for a single revolving ion does not change appreciably over the spatial extent of the small crystals we consider here. Figure 3.6 shows the cooling of the COM mode for crystals with $N = 1, 2, 19$ and 37 ions. For $N = 1, 2$ we simply take the ion(s) to be revolving at a distance of 20 μm from the trap center, and diametrically opposite each other in the $N = 2$ case. In the case of multi-ion crystals ($N > 2$), the equilibrium configuration of the crystal and the mode frequencies and eigenvectors are solved for following the procedure in Ref. [124]. We assume that a preceding Doppler cooling stage initializes the COM mode to a thermal state with $\bar{n} = 5$. We choose the initial $\bar{n}$ of the remaining drumhead modes assuming that they are initially in thermal equilibrium with the COM

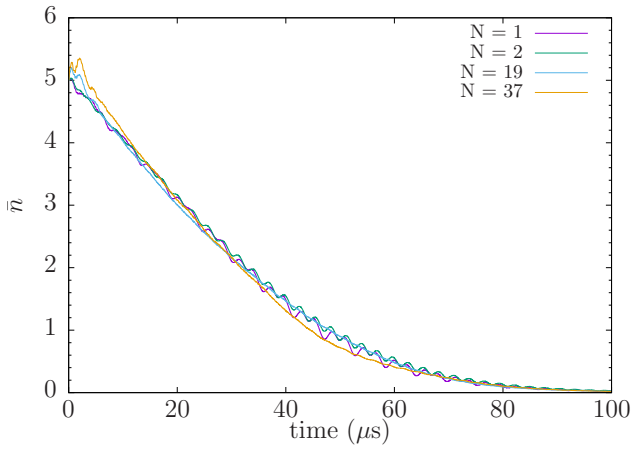

Figure 3.6: Cooling curves for the center-of-mass (COM) mode for crystals with different ion numbers, calculated using the Gaussian model (GM), showing rapid near ground-state cooling within 100 μs. However, the cooling rates are almost identical for all of these crystals. Here, $\Delta^0/2\pi = 360$ MHz, $\Omega_1/2\pi = \Omega_2/2\pi = \Omega_{\text{opt}}(\Delta^0)/2\pi \approx 33.9$ MHz.

mode. Qualitatively, the COM mode rapidly cools to near ground-state occupations within 100 microseconds. However, the cooling curves for the different crystals are nearly identical, showing that the net cooling rate of the COM mode, within the Gaussian framework, is approximately independent of the number of ions. For the multi-ion crystals, we observe an initial heating effect that is also observed experimentally [58]. We attribute the initial heating to transient electronic transitions until the electronic state of the ions reaches close to the steady state, at which point the cooling begins.

3.6.2 Benchmarking the Gaussian Model: Single-ion results

Since we are able to perform full density matrix (DM) computations in the single-ion case, we proceed to compare the cooling transients from the GM with the full DM results. Figure 3.7 shows the cooling curves from the GM (black, dashed) and the full DM calculation (red, solid) for a single revolving ion at $r = 0, 20, 40$ and 60 μm from the trap center, with $\Delta^0/2\pi = 360$ MHz. While both models qualitatively indicate that the cooling rate is roughly the same at these different radii, the cooling rate obtained from the GM is quantitatively very different from the full DM result. This indicates that keeping track of only means and covariances is not sufficient to accurately capture

the cooling curve.

The GM assumes that in the combined phase space of all the system degrees of freedom (DOF), the joint (quasi)-probability distribution of these DOF remains Gaussian at all times. In reality, while the initial distribution is Gaussian, evolution under the subsequent dynamics generally distorts the distribution so that it is no longer Gaussian at later times. A systematic way to capture this effect is to construct moments by averaging the evolution of the corresponding phase space variables (or products of variables) over a large number of trajectories, where the initial conditions of these variables in each trajectory are chosen randomly from their initial distribution (see Table 3.3). Such a sampling and averaging procedure captures the build-up of non-trivial third and higher order cumulants that are neglected in the GM. We note that this approach is in the same spirit as the Truncated Wigner Approximation (TWA) used in calculating the dynamics of spin-spin and spin-boson models [94, 9, 106, 92]. Moreover, we track separate phase space variables corresponding to system operators as well as operator pairs, and evolve these variables using the same equations of motion as in the GM (Appendix A.1), but for many trajectories. We thereby perform beyond

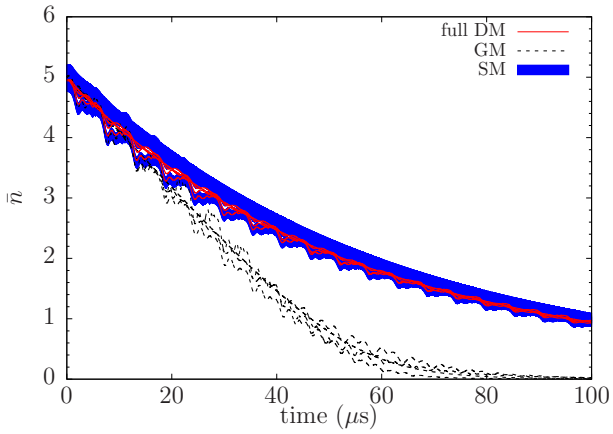

Figure 3.7: Cooling curve for a single revolving ion, located at $r = 0, 20, 40$ and 60 μm from the trap center, computed using three numerical approaches: (i) Time evolution of the full density matrix (full DM), (ii) the Gaussian model (GM) and (iii) the Sampling model (SM) using 2096 trajectories. The cooling curves from the GM do not agree with the full DM curves. However, sampling the initial noise systematically (SM) accounts for beyond-Gaussian properties of the phase-space distribution of the system degrees of freedom, and reproduces the full DM curves very well. Here, $\Delta^0/2\pi = 360$ MHz, $\Omega_1/2\pi = \Omega_2/2\pi = \Omega_{\rm opt}(\Delta^0)/2\pi \approx 33.9$ MHz.

mean-field calculations [92] that capture those contributions to the covariances between system operators which develop as a result of the subsequent diffusive-dissipative dynamics. We refer to this method as the Sampling model (SM). Table 3.3 summarizes the implementational differences between the Gaussian and the beyond-Gaussian Sampling model.

Model	Trajectories	Initial condition
Gaussian (GM)	1	$\langle b_n \rangle(0) = 0,$ $\langle b_n^\dagger b_n \rangle(0) = \bar{n}_n(0)$
Sampling (SM)	Many	$\mathrm{Re}\{\langle b_n \rangle(0)\} = \mathrm{Gaus}(0, \sqrt{\bar{n}_n/2}),$ $\mathrm{Im}\{\langle b_n \rangle(0)\} = \mathrm{Gaus}(0, \sqrt{\bar{n}_n/2}),$ $\langle b_n^\dagger b_n(0) \rangle = \lvert\langle b_n \rangle(0)\rvert^2$

Table 3.3: Implementational differences between the Gaussian and Sampling models. Here $\mathrm{Gaus}(0, \sigma)$ is a Gaussian distributed random variable with zero mean and standard deviation σ, and $\bar{n}_n$ are the initial thermal mode occupations. In the sampling model, the quantity $\langle A \rangle$ simply denotes the value of the respective phase space variable in that trajectory, and is **not** the mean value of the operator A. Instead, the mean value of A is given by the average of $\langle A \rangle$ over many trajectories with random initial conditions drawn from the initial phase space distribution. We note that we only sample the initial thermal distribution of the normal modes, and initialize the electronic DOF in the same way as in the GM, i.e. $\langle \sigma_{\alpha\beta}^j \rangle = 1$ when $\alpha = \beta = g_1$.

In Fig. 3.7 we show the cooling curves from the SM along with the full DM as well as GM results for the single revolving ion. Since the SM involves averaging over multiple trajectories with randomly drawn initial conditions, the cooling curves are shown as 1-σ confidence intervals instead of a line plot. The SM cooling curves agree very well with the full DM result, indicating that beyond-Gaussian correlations develop during the cooling process that lower the cooling rate.

3.6.3 Results from the Sampling model

The SM predicts that the cooling rate of the COM mode increases with the number of ions N in the crystal. In Fig. 3.8, we plot the cooling curve for the COM mode for crystals with $N = 1, 2, 19$ and 37 ions. The cooling is faster in the $N = 2$ case than in the single ion case, and even faster in the 19 and 37 ion crystals. The inset shows the ratio of the cooling rate R_N of an N-ion crystal

to the rate R_1 for a single ion. With the parameters used, and for these small crystals, the cooling rate scales as $\sim N^{0.3}$, highlighting that EIT cooling of multiple ions cannot be explained trivially as the net cooling resulting from the individual ions. Rather, the N-dependency of the cooling rate indicates the intrinsic many-body nature of this problem. We note, however, that for fixed laser parameters, the adverse effects of the time-varying Doppler shifts is expected to slow down the cooling enhancement with increasing N as ions are added further from the trap center. Moreover, with different laser parameters, the scaling with N could also vary. Finally, the rapid nature of EIT cooling is evident from the time constant $\tau \approx 21$ μs for the cooling curve of the 37 ion crystal.

3.7 Cooling over the full bandwidth

The full bandwidth of drumhead modes are typically cooled to near ground-state occupancies in a single experimental application of EIT cooling with a fixed set of parameters. We recall that the cooling parameters are set according to the expected optimum condition, Eq. (3.14), for cooling the COM mode, which is the highest frequency drumhead mode with $\omega_{\mathrm{COM}}/2\pi = 1.59$ MHz. In

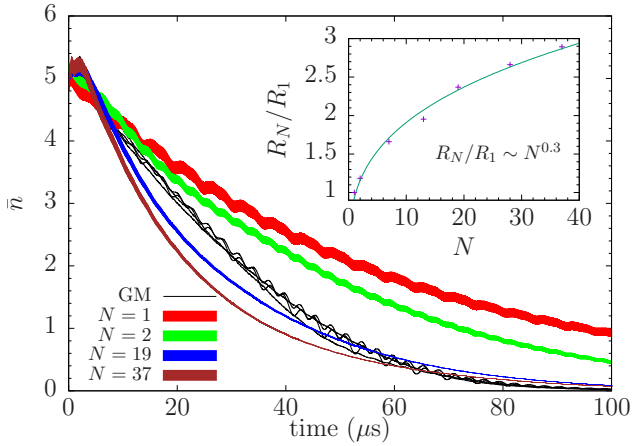

Figure 3.8: Cooling curves for the center-of-mass (COM) mode for crystals with different ion numbers, calculated using the Sampling model (SM) with 2048 trajectories. The SM predicts that the cooling rate increases with ion number N. The cooling curves from the GM (Fig. 3.6) are also shown for comparison, where the N-dependency of the cooling rate does not manifest. Inset: Cooling rate of an N-ion crystal R_N relative to the single-ion rate R_1 extracted from the SM (markers). A power-law fit (solid line) shows that the cooling rate scales as $\sim N^{0.3}$ for the parameters used. Here, $\Delta^0/2\pi = 360$ MHz, $\Omega_1/2\pi = \Omega_2/2\pi = \Omega_{\mathrm{opt}}(\Delta^0)/2\pi \approx 33.9$ MHz.

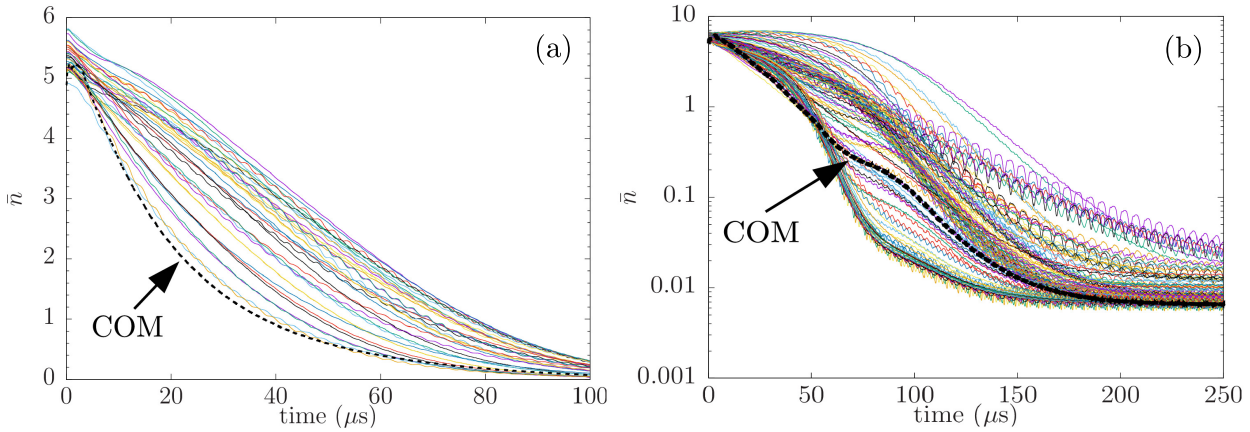

Figure 3.9: (a) Cooling curves for all the drumhead modes of a 37-ion crystal with bandwidth approximately $2\pi \times 185$ kHz, computed using the SM, showing efficient cooling within 100 μs. Here, $\Delta^0/2\pi = 360$ MHz, $\Omega_1 = \Omega_2 = \Omega_{\rm opt}(\Delta^0) \approx 33.9$ MHz. (b) GM cooling curves for all the drumhead modes of a 120-ion crystal with bandwidth approximately $2\pi \times 376$ kHz, showing near ground-state, steady-state occupations of all the modes after few hundred microseconds of EIT cooling. Note that the y-axis is plotted in logscale. Here, $\Delta^0/2\pi = 400$ MHz, $\Omega_1/2\pi = \Omega_2/2\pi = \Omega_{\rm opt}(\Delta^0)/2\pi \approx 35.7$ MHz. The same rotating wall frequency, $\omega_r/2\pi = 180$ kHz was used in both cases.

Fig. 3.9(a), we show the cooling transients for all the tranverse modes of a 37-ion crystal, calculated using the SM. The bandwidth of the drumhead modes is approximately $2\pi \times 185$ kHz. All the modes are observed to reach near ground-state occupations within 100 microseconds.

The computational complexity of a single trajectory in the SM scales as N^3 with the number of ions N, thereby making trajectory computations for large crystals ($\gtrsim 60$) untractable. However, the GM and SM will result in the same steady-state results since they only differ in the initial conditions, and eventually dissipation leads to the system of equations losing memory of its initial conditions. Therefore, the GM can be used to study the final temperatures that result from EIT cooling of large ion crystals, as shown in Fig. 3.9(b) for a 120-ion crystal. From initial occupations in the range $\bar{n} \approx 5 - 7$, all the modes are cooled down to $\bar{n} < 0.1$, showing the efficient cooling over the full bandwidth of drumhead modes, which in this case is approximately $2\pi \times 376$ kHz. We note that the experimentally observed occupations are expected to be somewhat higher than the steady-state values attained here because of the approximate model used in the simulations. Although the GM cooling transients are not completely reliable, they nevertheless indicate that a

few hundred microseconds of EIT cooling is sufficient to achieve these very low occupations.

3.8 Sensitivity to laser alignment

In modeling the EIT cooling in Sections 3.5, 3.6 and 3.7, we have assumed that the lasers are perfectly aligned, i.e. $k_{2,x} = k_{1,x}$, so that their difference wavevector is along the z-axis. In practice, a small misalignment of the EIT lasers could result in a component of the difference wavevector along the in-plane x-axis, because $k_{2,x} \neq k_{1,x}$. As a result, the detunings of these dressing lasers are now modulated unequally by Doppler shifts arising from the large amplitude in-plane rotation of the ion crystal, so that the instantaneous detunings of the two lasers as seen by the ion, $\Delta_\mu(t) = \Delta_\mu^0 - k_{\mu,x} v_x(t)$ with $\mu = 1, 2$, are no longer identical.

We study the effect of such a misalignment by considering a single ion revolving at different distances r from the trap center. We introduce a small misalignment $\delta\theta$ that modifies the perfectly aligned $\mathbf{k}_2 \rightarrow \mathbf{k}_2^{(\mathrm{m})}$ such that,

$$\begin{aligned} k_{2,x}^{(\mathrm{m})} &= k_{2,x}\cos\delta\theta + k_{2,z}\sin\delta\theta \\ k_{2,z}^{(\mathrm{m})} &= k_{2,z}\cos\delta\theta - k_{2,x}\sin\delta\theta, \end{aligned} \tag{3.16}$$

where the subscript (m) denotes the misaligned $\mathbf{k}_2$ vector.

Figure 3.10 shows the final steady-state occupation $\bar{n}$ of a single ion revolving around the trap center at different radii r, as the misalignment angle $\delta\theta$ is varied. We set the detuning $\Delta^0/2\pi = 400$ MHz, which ensures that for $r \leq 110$ μm, the revolving ion experiences effective blue detuning throughout its trajectory. The steady-state $\bar{n}$ begins to significantly increase only when $|\delta\theta| \gtrsim 1^\circ$, at which point the plot still indicates $\bar{n} \ll 1$. As r varies from 25 μm to 75 μm, the sensitivity to $\delta\theta$ also increases with r. For $r = 100$ μm, the ion experiences only small blue detunings for parts of its trajectory, resulting in inefficient cooling in these regions even with perfect alignment. As a result, the final temperature is not very sensitive to small misalignments such that $|\delta\theta| \lesssim 0.5^\circ$. However, the final temperature grows sharply as $|\delta\theta|$ increases beyond this value.

In the NIST EIT cooling experiment, the misalignment between the two EIT wavevectors

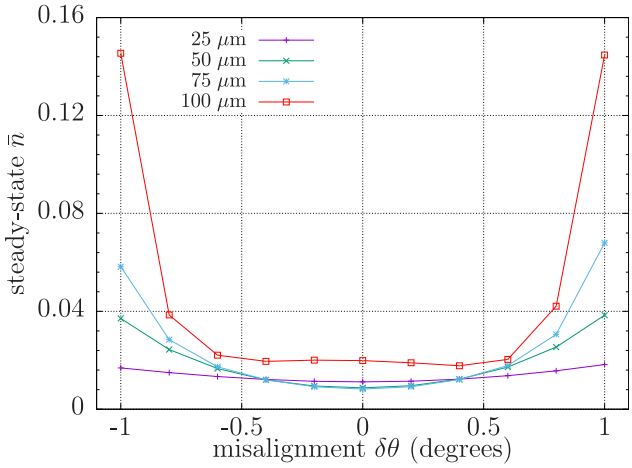

Figure 3.10: Steady-state occupation as a function of the misalignment angle $\delta\theta$ for a single ion revolving around the trap center at different radii. The final occupation is not very sensitive to small misalignments ($\delta\theta \leq 1^\circ$) of the EIT wavevectors. Here, $\Delta^0/2\pi = 400$ MHz, $\Omega_1/2\pi = \Omega_2/2\pi = \Omega_{\rm opt}(\Delta^0)/2\pi \approx 35.7$ MHz.

was estimated to be $< 0.2^\circ$ [58], ensuring that the cooling is negligibly affected by the in-plane crystal rotation. We note, however, that our analysis of the laser misalignment does not consider the potential adverse effect of the EIT lasers on the in-plane modes, which in turn could degrade the cooling of the drumhead modes. Such an analysis might result in a more stringent restriction on the tolerable range of $\delta\theta$.

3.9 Conclusion

Our numerical study shows that EIT cooling is a robust technique for cooling all the drumhead modes of two-dimensional ion crystals in Penning traps to near ground-state occupancies. EIT cooling relies on quantum interference effects for its operation, and prior to our work, the chances for its success, dependent on delicate cancellations of absorption amplitudes, in a challenging setting such as a Penning trap were very uncertain. Multiple factors could have potentially led to the failure of EIT cooling, namely, Doppler shifts, insufficient separation of electronic and motional timescales, as well as simultaneous cooling of multiple ions. Our predictions for the success of EIT cooling have been validated by the successul experimental demonstration of EIT cooling of crystals with more

than 100 ions in the NIST Penning trap [58]. Quantitative measurements of the cooling rate and final occupation of the COM mode, as well as qualitative features observed over the full bandwidth of modes are consistent with the expectations from our numerical study. These theoretical and experimental results highlight the robustness of EIT cooling and make it an attractive scheme to cool large chains or arrays of trapped ions in other settings [89, 96].

In the future, an important aspect to investigate is the effect of higher-order anharmonic terms in the trap potential, and more importantly, in the Coulomb interaction. These anharmonic terms not only result in additional coupling of the different drumhead modes to each other, but also couple these modes to the thermal motion associated with the in-plane modes. An understanding of these anharmonic couplings, at least for small ion crystals, will provide great insight into whether EIT cooling of the drumhead modes can also indirectly cool the in-plane modes, and also conversely, how the temperature of the in-plane modes could limit the achievable drumhead mode temperatures as well as cooling rates. Finally, while we have numerically observed and also found experimental support for the enhancement in the cooling rate with the number of ions, an intuitive explanation for this surprising feature will greatly illuminate the role played by many-body physics in the cooling dynamics.

Chapter 4

Near ground-state cooling large trapped ion crystals: Experimental results

In the last chapter, we presented numerical results that demonstrated the effectiveness of EIT cooling when implemented on large ion crystals in Penning traps. Here, we will present results from the EIT cooling experiment performed with the NIST Penning trap. The focus in our presentation will be on how the data validates the features predicted by our theoretical modeling. Details about the experimental implementation can be found in Ref. [58].

The thermometry of the drumhead modes in the NIST Penning trap is performed in a rather unique manner, using the so-called optical dipole force (ODF). In order to understand the data, a basic introduction to the ODF and its application in thermometry is required. We will therefore begin this chapter with a description of the thermometry technique. Next, we will present quantitative measurements on the center-of-mass mode of large crystals that reveal mean occupations close to zero, and cooling rates that are faster than single-ion rates. We will then present data acquired on the full bandwidth of drumhead modes that provides qualitative evidence for significant sub-Doppler cooling of all these modes. We will discuss how the smearing of sharp features in the ODF spectrum inhibit a quantitative analysis over the full bandwidth of modes. As a starting point for future studies, we will present a model based on in-plane thermal motion that attempts to explain the smearing out of the spectrum.

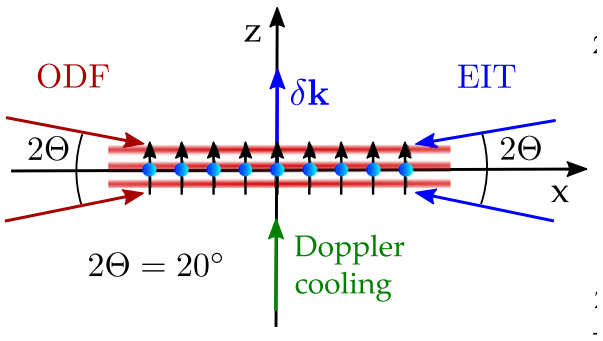

Figure 4.1: Schematic of the NIST EIT cooling experiment, showing the EIT lasers and ODF lasers incident on the ions at angles of $\pm 10^\circ$ to the crystal plane. Figure credit: Elena Jordan, NIST.

4.1 The Optical Dipole Force

One way to interpret the optical dipole force (ODF) is as a 'spin'-dependent force, where the two states composing the pseudospin correspond to $2s^2S_{1/2}(m_J = -1/2)$ and $2s^2S_{1/2}(m_J = +1/2)$. Therefore, we will switch to labeling these states by $|\downarrow\rangle$ and $|\uparrow\rangle$ respectively, instead of the $|g_1\rangle$, $|g_2\rangle$ notation used in the previous chapter.

4.1.1 Physical mechanism

The optical dipole force (ODF) is generated by two lasers, termed the ODF lasers, that are incident on the crystal at angles of $\pm 10^\circ$ with respect to the crystal plane, as illustrated in Fig. 4.1. These lasers couple the spin states to optically excited states in the $2p^2P_{3/2}$ manifold and lead to AC Stark shifts on the spin states.

First, let us consider the case when only one of the ODF lasers is on. For any particular detuning, there exists a laser polarization such that the two spin states experience the exact same AC Stark shift [105]. Next, consider the case when both lasers simultaneously address the crystal. From the geometry, it is clear the difference wavevector $\delta\mathbf{k}$ of the two lasers lies along the z axis, similar to the pair of EIT lasers. In addition, the difference frequency μ_r of the ODF lasers can be tuned using an acousto-optic modulator. The net intensity of the two lasers now includes an interference term which has the form $\sim \sin(\delta k z + \mu_r t)$. For a specific choice of detuning and at

fixed z, t, this interference term results in additional AC Stark shifts for the spin states that have equal magnitude $|\delta_{\mathrm{AC}}|$, but are opposite in sign [105]. For a single ion, the Hamiltonian for this interaction can be written as

$$\hat{H}_{\mathrm{ODF}} = \hbar|\delta_{\mathrm{AC}}| \sin\left(\delta k \hat{z} + \mu_r t\right) \hat{\sigma}_z. \tag{4.1}$$

In the Lamb-Dicke regime ($\delta k \sqrt{\langle \hat{z}^2 \rangle} \ll 1$), this interaction simplifies to

$$\hat{H}_{\mathrm{ODF}} \approx F_0 \cos\left(\mu_r t\right) \hat{z} \hat{\sigma}_z, \tag{4.2}$$

where $F_0 = \hbar|\delta_{\mathrm{AC}}|\delta k$ has dimensions of force. The difference frequency μ_r can be tuned on resonance with the various frequency components of the drumhead motion, and is therefore typically varied in the range $\sim$ 900 kHz to 1.6 MHz. As a result, the z-independent term that appears in the Taylor expansion is 'rapidly oscillating' at frequency μ_r and therefore has been dropped while going from Eq. (4.1) to Eq. (4.2).

For a crystal with N ions, the ODF Hamiltonian straightforwardly generalizes to

$$\hat{H}_{\mathrm{ODF}} = F_0 \cos\left(\mu_r t\right) \sum_{j=1}^{N} \hat{z}_j \hat{\sigma}_j^z. \tag{4.3}$$

In Eq. (4.3), the position operator for each ion is time-dependent, and can be expanded in terms of the N drumhead modes as

$$\hat{z}_j(t) = \sum_n \sqrt{\frac{\hbar}{2M\omega_n}} \mathcal{M}_{jn} \left(\hat{b}_n e^{-i\omega_n t} + \hat{b}_n^\dagger e^{i\omega_n t} \right). \tag{4.4}$$

4.1.2 Interpretation

The ODF Hamiltonian, Eq. (4.2), can be interpreted in two equivalent ways. First, the grouping $\left[F_0 \cos\left(\mu_r t\right) \hat{\sigma}_z\right] \hat{z}$ leads to its interpretation as a force acting on the ion, whose sign is dependent on the electronic spin state. This interpretation gives rise to the 'optical dipole force' or 'spin-dependent force' terminology. Alternatively, the grouping $\left[F_0 \cos\left(\mu_r t\right) \hat{z}\right] \hat{\sigma}_z$ gives an interpretation of a spatially dependent differential AC Stark shift between the two spin states. That is, as the ion oscillates about the crystal plane $z = 0$, an equal superposition state of $|{\downarrow}\rangle$

and $|\uparrow\rangle$, initialized say along the x-axis of the Bloch sphere, will precess on the equatorial plane and accumulate a relative phase that sensitively depends on the nature of the ion's out-of-plane motion. The contribution of specific drumhead modes can be selectively enhanced and probed by tuning the difference frequency μ_r close to these mode frequencies. We note that when μ_r is tuned exactly on resonance with a mode, the resulting AC Stark shift is effectively mixed down to DC and results in spin precession at a constant rate. The AC Stark shift interpretation is particularly useful in understanding how the ODF can be used for thermometry.

4.2 Thermometry with the ODF

In order to measure the temperature of a mode, the ODF interaction is applied as part of a Ramsey-style sequence as shown in Fig. 4.2 [105, 58]. First, all spins are initialized in $|\uparrow\rangle$. A $\pi/2$ rotation about the y axis results in an equal superpositon of $|\downarrow\rangle$ and $|\uparrow\rangle$ along the x axis. The ODF interaction is then applied for an arm time τ, during which the spins precess on the equatorial plane because of the motion of the ions. Next, an echo pulse of duration t_π is applied about the x axis. This pulse is intended to cancel unwanted phase accumulations, say because of magnetic field inhomogeneities. The echo is followed by a second arm of duration τ during which the ODF interaction is applied again. Finally, a second $\pi/2$ rotation about the y axis converts the accumulated phase into a population difference. If no phase was accumulated, all the spins end up in $|\downarrow\rangle$. Otherwise, there is a non-zero probability to detect the spins in $|\uparrow\rangle$ and this population can be detected via fluorescence. For this reason, $|\uparrow\rangle$ is referred to as the 'bright' state and the fraction of ions in this state is called the 'bright fraction'. In principle, an ODF spectrum for a mode can be generated by plotting the measured bright fraction as a function of the difference frequency μ_r, as it is stepped across the mode frequency. A single measurement merely collapses each spin to $|\downarrow\rangle$ or $|\uparrow\rangle$. In order to precisely measure the bright fraction, the cooling and ODF sequence is repeated a large number of times (~ 100) at each μ_r value so that sufficient statistics accumulate to reveal the true bright state probability.

We assume that the drumhead modes can be described by thermal states both after Doppler

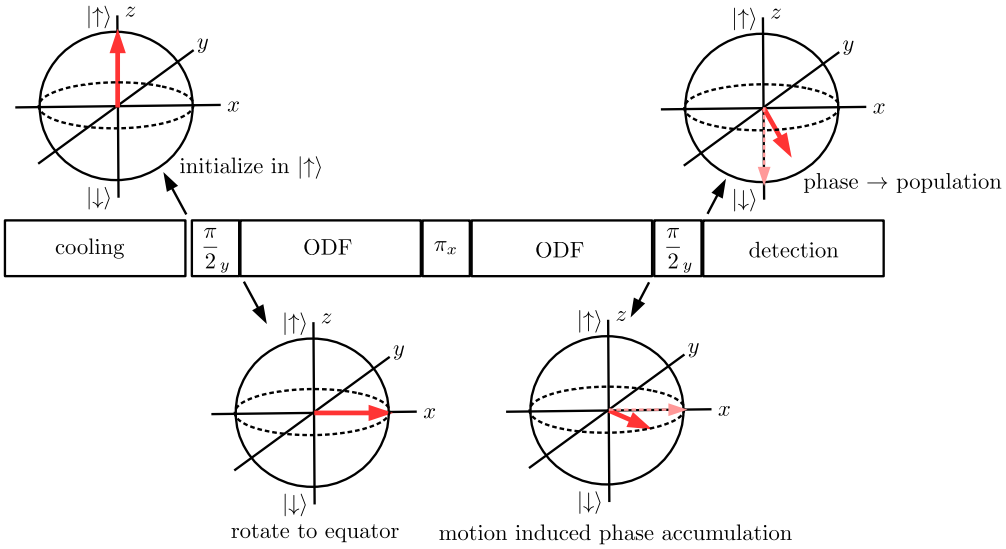

Figure 4.2: Schematic of the thermometry sequence involving the ODF interaction. Bloch sphere pictures indicate the spin state of an ion at different points of the sequence.

cooling as well as after EIT cooling. One interpretation of thermal motion is that in each trial of the experiment, the ions are left with varying motional energies after the cooling. As a result, in each trial of the ODF sequence, any particular spin will accumulate varying amounts of relative phase between the two spin states. When averaged over a large number of cooling and measurement sequences, the net effect is that the spin appears to have 'dephased'. Therefore, measuring the bright fraction is often termed as a measurement of the 'motion-induced spin dephasing' [104].

4.2.1 Analytical formula for the bright fraction

The Hamiltonian, Eq. (4.3), is special because the propagator $\hat{U}(t)$ associated with it can be computed exactly [123, 34]. This property makes the ODF Hamiltonian one of the best studied many-body spin-boson models, with analytical formulae calculable for all observables of interest. In this section, we present an analytical formula for the bright fraction at the end of the thermometry sequence, which can be used to fit an experimentally measured ODF spectrum in order to measure mode temperatures. This formula is a straightforward adaptation of analytical expressions that have been rigorously derived elsewhere by other researchers [123, 34, 102], so we briefly sketch the

derivation in Appendix A.2.

The bright fraction at the end of the thermometry sequence is given by

$$P\left(|\uparrow\rangle\right) = \frac{1}{N}\sum_{j=1}^{N}\left(\frac{1-e^{-2\Gamma\tau}C_{ss}^{j}C_{sm}^{j}}{2}\right), \tag{4.5}$$

where the spin-motion contribution C_{sm}^{j} is an exponential involving a summation over all the drumhead modes, given by

$$C_{sm}^{j} = \exp\left\{-2\sum_{n=1}^{N}|\alpha_{nj}|^{2}\left(2\bar{n}_{n}+1\right)\right\} \tag{4.6}$$

and the spin-spin contribution C_{ss}^{j} is a product over the ions, given by

$$C_{ss}^{j} = \prod_{k\neq j}\cos\left(4J_{jk}\right). \tag{4.7}$$

In writing the formula for the bright fraction, we have introduced new symbols α_{nj} and J_{jk} for which exact analytical expressions are presented in Appendix A.2. We use these expressions to numerically compute the bright fraction in order to compare with and fit the experimentally measured ODF spectrum. Importantly, these coupling constants depend on (a) the ODF difference frequency μ_r, which appears in the expressions for these quantities in the form $\delta_n = \mu_r - \omega_n$ and (b) the mode occupations $\bar{n}_n$. These dependencies enable the use of the ODF spectrum in thermometry. In addition, they also depend on the ODF amplitude F_0, arm time τ, echo time t_π, and also explicitly on the drumhead mode frequencies ω_n and displacements $\mathcal{M}_{jn}$. The factor $e^{-2\Gamma\tau}$ in Eq. (4.5) accounts for decoherence arising from free-space scattering induced by the ODF lasers.

4.3 Temperature measurements on the COM mode

For values of μ_r close to the COM mode frequency, denoted as ω_1 here, contributions from other modes can be neglected. The identical coupling of the COM mode to all ions results in simple expressions $C_{sm} = \exp\left\{-2|\alpha|^{2}\left(2\bar{n}+1\right)\right\}$ and $C_{ss} = \left[\cos\left(4J\right)\right]^{N-1}$ that are independent of j. For simplicity, here we denote $\bar{n} \equiv \bar{n}_1$. Once again, we provide expressions for α and J in Appendix A.2. The bright fraction is simply given by

$$P\left(|\uparrow\rangle\right) = \frac{1}{2}\left(1-e^{-2\Gamma\tau}C_{ss}C_{sm}\right). \tag{4.8}$$

As μ_r is stepped across the COM mode, Eq. (4.8) predicts qualitatively different lineshapes for the spectrum of $P(|\uparrow\rangle)$ versus μ_r in regimes of high and low $\bar{n}$ values, when other parameters are held fixed. A crucial insight into this feature is obtained by noting that the term C_{ss} is independent of $\bar{n}$ while C_{sm} decreases exponentially with $\bar{n}$. Furthermore, the product of these two terms is then subtracted from a constant value of 1. At low $\bar{n}$, C_{sm} does not suppress the features resulting from C_{ss} and leads to a complex lineshape. At high $\bar{n}$, C_{sm} is very small and strongly suppresses features resulting from C_{ss}, leading to a simpler lineshape. Moreover, the larger suppression of C_{ss} results in greater values of $P(|\uparrow\rangle)$ as $\bar{n}$ increases. In fact, $P(|\uparrow\rangle) \to 1/2$ as $\bar{n} \to \infty$, except for discrete values of μ_r where $|\alpha|^2 = 0$. Therefore, the spectrum after Doppler cooling can be expected to be higher as well as simpler in structure, whereas the spectrum after EIT cooling is expected to be lower and relatively more complex. In general, with similar parameters used for the ODF sequences after Doppler and EIT cooling, the above argument leads us to expect a lower bright fraction across the entire bandwidth of drumhead modes after EIT cooling.

Such features are indeed observed in the experimentally measured ODF spectrum for μ_r close to the COM mode, an example of which is shown in Fig. 4.3 for a crystal of 158 ± 10 ions. The data set in black is measured immediately after Doppler cooling, whereas the blue data set is measured after an additional 200 μs of EIT cooling. The spectrum after Doppler cooling is higher and two peaked, whereas the spectrum after EIT cooling is lower but features four peak-like structures. The same formula, Eq. (4.8), is used to fit the spectrum in both cases, resulting in measured $\bar{n}$ values of 5.6 ± 1.1 in the Doppler cooling case and 0.28 ± 0.18 in the EIT cooling case. These measurements quantitatively demonstrate near ground-state cooling of the COM mode within just a few hundred microseconds of EIT cooling. We note that, although we considered the case of an equal ODF amplitude F_0 in motivating the expected lineshapes in the two cases, the spectrum after EIT cooling is typically taken with a somewhat higher F_0 value.

By measuring $\bar{n}$ after varying durations of EIT cooling, a cooling rate can be measured for the COM mode. Figure 4.4 shows a measurement of $\bar{n}$ versus cooling time for a crystal with 190 ± 10 ions. An exponential fit to the data reveals a cooling time constant of $\tau_{\text{cool}} = 27.6 \pm 1.7$ μs for this

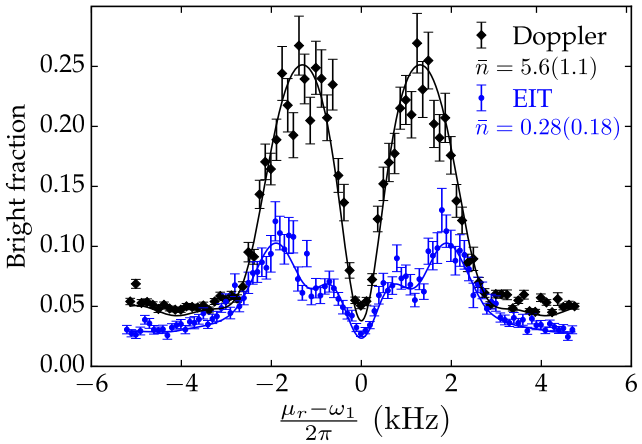

Figure 4.3: ODF spectra showing the bright fraction as the ODF difference frequency is stepped across the COM mode frequency ω_1. The black and blue data are respectively measured after Doppler cooling and 200 μs of additional EIT cooling on a crystal with 158 ± 10 ions. The measured $\bar{n}$ values in each case are obtained by fitting the data with the formula Eq. (4.8). Figure and data credit: Bollinger group, NIST.

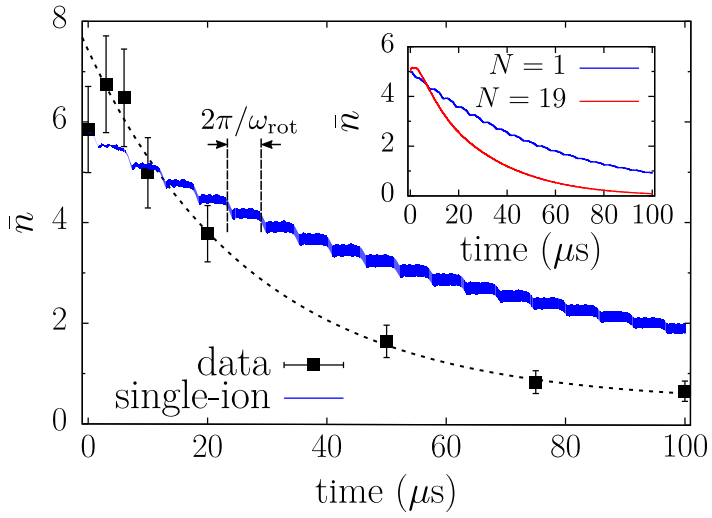

Figure 4.4: Measured thermal occupation $\bar{n}$ of the COM mode (black) as a function of the cooling time for a crystal with 190 ± 10 ions. The measured cooling time constant of approximately 28 μs corresponds to a rate that is faster than that theoretically expected from separate cooling of each ion in the trap (blue). Inset: We recall the cooling transients resulting from the Sampling Model presented in Chapter 3, where the cooling rate of the COM mode increases with ion number. Experimental data credit: Bollinger group, NIST.

particular set of EIT cooling parameters [58]. The rapid cooling is consistent with results from our theory, where the observed time constant is typically a few tens of microseconds.

An exciting observation is that the measured cooling rate is faster than the average rate theoretically expected if each ion was independently cooled in the trap (Fig. 4.4, blue curve in main panel). For this comparison, we compute single-ion cooling transients for ions revolving at different radii from the trap center, and then average by weighting each transient by the number of ions approximately situated at that radius. The stepwise behavior is merely an artifact caused by choosing the same initial phase of revolution for each transient. The faster rate of cooling in the multi-ion crystal is consistent with the numerical observation that the cooling rate of the COM mode increases with ion number, a result that we recall in the inset of Fig. 4.4. In the future, better understanding of this speed-up phenomenon can be obtained by performing cooling rate measurements on small ion crystals ($N < 60$), where direct theory-experiment comparisons are feasible.

4.4 Measurements over the full bandwidth

Our modeling predicts that with a fixed set of experimental parameters, EIT cooling should be able to cool down the entire bandwidth of drumhead modes close to their ground states within a few hundred microseconds. To verify this experimentally, the cooling and ODF sequence is repeatedly applied, keeping the cooling parameters fixed while scanning the ODF difference frequency over the full bandwidth of the drumhead modes. Figure 4.5 shows the ODF spectrum obtained using a crystal with 158 ± 10 ions, after Doppler cooling only (red) and after 300 μs of additional EIT cooling (blue). A steep drop in the bright fraction is observed across the entire bandwidth of modes, providing evidence for strong sub-Doppler cooling of all the drumhead modes.

A natural next step is to use this spectrum and the formula, Eq. (4.5), to quantitatively estimate the mean occupations for various drumhead modes. However, the measured spectrum is not easily amenable to such a quantitative analysis. The qualitative differences between the theoretically expected and measured spectra already manifest in smaller ion crystals, where a comparative study is easier to carry out. Figure 4.6(a) shows the theoretically expected ODF spectra with a 79 ion crystal, for the cases when all the modes have $\bar{n} = 6.0$ and $\bar{n} = 0.26$

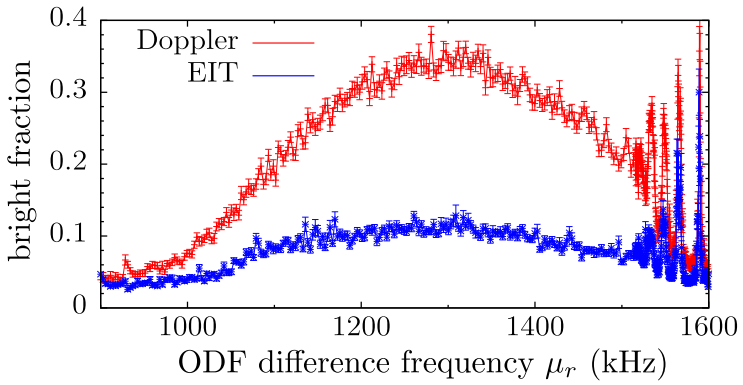

Figure 4.5: ODF spectrum measured over the full bandwidth of drumhead modes after Doppler cooling only (red) and after 300 μs of additional EIT cooling (blue), for a crystal with 158 ± 10 ions. The significant reduction in bright fraction over the entire bandwidth after EIT cooling is evidence of strong sub-Doppler cooling of all the drumhead modes. Data credit: Bollinger group, NIST.

(green and orange curves respectively). The ODF parameters correspond to the experimental data presented in Fig. 4.6(b). The theory curves confirm two of our intuitive expectations. One, the bright fraction at low $\bar{n}$ is consistently lower than at high $\bar{n}$ over the full bandwidth.[1] Two, the ODF spectrum displays sharp peaks that are expected when μ_r is tuned close to a mode or a cluster of modes.

In comparison, Fig. 4.6(b) shows the spectra measured using a crystal with 79 ± 5 ions, after Doppler cooling only (red) and after additional EIT cooling (blue). In the latter spectrum, the measured $\bar{n}$ for the COM mode is 0.26 ± 0.38, motivating our choice of $\bar{n}$ for the corresponding theory curve. While the spectrum after EIT cooling is indeed lower than that after Doppler cooling only, the sharp features predicted by the theory have smeared out into a smooth continuum. A quantitative analysis of this spectrum is not possible without first understanding the reason behind this qualitative difference between theory and experiment.

The smearing of the ODF spectrum suggests fluctuations in the drumhead mode frequencies. To investigate this possibility, we carry out a numerical simulation that is inspired by the experimental protocol used to obtain the spectrum. We assume that the mode frequencies remain

[1] This feature manifests even though the effective amplitude F_0 for the $\bar{n} = 0.26$ case is somewhat larger than the $\bar{n} = 6.0$ case.

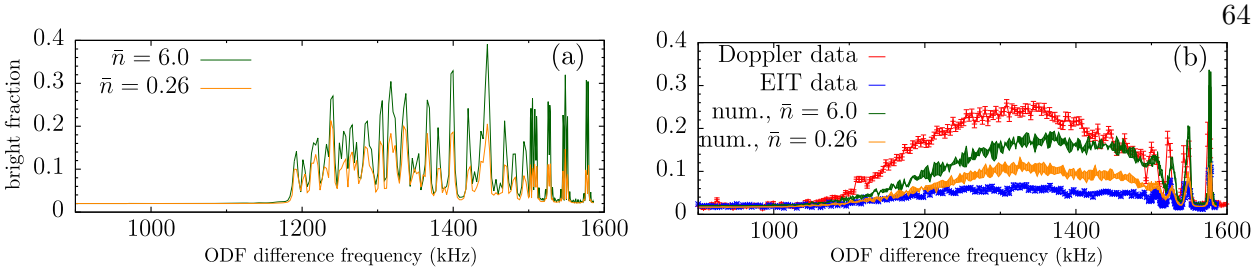

Figure 4.6: Qualitative differences between theory and experimentally measured ODF spectra, exemplified using a 79 ion crystal. (a) Theoretically expected spectrum at high and low $\bar{n}$ values are spiky and partially resolve the modes. (b) Experimentally measured spectra (red and blue) display a smooth continuum. Theory incorporating ad hoc mode frequency fluctuations smear the sharp features seen in (a) and lead to curves (green and orange) that resemble the measured spectra. Experimental data credit: Bollinger group, NIST.

constant within the duration of a single ODF sequence, but fluctuate from one trial to the next. To simulate this, we first numerically obtain the drumhead mode frequencies ω_n and amplitudes $\mathcal{M}_{jn}$ for the equilibrium crystal configuration [124], which are used to generate the theory curves in Fig. 4.6(a). Next, for each value of μ_r, we add independent Gaussian distributed fluctuations to each mode frequency and compute the bright fraction. We repeat this several tens of times at every μ_r value and average over all the trials. We assume that the magnitude of fluctuations increases with decreasing mode frequency. Repeating this process for μ_r spanning the full bandwidth leads to the theory curves shown in Fig. 4.6(b) (green and orange). These curves were generated assuming frequency fluctuations that linearly increase from 1 kHz for the second-highest frequency mode to 80 kHz for the lowest frequency mode. Clearly, these curves suggest that frequency fluctuations strongly affect the measured spectrum.

The similar profiles of the theory (orange) and data (blue) measured after EIT cooling enable us to make qualitative assessments of the drumhead mode temperatures. The measured bright fraction after EIT cooling is below the corresponding theory curve, strongly suggesting near ground-state cooling over the entire bandwidth of drumhead modes. In the case of only Doppler cooling, there is qualitative agreement at higher frequencies, but the measured bright fraction at low frequencies is consistently higher than theory predictions with reasonable $\bar{n}$ values. We have observed these general trends over a range of data sets measured after both types of cooling, and with varying

ion numbers.

For improving the analysis of these spectra, the ad hoc frequency fluctuations assumed so far in this study have to be replaced by a physically motivated model. To explain the EIT data, the effect of frequency fluctuations on the spin-spin interaction signal, which is dominant at low temperatures, is required. In the Doppler cooling case, the large temperatures should allow for a numerical model that neglects quantum effects [105], making a first analysis far easier in this case. Some initial steps towards developing a physical model of mode frequency fluctuations and modeling the spectrum measured after Doppler cooling are described in Section 4.5.

4.5 Physical model for mode frequency fluctuations

The Coulomb interaction is intrinsically anharmonic, and therefore introduces coupling between the in-plane and out-of-plane motion even when the trapping potential is purely harmonic. We speculate that this coupling is the primary reason for the observed drumhead mode frequency fluctuations. To understand the motivation for this hypothesis, a brief introduction to the classical dynamics of ions in a Penning trap is first required.

4.5.1 Classical dynamics of ions in a Penning trap

Following Ref. [124], we write down the Lagrangian for a collection of N ions in a Penning trap. The Lagrangian for this system is

$$L = \sum_{j=1}^{N} \left[\frac{1}{2} m_j \dot{\mathbf{r}}_j \cdot \dot{\mathbf{r}}_j - e\phi_j + e\mathbf{A}_j \cdot \dot{\mathbf{r}}_j \right]. \tag{4.9}$$

Here, $\mathbf{A}_j = (\mathbf{B} \times \mathbf{r}_j)/2$ is the vector potential associated with the magnetic field $\mathbf{B} = B_z \mathbf{e}_z$ in the symmetric gauge. Therefore, $\mathbf{A}_j = -B_z(y\mathbf{e}_x - x\mathbf{e}_y)/2$. The potential ϕ_j experienced by each ion is

$$\phi_j(t) = V_0 \left[z_j^2 - \frac{1}{2}\rho_j^2 \right] + V_W \rho_j^2 \cos\left[2(\theta_j + \Omega t\right] + \frac{k_e e}{2} \sum_{k \neq j} \frac{1}{r_{kj}}. \tag{4.10}$$

The first term represents the quadrupole electric potential, the second term is the rotating wall potential while the third term describes the inter-ion Coulomb potential. Here, we have used the

shorthand $k_e = 1/(4\pi\epsilon_0)$ with ϵ_0 the permittivity of free space. In writing Eq. (4.10), we have used the radial coordinate $\rho_j = \sqrt{x_j^2 + y_j^2}$ and the angular coordinate $\theta_j = \tan^{-1}(y_j/x_j)$.

4.5.1.1 Transformation to the rotating frame

In a frame rotating at angular frequency Ω, the Lagrangian becomes time independent. The coordinates in the rotating frame $x_j^R(t), y_j^R(t)$ are related to the coordinates in the lab frame $x_j(t), y_j(t)$ as [124]

$$\begin{pmatrix} x_j \\ y_j \end{pmatrix} = \begin{pmatrix} \cos\Omega t & \sin\Omega t \\ -\sin\Omega t & \cos\Omega t \end{pmatrix} \begin{pmatrix} x_j^R \\ y_j^R \end{pmatrix}. \tag{4.11}$$

Direct substitution of this relation into Eq. (4.9) and Eq. (4.10) gives the Lagrangian in the rotating frame as

$$L = \sum_{j=1}^{N} \left[\frac{1}{2} m_j \dot{\mathbf{r}}_j^R \cdot \dot{\mathbf{r}}_j^R - e\phi_j^R - \frac{eB_{\text{eff},j}[\Omega]}{2} (\dot{x}_j^R y_j^R - \dot{y}_j^R x_j^R) \right], \tag{4.12}$$

where $B_{\text{eff},j}[\Omega] = B_z - 2m_j\Omega/e$ and

$$e\phi_j^R = eV_0(z_j^R)^2 + \frac{1}{2}\left(eB_z\Omega - m_j\Omega^2 - eV_0\right)(\rho_j^R)^2 + eV_W[(x_j^R)^2 - (y_j^R)^2] + \frac{k_e e^2}{2} \sum_{k\neq j} \frac{1}{r_{kj}^R}. \tag{4.13}$$

Henceforth, we drop the R subscript, and work in the rotating frame, unless explicitly mentioned otherwise.

4.5.1.2 Dimensionless units

We now make the problem dimensionless by introducing certain characteristic scales. The axial trapping strength can be characterized in terms of the trapping frequency ω_z for a single $^9\text{Be}^+$ ion with mass m_{Be}, i.e. $eV_0 = m_{\text{Be}}\omega_z^2/2$. We define the scale factors

$$m_0 = m_{\text{Be}},\ l_0 = \left(\frac{2k_e e^2}{m_{\text{Be}}\omega_z^2}\right)^{1/3},\ t_0 = 1/\omega_z, \tag{4.14}$$

for mass, length and time respectively. In these new units, frequencies are specified relative to ω_z. A characteristic energy scale that can be constructed out of these base units is

$$E_0 = \frac{1}{2} m_0 l_0^2 t_0^{-2} \equiv eV_0 l_0^2. \tag{4.15}$$

We normalize the Lagrangian, Eq. (4.12), by this characteristic energy to obtain $\tilde{L} = L/E_0$, given by

$$\tilde{L} = \sum_{j=1}^{N} \left[\tilde{m}_j \dot{\tilde{\mathbf{r}}}_j \cdot \dot{\tilde{\mathbf{r}}}_j - \widetilde{e\phi}_j - \tilde{\omega}'_{c,j}[\Omega](\dot{\tilde{x}}_j \tilde{y}_j - \dot{\tilde{y}}_j \tilde{x}_j) \right], \tag{4.16}$$

where the $\tilde{\cdot}$ indicates normalization with respect to the respective characteristic scales. Here, $\tilde{\omega}'_{c,j} = \tilde{\omega}_c - 2\tilde{m}_j\tilde{\Omega}$ is an effective normalized cyclotron frequency with $\omega_c = eB_z/m_{\mathrm{Be}}$, and $\tilde{\omega}_c = \omega_c/\omega_z$, $\tilde{\Omega} = \Omega/\omega_z$ and $\tilde{m}_j = m_j/m_{\mathrm{Be}}$. The effective potential energy term is

$$\widetilde{e\phi}_j = \tilde{z}_j^2 + \left(\tilde{\omega}_c\tilde{\Omega} - \tilde{m}_j\tilde{\Omega}^2 - \frac{1}{2} \right) \tilde{\rho}_j^2 + C_W \left(\tilde{x}_j^2 - \tilde{y}_j^2 \right) + \frac{1}{2} \sum_{k \neq j} \frac{1}{\tilde{r}_{kj}}. \tag{4.17}$$

Here $C_W = V_W/V_0$ is the dimensionless rotating wall strength. Note how simple the Coulomb interaction becomes in these scaled variables. We note that the Lagrangian, Eq. (4.16), generically allows for the presence of ions with different masses and can therefore be used to study the effect of impurity ions [79].

4.5.1.3 Euler-Lagrange equations of motion

Defining the mechanical momentum $\tilde{\mathbf{\Pi}}_j = \tilde{m}_j \dot{\tilde{r}}_j$, we obtain the equations of motion along the three directions as a set of first order coupled differential equations. The positions are updated trivially as

$$\dot{\tilde{r}}_j = \frac{1}{\tilde{m}_j} \tilde{\mathbf{\Pi}}_j \tag{4.18}$$

by construction. The momentum components evolve as

$$\begin{aligned}
\dot{\tilde{\Pi}}_j^x &= -\left(\tilde{\omega}_c\tilde{\Omega} - \tilde{m}_j\tilde{\Omega}^2 - \frac{1}{2} + C_W \right) \tilde{x}_j + \frac{\tilde{\omega}'_{c,j}[\Omega]}{\tilde{m}_j} \Pi_j^y + \frac{1}{2} \sum_{k \neq j} \frac{\tilde{x}_j - \tilde{x}_k}{\tilde{r}_{kj}^3}, \\
\dot{\tilde{\Pi}}_j^y &= -\left(\tilde{\omega}_c\tilde{\Omega} - \tilde{m}_j\tilde{\Omega}^2 - \frac{1}{2} - C_W \right) \tilde{y}_j - \frac{\tilde{\omega}'_{c,j}[\Omega]}{\tilde{m}_j} \Pi_j^x + \frac{1}{2} \sum_{k \neq j} \frac{\tilde{y}_j - \tilde{y}_k}{\tilde{r}_{kj}^3}, \\
\dot{\tilde{\Pi}}_j^z &= -\tilde{z}_j + \frac{1}{2} \sum_{k \neq j} \frac{\tilde{z}_j - \tilde{z}_k}{\tilde{r}_{kj}^3}.
\end{aligned} \tag{4.19}$$

Here, the $\cdot$ now indicates the time derivative with respect to the scaled time $\tilde{t}$.

4.5.1.4 Nature of normal modes for planar crystals

We can roughly motivate the typical frequency ranges of the three branches of modes, summarized in Table 3.1, using characteristic frequencies constructed out of the trap parameters. First, we recall that the drumhead center-of-mass mode frequency is set by the axial trapping frequency and is typically $\omega_1 = \omega_z \approx 2\pi \times 1.57 - 1.59$ MHz in this work. In the crystal plane, the high frequency cyclotron modes have frequencies close to the cyclotron frequency $\omega_c = eB/m_{\mathrm{Be}}$. For the NIST Penning trap, $\omega_c \approx 2\pi \times 7.6$ MHz. In addition, large amplitude in-plane motion occurs on a slower time scale and is governed by the magnetron modes. These modes have frequencies below the magnetron frequency of $\omega_m = \left(\omega_c - \sqrt{\omega_c^2 - 2\omega_z^2}\right)/2$. Typically, $\omega_m \approx 2\pi \times 170$ kHz for the parameters of the NIST Penning trap. In the absence of a rotating wall potential, the lowest frequency magnetron mode, called the rocking mode, acquires zero frequency and can be thought of as a Goldstone mode arising from the spontaneous breaking of rotational symmetry. In the presence of a weak wall potential, this rocking mode acquires a small non-zero frequency.

4.5.2 The thermal snapshot picture

We are now ready to discuss an intuitive model for drumhead mode frequency fluctuations. During a single time period associated with a typical magnetron frequency ($\sim 10 - 100$ kHz), every drumhead mode ($\gtrsim 1$ MHz) completes several oscillations. In an extreme, even unrealistic, simplification, we can imagine the ions to be frozen in plane at different points along their magnetron motion trajectories, while they execute rapid motion out-of-plane. Further, we are assuming that the cyclotron motion has very small amplitude and can be neglected for the sake of this argument. For each frozen configuration, we can follow the procedure of Ref. [124] and perform a normal mode analysis in the out-of-plane direction and sort the drumhead modes in descending order. We can then repeat this exercise a large number of times and histogram the sorted modes into frequency bins to study the spread in the mode frequencies.

In order to execute this program, we extensively use the Metropolis-Hastings (MH) algo-

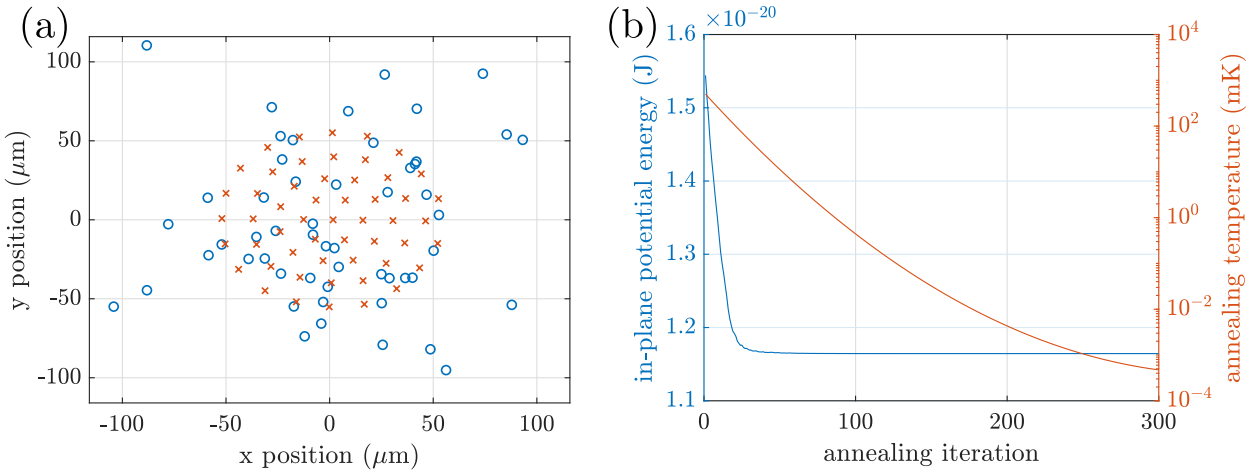

Figure 4.7: Simulated annealing to find the minimum energy configuration of a 53 ion crystal. (a) Ion positions before (blue) and after (orange) the simulated annealing procedure. (b) Annealing temperature and in-plane potential energy versus annealing iteration.

rithm [2] . In fact, the MH algorithm is the building block of the global minimization technique of simulated annealing. Therefore, we first realize a minimum energy configuration using the simulated annealing technique and the potential energy for the $x-y$ coordinates as the cost function. Figure 4.7(a) shows a minimum energy crystal (orange) obtained using simulated annealing, starting from a random configuration (blue). The parameters used for this study are $N = 53$ ions, $\omega_z = 2\pi \times 1.575$ MHz and $\Omega = 2\pi \times 187$ kHz, deviating from the conventional 180 kHz rotation frequency. The wall potential is $V_W = 5.3$ V. Figure 4.7(b) shows how the annealing temperature is decreased with each successive iteration and also plots the decreasing in-plane potential energy as the simulated annealing proceeds.

Next, we introduce a temperature $T_\perp$ that characterizes the excess thermal energy in the in-plane configuration. We use the MH algorithm with the in-plane potential energy as the cost function to generate a sequence of snapshots corresponding to the temperature $T_\perp$. Figure 4.8(a) captures the deviation of ion positions in a typical thermal configuration (orange) with $T_\perp = 10$ mK, from the corresponding positions in the minimum energy configuration (blue). The MH algorithm proceeds by attempting to perturb the position of each ion in succession. Going through each ion

[2] See Ref. [91] for an introduction to this technique, which is referred to as the Metropolis Monte Carlo algorithm.

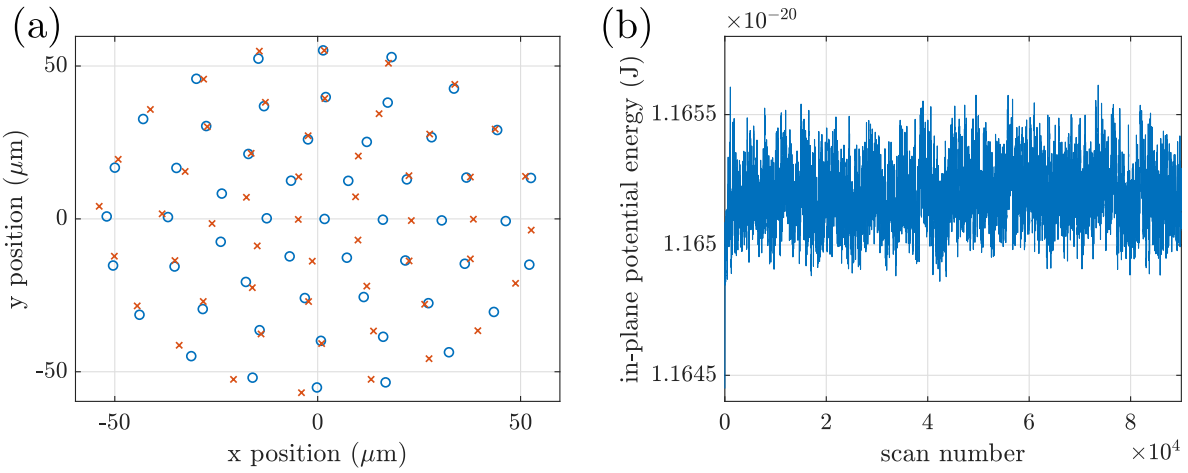

Figure 4.8: Metropolis-Hastings algorithm to find thermal snapshots of the in-plane configuration. (a) Thermal snapshot (orange) with $T_\perp = 10$ mK compared to the minimum energy configuration (blue). (b) Thermalization of the in-plane potential energy as the MH algorithm repeatedly scans over all the ions in the crystal.

in the crystal completes one scan. Figure 4.8(b) plots the in-plane potential energy versus scan number and confirms that typical configurations for the set temperature are reached within the first 10^4 scans. Compared to the minimum energy configuration, typical configurations at a set temperature $T_\perp$ correspond to an average potential energy increase of approximately $k_B T_\perp$ per ion, accounting for the two spatial degrees of freedom.

For each value of $T_\perp$, we then perform a normal mode analysis on 2000 snapshots. Successive snapshots are chosen 40 scans apart to ensure that they are sufficiently uncorrelated. Figure 4.9 shows the histograms of drumhead frequencies for $T_\perp = 0, 1$ and 10 mK. As $T_\perp$ increases, the spectrum transitions from being spiky and fully resolved to a smooth and continuous distribution where only the first few modes are resolvable.

We can also directly study the effect of $T_\perp$ on the ODF spectrum. For this purpose, we realize 48 different in-plane configurations at each value of $T_\perp$, feed in the normal mode spectrum corresponding to each realization into the analytic formula for the ODF spectrum (Eq. (4.5)), and average the spectrum over all the realizations. The results are shown in Fig. 4.10. For comparison, we also show the location of the normal modes for the minimum energy configuration. Clearly,

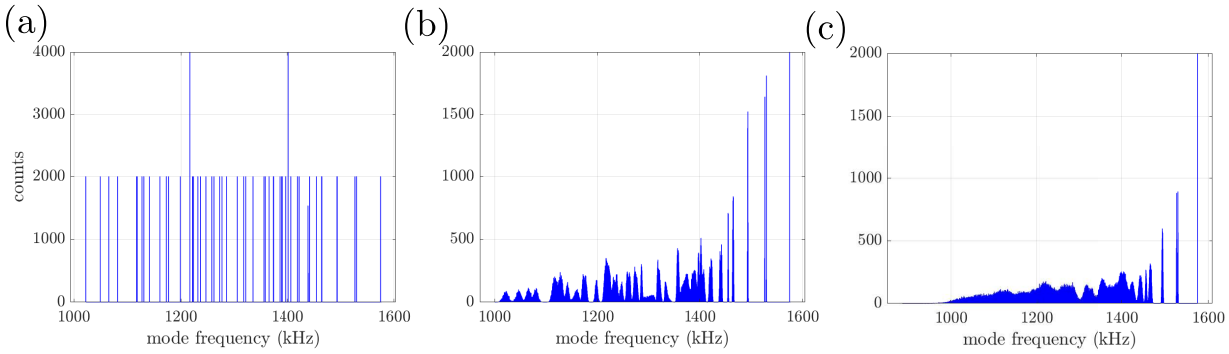

Figure 4.9: Histograms of sorted drumhead modes for 2000 realizations of the in-plane configurations with (a) $T_\perp = 0$ mK, (b) $T_\perp = 1$ mK and (c) $T_\perp = 10$ mK. The bin size is 0.5 kHz. In the 0 mK case, some of the bins carry counts that are not a multiple of 2000 possibly because of round-off errors affecting the binning algorithm or because of slight fluctuations in mode frequencies as the MH algorithm might have found lower energy configurations.

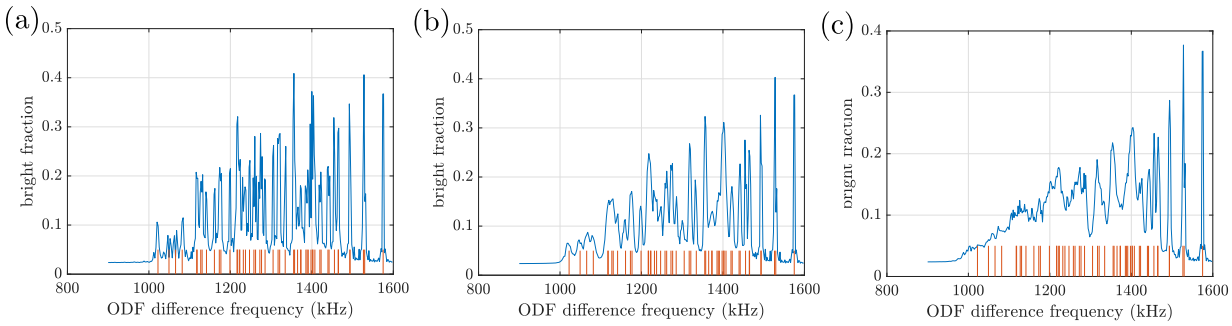

Figure 4.10: ODF spectra computed by averaging over the bright fraction expected from the normal modes of 48 thermal snapshots of the in-plane configuration. Here, (a) $T_\perp = 0$ mK, (b) $T_\perp = 1$ mK and (c) $T_\perp = 10$ mK. We have assumed $\bar{n} = 6$ for all the modes. Also shown are the mode frequencies for the minimum energy configuration.

the ODF spectrum smoothens out with increasing value of $T_\perp$, further supporting the case that in-plane position fluctuations might explain the experimentally measured drumhead spectra.

4.5.3 Molecular dynamics simulations

After establishing an intuitive argument for why thermal in-plane fluctuations may lead to drumhead mode fluctuations, we proceed to verify this idea by brute force molecular dynamics simulations.

The initial conditions for the position and momentum degrees of freedom of the ions are

set using an adaptation of the MH algorithm. First, the MH algorithm is applied using the total Hamiltonian of the system as the cost function. The Hamiltonian can be obtained from the Lagrangian, Eq. (4.16), using a Legendre transformation. When written in terms of the positions and the mechanical momenta, instead of the canonical momenta, the Hamiltonian is separable and therefore the positions and momenta can be sampled separately [33]. Note, however, that as in the case of the in-plane potential energy, the sampling of the ion positions cannot be performed independently for each ion because of the Coulomb interaction.

We would like to study the effect of changing the in-plane temperature $T_\perp$ as the out-of-plane temperature T_z is held fixed. Therefore, we first apply the MH algorithm for the full set of $6N$ degrees of freedom using $T_\perp$ as the temperature. Then, we scale the position and momentum fluctuations of each ion in the out-of-plane direction by a factor of $\sqrt{T_z/T_\perp}$ in order to approximately set an unequal temperature in the z direction. When $T_\perp = 0$, we first follow the above procedure for a value $T_\perp \neq 0$ and then additionally reset the fluctuations in the in-plane positions and momenta to zero.

To study the dynamics, we use a 4th order Runge-Kutta integrator to evolve the Euler-Lagrange equations of motion (Eqs. (4.18 and (4.19). First, we consider the power spectrum, obtained by taking the Fourier transform of the drumhead motion [119]. In Fig. 4.11, we compare the power spectrum in the three cases when $T_\perp = 0, 1$ and 10 mK. In all cases, the out-of-plane temperature is held fixed at $T_z = 0.5$ mK. As $T_\perp$ increases, the power spectrum broadens into a smooth continuum where the modes beyond the highest frequency ones are no longer resolvable. This observation is consistent with the intuitive 'thermal snapshot' picture presented in Section 4.5.2.

4.5.3.1 ODF spectrum from molecular dynamics simulations

We can also extract the expected ODF spectrum from the molecular dynamics simulation. Since the motion is treated classically, this analysis ignores the effect of the zero-point motion and the phonon-mediated spin-spin interaction on the bright fraction (see Eq. (4.5)).

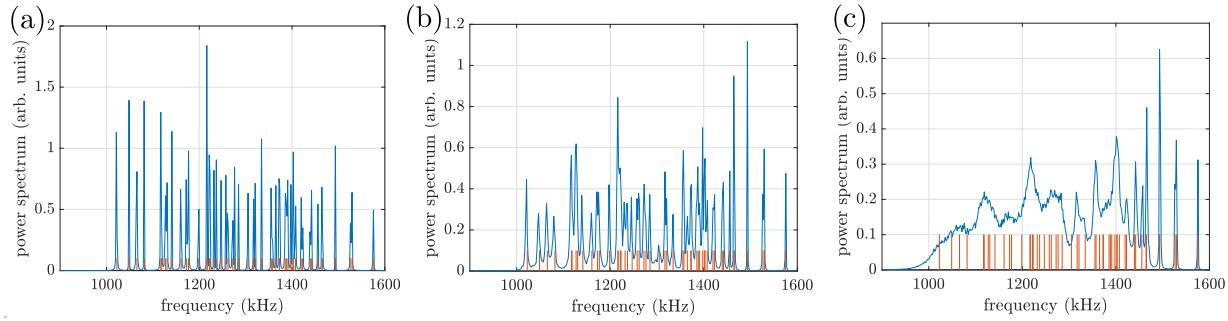

Figure 4.11: Power spectra of the drumhead motion from molecular dynamics simulations. Here, $T_z = 0.5$ mK, and (a) $T_\perp = 0$ mK, (b) $T_\perp = 1$ mK and (c) $T_\perp = 10$ mK.

The ODF interaction Hamiltonian for ion j is

$$H^j_{\mathrm{ODF}} = F_0 \cos(\mu_{\mathrm{R}} t) z_j \hat{\sigma}^z_j. \tag{4.20}$$

First, we investigate the effect of H_{ODF} on the motion. In addition to the trap dynamics, the equation for the momentum p^z_j picks up an additional term

$$\frac{d}{dt} p^z_j = -F_0 \cos(\mu_{\mathrm{R}} t) \langle \hat{\sigma}^z_j \rangle. \tag{4.21}$$

However, $\langle \hat{\sigma}^z_j \rangle \approx 0$ since all the spins precess on the equator for the ODF sequence. Therefore, the effect of the ODF interaction on the ion motion can be neglected when the motion is treated classically, as in the molecular dynamics simulations.

Next, we investigate the effect on the spin. For the quantity $\langle \hat{\sigma}^+_j \rangle$, we get

$$\frac{d}{dt} \langle \hat{\sigma}^+_j \rangle = \frac{1}{\hbar} 2 i F_0 \cos(\mu_{\mathrm{R}} t) z_j \langle \hat{\sigma}^+_j \rangle. \tag{4.22}$$

From this, we see that the time evolution of $\langle \hat{\sigma}^+_j \rangle$ is given by

$$\langle \hat{\sigma}^+_j \rangle(t) = \langle \hat{\sigma}^+_j \rangle(0) \exp\left[\frac{1}{\hbar} 2 i F_0 \int_0^t dt' z_j(t') \cos(\mu_{\mathrm{R}} t') \right], \tag{4.23}$$

with the initial value $\langle \hat{\sigma}^+_j \rangle(0) = 1/2$. Knowing that the bright fraction after the ODF sequence is related to $\langle \hat{\sigma}^x_j \rangle$ before the final state rotation, we immediately obtain

$$P_j(\uparrow) = \frac{1}{2} \left(1 - e^{-2\Gamma\tau} \cos A_j \right), \tag{4.24}$$

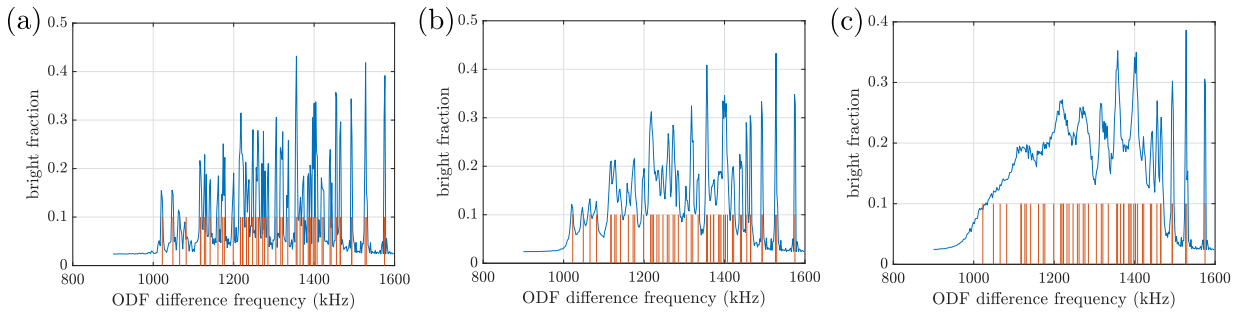

Figure 4.12: ODF spectra computed from molecular dynamics simulations. Here, $T_z = 0.5$ mK, and (a) $T_\perp = 0$ mK, (b) $T_\perp = 1$ mK and (c) $T_\perp = 10$ mK.

where

$$A_j = \frac{2F_0}{\hbar} \int_0^t dt' z_j(t') \cos(\mu_R t'). \tag{4.25}$$

We have included the effect of decoherence by introducing the factor of $e^{-2\Gamma\tau}$ as in Eq. (4.5). To simulate the actual ODF sequence, the force F_0 is multiplied by a factor $g(t)$, which takes the value 1 for $t < \tau$, 0 during the echo time and -1 for $t > \tau + t_\pi$. The sequence ends at $t = 2\tau + t_\pi$.

In Fig. 4.12, we plot the ODF spectrum for the three cases with $T_\perp = 0, 1$ mK and 10 mK. Each spectrum was generated by averaging the bright fraction over 48 realizations of the initial conditions. The ODF spectrum at $T_\perp = 10$ mK is reminiscent of experimentally observed spectra and strongly suggests that thermal energy in the in-plane modes is the primary reason for drumhead mode frequency fluctuations.

In the case of a simple harmonic oscillator, thermal initial conditions can be realized by simply providing velocity kicks corresponding to twice the temperature and setting the position coordinate to zero. The oscillator dynamics will eventually mix the velocity fluctuations into position to give thermal snapshots of the harmonic oscillator. Because of the magnetic field, the in-plane cyclotron and magnetron modes are not such simple harmonic oscillator modes. Therefore, we find that initializing the ions by in-plane velocity kicks is qualitatively very different to additionally initializing the positions via the Metropolis-Hastings algorithm. We find that, even at $T_\perp = 10$ mK, the velocity-kick initialization typically leads to a spiky power spectrum and ODF spectrum, in contrast to the MH based initialization. Based on videos of the in-plane dynamics, we speculate

that the velocity-kick initialization predominantly excites the high-frequency, small-amplitude cyclotron modes, whereas the MH based initialization also excites the low-frequency, large amplitude magnetron modes. The large amplitudes of the latter modes are responsible for significant changes in the instantaneous in-plane configuration, leading to drumhead mode frequency fluctuations.

4.5.4 Further extensions of this study

In order to improve the qualitative and quantitative agreement with measured ODF spectra, several extensions are possible. It is now known that when the EIT measurements were taken, the trap was actually operating with a small anharmonic potential. The addition of such a C_4 term may further smear out the ODF spectrum. Further, the role of impurities has to be investigated. This will require data sets where the number and type of impurities are measured. While here the initial conditions have been assumed to correspond to some temperature, a more realistic simulation could first apply Doppler cooling as in the experiment and use the initial conditions resulting from this process [119]. Studying the ODF spectra obtained after EIT cooling is more complicated because quantum effects of the ion motion must be properly accounted for at such low temperatures.

Chapter 5

Real-time phase tracking: Formalism

Many applications in quantum metrology rely on the dynamics of pseudospin-1/2 systems with two long-lived quantum states, $|\uparrow\rangle$ and $|\downarrow\rangle$. After preparing an equal superposition of these two states, a physical interaction is studied by investigating its effect on the relative phase $\phi(t)$, with the state of each spin evolving in time as $|\psi(t)\rangle = \left(|\downarrow\rangle + e^{i\phi(t)}\,|\uparrow\rangle\right)/\sqrt{2}$. In this chapter, we will describe a novel scheme that enables continuous tracking of this relative phase. Our scheme continuously and directly measures the real-time phase $\phi(t)$ unlike the widely used Ramsey sequence [95, 86, 49, 60, 6, 100, 108, 125, 97, 48, 43, 39], which indirectly measures the net accumulated phase $\phi(T)$ during an interrogation time T. The typically destructive readout in a Ramsey sequence requires multiple state resets, rotations and repetitions of the sequence to infer the phase at different times from a population difference. In contrast, a single run of our protocol yields a continuous time series of phase measurements. Therefore, our scheme enables real-time tracking of time-varying signals that are not reproducible.

As an added benefit, our scheme yields continuous phase estimates with precision well beyond the standard quantum limit (SQL) of $\Delta\phi_{\mathrm{SQL}} = 1/\sqrt{N}$ radians that limits readout precision with N unentangled spins. In comparison to several proposals and experiments [62, 71, 107, 67, 11, 26, 52] that have demonstrated squeezed states with precision beyond the SQL, our scheme enjoys the advantage that the squeezing is produced, the phase accumulated, and the readout performed, all in the same spin quadrature.

Recent experiments have demonstrated phase tracking of a spin using quantum non-demolition

(QND) measurements via a Faraday rotation angle [25]. In contrast, our proposal is based on interfering Raman transitions in a cavity and enables an intuitive interpretation of phase tracking in terms of elementary atom-cavity interactions that nearly balance one another. Our scheme directly reveals a phasor precessing in the equatorial plane of a Bloch sphere, in the spirit of the "hand on a clock" analogy at the core of quantum metrology.

Such interfering cavity-assisted Raman transitions have been considered previously for deterministic squeezing schemes [115] and quantum simulations of the Dicke model [32, 7, 136]. The frequency arrangement of our drive lasers is also related to two-tone drive schemes for back-action evading measurements of mechanical oscillators [16, 23, 15] and for measuring the state of individual superconducting qubits [45, 35].

We represent the collective angular momentum of N atomic spins by a classical Bloch vector of length $N/2$ with components J_x, J_y, J_z. With all spins initially in the same equal superposition state, the Bloch vector lies in the equatorial plane along a direction that we define as the y-axis. As the phase evolves, the Bloch vector acquires a small x-component, $J_x = \frac{N}{2}\sin\phi(t) \approx \frac{N}{2}\phi(t)$, for small deflections, and we propose a straightforward extension to large deflections in the conclusion. We arrange atom-cavity interactions wherein a cavity field quadrature is sourced by J_x. Continuous homodyne detection of this quadrature amounts to real-time, continuous, QND measurement of $\phi(t)$.

We proceed by first introducing the setup under consideration. We then provide an intuitive picture based on classical Bloch vectors that outlines the essential mechanism by which the phase can be tracked. After rigorously deriving the quantum non-demolition Hamiltonian, we introduce the stochastic master equation governing the dynamics of the atom-cavity system under continuous measurement. We employ a Gaussian state approximation to derive dynamical equations for observables from this master equation.

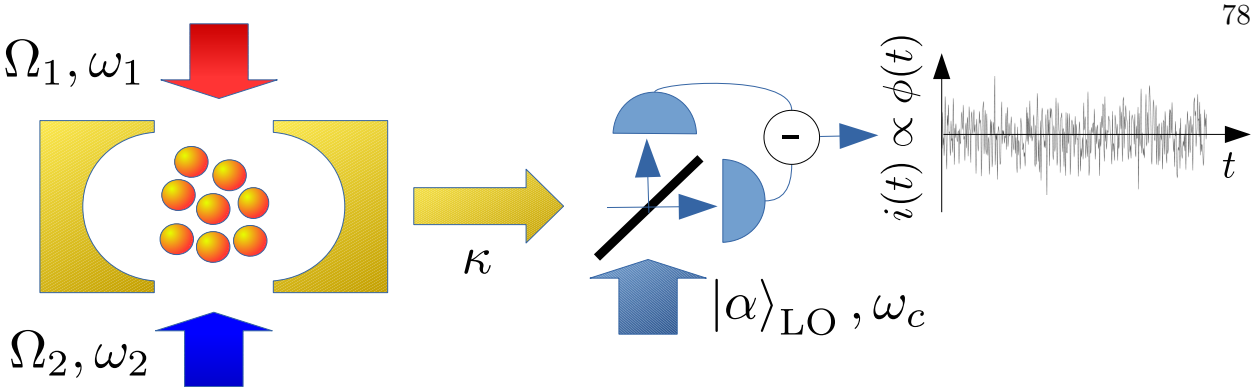

Figure 5.1: Schematic for continuous, real-time phase tracking. Two lasers drive a collection of atoms to interact with a cavity mode. The relative phase $\phi(t)$ can be continuously tracked by homodyne detection of the field leaking out.

5.1 Setup and basic mechanism

We consider N atoms trapped at the antinodes of a cavity with resonance frequency ω_c and decay rate κ, as shown in Fig. 5.1. The states $|\downarrow\rangle$ and $|\uparrow\rangle$ have an energy separation $\hbar\omega_0 \gg \hbar\kappa$ and form a pseudospin-1/2 system described by the Pauli spin operators $\hat{\sigma}_i$, $i = x, y, z$, with raising (lowering) operators $\hat{\sigma}_+$ ($\hat{\sigma}_-$). The N atoms form a collective spin with total angular momentum components $\hat{J}_x, \hat{J}_y, \hat{J}_z$, with $\hat{J}_i = \sum_{j=1}^{N} \hat{\sigma}_i^j/2$. We assume the dipole-allowed transitions $|\downarrow\rangle \leftrightarrow |e\rangle$ and $|\uparrow\rangle \leftrightarrow |e\rangle$ with frequencies $\omega_{\downarrow e}$ and $\omega_{\uparrow e}$ to be respectively driven using lasers with frequencies ω_1 and ω_2 in a far-detuned regime with detuning $\Delta \gg \omega_0, \kappa$, allowing for the adiabatic elimination of $|e\rangle$ [56]. The two drive lasers differ by a frequency $2\omega_0$ (Fig. 5.2(b)) and do not by themselves drive $|\downarrow\rangle \leftrightarrow |\uparrow\rangle$ Raman transitions; however, they are symmetrically detuned by ω_0 from ω_c and participate in cavity-assisted Raman transitions as illustrated in Fig. 5.2(b). When the Rabi frequencies of the two drive lasers are balanced, i.e. $\Omega_1 = \Omega_2 = \Omega_0$, the atom-cavity Hamiltonian, to leading order in $1/\Delta$, is simply the sum of a Jaynes-Cummings and an anti-Jaynes-Cummings interaction and is given by

$$\hat{H}_{\rm QND} = \frac{\hbar\Omega_{\rm QND}}{2}\hat{X}\hat{J}_x. \tag{5.1}$$

Here $\hat{X} = (\hat{a} + \hat{a}^\dagger)/\sqrt{2}$ is the amplitude quadrature, with $\hat{a}, \hat{a}^\dagger$ the annihilation and creation operators for the cavity mode, and $\hat{Y} = (\hat{a} - \hat{a}^\dagger)/\sqrt{2}i$ is the conjugate phase quadrature such

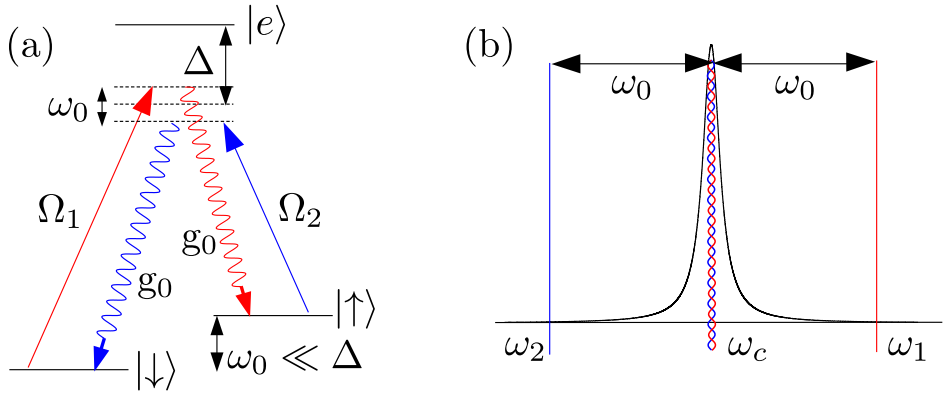

Figure 5.2: (a) Cavity-assisted Raman transitions: The red (blue) pathway leads to the emission of a cavity photon accompanied by a spin flip $|\downarrow\rangle \to |\uparrow\rangle$ ($|\uparrow\rangle \to |\downarrow\rangle$). (b) Hierarchy of frequencies.

that $[\hat{X}, \hat{Y}] = i$. The atom-cavity interaction strength is $\Omega_{\rm QND} = \sqrt{2}\Omega_0 g_0/\Delta$ with g_0 the single atom-cavity vacuum Rabi frequency. For the interested reader, a detailed derivation of $\hat{H}_{\rm QND}$ is presented in Section 5.2. If the two drive lasers have initial phases ψ_1 and ψ_2, the cavity quadrature $\left(\hat{a}^\dagger e^{i(\psi_1+\psi_2)/2} + \text{ H.c.}\right)$ is coupled to the spin component $\left(\hat{J}_+ e^{i(\psi_1-\psi_2)/2} + \text{ H.c.}\right)$, where $\hat{J}_+ = \hat{J}_x + i\hat{J}_y$. Here we assume $\psi_1 = \psi_2 = 0$ without loss of generality.

Classically, the intracavity fields established by the two balanced drives exactly cancel when $J_x = 0$ (Fig. 5.3). However, even with $\langle \hat{J}_x \rangle = 0$, $\langle \hat{J}_x^2 \rangle \neq 0$, i.e. quantum fluctuations source the Y quadrature of the cavity field. In the regime $\kappa^2 \gg N\Omega_{\rm QND}^2$, $\hat{Y}$ is slaved to $\hat{J}_x$ as

$$\hat{Y}(t) \approx -\frac{\Omega_{\rm QND}}{\kappa}\hat{J}_x(t) + \hat{\mathcal{F}}(t), \tag{5.2}$$

where the noise operator $\hat{\mathcal{F}}(t)$ arises from coupling of the cavity mode to external modes through the lossy mirror (Fig. 5.1) [133, 82]. The field leaking out is to be monitored via balanced homodyne detection using a local oscillator at frequency $(\omega_1 + \omega_2)/2$ with phase tuned to detect the output field quadrature that is sourced by the intracavity Y quadrature. The photocurrent thus recorded is a measurement of the Y quadrature which, from Eq. (5.2), amounts to measuring J_x.

Measurement back-action in the J_z quadrature arises because of the indistinguishability of the two pathways that give rise to the intracavity field (Fig. 5.1(b)): The field leaking out is consistent with equal probability amplitudes for tipping the Bloch vector above or below the equator and

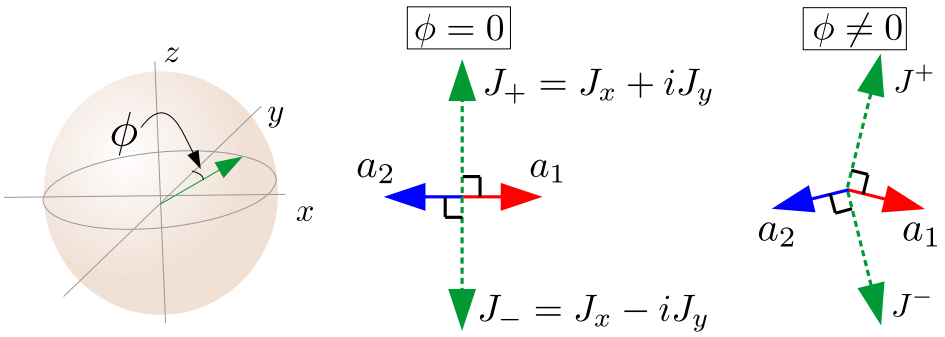

Figure 5.3: Classical Bloch vector picture: The red and blue pathways set up balanced, opposing superradiance pathways that lead to a coherent cancellation of the intracavity field when the Bloch vector (green) is along the y-axis ($\phi = 0$). When the Bloch vector has a small x-component ($\phi \neq 0$), the intracavity field from the two pathways add constructively, giving rise to non-zero output field.

therefore increases the spread in J_z without affecting its mean value.

5.2 Derivation of the QND Hamiltonian

Here, we systematically derive $\hat{H}_{\mathrm{QND}}$ starting from basic atom-cavity interactions and by using effective Hamiltonian theory. This section can be skipped if the reader is not interested in the details of this derivation.

The basic Hamiltonian for the interaction of the atoms with the drive lasers and cavity mode is ($\hbar = 1$ in this Section)

$$\begin{aligned}\hat{H} = {} & \omega_c \hat{a}^\dagger \hat{a} - \omega_{\downarrow e} \sum_j |\downarrow\rangle_j \langle\downarrow| - \omega_{\uparrow e} \sum_j |\uparrow\rangle_j \langle\uparrow| \\ & + \sum_j \left(\frac{\Omega_1}{2} |e\rangle_j \langle\downarrow| \, e^{-i\omega_1 t} + \frac{\Omega_2}{2} |e\rangle_j \langle\uparrow| \, e^{-i\omega_2 t} + \text{ H.c.} \right) \\ & + \sum_j \left(\frac{g_1}{2} \hat{a} \, |e\rangle_j \langle\downarrow| + \frac{g_2}{2} \hat{a} \, |e\rangle_j \langle\uparrow| + \text{ H.c.} \right). \end{aligned} \tag{5.3}$$

The drive laser frequencies are arranged such that $\omega_1 = \omega_c + \omega_0$ and $\omega_2 = \omega_c - \omega_0$. We assume that the splitting $\omega_{\downarrow e} - \omega_{\uparrow e}$ between the spin states, nominally ω_0, can be slightly modified, e.g. by a weak external magnetic field that we wish to sense, i.e. $\omega_{\downarrow e} - \omega_{\uparrow e} = \omega_0 + 2\delta$, where δ ($-\delta$) is the shift of the $|\uparrow\rangle$ ($|\downarrow\rangle$) state.

The detunings of the drive lasers from the atomic transitions are given by $\Delta_1 = \omega_1 - \omega_{\downarrow e} =$

$-\Delta+\omega_0/2-\delta$ and $\Delta_2=\omega_2-\omega_{\uparrow e}=-\Delta-\omega_0/2+\delta$. Similarly, the detunings of the cavity mode from the atomic transitions are $\Delta_1^c=\omega_c-\omega_{\downarrow e}=-\Delta-\omega_0/2-\delta$ and $\Delta_2^c=\omega_c-\omega_{\uparrow e}=-\Delta+\omega_0/2+\delta$.

We write the interaction Hamiltonian expressing the energy requirements in Eq. (5.3) using complex exponentials involving these detunings as

$$\begin{aligned}\hat{H}_I(t) &= \sum_j\left(\frac{\Omega_1}{2}\left|e\right\rangle_j\left\langle\downarrow\right|e^{-i\Delta_1 t}+\frac{\Omega_2}{2}\left|e\right\rangle_j\left\langle\uparrow\right|e^{-i\Delta_2 t}+\text{ H.c.}\right)\\ &+ \sum_j\left(\frac{g_1}{2}\hat{a}\left|e\right\rangle_j\left\langle\downarrow\right|e^{-i\Delta_1^c t}+\frac{g_2}{2}\hat{a}\left|e\right\rangle_j\left\langle\uparrow\right|e^{-i\Delta_2^c t}+\text{ H.c.}\right).\end{aligned}\tag{5.4}$$

We use the effective Hamiltonian theory of Ref. [56] to derive the effective Hamiltonian in the limit where the detunings are all much greater than the Rabi frequencies. This effective Hamiltonian has three parts

$$\hat{H}_{\text{eff}}(t)=\hat{H}_{\text{Stark}}(t)+\hat{H}_{\text{atom-atom}}(t)+\hat{H}_{\text{Raman}}(t),\tag{5.5}$$

where

$$\begin{aligned}\hat{H}_{\text{Stark}}(t)&=\sum_j\frac{|\Omega_1|^2}{4\Delta_1}\left(\left|\downarrow\right\rangle_j\left\langle\downarrow\right|-\left|e\right\rangle_j\left\langle e\right|\right)\\ &+\sum_j\frac{g_1^2}{4\Delta_1^c}\left(\hat{a}^\dagger\hat{a}\left(\left|\downarrow\right\rangle_j\left\langle\downarrow\right|-\left|e\right\rangle_j\left\langle e\right|\right)-\left|e\right\rangle_j\left\langle e\right|\right)\\ &+\sum_j\frac{\Omega_1 g_1}{4h(\Delta_1,\Delta_1^c)}\hat{a}^\dagger\left(\left|\downarrow\right\rangle_j\left\langle\downarrow\right|-\left|e\right\rangle_j\left\langle e\right|\right)e^{i(\Delta_1^c-\Delta_1)t}+\text{ H.c.}\\ &+\downarrow\rightarrow\uparrow\ (1\rightarrow 2),\end{aligned}\tag{5.6}$$

$$\begin{aligned}\hat{H}_{\text{atom-atom}}(t)= &-\sum_{j,k\neq j}\frac{g_1^2}{4\Delta_1^c}\left|e\right\rangle_j\left\langle\downarrow\right|\otimes\left|\downarrow\right\rangle_k\left\langle e\right|+\downarrow\rightarrow\uparrow\ (1\rightarrow 2)\\ &-\sum_{j,k\neq j}\frac{g_1 g_2}{4h(\Delta_1^c,\Delta_2^c)}\left(\left|\uparrow\right\rangle_j\left\langle e\right|\otimes\left|e\right\rangle_k\left\langle\downarrow\right|e^{i(\Delta_2^c-\Delta_1^c)t}+\text{ H.c.}\right),\end{aligned}\tag{5.7}$$

and

$$\begin{aligned}\hat{H}_{\text{Raman}}(t) = &\sum_j \frac{\Omega_1\Omega_2^*}{4h(\Delta_1,\Delta_2)} \left|\uparrow\right\rangle_j \left\langle\downarrow\right| e^{i(\Delta_2-\Delta_1)t} + \text{ H.c.} \\ &+ \sum_j \frac{g_1 g_2}{4h(\Delta_1^c,\Delta_2^c)} \hat{a}^\dagger\hat{a} \left|\uparrow\right\rangle_j \left\langle\downarrow\right| e^{i(\Delta_2^c-\Delta_1^c)t} + \text{ H.c.} \\ &+ \sum_j \frac{\Omega_1 g_2}{4h(\Delta_1,\Delta_2^c)} \hat{a}^\dagger \left|\uparrow\right\rangle_j \left\langle\downarrow\right| e^{i(\Delta_2^c-\Delta_1)t} + \text{ H.c.} \\ &+ \sum_j \frac{\Omega_2 g_1}{4h(\Delta_2,\Delta_1^c)} \hat{a}^\dagger \left|\downarrow\right\rangle_j \left\langle\uparrow\right| e^{i(\Delta_1^c-\Delta_2)t} + \text{ H.c.} \end{aligned} \tag{5.8}$$

In the above expressions, $h(a,b) = 2/(a^{-1}+b^{-1})$ is the harmonic mean of a and b. All terms in the effective Hamiltonian conserve the number of excitations in $|e\rangle$. This means that if the atoms are initially in the $|\downarrow\rangle - |\uparrow\rangle$ manifold, then the state $|e\rangle$ is negligibly populated and all interactions involving this level, and consequently, $\hat{H}_{\text{atom-atom}}(t)$, can be dropped. Expressing the difference detunings in the complex exponentials in terms of Δ, ω_0, and δ shows the presence of rapidly oscillating terms with frequency $\sim \omega_0$ and slowly varying terms with zero frequency or a small frequency δ. For $\Omega_1 \approx \Omega_2 \sim \Omega$, the rapidly oscillating terms can be neglected since we operate in the regime where $\Omega^2/\Delta \ll \omega_0$. The resulting Hamiltonian consists of

$$\begin{aligned}\hat{H}_{\text{Stark}}(t) = &\sum_j \frac{|\Omega_1|^2}{4\Delta_1} \left|\downarrow\right\rangle_j \left\langle\downarrow\right| + \sum_j \frac{g_1^2}{4\Delta_1^c} \hat{a}^\dagger\hat{a} \left|\downarrow\right\rangle_j \left\langle\downarrow\right| \\ &+ \downarrow\!\to\!\uparrow \;\; (1 \to 2) \end{aligned} \tag{5.9}$$

and

$$\begin{aligned}\hat{H}_{\text{Raman}}(t) = &\sum_j \frac{\Omega_1 g_2}{4h(\Delta_1,\Delta_2^c)} \hat{a}^\dagger \left|\uparrow\right\rangle_j \left\langle\downarrow\right| e^{2i\delta t} + \text{ H.c.} \\ &+ \sum_j \frac{\Omega_2 g_1}{4h(\Delta_2,\Delta_1^c)} \hat{a}^\dagger \left|\downarrow\right\rangle_j \left\langle\uparrow\right| e^{-2i\delta t} + \text{ H.c.} \end{aligned} \tag{5.10}$$

5.2.1 Simple picture

For $\Delta \gg \omega_0$, we can make the substitution $\Delta_1, \Delta_2, \Delta_1^c, \Delta_2^c \to -\Delta$. Then, with $\Omega_1 = \Omega_2 = \Omega_0$, the Stark shifts from the drive lasers shift the two spin states identically and therefore lead to an overall energy shift of $-N\Omega_0^2/4\Delta$, where we assume Ω_0 is real. Similarly, with $g_1 = g_2 = g_0$, the

frequency of the cavity mode is shifted by an amount $-Ng_0^2/4\Delta$ on account of the atom-cavity interaction. This can be compensated for by shifting the frequency of the drive lasers by the same amount. Introducing the collective angular momentum operators $\hat{J}_+ \equiv \sum_j |\uparrow\rangle_j \langle\downarrow|$, $\hat{J}_- \equiv \hat{J}_+^\dagger$, and $\hat{J}_z \equiv \sum_j \left(|\uparrow\rangle_j \langle\uparrow| - |\downarrow\rangle_j \langle\downarrow|\right)/2$, we can express the effective Hamiltonian as

$$\hat{H}_{\text{eff}} = 2\delta \hat{J}_z + \frac{\Omega_0 g_0}{4\Delta}\left(\hat{a} + \hat{a}^\dagger\right)\left(\hat{J}_+ + \hat{J}_-\right), \tag{5.11}$$

where we have let $\Omega_0 \to -\Omega_0$. The second term on the RHS is precisely the QND Hamiltonian, Eq. 5.1. This coarse-grained Hamiltonian is valid over time intervals $\Delta t \gg T_{\omega_0} \equiv 2\pi/\omega_0$, and therefore, we require $\delta \ll \omega_0$ and that δ is approximately constant over the interval Δt. Mathematically, the latter implies $d\ln\delta/dt \ll 1/\Delta t \ll \omega_0/2\pi$.

5.2.2 Accounting for ω_0/Δ

For $\delta \approx 0$, $h(\Delta_1, \Delta_2^c) = \Delta_1$ and $h(\Delta_2, \Delta_1^c) = \Delta_2$. To isolate the balanced cavity-assisted Raman transitions, three requirements have to be satisfied [32]:

(1) Equal drive laser Stark shifts on both spin states: $\Omega_1^2/4\Delta_1 = \Omega_2^2/4\Delta_2$.

(2) Equal frequency shift of cavity mode per atom in either spin state: $g_1^2/4\Delta_1^c = g_2^2/4\Delta_2^c$.

(3) Balanced Raman transitions: $\Omega_1 g_2/4\Delta_1 = \Omega_2 g_1/4\Delta_2$.

We note that arranging Ω_1/Ω_2 and g_1/g_2 to satisfy (1) and (2) above automatically results in satisfying requirement (3).

5.2.3 Note concerning drive laser frequencies

In practice, the frequency arrangement of the drive lasers requires their average frequency ω_{av} to be tuned well within the cavity linewidth, i.e. $|\omega_c - \omega_{\text{av}}| \ll \kappa$. The difference frequency $\omega_1 - \omega_2$ is relatively easier to stabilize, and deviations from $2\omega_0$ manifest as a growth of the phase over time that can be measured and statistically modeled.

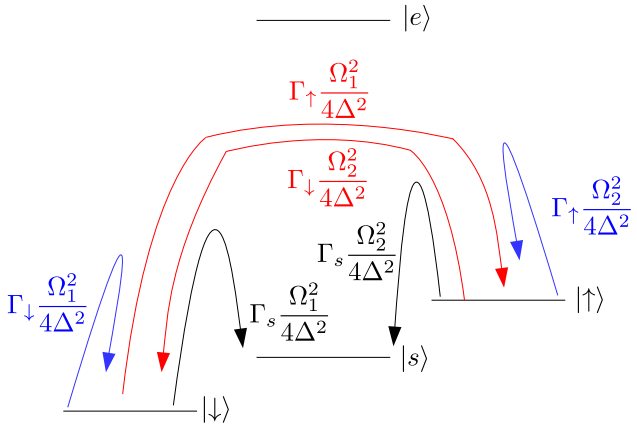

Figure 5.4: Free-space scattering processes considered in our model: Rayleigh scattering (blue), Raman scattering (red) and atom loss (black).

5.3 Phenomenological free-space scattering model

The drive lasers also lead to undesirable, off-resonant free-space scattering processes with total rate $\gamma_{\rm sc}$ that degrade atomic coherence. We consider three such single-atom decoherence mechanisms: (a) dephasing with probability r_d: random rotation about the z-axis, (b) spontaneous Raman spin flips : $|\downarrow\rangle \rightarrow |\uparrow\rangle$ ($r_{\downarrow\uparrow}$) and $|\uparrow\rangle \rightarrow |\downarrow\rangle$ ($r_{\uparrow\downarrow}$), and (c) atom loss (r_l): the atom decays to a state $|s\rangle$ outside the $|\downarrow\rangle - |\uparrow\rangle$ manifold and no longer interacts with the cavity mode. The probabilities are related by $r_d + r_{\downarrow\uparrow} + r_{\uparrow\downarrow} + r_l = 1$.

Fig. 5.4 shows the various free-space scattering (FSS) processes considered in our model. The lifetime of the excited state is $\Gamma = \Gamma_\downarrow + \Gamma_\uparrow + \Gamma_s$.

The dephasing rate is set by the total rate of Rayleigh scattering [110]:

$$\text{Dephasing:}\quad \Gamma_\downarrow \frac{\Omega_1^2}{4\Delta^2} + \Gamma_\uparrow \frac{\Omega_2^2}{4\Delta^2}. \tag{5.12}$$

Raman spin flips ($|\downarrow\rangle \rightarrow |\uparrow\rangle$) occur with rate $\Gamma_\uparrow \frac{\Omega_1^2}{4\Delta^2}$, while $|\uparrow\rangle \rightarrow |\downarrow\rangle$ occur at rate $\Gamma_\downarrow \frac{\Omega_2^2}{4\Delta^2}$ [110]. Finally, atom loss occurs at a net rate given by

$$\text{Atom loss:}\quad \Gamma_s \left(\frac{\Omega_1^2}{4\Delta^2} + \frac{\Omega_2^2}{4\Delta^2} \right). \tag{5.13}$$

With $\Omega_1 \approx \Omega_2 \equiv \Omega_0$, the probabilities for the different FSS channels are

$$r_d = \frac{\Gamma_\downarrow + \Gamma_\uparrow}{2\Gamma},\ r_{\downarrow\uparrow} = \frac{\Gamma_\uparrow}{2\Gamma},\ r_{\uparrow\downarrow} = \frac{\Gamma_\downarrow}{2\Gamma},\ r_l = \frac{\Gamma_s}{\Gamma}. \tag{5.14}$$

The total FSS rate is

$$\gamma_{\rm sc} = 2\Gamma\frac{\Omega_0^2}{4\Delta^2}. \tag{5.15}$$

While presenting our numerical results in Chapter 6, we adopt a "symmetric loss" model wherein the three decoherence mechanisms degrade the atomic coherence at equal rates, and spin-flips in either direction occur with equal probability. This implies $r_d = 1/3$, $r_{\downarrow\uparrow} = r_{\uparrow\downarrow} = 1/6$ and $r_l = 1/3$. Such a model corresponds to $\Gamma_\downarrow = \Gamma_\uparrow = \Gamma_s = \Gamma/3$. In this case, from Eq. (5.14), $r_d = 1/3$, $r_{\downarrow\uparrow} = r_{\uparrow\downarrow} = 1/6$ and $r_l = 1/3$.

Our simple phenomenological model captures the FSS processes expected when a three-level system is driven by two lasers whose difference frequency is far detuned from the two-photon resonance. In practice, scattering from any additional excited states should be considered. Detailed modeling of a real experiment will benefit from a rigorous first-principles derivation of the effects of free-space scattering that also accounts for the cavity mode, as shown in Refs. [13, 115].

5.4 Stochastic master equation

Under continuous measurement, the dynamics of the density matrix ρ of the atom-cavity system is governed by the stochastic master equation [129, 15, 131]:

$$\begin{aligned}\dot\rho = \quad & -i/\hbar[\hat H_{\rm QND},\rho] + \kappa\mathcal{D}[\hat a]\rho + \gamma_{\rm sc}\textstyle\sum_{j=1}^{N}\mathcal{L}_1^j\rho \\ & +\sqrt{\eta\kappa}\xi(t)\left(i\rho\hat a^\dagger - i\hat a\rho - \sqrt{2}\langle\hat Y\rangle\rho\right),\end{aligned} \tag{5.16}$$

with decoherence effects bundled in $\mathcal{L}_1^j\rho$, given by

$$\begin{aligned}\mathcal{L}_1^j\rho \;=\;& r_{\downarrow\uparrow}\mathcal{D}[\hat\sigma_+^j]\rho + r_{\uparrow\downarrow}\mathcal{D}[\hat\sigma_-^j]\rho + \frac{r_d}{4}\mathcal{D}[\hat\sigma_z^j]\rho \\ +\;& \frac{r_l}{2}\left(\mathcal{D}\left[|s\rangle_j\langle\downarrow|_j\right]\rho + \mathcal{D}\left[|s\rangle_j\langle\uparrow|_j\right]\rho\right),\end{aligned} \tag{5.17}$$

with $\mathcal{D}[\hat O]\rho = \hat O\rho\hat O^\dagger - \hat O^\dagger\hat O\rho/2 - \rho\hat O^\dagger\hat O/2$, the Lindblad dissipator. In Eq. (5.16), η is the detection efficiency, and $\xi(t)$ is a white-noise process satisfying $\overline{\xi(t)} = 0$ and $\overline{\xi(t)\xi(t')} = \delta(t-t')$. The measured photocurrent $i(t)$ is

$$i(t) = \mathcal{G}e|\alpha_{\rm LO}|\left(\eta\sqrt{2\kappa}\langle\hat Y\rangle + \sqrt{\eta}\xi(t)\right), \tag{5.18}$$

with detector gain $\mathcal{G}$, electronic charge e, and local oscillator photon flux $|\alpha_{\rm LO}|^2$ with units of photons/time.

5.5 Gaussian state approximation

With no decoherence, measuring for very long times will result in preparing states arbitrarily close to Dicke states in the J_x basis. However, decoherence restricts the maximum achievable squeezing well before the state begins to wrap around the Bloch sphere. This enables a Gaussian approximation where we only track the dynamics of the means and covariances of all operators and pairs of operators of the atom-cavity system. The 5 operators $\hat{X}, \hat{Y}, \hat{J}_x, \hat{J}_y$ and $\hat{J}_z$ result in a total of 20 dynamical equations.

To derive these equations, we first rewrite Eq. (5.16) as

$$\begin{aligned} d\rho &= \left(-i/\hbar[\hat{H}_{\rm QND},\rho] + \kappa\mathcal{D}[\hat{a}]\rho + \gamma_{\rm sc}\sum_{j=1}^{N}\mathcal{L}_1^j\rho\right)dt \\ &+ \sqrt{\eta\kappa}dW(t)\left(i\rho\hat{a}^\dagger - i\hat{a}\rho - \sqrt{2}\langle\hat{Y}\rangle\rho\right), \end{aligned} \tag{5.19}$$

where $dW(t)$ is a Wiener increment that satisfies $\overline{dW(t)} = 0$ and $dW(t)^2 = dt$ [120].

The expectation value of an operator $\hat{O}$ is given by $\langle\hat{O}\rangle = \mathrm{Tr}\left[\hat{O}\rho\right]$ and, consequently, $\langle\dot{\hat{O}}\rangle = \mathrm{Tr}\left[\hat{O}\dot{\rho}\right]$. We keep track of only the means and covariances of the five operators $\hat{X}, \hat{Y}, \hat{J}_x, \hat{J}_y$ and $\hat{J}_z$. We truncate these evolution equations at second order by factorizing third order moments of the type $\langle\hat{O}_1\hat{O}_2\hat{O}_3\rangle$ as

$$\langle\hat{O}_1\hat{O}_2\hat{O}_3\rangle \approx \langle\hat{O}_1\hat{O}_2\rangle\langle\hat{O}_3\rangle + \langle\hat{O}_2\hat{O}_3\rangle\langle\hat{O}_1\rangle + \langle\hat{O}_1\hat{O}_3\rangle\langle\hat{O}_2\rangle - 2\langle\hat{O}_1\rangle\langle\hat{O}_2\rangle\langle\hat{O}_3\rangle. \tag{5.20}$$

This procedure leads to five equations governing the means of the operators that have the typical form of stochastic differential equations: $d\langle\hat{O}\rangle = a dt + b dW$. The time evolution of the fifteen covariances, on the other hand, are governed by ordinary differential equations that have no terms proportional to dW. This structure is a direct consequence of the Gaussian approximation we employ. We reproduce these equations below.

We use the notation $\langle \ldots \rangle$ to denote means and $\langle \ldots \rangle_c$ to denote (co)variances evaluated using the stochastic master equation, Eq. (5.19). The covariance is defined as $\langle \hat{O}_1 \hat{O}_2 \rangle_c = (\langle \hat{O}_1 \hat{O}_2 \rangle + \langle \hat{O}_2 \hat{O}_1 \rangle)/2 - \langle \hat{O}_1 \rangle \langle \hat{O}_2 \rangle$.

5.5.1 Operator means

The operator means obey the following set of equations.

$$\begin{aligned}
d\langle \hat{X} \rangle &= -\frac{\kappa}{2}\langle \hat{X} \rangle dt + 2\sqrt{\frac{\eta\kappa}{2}}\langle \hat{X}\hat{Y} \rangle_c dW \\
d\langle \hat{Y} \rangle &= -\left(\frac{\kappa}{2}\langle \hat{Y} \rangle + \frac{\Omega_{\mathrm{QND}}}{2}\langle \hat{J}_x \rangle\right) dt + \sqrt{\frac{\eta\kappa}{2}}\left(2\langle \hat{Y}^2 \rangle_c - 1\right) dW \\
d\langle \hat{J}_x \rangle &= -\frac{\gamma_{\mathrm{sc}}}{2}\langle \hat{J}_x \rangle dt + 2\sqrt{\frac{\eta\kappa}{2}}\langle \hat{Y}\hat{J}_x \rangle_c dW \\
d\langle \hat{J}_y \rangle &= -\left[\frac{\gamma_{\mathrm{sc}}}{2}\langle \hat{J}_y \rangle + \frac{\Omega_{\mathrm{QND}}}{2}\left(\langle \hat{X}\hat{J}_z \rangle_c + \langle \hat{X} \rangle \langle \hat{J}_z \rangle\right)\right] dt + 2\sqrt{\frac{\eta\kappa}{2}}\langle \hat{Y}\hat{J}_y \rangle_c dW \\
d\langle \hat{J}_z \rangle &= -\left[\gamma_{\mathrm{sc}}\left(\left(r_{\uparrow\downarrow} + r_{\downarrow\uparrow} + \frac{r_l}{2}\right)\langle \hat{J}_z \rangle + \left(r_{\uparrow\downarrow} - r_{\downarrow\uparrow}\right)\frac{N}{2}\right) - \frac{\Omega_{\mathrm{QND}}}{2}\left(\langle \hat{X}\hat{J}_y \rangle_c + \langle \hat{X} \rangle \langle \hat{J}_y \rangle\right)\right] dt \\
&\quad + 2\sqrt{\frac{\eta\kappa}{2}}\langle \hat{Y}\hat{J}_z \rangle_c dW
\end{aligned} \tag{5.21}$$

5.5.2 Operator covariances

Operator covariance are governed by the following sets of equations.

$$\begin{aligned}
\frac{d}{dt}\langle \hat{X}^2 \rangle_c &= -\kappa\left(\langle \hat{X}^2 \rangle_c - \frac{1}{2}\right) - 2\eta\kappa\langle \hat{X}\hat{Y} \rangle_c^2 \\
\frac{d}{dt}\langle \hat{Y}^2 \rangle_c &= -\kappa\left(\langle \hat{Y}^2 \rangle_c - \frac{1}{2}\right) - \Omega_{\mathrm{QND}}\langle \hat{Y}\hat{J}_x \rangle_c - \frac{\eta\kappa}{2}\left(2\langle \hat{Y}^2 \rangle_c - 1\right)^2 \\
\frac{d}{dt}\langle \hat{X}\hat{Y} \rangle_c &= -\kappa\langle \hat{X}\hat{Y} \rangle_c - \frac{\Omega_{\mathrm{QND}}}{2}\langle \hat{X}\hat{J}_x \rangle_c - \eta\kappa\langle \hat{X}\hat{Y} \rangle_c \left(2\langle \hat{Y}^2 \rangle_c - 1\right)
\end{aligned} \tag{5.22}$$

$$\begin{aligned}
\frac{d}{dt}\langle \hat{X}\hat{J}_x \rangle_c &= -\left(\frac{\kappa + \gamma_{\mathrm{sc}}}{2}\right)\langle \hat{X}\hat{J}_x \rangle_c - 2\eta\kappa\langle \hat{Y}\hat{J}_x \rangle_c \langle \hat{X}\hat{Y} \rangle_c \\
\frac{d}{dt}\langle \hat{X}\hat{J}_y \rangle_c &= -\left(\frac{\kappa + \gamma_{\mathrm{sc}}}{2}\right)\langle \hat{X}\hat{J}_y \rangle_c - \frac{\Omega_{\mathrm{QND}}}{2}\left(\langle \hat{X}\hat{J}_z \rangle_c \langle \hat{X} \rangle + \langle \hat{X}^2 \rangle_c \langle \hat{J}_z \rangle\right) - 2\eta\kappa\langle \hat{Y}\hat{J}_y \rangle_c \langle \hat{X}\hat{Y} \rangle_c \\
\frac{d}{dt}\langle \hat{X}\hat{J}_z \rangle_c &= -\left(\frac{\kappa}{2} + \gamma_{\mathrm{sc}}\left(r_{\uparrow\downarrow} + r_{\downarrow\uparrow} + \frac{r_l}{2}\right)\right)\langle \hat{X}\hat{J}_z \rangle_c + \frac{\Omega_{\mathrm{QND}}}{2}\left(\langle \hat{X}\hat{J}_y \rangle_c \langle \hat{X} \rangle + \langle \hat{X}^2 \rangle_c \langle \hat{J}_y \rangle\right) \\
&\quad - 2\eta\kappa\langle \hat{Y}\hat{J}_z \rangle_c \langle \hat{X}\hat{Y} \rangle_c
\end{aligned} \tag{5.23}$$

$$
\begin{aligned}
\frac{d}{dt}\langle\hat{Y}\hat{J}_x\rangle_c &= -\left(\frac{\kappa+\gamma_{\rm sc}}{2}\right)\langle\hat{Y}\hat{J}_x\rangle_c - \frac{\Omega_{\rm QND}}{2}\langle\hat{J}_x^2\rangle_c - \eta\kappa\langle\hat{Y}\hat{J}_x\rangle_c\left(2\langle\hat{Y}^2\rangle_c - 1\right)\\
\frac{d}{dt}\langle\hat{Y}\hat{J}_y\rangle_c &= -\left(\frac{\kappa+\gamma_{\rm sc}}{2}\right)\langle\hat{Y}\hat{J}_y\rangle_c - \frac{\Omega_{\rm QND}}{2}\left(\langle\hat{J}_x\hat{J}_y\rangle_c + \langle\hat{X}\hat{Y}\rangle_c\langle\hat{J}_z\rangle + \langle\hat{Y}\hat{J}_z\rangle_c\langle\hat{X}\rangle\right)\\
&\quad -\eta\kappa\langle\hat{Y}\hat{J}_y\rangle_c\left(2\langle\hat{Y}^2\rangle_c - 1\right)\\
\frac{d}{dt}\langle\hat{Y}\hat{J}_z\rangle_c &= -\left(\frac{\kappa}{2} + \gamma_{\rm sc}\left(r_{\uparrow\downarrow} + r_{\downarrow\uparrow} + \frac{r_l}{2}\right)\right)\langle\hat{Y}\hat{J}_z\rangle_c\\
&\quad -\frac{\Omega_{\rm QND}}{2}\left(\langle\hat{J}_z\hat{J}_x\rangle_c - \langle\hat{X}\hat{Y}\rangle_c\langle\hat{J}_y\rangle - \langle\hat{Y}\hat{J}_y\rangle_c\langle\hat{X}\rangle\right) - \eta\kappa\langle\hat{Y}\hat{J}_z\rangle_c\left(2\langle\hat{Y}^2\rangle_c - 1\right)
\end{aligned}
\tag{5.24}
$$

$$
\begin{aligned}
\frac{d}{dt}\langle\hat{J}_x^2\rangle_c &= -\gamma_{\rm sc}\left(\langle\hat{J}_x^2\rangle_c - \left(r_{\uparrow\downarrow} + r_{\downarrow\uparrow} + r_d + \frac{r_l}{2}\right)\frac{N}{4}\right) - 2\eta\kappa\langle\hat{Y}\hat{J}_x\rangle_c^2\\
\frac{d}{dt}\langle\hat{J}_y^2\rangle_c &= -\gamma_{\rm sc}\left(\langle\hat{J}_y^2\rangle_c - \left(r_{\uparrow\downarrow} + r_{\downarrow\uparrow} + r_d + \frac{r_l}{2}\right)\frac{N}{4}\right) - \Omega_{\rm QND}\left(\langle\hat{X}\hat{J}_y\rangle_c\langle\hat{J}_z\rangle + \langle\hat{J}_y\hat{J}_z\rangle_c\langle\hat{X}\rangle\right)\\
&\quad -2\eta\kappa\langle\hat{Y}\hat{J}_y\rangle_c^2\\
\frac{d}{dt}\langle\hat{J}_z^2\rangle_c &= -\gamma_{\rm sc}\left(\left(2r_{\uparrow\downarrow} + 2r_{\downarrow\uparrow} + r_l\right)\langle\hat{J}_z^2\rangle_c - r_{\uparrow\downarrow}\left(\frac{N}{2} + \langle\hat{J}_z\rangle\right) - r_{\downarrow\uparrow}\left(\frac{N}{2} - \langle\hat{J}_z\rangle\right) - r_l\frac{N}{8}\right)\\
&\quad +\Omega_{\rm QND}\left(\langle\hat{X}\hat{J}_z\rangle_c\langle\hat{J}_y\rangle + \langle\hat{J}_y\hat{J}_z\rangle_c\langle\hat{X}\rangle\right) - 2\eta\kappa\langle\hat{Y}\hat{J}_z\rangle_c^2
\end{aligned}
\tag{5.25}
$$

$$
\begin{aligned}
\frac{d}{dt}\langle\hat{J}_x\hat{J}_y\rangle_c &= -\gamma_{\rm sc}\langle\hat{J}_x\hat{J}_y\rangle_c - \frac{\Omega_{\rm QND}}{2}\left(\langle\hat{X}\hat{J}_x\rangle_c\langle\hat{J}_z\rangle + \langle\hat{J}_z\hat{J}_x\rangle_c\langle\hat{X}\rangle\right) - 2\eta\kappa\langle\hat{Y}\hat{J}_x\rangle_c\langle\hat{Y}\hat{J}_y\rangle_c\\
\frac{d}{dt}\langle\hat{J}_y\hat{J}_z\rangle_c &= -\gamma_{\rm sc}\left(\left(\frac{3}{2}r_{\uparrow\downarrow} + \frac{3}{2}r_{\downarrow\uparrow} + \frac{r_d}{2} + r_l\right)\langle\hat{J}_y\hat{J}_z\rangle_c - \left(\frac{r_{\uparrow\downarrow} - r_{\downarrow\uparrow}}{2}\right)\langle\hat{J}_y\rangle\right)\\
&\quad + \frac{\Omega_{\rm QND}}{2}\left(\langle\hat{X}\hat{J}_y\rangle_c\langle\hat{J}_y\rangle + \langle\hat{J}_y^2\rangle_c\langle\hat{X}\rangle - \langle\hat{X}\hat{J}_z\rangle_c\langle\hat{J}_z\rangle - \langle\hat{J}_z^2\rangle_c\langle\hat{X}\rangle\right) - 2\eta\kappa\langle\hat{Y}\hat{J}_y\rangle_c\langle\hat{Y}\hat{J}_z\rangle_c\\
\frac{d}{dt}\langle\hat{J}_z\hat{J}_x\rangle_c &= -\gamma_{\rm sc}\left(\left(\frac{3}{2}r_{\uparrow\downarrow} + \frac{3}{2}r_{\downarrow\uparrow} + \frac{r_d}{2} + r_l\right)\langle\hat{J}_z\hat{J}_x\rangle_c - \left(\frac{r_{\uparrow\downarrow} - r_{\downarrow\uparrow}}{2}\right)\langle\hat{J}_x\rangle\right)\\
&\quad + \frac{\Omega_{\rm QND}}{2}\left(\langle\hat{X}\hat{J}_x\rangle_c\langle\hat{J}_y\rangle + \langle\hat{J}_x\hat{J}_y\rangle_c\langle\hat{X}\rangle\right) - 2\eta\kappa\langle\hat{Y}\hat{J}_z\rangle_c\langle\hat{Y}\hat{J}_x\rangle_c
\end{aligned}
\tag{5.26}
$$

5.5.3 Some comments on the equations of motion

The above equations describe the conditional evolution when no external phase modulation is applied. Such a modulation can be straightforwardly accounted for by including the contributions of an additional Hamiltonian term $\propto \hat{J}_z$, such as the first term on the RHS of Eq. (5.11), to the equations of motion of the means and covariances.

In deriving the above equations, we have accounted for the contribution of the atom loss terms (proportional to r_l) to the loss of coherence and the increase in diffusion. We note that atom

loss reduces the effective number of atoms N_{eff} that interact with the cavity mode. However, we simply use the total number N wherever N_{eff} explicitly appears in these equations. That is, we account for $\dot{N}_{\text{eff}} = -r_l \gamma_{\text{sc}} N_{\text{eff}}$ that leads to increased diffusion of the atomic spin components, but approximate $N_{\text{eff}} \approx N$ everywhere in the above equations.

5.5.4 Numerical evolution

We numerically evolve the dynamical equations for the means and covariances using a variation of the Improved Euler scheme for integrating stochastic differential equations [98]. Our numerical results are obtained using a C++ program that employs linear algebra features provided by Eigen [44], a C++ template library. The Wiener increments and random numbers required for numerical integration are obtained using random number generators from the GNU Scientific Library [38]. Numerically, the infinite bandwidth of $i(t)$ (Eq. (5.18)) means that the data sampling time step must equal the simulation time step.

Chapter 6

Real-time phase tracking: Numerical experiments

In this chapter, we will use the Gaussian equations that we derived in the previous chapter to perform numerical simulations that demonstrate real-time phase tracking below the standard quantum limit. We will also discuss connections with the Ramsey sequence and derive an analytic expression for the optimum metrological gain achievable when our scheme is used as a Ramsey-like sequence. We conclude with a discussion on the advantages of combining our proposal with a feedback scheme.

6.1 Estimating the phase

To estimate the phase, we average the simulated photocurrent (Eq. (5.18)) in a time window $[T_i, T_f]$ to obtain an estimate as

$$J_x^{(m)} = -\frac{\kappa}{\Omega_{\rm QND}} Y^{(m)} = \frac{-(\mathcal{G}e|\alpha_{\rm LO}|)^{-1}}{\eta\sqrt{C\gamma_{\rm sc}}(T_f - T_i)} \int_{T_i}^{T_f} i(t)dt, \tag{6.1}$$

where $C = 2\Omega_{\rm QND}^2/\kappa\gamma_{\rm sc}$ is the dimensionless atom-cavity cooperativity. The phase is estimated as $\phi^{(m)} = (J_x^{(m)}/(N/2))/\mathcal{V}(t)$, where the visibility $\mathcal{V}(t) \approx e^{-\gamma_{\rm sc}t/2}e^{-(C\gamma_{\rm sc}/4)t/2}$ accounts for the shortening of the Bloch vector, evaluated either at the window center or end depending on where the phase is estimated. For $C \ll 1$, free-space scattering is the main reason for shortening of the Bloch vector, whereas for $C \gg 1$, measurement-induced squeezing is the dominant contribution. While we use a simple averaging procedure for clarity, optimal filters, such as Kalman filters, can be applied for superior phase tracking [40, 117, 14].

The precision of the phase estimate in a window is determined by the window duration. A characteristic time, $T_0 = (\eta C \gamma_{\rm sc})^{-1}/(N/4)$, is the time required to average down the photon shot-noise ($\xi(t)$ term, Eq. (5.18)) in estimating $J_x^{(m)}$ (Eq. (6.1)) to the standard quantum limit $\Delta J^2_{x,\rm SQL} = N/4$.

6.1.1 Note concerning the cooperativity

We have defined the cooperativity C in terms of the two-photon rates $\Omega_{\rm QND}$ and $\gamma_{\rm sc}$. With the explicit form of $\gamma_{\rm sc}$ in Eq. (5.15), and the expression $\Omega_{\rm QND} = \sqrt{2}\Omega_0 g_0/\Delta$, we can express C in terms of the single-photon coupling strength g_0 and the lifetime Γ of the state $|e\rangle$ as

$$C = 2\frac{\Omega^2_{\rm QND}}{\kappa\gamma_{\rm sc}} = 8\frac{g_0^2}{\kappa\Gamma}. \tag{6.2}$$

We note that our definition of C differs from the usual definition [81] by a factor of 8. However, as Eq. (6.4) later shows, with our definition of C, the rate $\eta C\gamma_{\rm sc}$ takes on the simple interpretation as the rate at which the variance in J_x decreases as the field leaking out from the cavity is monitored. Here, η is as usual the detection efficiency of the photodetectors used for homodyne detection. With perfect detectors ($\eta = 1$), C is therefore the ratio of the rates of the desirable and undesirable processes.

6.2 Parameters for numerical experiments

For our numerical experiments, we use $N = 10^5$ atoms identically coupled to a cavity mode with $C = 0.1$, unless specified otherwise. We work in a bad-cavity regime such that $NC\gamma_{\rm sc} = 0.2\kappa$, achievable by arranging for $\Omega_{\rm QND} = 10^{-3}\kappa$. We adopt the "symmetric loss" model for free space scattering that is described in Section 5.3. However, our results are not very sensitive to the specific choice of relative rates. The loss in visibility only depends on the total decoherence rate, while the measurement of J_x marginally improves if the atom loss channel is dominant (see Eq. (6.11)). Finally, the detection efficiency is assumed to be $\eta = 0.4$ [26].

6.3 Real-time phase tracking: A demonstration

We now demonstrate the ability of our scheme to track in real-time, a phase modulation $\phi^{(a)}(t)$ applied for $t > 0$ (Fig. 6.1(a, black solid line)). At time $t = -50T_0$, the collective spin is initialized to a coherent spin state (CSS) along the y-axis whose initial phase is $\phi_0 = 0$. First, measuring the photocurrent in the state preparation window $[-50T_0, 0]$ gives a phase estimate $\phi_0^{(m)}$ (blue triangle). This estimate is obtained at the end of this window using the procedure described below Eq. (6.1). The value of $\phi_0^{(m)}$ varies from trial-to-trial with a variance $\Delta\phi^2_{\rm SQL} = 1/N$ corresponding to the phase uncertainty of the initial CSS. The long state preparation window ensures strong averaging down of the photon shot-noise, leading to a state with reduced phase uncertainty around $\phi_0^{(m)}$, i.e. a spin squeezed state (SSS). For the subsequent real-time tracking, two choices for the initial phase reference could be used: $\phi_0(=0)$ or $\phi_0^{(m)}$.

During the time $[0, 200T_0]$, we average the photocurrent in windows of duration $8T_0$ to extract a raw phase estimate $\phi^{(m)}(j)$ for window $j = 1, 2, \ldots$. We construct two estimates for the phase at the window centers, $\phi^{(m)}_{\rm CSS}(j) = \phi^{(m)}(j) - \phi_0$ (hollow red squares), and $\phi^{(m)}_{\rm SSS}(j) = \phi^{(m)}(j) - \phi_0^{(m)}$ (filled blue squares). The precision of these estimates is determined not just by the window duration over which the raw estimate is obtained, but also by the precision of the phase reference. To determine the single-run precision of these estimates, we run 2048 trials of the experiment and histogram the error in these estimates, an example of which is shown in Fig. 6.1(b) for the window $[48T_0, 56T_0]$. The estimates $\phi^{(m)}_{\rm CSS}$ use the imprecise zero phase ϕ_0 of the initial CSS as reference, and lead to a broad error histogram (red). In contrast, the estimates $\phi^{(m)}_{\rm SSS}$ lead to a narrow error histogram (blue) whose spread is instead dominated by the imprecision in obtaining the raw estimates $\phi^{(m)}(j)$ over short windows (here, $8T_0$), demonstrating the improved precision of the phase reference $\phi_0^{(m)}$ over ϕ_0 [1] . In Fig. 6.1(c) we show that the variance $\Delta\phi^2_{\rm SSS}$ of the estimates $\phi^{(m)}_{\rm SSS}$ is significantly less than $\Delta\phi^2_{\rm SQL}$ in all windows over the time we consider here, demonstrating the potential for real-time phase tracking with precision beyond the SQL.

[1] If only the form, and not the precise value, of an AC signal is to be tracked in a single run, the choice of initial phase reference is irrelevant, making the state preparation step unnecessary.

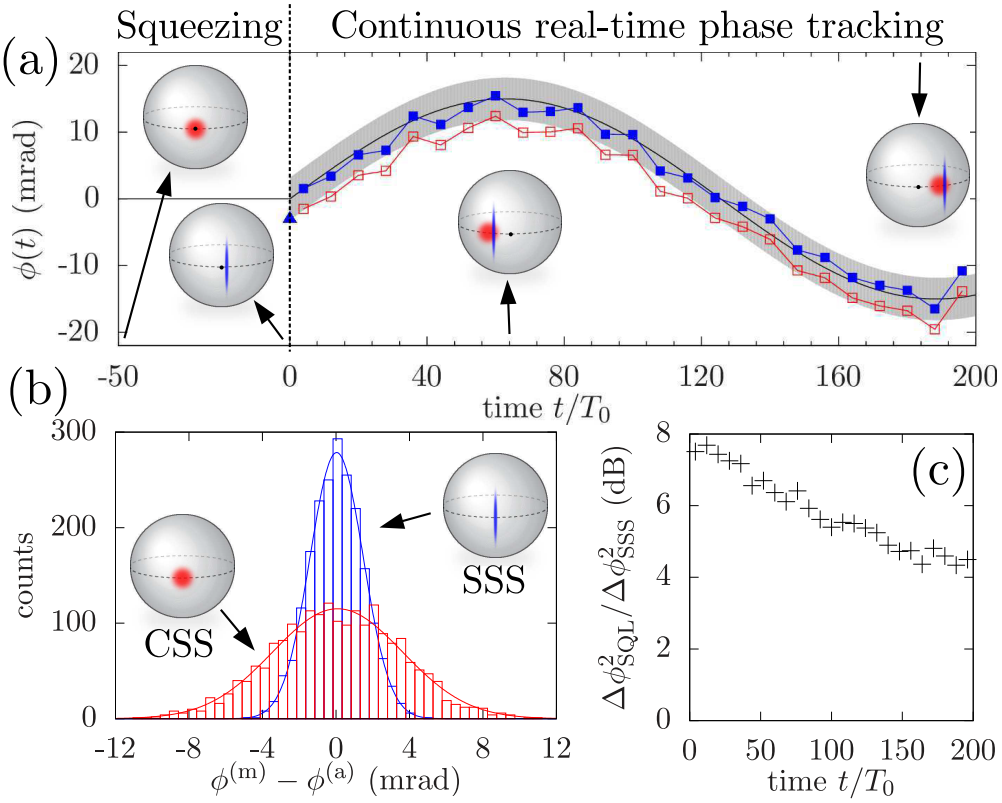

Figure 6.1: Real-time continuous tracking of a time-varying phase. (a) A single experimental run: A squeezed state is prepared during $[-50T_0, 0]$, with the initial measured phase $\phi_0^{(m)}$ (blue triangle) varying in each run. Subsequently, a phase modulation $\phi^{(a)}(t) = 15$ mrad $\times \sin(t/40T_0)$ (black line) is applied e.g. using a time-varying magnetic field. The blue, filled (red, hollow) markers are estimates $\phi_{\mathrm{SSS}}^{(m)}$ ($\phi_{\mathrm{CSS}}^{(m)}$) of the phase using the measured photocurrent in windows of duration $8T_0$ that account for (do not account for) the initial offset $\phi_0^{(m)}$. The gray shaded region indicates the 1-σ SQL tolerance for this applied signal. Representative Bloch spheres for $t \leq 0$ indicate the state before and after the state preparation stage. For $t > 0$, Bloch spheres indicate the deflection of the spin as a result of the phase modulation (black dots on the spheres indicate the zero phase reference), as well as the equivalent spin state used for the respective estimates $\phi_{\mathrm{CSS}}^{(m)}$, $\phi_{\mathrm{SSS}}^{(m)}$. (b) Histogram of phase errors $\phi_{\mathrm{SSS}}^{(m)} - \phi^{(a)}$ (blue) and $\phi_{\mathrm{CSS}}^{(m)} - \phi^{(a)}$ (red) over 2048 runs in one particular measurement window $[48T_0, 56T_0]$. (c) Single-run precision gain of the estimates $\phi_{\mathrm{SSS}}^{(m)}$ relative to the SQL at different window centers t. Here, $\Delta\phi^2_{\mathrm{SSS}}$ is the variance of Gaussian fits to histograms such as the blue histogram in (b). Decoherence results in decreased gain over time.

6.4 Use as a Ramsey sequence

First, we note an advantage of our scheme, namely that the same photocurrent data from a single run can be analyzed using multiple methods to extract varying information. As a demonstration, we use varying window durations T_W to extract precise timing and amplitude information from a sudden jump in phase (at $T_J = 50T_0$ in Fig. 6.2(a)). Starting with an initial CSS at $t = 0$, we continuously estimate the phase by averaging the photocurrent over moving windows of durations $T_W = 2T_0$ (red) and $T_W = 20T_0$ (blue). Clearly, the shorter window reproduces the time variation of the phase more precisely. To estimate the amplitude of the jump ϕ_J, we compute the difference $\phi_J^{(m)}$ in the estimates $\phi_{W_1}^{(m)}, \phi_{W_2}^{(m)}$ in the two windows $W_1 \equiv [T_J - T_W, T_J]$ and $W_2 \equiv [T_J, T_J + T_W]$ that border the jump time T_J (Fig. 6.2(b))[2] . While the shorter window results in faster response, the longer window gives a more precise estimate of the jump amplitude (Fig. 6.2(c)).

Alternatively, the sudden phase jump in the protocol depicted in Fig. 6.2(b) can be replaced with a "dark" phase accumulation time of duration T_D where no measurements are performed. The scheme can then be identified as a Ramsey-like sequence where a squeezed state is prepared in W_1, phase accumulates in an interrogation time T_D, and finally, phase is read out in W_2, without ever converting the phase information into a population difference. In this Ramsey mode, the achievable gain in phase resolution using the prepared squeezed state compared to a CSS is

$$\frac{\Delta\phi^2_{\mathrm{SQL}}}{\Delta\phi^2} = \frac{\Delta J^2_{x,\mathrm{SQL}}}{\left(\Delta J^{(m)}_{x,\mathrm{diff}}\right)^2}\mathcal{V}^2, \tag{6.3}$$

where $J^{(m)}_{x,\mathrm{diff}} = J^{(m)}_{x,W_2} - J^{(m)}_{x,W_1}$ and $\mathcal{V}$ is the visibility at the end of the first window [11, 26]. Fig. 6.2(d) plots the numerically extracted gain (markers) versus the window duration T_W for different values of cooperativity C. Gaussian fits to histograms of $J^{(m)}_{x,\mathrm{diff}}$ were used to extract values for $(\Delta J^{(m)}_{x,\mathrm{diff}})^2$.

[2] For simplicity, we assume that the jump time of our test signal is known in advance. In practice, the jump time and amplitude can be simultaneously estimated using tools from optimal filtering theory.

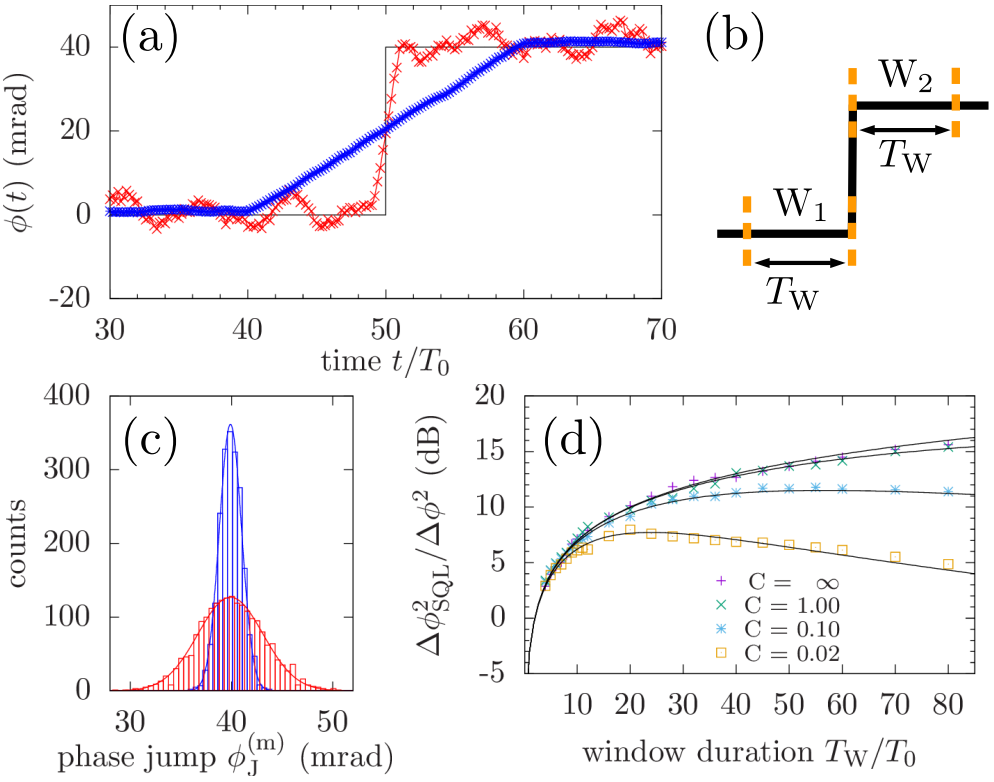

Figure 6.2: (a) A sudden jump in the phase with amplitude $\phi_J = 40$ mrad at $T_J = 50T_0$ is tracked in the same run using moving windows of durations $T_W = 2T_0$ (red) and $T_W = 20T_0$ (blue), showing the faster response of the shorter window. (b) Protocol to estimate ϕ_J. (c) Histograms, over 2048 runs, of $\phi_J^{(m)}$ for $T_W = 2T_0$ (red) and $T_W = 20T_0$ (blue), demonstrating the greater precision of the longer window. For $T_W = 2T_0$, W_2 was offset by a small time $0.2T_0$ to allow transients on timescales of κ^{-1} to decay. (d) Gain in precision over a CSS in Ramsey mode as the duration of W_1 and W_2 is varied, for fixed $C\gamma_{sc}$ and different values of C. Analytic results (lines) calculated using Eqs. (6.3) and (6.11) are in excellent agreement with simulations (markers).

6.5 Analytic expression for variance in the difference measurement

To understand the numerically observed trend, we work with the equations derived in Section 5.5 to obtain an analytic expression for $(\Delta J^{(m)}_{x,\mathrm{diff}})^2$. The time evolution of the conditional variance $\langle \hat{J}_x^2 \rangle_c$ satisfies the Riccati equation

$$\frac{d}{dt}\langle \hat{J}_x^2 \rangle_c = -\gamma_{\mathrm{sc}} \left(\langle \hat{J}_x^2 \rangle_c - \beta \frac{N}{4} \right) - \eta C \gamma_{\mathrm{sc}} \langle \hat{J}_x^2 \rangle_c^2, \tag{6.4}$$

where we have used the bad-cavity limit to adiabatically eliminate $\langle \hat{Y} \hat{J}_x \rangle_c$ and substitute it with the quantity $-(\Omega_{\mathrm{QND}}/\kappa)\langle \hat{J}_x^2 \rangle_c$ in the equation for $\langle \hat{J}_x^2 \rangle_c$. In the regime where $\sqrt{NC} \gg 1$ and $\sqrt{\beta\eta NC} \gg 1$, the solution to Eq. (6.4) simplifies to

$$\langle \hat{J}_x^2(t) \rangle_c = \frac{N}{4} \sqrt{\frac{4\beta}{NC\eta}} \coth \left[\sqrt{\frac{\beta NC}{4\eta}} \gamma_{\mathrm{sc}} t + \sqrt{\frac{4\beta}{NC\eta}} \right]. \tag{6.5}$$

The conditional mean $\langle \hat{J}_x \rangle$ is given by

$$\langle \hat{J}_x(t) \rangle = -\sqrt{\eta C \gamma_{\mathrm{sc}}} \int_0^t dt' \langle \hat{J}_x^2(t') \rangle_c e^{-\frac{\gamma_{\mathrm{sc}}}{2}(t-t')} \xi(t'). \tag{6.6}$$

From Eq. (5) and the bad-cavity relation $\langle \hat{Y} \rangle = -(\Omega_{\mathrm{QND}}/\kappa)\langle \hat{J}_x \rangle$, the instantaneous photocurrent $i(t)$ carries information about $\langle \hat{J}_x \rangle$ but is corrupted by photon shot noise. Using Eq. (6), the estimate $J_x^{(m)}$ from the photocurrent measured in an interval $[T_i, T_f]$ is related to the conditional mean $\langle \hat{J}_x \rangle$ as

$$J_x^{(m)} = \frac{1}{T_f - T_i} \int_{T_i}^{T_f} dt \left(\langle \hat{J}_x(t) \rangle - \frac{1}{\sqrt{\eta C \gamma_{\mathrm{sc}}}} \xi(t) \right), \tag{6.7}$$

where $\langle \hat{J}_x \rangle$ satisfies Eq. (6.6). In deriving Eq. (8), we perform the first measurement $J^{(m)}_{x,1}(T_W)$ over the window $[0, T_W]$, and the second measurement $J^{(m)}_{x,2}(T_W)$ over the window $[T_W, 2T_W]$. The variance in the difference measurement $(\Delta J^{(m)}_{x,\mathrm{diff}})^2(T_W)$ is given by

$$(\Delta J^{(m)}_{x,\mathrm{diff}})^2(T_W) = \overline{\left(J^{(m)}_{x,2}(T_W) - J^{(m)}_{x,1}(T_W) \right)^2}, \tag{6.8}$$

where the overbar indicates averaging over all possible realizations of the noise $\xi(t)$, which has the properties $\overline{\xi(t)} = 0$ and $\overline{\xi(t)\xi(t')} = \delta(t - t')$. We use the approximation that $\gamma_{\mathrm{sc}} T_W \ll 1$ for the

measurement windows we consider, so that the exponential factor in Eq. (6.6) can be set to unity. The resulting integrals can be evaluated analytically, resulting in

$$(\Delta J_{x,1}^{(m)})^2(T_W) = \frac{N}{4}\left(1 + \frac{T_0}{T_W} + \frac{4\beta}{3\eta NC}\frac{T_W}{T_0}\right) \tag{6.9}$$

for the variance in the first measurement, and

$$(\Delta J_{x,2}^{(m)})^2(T_W) = \frac{N}{4}\left(1 + \frac{T_0}{T_W} + \frac{16\beta}{3\eta NC}\frac{T_W}{T_0}\right) \tag{6.10}$$

for the variance in the second measurement. For the variance in the difference measurement, we get

$$\frac{(\Delta J_{x,\mathrm{diff}}^{(m)})^2(T_W)}{\Delta J_{x,\mathrm{SQL}}^2} = 2\frac{T_0}{T_W} + \frac{8\beta}{3\eta NC}\frac{T_W}{T_0}, \tag{6.11}$$

where $\beta = r_d + r_{\downarrow\uparrow} + r_{\uparrow\downarrow} + r_l/2$, giving a minimum normalized variance of $8\sqrt{\beta/3\eta NC}$ at $T_W^{\mathrm{opt}} = T_0\sqrt{3\eta NC/4\beta}$. The expression for β shows that the normalized variance is not very sensitive to the relative probabilities of the decoherence mechanisms. For typical values of $C \sim 0.1$ and $N \sim 10^5$, Fig. 6.2(d) shows that a gain upwards of 11 dB can be achieved. The $(NC)^{-1/2}$ scaling of the minimum normalized variance in $J_{x,\mathrm{diff}}^{(m)}$ leads to an optimal phase resolution scaling as $\Delta\phi \sim N^{-3/4}$ compared to $\Delta\phi_{\mathrm{SQL}} = N^{-1/2}$ radians.

6.5.1 Physical explanation for optimum measurement window

Although the photon shot noise is averaged down as the measurement window T_W is increased, undetected photons emitted via free-space scattering (FSS) lead to increased ignorance about the actual state of the collective spin. The photocurrent measurements in the initial parts of the measurement window are no longer as reliable in estimating the current value of J_x as those in the latter parts, since FSS has significantly affected the collective spin state. Since $J_{x,\mathrm{diff}}^{(m)}$ is the difference of measurements in two such windows, for very large T_W, the correlation in these two measurements decreases as a result of FSS. The upshot: The window has an optimum duration below which the measurement suffers from photon shot-noise, and above which it is affected by FSS.

6.5.2 Absence of noticeable Zeno effect

A natural question concerns the quantum Zeno effect: Does the real-time phase measurement inhibit the evolution of the phase? For the parameters used in the simulations, we do not observe any noticeable Zeno effect. Here, we describe a theoretical situation where it can likely be observed. In the absence of free-space scattering, Eq. (6.9) implies that measuring for very long times suppresses the photon shot noise arbitrarily, and that the variance of the measurement is eventually limited only by the spread of the initial CSS over the eigenstates of $\hat{J}_x$. Although our Gaussian theory cannot describe this extreme limit, we can use Eq. (6.9) to qualitatively estimate the time required to resolve such eigenstates by assuming that the photon shot noise contribution $NT_0/T_W \sim 1$, leading to $T_W \sim NT_0$. The Zeno effect can be observed if the phase evolves by $1/N$ radians on a timescale $\gtrsim NT_0$, translating to a phase modulation rate $\sim 1/(N^2T_0) \sim C\gamma_{\mathrm{sc}}/N$. In the simulations, free-space scattering takes over well before the $\hat{J}_x$ eigenstates can be resolved and we only prepare squeezed states with variance a factor of $\mathcal{O}(1-10)$ below the SQL. Furthermore, the peak modulation rate, for example, in Fig. 6.1, is $\sim 10^7$ times greater than $1/(N^2T_0)$. These factors probably suggest why the Zeno effect is not noticeable in our simulations.

6.6 Advantage of a feedback loop

While Ramsey sequences only measure phase changes unambiguously in the interval $[-\pi/2, \pi/2]$, our scheme readily extends to tracking large excursions $|\phi(t)| \gg \pi$: The measured current $i(t)$ can be used in a feedback loop [128, 2, 130, 127, 120] to adjust the differential phase offset $\psi_1 - \psi_2$ of the drive lasers such that $i(t)$ is continuously driven back to zero. The feedback loop continuously adjusts the spin component probed by the cavity mode such that it is always perpendicular to the mean spin direction, while mapping the phase $\phi(t)$ onto the feedback signal as $\phi(t) = (\psi_1 - \psi_2)/2$. This way, large phase excursions can be tracked while remaining in the small angle measurement limit. By encoding the spins in hyperfine levels that have an intrinsic splitting, our scheme has the unique capability to greatly increase the unambiguous interval of phase evolution that can be

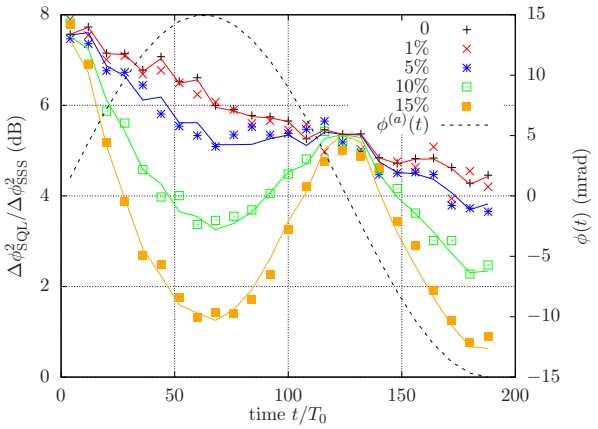

Figure 6.3: Effect of number fluctuations on real-time phase tracking. Single-run precision gain computed using error histograms of 2048 experimental runs (compare to Fig. 6.1(c)). Parameters are from Fig. 6.1, except that the number of atoms in each run is variable, with a mean of $\bar{N} = 10^5$ and $\Delta N/\bar{N}$ indicated by the percentages. Data points (markers) extracted from the numerical experiments are in very good agreement with semi-analytic results (solid lines) obtained using the simple expression in Eq. (6.13) that accounts for number fluctuations. The black dashed line plots the applied phase modulation, for reference.

continuously tracked, for example in atomic clocks. While feedback schemes using intermittent non-demolition population measurements have been used to extend this interval in a Ramsey-like sequence [63], our scheme continuously tracks the phase and removes the need for state rotations altogether. Another benefit of feedback is that it greatly suppresses sensitivity to variations or uncertainties in scale factors relating $i(t)$ to $\phi(t)$, including uncertainties in atom number, as we demonstrate below.

6.6.1 Atom number fluctuations

Here, we show why the number fluctuations are not important in a practical realization of our proposal that implements feedback.

In the small angle limit, the measured phase is linearly related to $J_x^{(m)}$ as

$$\phi^{(m)} = \frac{2J_x^{(m)}}{\mathcal{V}N}, \tag{6.12}$$

where $\mathcal{V}$ is the visibility and N is the number of atoms. So far, we have assumed fluctuations only

in $J_x^{(m)}$. In addition, when N is not precisely known, the error in $\phi^{(m)}$ is given by

$$(\Delta\phi^{(m)})^2 \approx \left(\frac{2}{\mathcal{V}N}\right)^2 (\Delta J_x^{(m)})^2 + (\phi^{(m)})^2 \left(\frac{\Delta N}{N}\right)^2. \tag{6.13}$$

The expression in Eq. (6.13) is approximate because we neglect the covariance of fluctuations in J_x and N. The error from ΔN is negligible compared to the error from ΔJ_x when

$$(\phi^{(m)})^2 \ll \frac{4}{\mathcal{V}^2} \left(\frac{\Delta J_x^{(m)}}{\Delta N}\right)^2. \tag{6.14}$$

In other words, the presence of number fluctuations only sets an upper bound on the dynamical range of the phase that can be tracked, and does not impose a fundamental restriction.

In order to validate this argument, we introduce number fluctuations in our numerical experiments for the situation depicted in Fig. 6.1, see Fig. 6.3. When $\Delta N = 0$, we recover the results of Fig. 6.1(c). As we increase ΔN, the precision gain sharply falls in regions where the tracked phase has large amplitude. To verify the simple formula, Eq. (6.13), we take the numerically obtained variance in the absence of number fluctuations (black markers) as representing the $(\Delta J_x^{(m)})^2$ term in Eq. (6.13) and add, by hand, the contribution of the $(\Delta N)^2$ term, to obtain the solid lines shown in Fig. 6.3. The values of $\phi^{(m)}$ that enter this expression are approximated to be the values of the applied phase modulation (black dashed line) at the window centers. The very good agreement between the numerically extracted (markers) and semi-analytic (solid lines) results validate the expression, Eq. (6.13), for the error in ϕ.

Figure 6.3 and Eq. (6.13) imply that, in a practical realization, the effect of number fluctuations can be suppressed if the measured phase is always maintained close to zero. Feedback enables continuous tracking of large phase excursions in such a small angle measurement limit, and therefore greatly suppresses sensitivity to atom number fluctuations. In fact, by the same argument, a feedback loop will also suppress variations or uncertainties in any scale factors relating the measured current to the phase $\phi(t)$, and not just the atom number.

Chapter 7

Squeezing on momentum pseudospins: Formalism

Current Bragg interferometers operate in free space with state-of-the-art technology enabling control of large numbers of atoms [21, 55, 54, 20]. This technical progress has now achieved high signal-to-noise ratios for determining the relative phase shift. However, despite the use of large atom numbers, their operation can be completely described in terms of single-atom physics since the atoms are uncorrelated. As a result, regardless of whether further technical improvements are realized, the phase sensitivity of these interferometers in the near future will be fundamentally constrained by the SQL of $\Delta\phi_{\mathrm{SQL}} = 1/\sqrt{N}$ radians, where N is the number of atoms. Monotonically increasing N to improve precision suffers from problems such as practical limitations in trapping and cooling [122, 18], and uncontrolled phase changes that arise from atomic collisions [99]. Schemes to produce squeezed states of momentum pseudospins are therefore attractive as a means to achieve precision beyond the corresponding SQL for a given N. A major hurdle to producing such states in Bragg interferometers is that squeezing requires a channel for the atoms to controllably interact with each other, and such a channel is unavailable in current interferometer designs.

The recent demonstration of a hyperfine-changing Raman gravimeter operating inside an optical cavity [47] motivates us to envisage a similar operation of Bragg interferometers in cavities in the near future. The availability of a cavity mode naturally opens up a channel for mediating atom-atom interactions. Previous proposals for cavity-based squeezing on momentum spins [103] require significant experimental overhead dedicated to achieving squeezing while the actual interferometer itself operates in free space. Here, we propose an alternative approach that marries the generation of

cavity-mediated spin squeezing [76, 53, 88] with the well known advantages of operating the entire interferometer inside a cavity [47]. Importantly, our scheme does not require any experimental overhead to generate interactions beyond what is already needed to run a Bragg interferometer in a cavity. In fact, we show how all-to-all atomic interactions are generated by simply switching off one of the two Bragg lasers and suitably adjusting the frequency and power of the other.

The use of momentum pseudospins in Bragg interferometers necessitates two unique considerations. First, the atomic cloud will always have a non-zero momentum width even after velocity selection. This width can typically be neglected in the analysis with uncorrelated atoms. Second, momentum pseudospins cannot be considered as closed two level systems since the same pair of counterpropagating electromagnetic fields couples the pseudospin states to other momentum states, albeit with varying detunings. As a result, leakage to undesirable momentum states is unavoidable even while applying efficient Bragg pulses for spin rotations, and also when attempting to engineer interactions for spin squeezing. In our work, we account for the momentum width as well as leakage to undesirable states and show that they can be important when considering the efficiency of a spin squeezing protocol applied to momentum pseudospins. Nevertheless, as we demonstrate, appreciable spin squeezing can still be achieved under suitable and potentially realizable operating conditions.

In the process of accounting for the effects of momentum width and losses to undesirable states, we show how to extend modeling techniques originally developed for spin systems to interacting atoms in matter-wave interferometers where information is encoded in external degrees of freedom. This ability to map the continuous momentum variable onto a discrete quantum pseudospace allows us to directly employ methods developed for finite dimensional systems [106, 92, 70] . The techniques we use to study our system are widely applicable for investigations of beyond mean-field physics in a broad range of schemes involving interacting atoms whose momentum states are coupled by electromagnetic fields.

In this chapter, we will introduce a scheme to generate squeezing on momentum pseudospins and also develop the necessary framework to study the dynamics of this system. After describing

the system under consideration, we will first provide an intuitive explanation for why one can expect squeezing in this system. Next, we derive a master equation describing the atom-cavity interactions. Further, we also adiabatically eliminate the cavity mode to arrive at a second effective master equation for the atoms only. We also describe approximate numerical methods for each of the two master equations that enable us to obtain complementary insights into the squeezing dynamics.

7.1 Setup

We consider a collection of N atoms with mass M in a ring cavity with resonance frequency ω_c as shown in Fig. 7.1(a). Each atom consists of two electronic levels $|g\rangle$ and $|e\rangle$ with transition frequency ω_a. A laser with frequency ω_l drives one mode of the ring cavity. The cavity resonance is red detuned from the atomic transition by a detuning $\Delta_c = \omega_a - \omega_c > 0$, while the drive laser is detuned by $\Delta_l = \omega_a - \omega_l > 0$. The relative detuning of the laser and the cavity is $\Delta_{cl} = \omega_l - \omega_c \ll \Delta_c, \Delta_l$. Upon absorption or emission of a photon with wavevector $\mathbf{k}$, the momentum of an atom is shifted by $\hbar k$, where $k = |\mathbf{k}|$.

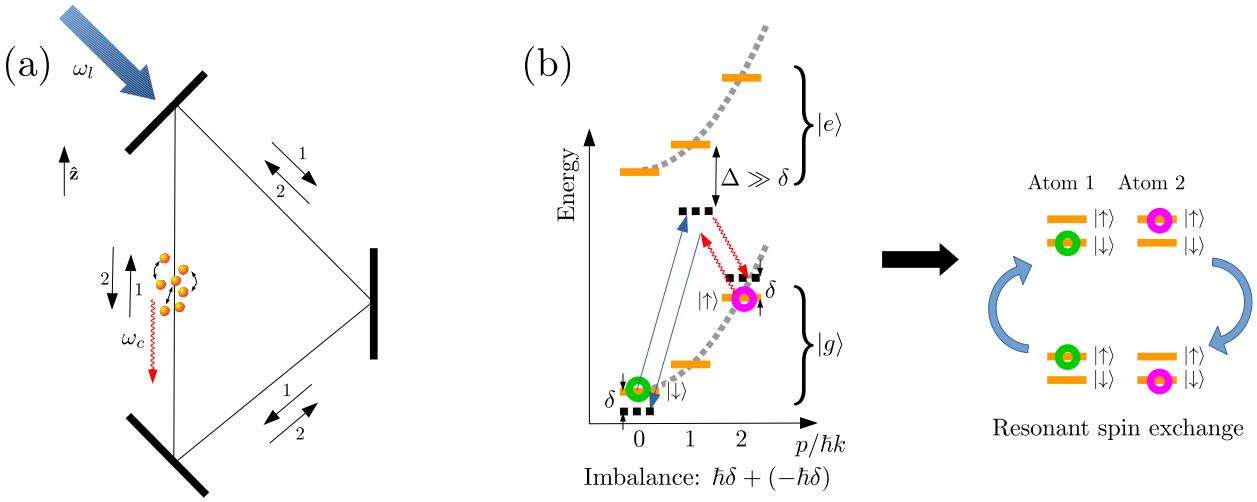

Figure 7.1: Experiment setup and working principle. (a) A cloud of atoms interacts with two counterpropagating modes of a ring cavity. One mode (mode 1) is driven at frequency ω_l, while the counterpropagating mode (mode 2) is in vacuum, i.e. not pumped. The scheme enables cavity-mediated interactions between every pair of atoms. (b) The excitation or de-excitation of a single atom is off-resonant. However, the exchange of excitation between two atoms is a resonant process.

7.2 Basic working principle

The underlying principle for how squeezing is generated in our scheme is summarized in Fig. 7.1(b) for the case when the pseudospin is encoded in the states $|\downarrow\rangle \equiv |g, 0\rangle$ and $|\uparrow\rangle \equiv |g, 2\hbar k\rangle$ with transition frequency $4\omega_r$, where $\omega_r = \hbar k^2/2M$ is the atomic recoil frequency. We denote the driven mode as mode 1 and the counterpropagating mode as mode 2. The drive laser frequency is arranged such that $\Delta_{cl} = \omega_l - \omega_c = 4\omega_r + \delta$, where δ is a two-photon detuning typically assumed to be > 0 in this work. The excitation of an atom from $|\downarrow\rangle$ to $|\uparrow\rangle$ (green circle in Fig. 7.1(b)) is facilitated by the absorption of a drive photon and subsequent emission into mode 2. The energy imbalance between the photon exchange and the spin excitation is

$$\Delta E_{\downarrow\to\uparrow} = (\hbar\omega_l - \hbar\omega_c) - 4\hbar\omega_r = \hbar\delta. \tag{7.1}$$

Similarly, the de-excitation of a second spin (magenta circle in Fig. 7.1(b)) is accompanied by the absorption of a photon in mode 2 and subsequent emission at the drive frequency, leading to an energy imbalance

$$\Delta E_{\uparrow\to\downarrow} = (\hbar\omega_c - \hbar\omega_l) - (-4\hbar\omega_r) = -\hbar\delta. \tag{7.2}$$

However, from Eqs (7.1) and (7.2), the simultaneous excitation of one atom and de-excitation of the other is resonant, facilitated by the four-photon process consisting of absorption of a drive photon, emission and absorption of a virtual cavity photon and subsequent return of the photon to the drive laser. Assuming that the cavity mode couples identically to all the atoms, the cavity mode cannot distinguish which atom was excited and which one was de-excited, leading to an effective Hamiltonian of the form

$$\hat{H}_{\text{eff}} \propto \hat{J}^- \hat{J}^+, \tag{7.3}$$

where $\hat{J}^\pm = \sum_{j=1}^{N} \hat{\sigma}_j^\pm$, with $\hat{\sigma}_j^+ = |\uparrow\rangle_j \langle\downarrow|$ and $\hat{\sigma}_j^- = \left(\hat{\sigma}_j^+\right)^\dagger$. The effective Hamiltonian, Eq. (7.3), can be expressed as

$$\hat{J}^- \hat{J}^+ = \hat{\mathbf{J}} \cdot \hat{\mathbf{J}} - \hat{J}^z \hat{J}^z - \hat{J}^z, \tag{7.4}$$

where $\hat{\mathbf{J}} = \hat{J}^x\hat{\mathbf{x}} + \hat{J}^y\hat{\mathbf{y}} + \hat{J}^z\hat{\mathbf{z}}$ and $\hat{J}^i$ for $i = x, y, z$ are the Cartesian components of the collective angular momentum $\hat{\mathbf{J}}$ formed by the momentum pseudospins.[1] The second term is the familiar one-axis twisting (OAT) interaction that gives rise to spin squeezed states useful for quantum metrology [76]. The first term, on the other hand, opens a many-body energy gap that has been experimentally observed, for example, using spins encoded in optical clock transitions [88]. We briefly discuss how the latter effect manifests in our system in Section 8.7.

7.3 Atom-cavity interactions

We now proceed to derive a master equation that reflects the underlying atom-cavity interaction at the heart of the resonant spin exchange intuitively described in the previous section. The Hamiltonian governing the dynamics of the atom-cavity system is

$$\begin{aligned}\hat{H} &= \sum_{j=1}^{N}\left(\frac{\hat{p}_j^2}{2M} + \frac{\hbar\omega_a}{2}(|e\rangle_j\langle e| - |g\rangle_j\langle g|)\right) + \sum_{s=1}^{2}\hbar\omega_c\hat{a}_s^\dagger\hat{a}_s \\ &+ \sum_{j=1}^{N}\sum_{s=1}^{2}\frac{\hbar g}{2}\left(\hat{a}_s e^{ik_s\hat{z}_j}|e\rangle_j\langle g| + \hat{a}_s^\dagger e^{-ik_s\hat{z}_j}|g\rangle_j\langle e|\right) \\ &+ \hbar\sqrt{\kappa}\left(\alpha e^{-i\omega_l t}\hat{a}_1^\dagger + \alpha^* e^{i\omega_l t}\hat{a}_1\right), \end{aligned} \tag{7.5}$$

where g is the atom-cavity vacuum Rabi frequency, κ is the cavity decay rate and α is the amplitude of the drive laser with $|\alpha|^2$ the photon flux in units of photons/time. The operators $\hat{a}_s^\dagger, \hat{a}_s$ for $s = 1, 2$ respectively describe the creation and annihilation of photons in modes 1 and 2 whose wavevectors satisfy $\mathbf{k}_1 = -\mathbf{k}_2 = k\hat{\mathbf{z}}$ (see Fig. (7.1)(a)). The operator $\hat{z}_j$ represents the position of atom j along the cavity axis. The decay of the cavity fields is accounted for by the standard Lindblad dissipator of the type $\mathcal{D}[\hat{O}]\rho = \hat{O}\rho\hat{O}^\dagger - \hat{O}^\dagger\hat{O}\rho/2 - \rho\hat{O}^\dagger\hat{O}/2$ for jump operator $\hat{O}$ and density matrix ρ. The resulting master equation is

$$\dot{\rho} = \frac{1}{i\hbar}\left[\hat{H}, \rho\right] + \sum_{s=1}^{2}\kappa\mathcal{D}[\hat{a}_s]\rho. \tag{7.6}$$

We neglect free-space scattering in our analysis since superradiant decay (Section (8.4)) is typically the dominant dissipation mechanism (see Appendix B.3 and discussion in Section 8.8).

[1] The symbols $\hat{\mathbf{x}}$, $\hat{\mathbf{y}}$ and $\hat{\mathbf{z}}$ refer to unit vectors along the coordinate axes and are not to be confused with position operators.

7.3.1 Adiabatic elimination of the excited state

First, we adiabatically eliminate the excited state $|e\rangle$ based on the large detuning of the drive lasers and cavity modes from the $|g\rangle \leftrightarrow |e\rangle$ transition (Section 7.3.1). We work in an interaction picture rotating at the drive frequency ω_l with free evolution Hamiltonian $H_f = \sum_j \hbar\omega_l/2(|e\rangle_j \langle e| - |g\rangle_j \langle g|) + \sum_s \hbar\omega_l \hat{a}_s^\dagger \hat{a}_s$. The resulting interaction picture Hamiltonian is

$$\begin{aligned}\hat{H}_I^{(1)} &= \sum_{j=1}^{N}\left(\frac{\hat{p}_j^2}{2M} + \frac{\hbar\Delta_l}{2}(|e\rangle_j \langle e| - |g\rangle_j \langle g|)\right) - \sum_{s=1}^{2}\hbar\Delta_{cl}\hat{a}_s^\dagger\hat{a}_s \\ &+ \sum_{j=1}^{N}\sum_{s=1}^{2}\frac{\hbar g}{2}\left(\hat{a}_s e^{ik_s\hat{z}_j}|e\rangle_j \langle g| + \hat{a}_s^\dagger e^{-ik_s\hat{z}_j}|g\rangle_j \langle e|\right) \\ &+ \hbar\sqrt{\kappa}\left(\alpha\hat{a}_1^\dagger + \alpha^*\hat{a}_1\right). \end{aligned} \tag{7.7}$$

The coherence operator $|e\rangle_j \langle g|$ satisfies the equation

$$\frac{d}{dt}|e\rangle_j \langle g| = i\Delta_l |e\rangle_j \langle g| - i\frac{g}{2}\sum_{s=1}^{2}\hat{a}_s^\dagger e^{-ik_s\hat{z}_j}\left(|e\rangle_j \langle e| - |g\rangle_j \langle g|\right). \tag{7.8}$$

In a far-detuned regime, we can set $|e\rangle_j \langle e| - |g\rangle_j \langle g| \approx -1$. We then transform to the cavity frame by substituting $\hat{a}_s^\dagger = \hat{a}_s^{\dagger,(c)} e^{i\Delta_{cl}t}$, $|e\rangle_j \langle g| = |e\rangle_j \langle g|^{(c)} e^{i\Delta_{cl}t}$ and adiabatically eliminate $|e\rangle_j \langle g|^{(c)}$ to get

$$|e\rangle_j \langle g|^{(c)} \approx -\frac{g}{2\Delta_c}\sum_{s=1}^{2}\hat{a}_s^{\dagger,(c)} e^{-ik_s\hat{z}_j}. \tag{7.9}$$

In the drive frame, the annihilation operator for a mode s satisfies the equation

$$\frac{d}{dt}\hat{a}_s = -\left(\frac{\kappa}{2} - i\Delta_{cl}\right)\hat{a}_s - i\frac{g}{2}\sum_{j=1}^{N} e^{-ik_s\hat{z}_j}|g\rangle_j \langle e| - i\sqrt{\kappa}\alpha\delta_{s,1} + \hat{F}_s, \tag{7.10}$$

where $\hat{F}_s$ is the noise operator associated with coupling to the modes outside the cavity. Using the hermitian conjugate of the expression, Eq. (7.9), leads to

$$\begin{aligned}\frac{d}{dt}\hat{a}_s &\approx -\left(\frac{\kappa}{2} - i\Delta_{cl}\right)\hat{a}_s + i\frac{g^2}{4\Delta_c}\sum_{j=1}^{N}\sum_{s'=1}^{2}\hat{a}_{s'}e^{-i(k_s - k_{s'})\hat{z}_j} \\ &- i\sqrt{\kappa}\alpha\delta_{s,1} + \hat{F}_s. \end{aligned} \tag{7.11}$$

These equations can be obtained from the effective Hamiltonian

$$\begin{aligned}\hat{H}_I^{(2)} &= \sum_{j=1}^{N}\frac{\hat{p}_j^2}{2M} - \sum_{s=1}^{2}\hbar\left(\Delta_{cl}+\frac{Ng^2}{4\Delta_c}\right)\hat{a}_s^\dagger\hat{a}_s \\ &- \sum_{j=1}^{N}\frac{\hbar g^2}{4\Delta_c}\left(\hat{a}_1^\dagger\hat{a}_2 e^{-ik_{\rm eff}\hat{z}_j}+\hat{a}_2^\dagger\hat{a}_1 e^{ik_{\rm eff}\hat{z}_j}\right) \\ &+ \hbar\sqrt{\kappa}\left(\alpha\hat{a}_1^\dagger+\alpha^*\hat{a}_1\right). \end{aligned} \tag{7.12}$$

Here $k_{\rm eff} = k_1 - k_2 = 2k$ is the effective wavevector. The cavity resonance is now shifted by $-Ng^2/4\Delta_c$ because of the presence of the atoms. Modifying the drive frequency $\omega_l \to \omega_l - Ng^2/4\Delta_c$ returns the detuning to Δ_{cl}.

7.3.2 Replacing mode 1 by a c-number

Further, on long timescales, the upwards propagating mode (mode 1) is composed of a macroscopic steady state amplitude with small fluctuations around this value. The macroscopic amplitude β ($|\beta| \gg 1$) is found from the mean-field equation

$$\dot{\beta} = -\left(\frac{\kappa}{2} - i\Delta_{cl}\right)\beta - i\sqrt{\kappa}\alpha. \tag{7.13}$$

For $t \gg \kappa^{-1}$, the steady-state value is $\beta = -i\sqrt{\kappa}\alpha/(\kappa/2 - i\Delta_{cl})$. We displace mode 1 by the amplitude β by making the transformation $\hat{a}_1 \to \beta + \hat{a}_1$. Apart from introducing some constant terms that can be neglected, the resulting Hamiltonian is

$$\begin{aligned}\hat{H}_{a-c} &= \sum_{j=1}^{N}\frac{\hat{p}_j^2}{2M} - \sum_{s=1}^{2}\hbar\Delta_{cl}\hat{a}_s^\dagger\hat{a}_s \\ &- \sum_{j=1}^{N}\frac{\hbar g^2}{4\Delta_c}\left(\beta^*\hat{a}_2 e^{-ik_{\rm eff}\hat{z}_j}+\beta\hat{a}_2^\dagger e^{ik_{\rm eff}\hat{z}_j}\right), \end{aligned} \tag{7.14}$$

with $k_{\rm eff} = k_1 - k_2 = 2k$ the effective wavevector along $\hat{\mathbf{z}}$. The dissipative part of the master equation remains the same. The second line of Eq. (7.14) reflects the dominant photon exchange between the macroscopic field in mode 1 and the vacuum of mode 2. In writing Eq. (7.14), we have neglected the small exchange process between the vacuum fields of the two modes. This approximation allows us to keep track of only mode 2 and ignore the other terms containing $\hat{a}_1$ in

the master equation since mode 1 only interacts with the atoms and mode 2 through the c-number β.

7.4 Momentum width using the $|n, q\rangle$ notation

The momentum shift operator $e^{\pm ik_{\rm eff}\hat{z}_j}$ appearing in Eq. (7.14) can only shift the momentum in units of $\hbar k_{\rm eff}$. For simplicity, we consider initial atomic states that are clustered around $|\downarrow\rangle \equiv |n_\downarrow \hbar k_{\rm eff}\rangle$, i.e. $\langle \hat{p}_j(0)\rangle = n_\downarrow \hbar k_{\rm eff}$, where $n_\downarrow$ is an integer. (A superposition of $|\downarrow\rangle$ and $|\uparrow\rangle \equiv n_\uparrow \hbar k_{\rm eff}$ with $n_\uparrow = n_\downarrow + 1$ can be subsequently obtained by a $\pi/2$ Bragg pulse.) We introduce two labels n, q to represent a momentum state as $|p\rangle \equiv |n, q\rangle$. The label n denotes the momentum center and is defined as

$$n = \left|\left| \frac{p}{\hbar k_{\rm eff}} \right|\right| \tag{7.15}$$

where $||x||$ denotes the nearest integer to x. The label q quantifies the deviation from a center and is defined as

$$q = p - n\hbar k_{\rm eff}. \tag{7.16}$$

We note that an initial offset from an integer multiple of $\hbar k_{\rm eff}$, i.e. $\langle \hat{p}_j(0)\rangle = n_\downarrow \hbar k_{\rm eff} + p_{\rm off}$ can be trivially accounted for by denoting states as $|p\rangle \equiv |n, q, p_{\rm off}\rangle$ so that $p = n\hbar k_{\rm eff} + q + p_{\rm off}$. Note that $|p_{\rm off}| < 1/2$ since larger values can be modeled as an offset about a shifted initial center $n_\downarrow \to n_\downarrow \pm 1$. Without loss of generality, we assume $p_{\rm off} = 0$.

The momentum width is characterized by a spread σ_q. We assume that the initial momentum spread σ_q is small compared to the difference between subsequent centers, i.e.

$$\frac{\sigma_q}{\hbar k_{\rm eff}} \ll 1. \tag{7.17}$$

Combined with the fact that the dynamics under Eq. (7.14) does not change the spread but only shifts the center, this assumption ensures that we can assume the orthogonality relation

$$\langle n', q'|n, q\rangle = \delta_{n,n'}\delta(q - q'), \tag{7.18}$$

for all momentum states that significantly participate in the dynamics.

7.5 Numerical solution: Semiclassical Langevin equations

The master equation governing the atom-cavity interactions is:

$$\dot{\rho}_{a-c} = \frac{1}{i\hbar}\left[\hat{H}_{a-c}, \rho_{a-c}\right] + \kappa\mathcal{D}[\hat{a}_2]\rho. \tag{7.19}$$

For an atom in the initial state $|n, q_j\rangle$, the momentum shift operator $e^{ik_{\text{eff}}\hat{z}_j}$ only shifts the center n but does not change q_j. As a result, it can be expressed as

$$e^{ik_{\text{eff}}\hat{z}_j} = \sum_{n=-\infty}^{\infty} |n+1, q_j\rangle_j \langle n, q_j| . \tag{7.20}$$

We define generalized population and coherence operators $\hat{\sigma}^j_{nm}$ as

$$\hat{\sigma}^j_{nm} = |n, q_j\rangle_j \langle m, q_j| . \tag{7.21}$$

We have dropped the label q_j in defining the operators $\hat{\sigma}^j_{nm}$, since an initial value of q_j remains constant during the subsequent dynamics governed by the master equation. The procedure to sample the initial value of q_j will be discussed shortly in Section 7.5.1.

The free energy term can be expressed as

$$\frac{\hat{p}_j^2}{2M} = \sum_{n=-\infty}^{\infty} \hbar\omega_n^j \hat{\sigma}^j_{nn}, \tag{7.22}$$

where $\hbar\omega_n^j = (n\hbar k_{\text{eff}} + q_j)^2/2M$. The frequency ω_n^j can be better expressed as

$$\omega_n^j = 4\omega_r \left(n^2 + 2n\tilde{q}_j\tilde{\sigma}_q + \tilde{q}_j^2\tilde{\sigma}_q^2\right), \tag{7.23}$$

where we have introduced the dimensionless quantities $\tilde{q} = q/\sigma_q$ and $\tilde{\sigma}_q = \sigma_q/\hbar k_{\text{eff}}$. The Hamiltonian, Eq. (7.14), can now be expressed as

$$\hat{H} = \sum_j \sum_n \hbar\omega_n^j \hat{\sigma}^j_{nn} - \hbar\Delta_{cl}\hat{a}_2^\dagger\hat{a}_2 - \sum_j \sum_n \frac{\hbar g^2}{4\Delta_c}\left(\beta^*\hat{a}_2\hat{\sigma}^j_{n,n+1} + \beta\hat{a}_2^\dagger\hat{\sigma}^j_{n+1,n}\right). \tag{7.24}$$

Expressed this way, the atom-cavity interaction is reminiscent of the detuned Tavis-Cummings model that is at the heart of cavity-based spin exchange schemes considered for optical clock transitions [53, 88]. The Hamiltonian governing the dynamics is dependent on the initially sampled value of q_j which enters through the frequencies ω_n^j.

We write down the dynamical equations for the corresponding c-numbers $s^j_{nm} \leftrightarrow \hat{\sigma}^j_{nm}$ and $\zeta \leftrightarrow \hat{a}_2$ within the truncated Wigner approximation (TWA) framework. The TWA technique involves evolving the classical equations of motion associated with the Hamiltonian subject to initial conditions sampled from the Wigner distribution of the initial state [94, 92]. While the sampling procedure accounts for the quantum and statistical uncertainties in the initial conditions, the time evolution governed by simple classical equations is a good approximation in a variety of situations since, in leading order, these equations remain unaffected by quantum fluctuations [94, 9, 106, 116, 113]. In the case of open systems, the coupling to the reservoir not only gives rise to additional damping terms in the classical equations but also introduces Langevin noise terms [9] with diffusion coefficients satisfying the Einstein relations [82]. The expectation value of any symmetrized product of operators is obtained directly by computing the corresponding c-number product, called the Weyl symbol, and averaging this quantity over several trajectories with appropriately sampled initial conditions and noise realizations [92]. The expectation values of operator products in a different ordering can be subsequently obtained through the use of appropriate commutation relations.

We introduce the effective coupling strength $g_{\text{eff}} = g^2|\beta|/2\Delta_c$ and without loss of generality assume that β is real. The c-number equations are

$$\begin{aligned}
\frac{d}{dt}s^j_{nm} &= -i(\omega^j_m - \omega^j_n)s^j_{nm} + i\frac{g_{\text{eff}}}{2}\left(\zeta^*\left(s^j_{n,m-1} - s^j_{n+1,m}\right) + \zeta\left(s^j_{n,m+1} - s^j_{n-1,m}\right)\right), \\
\frac{d}{dt}\zeta &= -\left(\frac{\kappa}{2} - i\Delta_{cl}\right)\zeta + i\frac{g_{\text{eff}}}{2}\sum_j\sum_n s^j_{n+1,n} + \sqrt{\frac{\kappa}{4}}\left(\xi_1(t) + i\xi_2(t)\right),
\end{aligned} \tag{7.25}$$

where $\xi_l(t)$ for $l = 1, 2$ are white-noise processes satisfying $\overline{\xi_l(t)} = 0$ and $\overline{\xi_l(t)\xi_{l'}(t')} = \delta_{l,l'}\delta(t - t')$. The bar indicates averaging over several trajectories with different noise realizations and initial conditions (see Section 7.5.1). The equation for ζ is a stochastic differential equation because of the noise arising from coupling to modes outside the cavity [9, 121]. We refer to this model as the multi-center model (MCM) because of its ability to track an arbitrary number of momentum centers.

7.5.1 Initial Conditions

The mode amplitude $\zeta = a + ib$ is initialized according to the Wigner distribution of a vacuum state as

$$P(a, t = 0) = P(b, t = 0) = \mathcal{N}(0, 1/2), \tag{7.26}$$

so that $\overline{|\zeta|^2} = \left(\langle \hat{a}_2^\dagger \hat{a}_2 \rangle + \langle \hat{a}_2 \hat{a}_2^\dagger \rangle\right)/2 = 1/2$. Here, $\mathcal{N}(\mu, \sigma)$ denotes a normal distribution with mean μ and standard deviation σ.

For the atoms, we first consider each atom to be in a state described by the density matrix

$$\rho^{(1)}(0) = \frac{1}{\sqrt{2\pi}\sigma_q} \int_{-\infty}^{\infty} dq \, e^{-q^2/2\sigma_q^2} \, |n_\downarrow, q\rangle \langle n_\downarrow, q| \tag{7.27}$$

where the restriction Eq. (7.17) ensures that states with $|q| \sim \hbar k_{\text{eff}}$ do not contribute significantly so that the limits of integration can be extended to $\pm\infty$.

We note that by using two labels n, q to characterize the momentum, we have effectively split the momentum phase space distribution into one for the discrete label n and one for the continuous label q. To sample q, we note that the momentum space distribution of the state described by Eq. (7.27) is Gaussian with spread σ_q. Therefore, in each trajectory, the value of q_j for any atom j is drawn as

$$P(q_j, t = 0) = \mathcal{N}(0, \sigma_q) \implies P(\tilde{q}_j, t = 0) = \mathcal{N}(0, 1). \tag{7.28}$$

In general, our approach in its present formulation is valid for any initial atomic density matrix that is diagonal in the momentum basis. The density matrix for atom j can then be interpreted as a probability distibution for the initial value of q_j from which this value can be sampled in each trajectory. As already noted, the value of q_j remains constant during the subsequent time evolution and the only effect of q_j is to modify the frequencies $\omega_n^j, \omega_m^j, \ldots$ that enter the Hamiltonian, Eq. (7.24), for each trajectory.

To appropriately sample the n-space distribution corresponding to the state described by Eq. (7.27), we note that the discrete levels $n, m, \ldots$ are reminiscent of the different m_J levels in a $2J+1$ spin manifold. Here, the choice of J depends on the number of discrete levels that participate

significantly in the dynamics. We initialize the c-numbers s^j_{nm} according to the DTWA (discrete truncated Wigner approximation) prescription [106, 92], namely,

$$\begin{aligned}
&s^j_{n_\downarrow,n_\downarrow} = 1,\\
&P(2\ \mathrm{Re}\{s^j_{n_\downarrow,m\neq n_\downarrow}\} = \pm 1) = P(2\ \mathrm{Im}\{s^j_{n_\downarrow,m\neq n_\downarrow}\} = \pm 1) = \frac{1}{2},\\
&s^j_{m\neq n_\downarrow,n_\downarrow} = \left(s^j_{n_\downarrow,m\neq n_\downarrow}\right)^*,\\
&s^j_{n\neq n_\downarrow,m\neq n_\downarrow} = 0.
\end{aligned} \tag{7.29}$$

We note that our choice of initial conditions is consistent with a formal generalization of the Truncated Wigner Approximation technique to systems with D discrete states on a given site [70].

Prior to implementing our squeezing protocol, a Bragg pulse rotates the state of each atom to an equal superposition of the $n_\downarrow, n_\uparrow$ centers. Starting with the initial conditions in Eq. (7.29), we obtain the c-number values corresponding to such an equal superposition by numerically implementing a fictitious instantaneous state rotation that rotates each spin to lie on the equatorial plane of the Bloch sphere formed by $n_\downarrow, n_\uparrow$ (Appendix B.1). The observables from the MCM simulations are averaged over 2000 trajectories in order to sample the initial conditions and noise realizations.

7.6 Effective atom-atom interactions

7.6.1 Elimination of the cavity field $\hat{a}_2$

The spin exchange dynamics anticipated in Section 7.2 is confirmed when mode 2 is adiabatically eliminated to obtain a master equation describing the effective atom-atom interactions. When mode 2 is negligibly excited, it can be considered as a reservoir in a vacuum state with density matrix $R_0 = |0\rangle\langle 0|$. We use the superoperator formalism to adiabatically eliminate mode 2 [19]. We split the master equation, Eq. (7.19), into system, reservoir as well as system-reservoir

Liouvillians. These terms are given by

$$\begin{aligned}
\mathcal{L}_S\rho_{a-c} &= -i\left[\sum_{j=1}^{N}\frac{\hat{p}_j^2}{2M\hbar},\rho_{a-c}\right],\\
\mathcal{L}_R\rho_{a-c} &= -i\left[-\Delta_{cl}\hat{a}_2^\dagger\hat{a}_2,\rho_{a-c}\right]+\kappa\mathcal{D}[\hat{a}_2]\rho_{a-c},\\
\mathcal{L}_{SR}\rho_{a-c} &= =-i\left[-\sum_{j=1}^{N}\frac{g^2}{4\Delta_c}\left(\beta^*\hat{a}_2e^{-ik_{\text{eff}}\hat{z}_j}+\beta\hat{a}_2^\dagger e^{ik_{\text{eff}}\hat{z}_j}\right),\rho_{a-c}\right].
\end{aligned}\tag{7.30}$$

We first transform to an interaction picture with $\mathcal{L}_0=\mathcal{L}_S+\mathcal{L}_R$. We then have

$$\dot{\tilde{\rho}}_{a-c}=\tilde{\mathcal{L}}_{SR}\tilde{\rho}_{a-c},\tag{7.31}$$

where $\tilde{\rho}_{a-c}=e^{-\mathcal{L}_0t}\rho_{a-c}$ and $\tilde{\mathcal{L}}_{SR}=e^{-\mathcal{L}_0t}\mathcal{L}_{SR}e^{\mathcal{L}_0t}$. We integrate Eq. (7.31) and substitute the formal solution for $\tilde{\rho}_{a-c}(t)$ in the same equation to get

$$\dot{\tilde{\rho}}_{a-c}=\tilde{\mathcal{L}}_{SR}(t)\tilde{\rho}_{a-c}(0)+\int_0^t dt'\tilde{\mathcal{L}}_{SR}(t)\tilde{\mathcal{L}}_{SR}(t')\tilde{\rho}_{a-c}(t').\tag{7.32}$$

We assume that mode 2 acts as a reservoir in the vacuum state, i.e. the reservoir density matrix is $R_0=|0\rangle\langle 0|$. At $t=0$, the initial uncorrelated state is $\tilde{\rho}_{a-c}(0)=\tilde{\rho}_a(0)R_0$, where $\tilde{\rho}_a(0)$ is the density matrix for the atomic ensemble. We then use a decorrelation approximation to write $\tilde{\rho}_{a-c}(t)\approx\tilde{\rho}_a(t)R_0$ for later times, and trace out mode 2 as

$$\dot{\tilde{\rho}}_a=\text{Tr}_R\left[\tilde{\mathcal{L}}_{SR}(t)\tilde{\rho}_a(0)R_0\right]+\int_0^t dt'\text{Tr}_R[\tilde{\mathcal{L}}_{SR}(t)\tilde{\mathcal{L}}_{SR}(t')\tilde{\rho}_a(t')R_0].\tag{7.33}$$

The first term vanishes because $\langle\hat{a}_2\rangle=\langle\hat{a}_2^\dagger\rangle=0$ in the vacuum state.

Next, we find the time evolution equations governing the superoperators associated with mode 2 that enter $\tilde{\mathcal{L}}_{SR}$, namely $\tilde{\hat{a}}_2\otimes\hat{I}$, $\tilde{\hat{a}}_2^\dagger\otimes\hat{I}$, $\hat{I}\otimes(\tilde{\hat{a}}_2)^T$ and $\hat{I}\otimes(\tilde{\hat{a}}_2^\dagger)^T$. Here $\hat{I}$ is the identity operator, i.e. $\hat{I}|n\rangle=|n\rangle$ for any Fock basis vector $|n\rangle$. The notation $\hat{A}\otimes(\hat{B})^T$ is to be understood as the operation $\hat{A}|n\rangle\langle m|\hat{B}$ for a vector $|n\rangle\langle m|$ in the Liouville space of mode 2 [110]. These equations are found to be

$$\begin{aligned}
\frac{d}{dt}\tilde{\hat{a}}_2\otimes\hat{I} &= -\left(\frac{\kappa}{2}-i\Delta_{cl}\right)\tilde{\hat{a}}_2\otimes\hat{I}\\
\frac{d}{dt}\hat{I}\otimes(\tilde{\hat{a}}_2)^T &= \left(\frac{\kappa}{2}+i\Delta_{cl}\right)\hat{I}\otimes(\tilde{\hat{a}}_2)^T-\kappa\left(\tilde{\hat{a}}_2\otimes\hat{I}\right).
\end{aligned}\tag{7.34}$$

The solution to this coupled set of differential equations is

$$\begin{aligned}\tilde{\hat{a}}_2 \otimes \hat{I}(t) &= \left(\hat{a}_2 \otimes \hat{I}\right) e^{-\left(\frac{\kappa}{2}-i\Delta_{cl}\right)t} \\ \hat{I} \otimes (\tilde{\hat{a}}_2)^T(t) &= \left[\hat{I} \otimes (\hat{a}_2)^T - \hat{a}_2 \otimes \hat{I}\right] e^{\left(\frac{\kappa}{2}+i\Delta_{cl}\right)t} + \left(\hat{a}_2 \otimes \hat{I}\right) e^{-\left(\frac{\kappa}{2}-i\Delta_{cl}\right)t}. \end{aligned} \tag{7.35}$$

Hermitian conjugation of these two equations yields the expressions for $\tilde{\hat{a}}_2^\dagger \otimes \hat{I}(t)$ and $\hat{I} \otimes (\tilde{\hat{a}}_2^\dagger)^T(t)$.

For brevity, we denote $\hat{S}_j \equiv e^{ik_{\rm eff}\hat{z}_j}$. From Eqs. (7.33) and (7.35), we arrive at

$$\begin{aligned}\dot{\tilde{\rho}}_a = -\left(\frac{g^2|\beta|}{4\Delta_c}\right)^2 \sum_{j,j'=1}^{N} \int_0^t dt' \quad & \Big[\tilde{\hat{S}}_j^\dagger(t)\tilde{\hat{S}}_{j'}(t')\tilde{\rho}_a(t')e^{-(\kappa/2-i\Delta_{cl})(t-t')} \\ & - \tilde{\hat{S}}_j(t)\tilde{\rho}_a(t')\tilde{\hat{S}}_{j'}^\dagger(t')e^{-(\kappa/2+i\Delta_{cl})(t-t')} \\ & - \tilde{\hat{S}}_{j'}(t')\tilde{\rho}_a(t')\tilde{\hat{S}}_j^\dagger(t)e^{-(\kappa/2-i\Delta_{cl})(t-t')} \\ & + \tilde{\rho}_a(t')\tilde{\hat{S}}_{j'}^\dagger(t')\tilde{\hat{S}}_j(t)e^{-(\kappa/2+i\Delta_{cl})(t-t')}\Big]. \end{aligned} \tag{7.36}$$

In arriving at Eq. (7.36), we have used the fact that the reservoir is approximately in the vacuum state to set $\langle \hat{a}_2\hat{a}_2\rangle = \langle \hat{a}_2^\dagger\hat{a}_2\rangle = 0$ and $\langle \hat{a}_2\hat{a}_2^\dagger\rangle = 1$. The time evolution of the system operator $\tilde{\hat{S}}_j(t)$ is given by

$$\tilde{\hat{S}}_j(t) = \exp\left(i\frac{\hat{p}_j^2}{2M\hbar}t\right) e^{ik_{\rm eff}\hat{z}_j} \exp\left(-i\frac{\hat{p}_j^2}{2M\hbar}t\right). \tag{7.37}$$

Once again, we introduce generalized population and coherence operators, but with an extra label q, as

$$\hat{\sigma}_{nm}^{j,q} = |n,q\rangle_j \langle m,q|, \tag{7.38}$$

and expand the momentum shift operator $e^{ik_{\rm eff}\hat{z}_j}$ as

$$e^{ik_{\rm eff}\hat{z}_j} = \sum_{n=-\infty}^{\infty} \int_{-\infty}^{\infty} dq \hat{\sigma}_{n+1,n}^{j,q}. \tag{7.39}$$

We then have

$$\tilde{\hat{S}}_j(t) = \sum_{n=-\infty}^{\infty} \int_{-\infty}^{\infty} dq e^{i\Delta\omega_n(q)t} \hat{\sigma}_{n+1,n}^{j,q}, \tag{7.40}$$

where we have introduced $\Delta\omega_n(q) = 4\omega_r\left(1+2n+2\tilde{q}\tilde{\sigma}_q\right)$. As an example, we explicitly write down the first term in Eq. (7.36):

$$\begin{aligned}-\left(\frac{g^2|\beta|}{4\Delta_c}\right)^2 \sum_{j,j'} \quad & \int_0^t dt' \sum_{n,n'} \int_{-\infty}^{\infty} dq \int_{-\infty}^{\infty} dq' \hat{\sigma}_{n,n+1}^{j,q} \hat{\sigma}_{n'+1,n'}^{j',q'} \tilde{\rho}_a(t') \times \\ & \exp\left[-\left(\frac{\kappa}{2} - i\delta_n(q)\right)t\right] \exp\left[\left(\frac{\kappa}{2} - i\delta_{n'}(q')\right)t'\right], \end{aligned} \tag{7.41}$$

where $\delta_n(q) \equiv \Delta_{cl} - \Delta\omega_n(q)$.

The restriction $\tilde{\sigma}_q \ll 1$ ensures that only operators associated with $q \ll \hbar k_{\text{eff}}$ contribute to the dynamics. We further assume that for the momentum centers that significantly participate in the dynamics, the corresponding $|\kappa/2 - i\delta_n(q)|$ is sufficiently 'large'. We will quantify this criterion self-consistently later on (see Section 7.6.1.1). Then, the integral over t' can be performed under a Markov approximation by setting $\tilde{\rho}_a(t') \approx \tilde{\rho}_a(t)$ to get

$$-\sum_{j,j'}\sum_{n,n'}\int_{-\infty}^{\infty} dq \int_{-\infty}^{\infty} dq' \frac{\left(g^2|\beta|/4\Delta_c\right)^2}{\frac{\kappa}{2} - i\delta_{n'}(q')} e^{-i(\Delta\omega_n(q) - \Delta\omega_{n'}(q'))t} \hat{\sigma}^{j,q}_{n,n+1}\hat{\sigma}^{j',q'}_{n'+1,n'}\tilde{\rho}_a(t). \tag{7.42}$$

We repeat this calculation for the remaining three terms. We define the coherent and dissipative coupling strengths as

$$\chi_n(q) = \left(\frac{g^2|\beta|}{4\Delta_c}\right)^2 \frac{\delta_n(q)}{\kappa^2/4 + (\delta_n(q))^2},\ \Gamma_n(q) = \left(\frac{g^2|\beta|}{4\Delta_c}\right)^2 \frac{\kappa/2}{\kappa^2/4 + (\delta_n(q))^2}, \tag{7.43}$$

and perform the reverse interaction picture transformation with $\mathcal{L}_0 = -\mathcal{L}_S$ to obtain an effective master equation governing the dynamics of ρ_a:

$$\begin{aligned}
\dot{\rho}_a &= \frac{1}{i\hbar}\left[\sum_{j=1}^{N}\sum_{n=-\infty}^{\infty}\int_{-\infty}^{\infty} dq\ \hbar\omega_n(q)\hat{\sigma}^{j,q}_{nn},\ \rho_a\right] \\
&- i\sum_{j,j'}\sum_{n,n'}\int_{-\infty}^{\infty} dq \int_{-\infty}^{\infty} dq' \chi_{n'}(q') \Big(\hat{\sigma}^{j,q}_{n,n+1}\hat{\sigma}^{j',q'}_{n'+1,n'}\rho_a - \rho_a\hat{\sigma}^{j',q'}_{n',n'+1}\hat{\sigma}^{j,q}_{n+1,n} \\
&\qquad + \hat{\sigma}^{j,q}_{n+1,n}\rho_a\hat{\sigma}^{j',q'}_{n',n'+1} - \hat{\sigma}^{j',q'}_{n'+1,n'}\rho_a\hat{\sigma}^{j,q}_{n,n+1}\Big) \\
&+ \sum_{j,j'}\sum_{n,n'}\int_{-\infty}^{\infty} dq \int_{-\infty}^{\infty} dq' \Gamma_{n'}(q') \Big(\hat{\sigma}^{j,q}_{n+1,n}\rho_a\hat{\sigma}^{j',q'}_{n',n'+1} + \hat{\sigma}^{j',q'}_{n'+1,n'}\rho_a\hat{\sigma}^{j,q}_{n,n+1} \\
&\qquad - \hat{\sigma}^{j,q}_{n,n+1}\hat{\sigma}^{j',q'}_{n'+1,n'}\rho_a - \rho_a\hat{\sigma}^{j',q'}_{n',n'+1}\hat{\sigma}^{j,q}_{n+1,n}\Big).
\end{aligned} \tag{7.44}$$

We make the simplifying assumption that $\chi_n(q) \approx \chi_n(0) \equiv \chi_n$, $\Gamma_n(q) \approx \Gamma_n(0) \equiv \Gamma_n$, that allows to pull χ_n, Γ_n outside the integrals. We find that this requirement constrains

$$\frac{\sigma_q}{\hbar k_{\text{eff}}} \ll \min_n\left(\frac{\delta_n}{16\omega_r}\right), \tag{7.45}$$

where $\delta_n \equiv \delta_n(0)$ and the values of n considered correspond to the centers that significantly participate in the dynamics. In deriving the simple expression in Eq. (7.45), we have assumed

that the dispersive interaction dominates, i.e. $\delta_n \gg \kappa/2$ for participating centers. For detunings $\delta_{n_\downarrow} \gg 4\omega_r$, Eq. (7.17) is clearly a more stringent requirement than Eq. (7.45).

Further, the simultaneous excitation and de-excitation of a pair of atoms is near-resonant only when the same centers are involved, which corresponds to terms with $n = n'$ in Eq. (7.44). For terms with $n = n' \pm 1$, the exchange process is energetically detuned by $8\omega_r$.[2] From these considerations, the effective master equation, Eq. (7.44), can be written as

$$\begin{aligned}
\dot{\rho}_a &= \frac{1}{i\hbar}\left[\sum_j \sum_n \int_{-\infty}^{\infty} dq\, \hbar\omega_n(q)\hat{\sigma}_{nn}^{j,q},\ \rho_a\right] \\
&- i\sum_{j,j'}\sum_n \chi_n \int_{-\infty}^{\infty} dq \int_{-\infty}^{\infty} dq' \left(\hat{\sigma}_{n,n+1}^{j,q}\hat{\sigma}_{n+1,n}^{j',q'}\rho_a - \rho_a\hat{\sigma}_{n,n+1}^{j',q'}\hat{\sigma}_{n+1,n}^{j,q}\right. \\
&\qquad \left. + \hat{\sigma}_{n+1,n}^{j,q}\rho_a\hat{\sigma}_{n,n+1}^{j',q'} - \hat{\sigma}_{n+1,n}^{j',q'}\rho_a\hat{\sigma}_{n,n+1}^{j,q}\right) \\
&+ \sum_{j,j'}\sum_n \Gamma_n \int_{-\infty}^{\infty} dq \int_{-\infty}^{\infty} dq' \left(\hat{\sigma}_{n+1,n}^{j,q}\rho_a\hat{\sigma}_{n,n+1}^{j',q'} + \hat{\sigma}_{n+1,n}^{j',q'}\rho_a\hat{\sigma}_{n,n+1}^{j,q}\right. \\
&\qquad \left. - \hat{\sigma}_{n,n+1}^{j,q}\hat{\sigma}_{n+1,n}^{j',q'}\rho_a - \rho_a\hat{\sigma}_{n,n+1}^{j',q'}\hat{\sigma}_{n+1,n}^{j,q}\right). \qquad (7.46)
\end{aligned}$$

The master equation can be considerably simplified now because the integrals over q, q' no longer involve χ and Γ. By interchanging the dummy variables $(j,q) \leftrightarrow (j',q')$, terms in the third line cancel. Also, the two terms on the second line can be cast in a Hamiltonian form. We then transform to an interaction picture with free evolution Hamiltonian

$$\hat{H}_f = \sum_j \sum_n \int_{-\infty}^{\infty} dq\, 4\hbar\omega_r \left(n^2 + \tilde{q}^2\tilde{\sigma}_q^2\right)\hat{\sigma}_{n,n}^{j,q}, \qquad (7.47)$$

and denote the interaction picture density matrix by $\tilde{\rho}_a$, to arrive at the effective master equation

$$\begin{aligned}
\dot{\tilde{\rho}}_a &= \frac{1}{i\hbar}\left[\hat{H}_{\text{eff}}, \tilde{\rho}_a\right] + \sum_{j,j'}\sum_n \Gamma_n \int_{-\infty}^{\infty} dq \int_{-\infty}^{\infty} dq' \left(2\hat{\sigma}_{n+1,n}^{j,q}\tilde{\rho}_a\hat{\sigma}_{n,n+1}^{j',q'}\right. \\
&\qquad \left. - \hat{\sigma}_{n,n+1}^{j',q'}\hat{\sigma}_{n+1,n}^{j,q}\tilde{\rho}_a - \tilde{\rho}_a\hat{\sigma}_{n,n+1}^{j',q'}\hat{\sigma}_{n+1,n}^{j,q}\right), \qquad (7.48)
\end{aligned}$$

[2] We note that ignoring terms with $n \neq n'$ amounts to assuming that rates of the order of $8\omega_r$ are 'rapidly oscillating'. Therefore, the model we derive here is strictly speaking only valid for squeezing rates $N\chi_{n_\downarrow} \ll 8\omega_r$, and cannot be expected to predict all features seen in the MCM in the strong driving regime (such as in Fig. 8.2, also see Appendix B.2) even when more than two centers are tracked.

where the Hamiltonian $\hat{H}_{\text{eff}}$ is given by

$$\begin{aligned}\hat{H}_{\text{eff}} &= \sum_j \sum_n \int_{-\infty}^{\infty} dq \, (8n\hbar\omega_r) \, (\tilde{q}\tilde{\sigma}_q) \, \hat{\sigma}^{j,q}_{n,n} \\ &+ \sum_{j,j'} \sum_n \hbar\chi_n \int_{-\infty}^{\infty} dq \int_{-\infty}^{\infty} dq' \hat{\sigma}^{j,q}_{n,n+1} \hat{\sigma}^{j',q'}_{n+1,n}. \end{aligned} \tag{7.49}$$

7.6.1.1 Validity of the Markov approximation

In Section 7.7, we will consider the evolution under the action of a truncated Hamiltonian, Eq. (7.57), derived from the more general Eq. (7.49). Additionally, when $\tilde{\sigma}_q \approx 0$, the truncated Hamiltonian results in squeezing at a rate $Q \sim N\chi_{n_\downarrow}$. The Markov approximation used in Eq. (7.41) involves retaining only the leading term in the integration-by-parts expansion of the integrand. Neglecting the next-to-leading term amounts to approximating that

$$\left| \frac{1}{\tilde{\rho}_a(t)} \frac{d\tilde{\rho}_a(t)/dt}{\kappa/2 - i\delta_{n_\downarrow}} \right| \ll 1. \tag{7.50}$$

Since the atomic dynamics proceeds at rate $\sim N\chi_{n_\downarrow}$, the Markov approximation requires that $|\kappa/2 - i\delta_{n_\downarrow}| \gg N\chi_{n_\downarrow}$.

7.6.2 Collective angular momentum operators

The resulting master equation can be compactly expressed in terms of operators analogous to collective angular momentum operators. We define operators $\hat{\mathcal{J}}^{\pm}_n, \hat{\mathcal{J}}^z_n$ acting on any two consecutive momentum centers $n, n+1$ as

$$\hat{\mathcal{J}}^+_n = \sum_{j=1}^{N} \int_{-\infty}^{\infty} dq \; \hat{\sigma}^{j,q}_{n+1,n}, \; \hat{\mathcal{J}}^-_n = \sum_{j=1}^{N} \int_{-\infty}^{\infty} dq \; \hat{\sigma}^{j,q}_{n,n+1}, \; \hat{\mathcal{J}}^z_n = \frac{1}{2} \sum_{j=1}^{N} \int_{-\infty}^{\infty} dq \; \left(\hat{\sigma}^{j,q}_{n+1,n+1} - \hat{\sigma}^{j,q}_{n,n} \right). \tag{7.51}$$

With $\hat{\mathcal{J}}^x_n = \left(\hat{\mathcal{J}}^+_n + \hat{\mathcal{J}}^-_n \right)/2$ and $\hat{\mathcal{J}}^y_n = \left(\hat{\mathcal{J}}^+_n - \hat{\mathcal{J}}^-_n \right)/2i$, the operators $\hat{\mathcal{J}}^x_n, \hat{\mathcal{J}}^y_n, \hat{\mathcal{J}}^z_n$ satisfy the usual angular momentum commutation relations

$$\left[\hat{\mathcal{J}}^j_n, \hat{\mathcal{J}}^k_n \right] = i\epsilon_{jkl} \hat{\mathcal{J}}^l_n, \tag{7.52}$$

where ϵ_{jkl} is the usual Levi-Civita symbol for the right-handed coordinate system formed by the x, y, z axes. Once again, the restriction on initial states, Eq. (7.17), ensures that the limits of

integration over q can be extended to $\pm\infty$ while still allowing the use of the orthogonality relation Eq. (7.18) in deriving the commutation rules in Eq. (7.52). Specifically, the collective spin consisting of the pseudospin-1/2 systems formed by the two centers $n_\downarrow, n_\uparrow$ are characterized by the operators $\hat{\mathcal{J}}^{\pm}_{n_\downarrow}, \hat{\mathcal{J}}^{z}_{n_\downarrow}$.

The master equation, Eq. (7.48), for the reduced density matrix $\tilde{\rho}_a$ can be expressed as

$$\dot{\tilde{\rho}}_a = \frac{1}{i\hbar}\left[\hat{H}_{\text{eff}}, \tilde{\rho}_a\right] + \sum_{n=-\infty}^{\infty} 2\Gamma_n \mathcal{L}[\hat{\mathcal{J}}^{+}_n]\tilde{\rho}_a, \tag{7.53}$$

with the effective Hamiltonian

$$\hat{H}_{\text{eff}} = \sum_{j=1}^{N}\sum_{n=-\infty}^{\infty}\int_{-\infty}^{\infty} dq\ (8n\hbar\omega_r)\,(\tilde{q}\tilde{\sigma}_q)\,\hat{\sigma}^{j,q}_{n,n} + \sum_{n=-\infty}^{\infty}\hbar\chi_n\hat{\mathcal{J}}^{-}_n\hat{\mathcal{J}}^{+}_n, \tag{7.54}$$

where the coherent and dissipative coupling strengths, χ_n and Γ_n, are defined as

$$\chi_n = \left(\frac{g^2|\beta|}{4\Delta_c}\right)^2 \frac{\delta_n}{\kappa^2/4+\delta_n^2},\ \Gamma_n = \left(\frac{g^2|\beta|}{4\Delta_c}\right)^2 \frac{\kappa/2}{\kappa^2/4+\delta_n^2}, \tag{7.55}$$

with $\delta_n \equiv \Delta_{cl} - 4\omega_r\,(1+2n)$. (Section 7.6.1).

7.7 Numerical solution: Cumulant theory for one and two-atom operators

To make computations tractable, we assume that the $n_\downarrow, n_\uparrow$ centers form a closed two-level system while studying the collective spin dynamics using the master equation, Eq. (7.53). To this effect, we truncate Eq. (7.53) as

$$\dot{\tilde{\rho}}_a = \frac{1}{i\hbar}\left[\hat{H}^{\text{T}}_{\text{eff}}, \tilde{\rho}_a\right] + 2\Gamma_{n_\downarrow}\mathcal{L}[\hat{\mathcal{J}}^{+}_{n_\downarrow}]\tilde{\rho}_a, \tag{7.56}$$

where the truncated Hamiltonian is

$$\hat{H}^{\text{T}}_{\text{eff}} = \sum_{j=1}^{N}\sum_{n=n_\downarrow,n_\uparrow}\int_{-\infty}^{\infty} dq\ (8n\hbar\omega_r)\,(\tilde{q}\tilde{\sigma}_q)\,\hat{\sigma}^{j,q}_{n,n} + \hbar\chi_{n_\downarrow}\hat{\mathcal{J}}^{-}_{n_\downarrow}\hat{\mathcal{J}}^{+}_{n_\downarrow}. \tag{7.57}$$

We recall that, with $\tilde{\sigma}_q = 0$, the effective Hamiltonian, Eq. (7.57), is analogous to the standard spin exchange/one-axis twisting model studied for closed two-level systems coupled to a cavity [76, 53, 88, 72] (also compare with Eq. (7.3)), and provides a reference model against which complications arising from the nature of momentum states can be contrasted.

Exact solutions even for the truncated master equation, Eq. (7.56), are computationally intractable because of the exponential scaling of the Liouville space with atom number. We use an approximate method where we only keep track of expectation values of single atom and two atom operators, of the type $\langle\hat{\sigma}^{1,q}_{n_a,n_b}\rangle$ and $\langle\hat{\sigma}^{1,q}_{n_a,n_b}\hat{\sigma}^{2,q'}_{n_c,n_d}\rangle$, where the n values can take either $n_\downarrow$ or $n_\uparrow$. Since we are ignoring the other momentum centers, we refer to this model as the two-center model (TCM). Furthermore, for the numerical simulation, we consider $2L+1$ discrete $\tilde{q}$ values to sample the Gaussian wavepacket within $r\sigma_q$ from center, where r is a small natural number, typically $r=3$. As a result, we have

$$\tilde{q}_j = \left(\frac{j}{L}-1\right) r,\ j=0,1,\ldots,2L. \tag{7.58}$$

For the one-atom operators, the evolution of the expectation value is given by the following equation.

$$\begin{aligned}
\frac{d}{dt}\langle\hat{\sigma}^{1,\tilde{q}}_{n_a,n_b}\rangle = &- \left(\Gamma_{n_\downarrow}\left(\delta_{n_a,n_\downarrow}+\delta_{n_b,n_\downarrow}\right)+i\chi_{n_\downarrow}\left(\delta_{n_b,n_\downarrow}-\delta_{n_a,n_\downarrow}\right)+8i\omega_r(n_b-n_a)\tilde{q}\right)\langle\hat{\sigma}^{1,\tilde{q}}_{n_a,n_b}\rangle \\
&+ \delta_{n_a,n_\uparrow}\delta_{n_b,n_\uparrow}2\Gamma_{n_\downarrow}\langle\hat{\sigma}^{1,\tilde{q}}_{n_\downarrow,n_\downarrow}\rangle \\
&+ \delta_{n_b,n_\uparrow}(N-1)\lambda^*_{n_\downarrow}\sum_j\langle\hat{\sigma}^{1,\tilde{q}}_{n_a,n_\downarrow}\hat{\sigma}^{2,\tilde{q}_j}_{n_\downarrow,n_\uparrow}\rangle \\
&- \delta_{n_b,n_\downarrow}(N-1)\lambda_{n_\downarrow}\sum_j\langle\hat{\sigma}^{1,\tilde{q}}_{n_a,n_\uparrow}\hat{\sigma}^{2,\tilde{q}_j}_{n_\uparrow,n_\downarrow}\rangle \\
&+ \delta_{n_a,n_\uparrow}(N-1)\lambda_{n_\downarrow}\sum_j\langle\hat{\sigma}^{1,\tilde{q}}_{n_\downarrow,n_b}\hat{\sigma}^{2,\tilde{q}_j}_{n_\uparrow,n_\downarrow}\rangle \\
&- \delta_{n_a,n_\downarrow}(N-1)\lambda^*_{n_\downarrow}\sum_j\langle\hat{\sigma}^{1,\tilde{q}}_{n_\uparrow,n_b}\hat{\sigma}^{2,\tilde{q}_j}_{n_\downarrow,n_\uparrow}\rangle,
\end{aligned} \tag{7.59}$$

where $\lambda_n=\Gamma_n+i\chi_n$ and the index j runs from 0 to $2L$.

The expectation values of two-atom operators are governed by the following equation.

$$\begin{aligned}
\frac{d}{dt}\langle\hat{\sigma}^{1,\tilde{q}}_{n_a,n_b}\hat{\sigma}^{2,\tilde{q}'}_{n_c,n_d}\rangle = &- \left(\Gamma_{n_\downarrow}\left(\delta_{n_a,n_\downarrow}+\delta_{n_b,n_\downarrow}+\delta_{n_c,n_\downarrow}+\delta_{n_d,n_\downarrow}\right)\right. \\
&\quad +i\chi_{n_\downarrow}\left(\delta_{n_b,n_\downarrow}-\delta_{n_a,n_\downarrow}+\delta_{n_d,n_\downarrow}-\delta_{n_c,n_\downarrow}\right) \\
&\quad \left.+8i\omega_r\left(\left(n_b-n_a\right)\tilde{q}+\left(n_d-n_c\right)\tilde{q}'\right)\right)\langle\hat{\sigma}^{1,\tilde{q}}_{n_a,n_b}\hat{\sigma}^{2,\tilde{q}'}_{n_c,n_d}\rangle \\
&- \delta_{n_b,n_\downarrow}\delta_{n_d,n_\uparrow}\lambda_{n_\downarrow}\langle\hat{\sigma}^{1,\tilde{q}}_{n_a,n_\uparrow}\hat{\sigma}^{2,\tilde{q}'}_{n_c,n_\downarrow}\rangle-\delta_{n_a,n_\uparrow}\delta_{n_c,n_\downarrow}\lambda^*_{n_\downarrow}\langle\hat{\sigma}^{1,\tilde{q}}_{n_\downarrow,n_b}\hat{\sigma}^{2,\tilde{q}'}_{n_\uparrow,n_d}\rangle
\end{aligned}$$

$$
\begin{aligned}
- \quad & \delta_{n_b,n_\uparrow}\delta_{n_d,n_\downarrow}\lambda_{n_\downarrow}\langle\hat{\sigma}^{1,\tilde{q}}_{n_a,n_\downarrow}\hat{\sigma}^{2,\tilde{q}'}_{n_c,n_\uparrow}\rangle - \delta_{n_a,n_\downarrow}\delta_{n_c,n_\uparrow}\lambda^*_{n_\downarrow}\langle\hat{\sigma}^{1,\tilde{q}}_{n_\uparrow,n_b}\hat{\sigma}^{2,\tilde{q}'}_{n_\downarrow,n_d}\rangle \\
+ \quad & \delta_{n_a,n_\uparrow}\delta_{n_b,n_\uparrow}2\Gamma_{n_\downarrow}\langle\hat{\sigma}^{1,\tilde{q}}_{n_\downarrow,n_\downarrow}\hat{\sigma}^{2,\tilde{q}'}_{n_c,n_d}\rangle + \delta_{n_c,n_\uparrow}\delta_{n_d,n_\uparrow}2\Gamma_{n_\downarrow}\langle\hat{\sigma}^{1,\tilde{q}}_{n_a,n_b}\hat{\sigma}^{2,\tilde{q}'}_{n_\downarrow,n_\downarrow}\rangle \\
+ \quad & \delta_{n_b,n_\uparrow}\delta_{n_c,n_\uparrow}2\Gamma_{n_\downarrow}\langle\hat{\sigma}^{1,\tilde{q}}_{n_a,n_\downarrow}\hat{\sigma}^{2,\tilde{q}'}_{n_\downarrow,n_d}\rangle + \delta_{n_a,n_\uparrow}\delta_{n_d,n_\uparrow}2\Gamma_{n_\downarrow}\langle\hat{\sigma}^{1,\tilde{q}}_{n_\downarrow,n_b}\hat{\sigma}^{2,\tilde{q}'}_{n_c,n_\downarrow}\rangle \\
+ \quad & \delta_{n_a,n_\uparrow}(N-2)\lambda_{n_\downarrow}\sum_j\langle\hat{\sigma}^{1,\tilde{q}}_{n_\downarrow,n_b}\hat{\sigma}^{2,\tilde{q}'}_{n_c,n_d}\hat{\sigma}^{3,\tilde{q}_j}_{n_\uparrow,n_\downarrow}\rangle \\
- \quad & \delta_{n_a,n_\downarrow}(N-2)\lambda^*_{n_\downarrow}\sum_j\langle\hat{\sigma}^{1,\tilde{q}}_{n_\uparrow,n_b}\hat{\sigma}^{2,\tilde{q}'}_{n_c,n_d}\hat{\sigma}^{3,\tilde{q}_j}_{n_\downarrow,n_\uparrow}\rangle \\
+ \quad & \delta_{n_c,n_\uparrow}(N-2)\lambda_{n_\downarrow}\sum_j\langle\hat{\sigma}^{1,\tilde{q}}_{n_a,n_b}\hat{\sigma}^{2,\tilde{q}'}_{n_\downarrow,n_d}\hat{\sigma}^{3,\tilde{q}_j}_{n_\uparrow,n_\downarrow}\rangle \\
- \quad & \delta_{n_c,n_\downarrow}(N-2)\lambda^*_{n_\downarrow}\sum_j\langle\hat{\sigma}^{1,\tilde{q}}_{n_a,n_b}\hat{\sigma}^{2,\tilde{q}'}_{n_\uparrow,n_d}\hat{\sigma}^{3,\tilde{q}_j}_{n_\downarrow,n_\uparrow}\rangle \\
+ \quad & \delta_{n_b,n_\uparrow}(N-2)\lambda^*_{n_\downarrow}\sum_j\langle\hat{\sigma}^{1,\tilde{q}}_{n_a,n_\downarrow}\hat{\sigma}^{2,\tilde{q}'}_{n_c,n_d}\hat{\sigma}^{3,\tilde{q}_j}_{n_\downarrow,n_\uparrow}\rangle \\
- \quad & \delta_{n_b,n_\downarrow}(N-2)\lambda_{n_\downarrow}\sum_j\langle\hat{\sigma}^{1,\tilde{q}}_{n_a,n_\uparrow}\hat{\sigma}^{2,\tilde{q}'}_{n_c,n_d}\hat{\sigma}^{3,\tilde{q}_j}_{n_\uparrow,n_\downarrow}\rangle \\
+ \quad & \delta_{n_d,n_\uparrow}(N-2)\lambda^*_{n_\downarrow}\sum_j\langle\hat{\sigma}^{1,\tilde{q}}_{n_a,n_b}\hat{\sigma}^{2,\tilde{q}'}_{n_c,n_\downarrow}\hat{\sigma}^{3,\tilde{q}_j}_{n_\downarrow,n_\uparrow}\rangle \\
- \quad & \delta_{n_d,n_\downarrow}(N-2)\lambda_{n_\downarrow}\sum_j\langle\hat{\sigma}^{1,\tilde{q}}_{n_a,n_b}\hat{\sigma}^{2,\tilde{q}'}_{n_c,n_\uparrow}\hat{\sigma}^{3,\tilde{q}_j}_{n_\uparrow,n_\downarrow}\rangle
\end{aligned}
\tag{7.60}
$$

To close the set of equations, we factorize the three-atom expectation values as

$$
\begin{aligned}
\langle\hat{\sigma}^{1,\tilde{q}}_{n_a,n_b}\hat{\sigma}^{2,\tilde{q}'}_{n_c,n_d}\hat{\sigma}^{3,\tilde{q}''}_{n_e,n_f}\rangle \approx \quad & \langle\hat{\sigma}^{1,\tilde{q}}_{n_a,n_b}\hat{\sigma}^{2,\tilde{q}'}_{n_c,n_d}\rangle\langle\hat{\sigma}^{1,\tilde{q}''}_{n_e,n_f}\rangle + \langle\hat{\sigma}^{1,\tilde{q}'}_{n_c,n_d}\hat{\sigma}^{2,\tilde{q}''}_{n_e,n_f}\rangle\langle\hat{\sigma}^{1,\tilde{q}}_{n_a,n_b}\rangle \\
+ \quad & \langle\hat{\sigma}^{1,\tilde{q}''}_{n_e,n_f}\hat{\sigma}^{2,\tilde{q}}_{n_a,n_b}\rangle\langle\hat{\sigma}^{1,\tilde{q}'}_{n_c,n_d}\rangle - 2\langle\hat{\sigma}^{1,\tilde{q}}_{n_a,n_b}\rangle\langle\hat{\sigma}^{2,\tilde{q}'}_{n_c,n_d}\rangle\langle\hat{\sigma}^{1,\tilde{q}''}_{n_e,n_f}\rangle.
\end{aligned}
\tag{7.61}
$$

To speed up computation, we identify "partial sums" which are recurring summations that appear in the evaluation of the right-hand-side of Eq. (7.59) and Eq. (7.60) for each $\tilde{q}, \tilde{q}'$, and evaluate these partial sums only once per time step (See Appendix A in Ref. [111]).

As in the MCM, the initial conditions are determined by the state described in Eq. (7.27). The one-atom expectation values are initialized as

$$
\langle\hat{\sigma}^{1,\tilde{q}}_{n_\downarrow,n_\downarrow}(0)\rangle = \frac{1}{\mathcal{N}}\frac{e^{-\tilde{q}^2/2}}{\sqrt{2\pi}}\Delta\tilde{q}, \tag{7.62}
$$

where $\Delta\tilde{q} = r/L$ is the spacing between adjacent $\tilde{q}$ values and the normalization constant

$$
\mathcal{N} = \sum_{j=0}^{2L}\frac{e^{-\tilde{q}_j^2/2}}{\sqrt{2\pi}}\Delta\tilde{q} \tag{7.63}
$$

ensures that the norm of the initial density matrix is unity even with a finite number of samples. The two-atom expectation values are initialized as

$$\langle \hat{\sigma}^{1,\tilde{q}}_{n_\downarrow,n_\downarrow} \hat{\sigma}^{2,\tilde{q}'}_{n_\downarrow,n_\downarrow}(0)\rangle = \langle \hat{\sigma}^{1,\tilde{q}}_{n_\downarrow,n_\downarrow}(0)\rangle \langle \hat{\sigma}^{1,\tilde{q}'}_{n_\downarrow,n_\downarrow}(0)\rangle. \tag{7.64}$$

Next, an instantaneous rotation transforms these quantities to correspond to a state that is an equal superposition of $n_\downarrow, n_\uparrow$ (Appendix B.1). The identical initial conditions for each atom and the permutation symmetry of the master equation enable us to avoid separate indices for every atom in the system, with the number of atoms N explicitly appearing in the equations for the quantities $\langle \hat{\sigma}^{1,q}_{n_a,n_b}\rangle$ and $\langle \hat{\sigma}^{1,q}_{n_a,n_b} \hat{\sigma}^{2,q'}_{n_c,n_d}\rangle$.

Chapter 8

Squeezing on momentum pseudospins: Results

We are now ready to investigate the efficiency of our proposed momentum-pseudospin squeezing scheme. As a concrete example, we consider parameters relevant for Bragg transitions on the $^1S_0 - {}^3P_1$ transition in Strontium [31]. We show that appreciable spin squeezing can be demonstrated using modest laser powers. First, we introduce the figure of merit for spin squeezing and outline the considerations leading to our choice of parameters. Then, we study the interplay of squeezing and superradiance, the dynamics under very fast squeezing, and the effect of a non-zero momentum width. We also discuss the manifestation of an experimentally observable many-body energy gap. We conclude this chapter with comments on the results and possible extensions of this work.

8.1 Spin squeezing: Figure of merit

The $\hat{\mathcal{J}}^z_{n_\downarrow}\hat{\mathcal{J}}^z_{n_\downarrow}$ term implicit in Eq. (7.57) (see Eq. (7.4)) can be exploited to prepare spin squeezed states. We recall that the Wineland squeezing parameter $\xi^2_{\rm R}$ [76] is defined as

$$\xi^2_{\rm R} = \frac{1}{\mathcal{C}^2}\frac{V_{\rm min}}{V_{\rm SQL}}. \tag{8.1}$$

Here, the contrast $\mathcal{C}$ is given by

$$\mathcal{C} = \frac{|\langle \hat{\mathbf{J}}_{\mathbf{n}_\downarrow}\rangle|}{N/2}, \tag{8.2}$$

where $\hat{\mathbf{J}}_{\mathbf{n}_\downarrow} = \hat{\mathcal{J}}^x_{n_\downarrow}\hat{\mathbf{x}} + \hat{\mathcal{J}}^y_{n_\downarrow}\hat{\mathbf{y}} + \hat{\mathcal{J}}^z_{n_\downarrow}\hat{\mathbf{z}}$. For a given state, $V_{\rm min}$ is the variance in a spin component in the plane perpendicular to the mean spin direction (characterized by the unit vector $\hat{\mathbf{n}}_{\rm MSD}$), minimized

over all axes in this plane. Mathematically,

$$V_{\min} = \min_{\hat{\mathbf{n}} \perp \hat{\mathbf{n}}_{\mathrm{MSD}}} \left\langle \left(\hat{\mathbf{J}}_{\mathbf{n}_\downarrow} \cdot \hat{\mathbf{n}} \right)^2 \right\rangle. \tag{8.3}$$

$V_{\mathrm{SQL}} = N/4$ sets the corresponding SQL for unentangled atoms and is the variance of any spin component in this plane for a coherent spin state [76].

8.2 Considerations for choosing parameters

First, we note that the single atom-cavity vacuum Rabi frequency can be expressed as $g = \sqrt{C\kappa\gamma}$, where C is the cooperativity of the cavity and γ is the inverse lifetime of the excited state. Our model imposes two constraints that limit $|\beta|$ to the range

$$1 \ll |\beta| \ll \frac{\Delta_c}{\sqrt{C\kappa\gamma}}, \tag{8.4}$$

where we have used $g = \sqrt{C\kappa\gamma}$. The lower bound $|\beta| \gg 1$ allows us to treat mode 1 as a classical field represented by the c-number β. The upper bound ensures that the excited state $|e\rangle$ is negligibly populated, i.e.

$$\frac{g^2|\beta|^2}{4\Delta_c^2} \ll 1, \tag{8.5}$$

thereby ensuring that the adiabatic elimination of $|e\rangle$ is valid. We work with $|\beta|$ values such that $|\beta| \geq 100$ and the excited state population is ≤ 0.01.

The constraint imposed by Eq. (8.4) translates to requirements on the laser power and limits on the squeezing rate. We express these requirements in terms of a ratio R characterizing the relative strength of the dissipative and dispersive interactions, defined as

$$R = \frac{\Gamma_{n_\downarrow}}{\chi_{n_\downarrow}} = \frac{\kappa}{2\delta_{n_\downarrow}}. \tag{8.6}$$

Experimentally, the steady-state photon number $|\beta|^2$ in mode 1 is set by the power in the drive laser as

$$|\beta|^2 = \frac{\kappa}{\kappa^2/4 + \Delta_{cl}^2} \left(\frac{P}{\hbar\omega_l} \right) \approx \frac{4R^2 P}{\hbar\omega_l \kappa}, \tag{8.7}$$

where the approximation assumes that $\delta_{n_\downarrow} \gg \omega_r$ so that $\Delta_{cl} \approx \delta_{n_\downarrow}$, and that the interactions are in the dispersive regime i.e. $R^2 \ll 1$. From Eq. (8.4) the required laser power range is

$$\frac{2500\kappa}{R^2} \leq \frac{P}{\hbar\omega_l} \leq \frac{\Delta_c^2}{100C\gamma R^2}. \tag{8.8}$$

In standard one-axis twisting with closed two level systems, squeezing proceeds at a characteristic rate $Q = N\chi_{n_\downarrow}$ [53, 72, 76]. From Eq. (7.55), the rate of squeezing Q is proportional to $|\beta|^2$, and consequently, the input power P, as

$$Q \approx |\beta|^2 \frac{\gamma^2\kappa}{8\Delta_c^2} NC^2R \approx \left(\frac{P}{\hbar\omega_l}\right) \frac{NC^2\gamma^2R^3}{2\Delta_c^2}, \tag{8.9}$$

where we have assumed $R^2 \ll 1$. Therefore, Q is constrained to the range

$$\left[1250\ R\left(\frac{\kappa C\gamma}{\Delta_c^2}\right)\right] NC\gamma \leq Q \leq \frac{R}{200} NC\gamma. \tag{8.10}$$

8.3 Parameters for the $^1\mathrm{S}_0 - {}^3\mathrm{P}_1$ transition in $^{88}\mathrm{Sr}$

Although our scheme is applicable to a wide variety of atomic species, here we consider its efficiency when it is implemented on the 689 nm $^1\mathrm{S}_0 - {}^3\mathrm{P}_1$ transition of ^{88}Sr. Our choice is motivated by the advantages of using ground-state ^{88}Sr in Bragg interferometers [31], such as its extremely small scattering cross-section, insensitivity to stray magnetic fields and ease of experimental manipulation, including accessing the parameter regimes required for our scheme. The inverse lifetime of the excited state is $\gamma/2\pi = 7.6$ kHz while the single photon recoil frequency is $\omega_r/2\pi = 4.74$ kHz. The spin-1/2 system is encoded in $|\downarrow\rangle \equiv |^1\mathrm{S}_0, 0\hbar k\rangle$ and $|\uparrow\rangle \equiv |^1\mathrm{S}_0, 2\hbar k\rangle$ implying that $n_\downarrow = 0, n_\uparrow = 1$. We consider $N = 10^3$ atoms in a cavity with decay rate $\kappa/2\pi = 100$ kHz, and with either of two cooperativities, $C = 1$ ($C = 10$). The single atom-cavity vacuum Rabi frequency $g = \sqrt{C\kappa\gamma}$ then takes the value $g/2\pi \approx 27.6$ kHz (87.2 kHz). We assume that the cavity resonance is detuned from the atomic transition such that $\Delta_c/2\pi = 200$ MHz.

Squeezing by one-axis twisting occurs when the dispersive interactions dominate, corresponding to the regime $R \ll 1$. We consider R in the range $0.025 - 0.2$ in our study, corresponding to

$\delta_{n_\downarrow}/2\pi \leq 2$ MHz. We operate in the regime $\Delta_c \gg NCR\gamma$, which ensures that the squeezing induced fields in both the modes, 1 and 2, are small compared to the macroscopic field $|\beta|$ in mode 1. Further model-enforced constraints (Section 8.2) restrict the photon number in mode 1, $|\beta|^2$, to the range $1 \times 10^4 - 2 \times 10^6$ ($1 \times 10^4 - 2 \times 10^5$). Experimentally, these constraints translate to varying the power P in the drive laser in a range 10 nW $-$ 150 μW (10 nW $-$ 15 μW), and achievable squeezing rates $Q/2\pi$ in the range 5 Hz $-$ 7.6 kHz (0.5 kHz $-$ 76 kHz) (Section 8.2). We only consider squeezing rates such that $Q/\delta_{n_\downarrow} \ll 1$ ($< 1/50$ in all simulations), allowing for the adiabatic elimination of mode 2 in deriving the two-center model (see Section 7.6.1.1). Even in this regime, while very slow rates are undesirable from a technical perspective, very fast squeezing with $Q \gtrsim \omega_r$ leads to coupling with momentum states outside the pseudospin manifold and degrades the squeezing, as we will demonstrate.

Finally, to account for the momentum width of the atomic cloud, we consider values $\tilde{\sigma}_q \leq 0.1$ to satisfy the requirement, Eq. (7.17), of our model. The dephasing rate $\mu_d = 4\sqrt{2}\omega_r\tilde{\sigma}_q$ associates a characteristic timescale to the momentum width. Specifically, for a collection of atoms initialized in the same, equal superposition between the two centers $n_\downarrow, n_\uparrow$ and undergoing free evolution, the contrast $\mathcal{C}$ decays as $\mathcal{C}(t) = e^{-\mu_d^2 t^2}$. With $\tilde{\sigma}_q \leq 0.1$, the corresponding maximum rate is $\mu_d/2\pi = 2.7$ kHz.

8.4 Limits set by superradiance

We first consider the case of $\tilde{\sigma}_q \approx 0$, i.e. negligible momentum width. Figure 8.1(a) plots the evolution of the spin squeezing parameter in the $C = 1$ case for values of R in the range $0.025 - 0.2$, and with $|\beta|^2 \approx 5.4 \times 10^5$. Modest laser powers, up to 40 μW, are sufficient to maintain this intracavity photon number for the range of R considered here (Section 8.2). In this parameter regime, the TCM (dashed) and MCM (solid) results agree excellently until ξ_{R}^2 reaches its minimum value. The minimum value of ξ_{R}^2 arises as a trade-off between the twisting dynamics that decreases V_{min} (Eq. (8.1) and fluctuations in superradiant decay from $n_\downarrow$ to $n_\uparrow$ that increase this quantity [53, 72]. For smaller R, the larger value of $\delta_{n_\downarrow}$ strongly suppresses dissipation relative to dispersive

interactions (Eq. (7.55)), leading to improved squeezing, i.e. smaller values of ξ^2_{R}. However, for fixed $|\beta|^2$, the absolute squeezing rate $N\chi_{n_\downarrow}$ also decreases with larger $\delta_{n_\downarrow}$ (Eq. (7.55)), leading to slower squeezing dynamics. Therefore, as summarized in the inset, smaller R values enable greater metrological gain, but the time taken for squeezing also increases when $|\beta|^2$ is fixed.

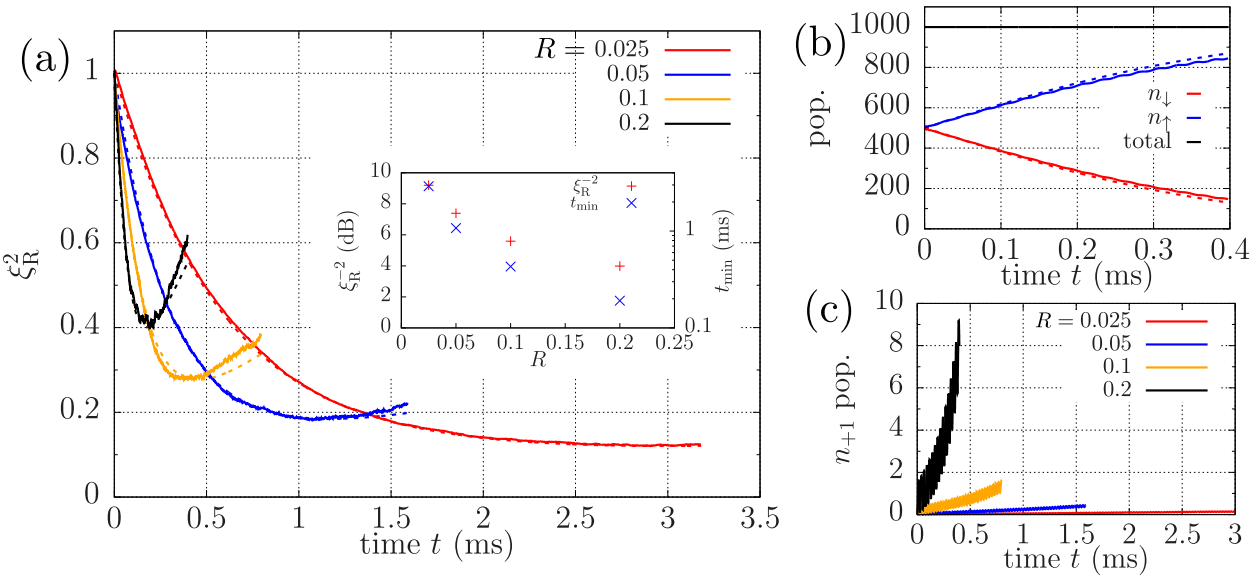

Figure 8.1: Interplay of squeezing and superradiance for different $R = \kappa/2\delta_{n_\downarrow}$ values. (a) Evolution of ξ^2_{R} for $R = 0.025, 0.05, 0.1, 0.2$. Inset: Maximum metrological gain (in dB) and time taken to achieve this gain. (b) Population in $n_\downarrow$, $n_\uparrow$ for $R = 0.2$, with total population in all centers adding up to $N = 10^3$. (c) Population in n_{+1} for different R values. In this panel, $N = 10^3$, $C = 1$, $|\beta|^2 \approx 5.4\times10^5$. Solid (dashed) lines represent MCM (TCM) results. Four centers, $n_\downarrow, n_\uparrow, n_{+1}, n_{+2}$, were tracked in the MCM simulations, with negligible population in n_{+2}.

The population dynamics at the different momentum centers reveal the effect of superradiance. Figure 8.1(b) shows the evolution of populations in $n_\downarrow, n_\uparrow$ for the case of $R = 0.2$. The rapid decrease (increase) in $n_\downarrow$ ($n_\uparrow$) population reflects superradiant decay on the $n_\downarrow \to n_\uparrow$ transition. Further, the MCM enables an investigation of the leakage to centers outside the spin manifold, highlighting the power of this technique. We denote the first k centers higher than $n_\uparrow$ as n_{+k}, and the first k centers lower than $n_\downarrow$ as n_{-k}. The MCM reveals that a small number of atoms (< 10) are lost to n_{+1} during the squeezing dynamics, as seen in Fig. 8.1(c) for the various R values. However, the excellent agreement between the TCM and MCM results in Fig. 8.1(a) indicates that in this parameter regime, the centers $n_\downarrow, n_\uparrow$ can be effectively treated as a closed two-level spin-1/2

manifold.

8.5 Squeezing faster and faster

A simple two-level model, such as the TCM, would predict that the squeezing rate can be arbitrarily increased by simply pumping in more laser power so that $|\beta|^2$ is increased. Figure 8.2(a) explores the evolution of ξ_{R}^2 in the case $C = 10$, $R = 0.05$ ($\delta_{n_\downarrow}/2\pi = 1$ MHz) for different values of $|\beta|^2/10^4$ in the range $2 - 16$. As expected, the TCM (dashed) predicts that ξ_{R}^2 attains the same minimum value faster when $|\beta|^2$ is increased. However, the MCM results (solid) present a different narrative: As $|\beta|^2$ increases, ξ_{R}^2 indeed attains its minimum faster, but this value also increases, signaling a degradation of squeezing. In fact, the metrological gain ξ_{R}^{-2} drops by ~ 3 dB (factor of 2) as $|\beta|^2$ increases from 2×10^4 to 16×10^4.

Large oscillations in the MCM curves as $|\beta|^2$ is increased indicates the breakdown of the two-center model. A study of the population dynamics at the different centers confirms this breakdown. As seen in Fig. 8.2(b), although the populations in $n_\downarrow$ ($n_\uparrow$) follow the general decreasing (increasing) trend expected from $n_\downarrow \to n_\uparrow$ superradiant decay, the TCM and MCM population transients significantly differ in the case of strong driving ($|\beta|^2/10^4 = 16$). Further, the MCM transients display pronounced oscillations with a frequency $\sim 8\omega_r$, corresponding to the relative detuning between the $n_\downarrow \leftrightarrow n_\uparrow$ and $n_\uparrow \leftrightarrow n_{+1}$, $n_{-1} \leftrightarrow n_\downarrow$ transitions.

Giant population oscillations in $n_{\pm 1}$, shown in Fig. 8.2(c-d), confirm the significant participation of these centers in the dynamics as $|\beta|^2$ increases. A simple Rabi oscillation model qualitatively explains the occupation of these states: The coherent superposition of the $n_\downarrow, n_\uparrow$ centers serves as a large collective spin that sources mode 2. Both cavity modes, 1 and 2, are now macroscopically occupied and drive two-photon Rabi oscillations between $n_\downarrow \leftrightarrow n_{-1}$ and $n_\uparrow \leftrightarrow n_{+1}$ with approximate two-photon detuning $8\omega_r$. We find that the maximum population $P_{n_{\pm 1}}^{\max}$ in $n_{\pm 1}$ predicted by this model is given by (see Appendix B.2)

$$P_{n_{\pm 1}}^{\max} \approx \frac{N}{2}\left(\frac{N\chi_{n_\downarrow}}{8\omega_r}\right)^2. \tag{8.11}$$

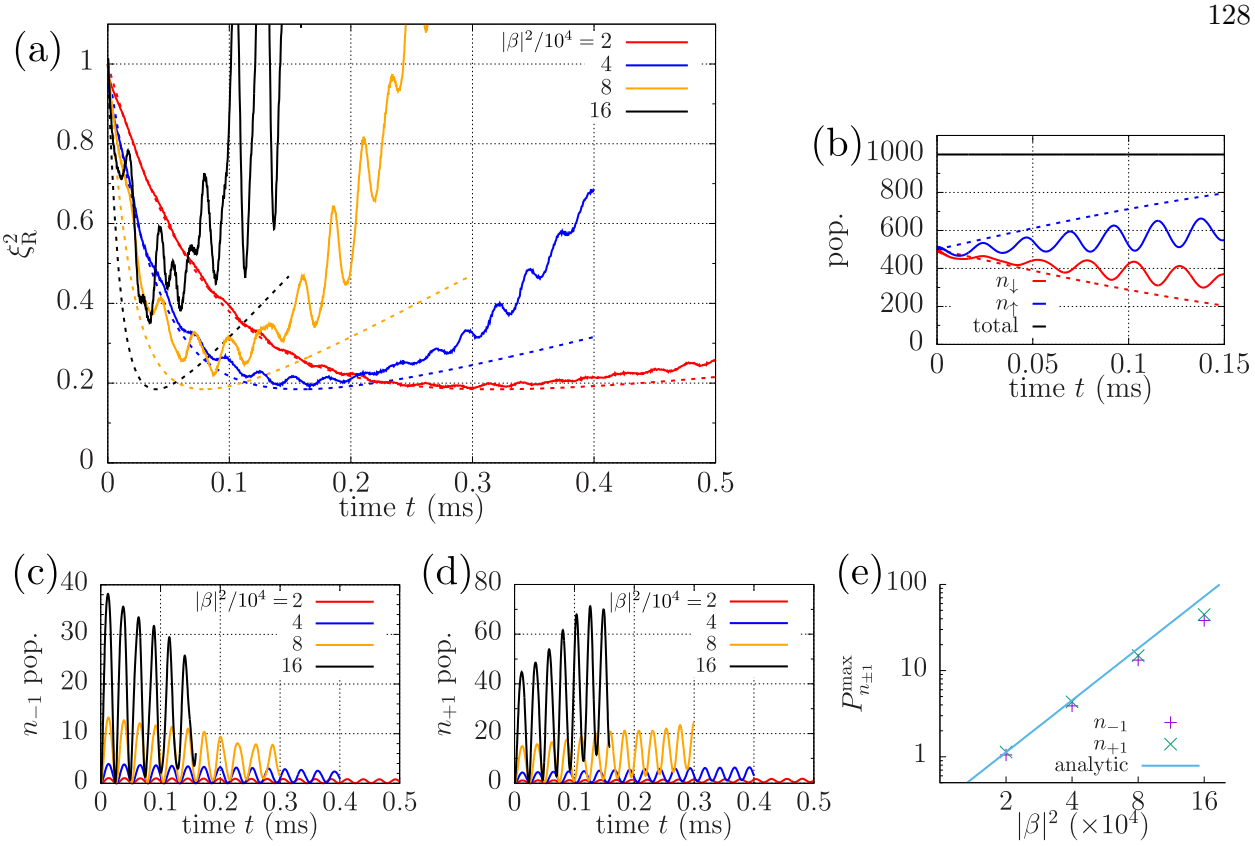

Figure 8.2: Squeezing faster and faster. (a) Evolution of ξ_R^2 for $|\beta|^2/10^4 = 2, 4, 8, 16$. (b) Population in $n_\downarrow$, $n_\uparrow$ for $|\beta|^2/10^4 = 16$, with total population in all centers adding up to $N = 10^3$. Solid (dashed) lines represent MCM (TCM) results. (c-d) Population in, respectively, n_{-1} and n_{+1} centers, for various drive strengths. (e) Comparison of simulated $n_{\pm1}$ populations to analytic result of Rabi oscillation model (see Text). In this panel, $N = 10^3$, $C = 10$ and $R = 0.05$. Six centers, $n_{-2}, n_{-1}, n_\downarrow, n_\uparrow, n_{+1}, n_{+2}$, were tracked in the MCM simulations with very low populations in $n_{\pm2}$.

Figure 8.2(e) compares the first oscillation peak in the $n_{\pm1}$ populations with the analytic formula Eq. (8.11). For small occupations (small $|\beta|^2$), the formula agrees very well with the simulations, whereas the discrepancy becomes about a factor of 2 at the largest occupation ($|\beta|^2 = 16 \times 10^4$). In this strong driving regime, the coherence that develops between $n_\uparrow, n_{+1}$ and $n_\downarrow, n_{-1}$ is no longer negligible and modifies the field in mode 2 considerably, leading to the breakdown of the simple Rabi oscillation picture presented here (Appendix B.2).

Finally, we note that Fig. 8.2(c) (Fig. 8.2(d)) displays trends such as the decrease (increase) in the amplitude of population oscillations in n_{-1} (n_{+1}) over time and the gradual deviation of the oscillation troughs from zero. These features likely arise from the complex interplay of the

Rabi flopping and cavity mediated superradiant decay on the $n_\downarrow \to n_\uparrow$, $n_{-1} \to n_\downarrow$ and $n_\uparrow \to n_{+1}$ transitions.

8.6 Effect of momentum width

We now consider the case when the atomic cloud has non-zero momentum width. For this study, we use the parameters from Fig. 8.2, i.e. $C = 10$ and $|\beta|^2/10^4 = 2, 4, 8, 16$. Fig. 8.3(a) shows the evolution of ξ^2_{R} for $\tilde{\sigma}_q = 0, 0.025, 0.05$ and 0.1 in the case when $|\beta|^2/10^4 = 4$. In this panel, the solid and dashed curves respectively indicate the MCM and TCM models. Three trends can be observed from this figure: (T1) When the rate of squeezing is fast relative to the dephasing ($\propto \tilde{\sigma}_q$), the ξ^2_{R} transient is similar (blue) to the zero width case (red) while the minimum value attained is greater indicating slight degradation of squeezing. (T2) For larger momentum width, the ξ^2_{R} transient displays oscillatory behavior signifying competition between squeezing and dephasing (orange). (T3) As the width increases further and dephasing dominates, ξ^2_{R} initially decreases slightly but then steeply increases to values well above unity, signaling rapid loss of squeezing (black).

These trends are summarized in Fig. 8.3(b), where the maximum metrological gain achievable is plotted as a function of $|\beta|^2$ for different values of $\tilde{\sigma}_q$. The $\tilde{\sigma}_q = 0$ case (red) reflects the study performed in Fig. 8.2 and shows that very strong driving lead to loss of squeezing as a result of coupling to other momentum centers. At the other extreme is the case of $\tilde{\sigma}_q = 0.1$ (black), where rapid dephasing leads to a complete loss of squeezing for weak driving, and barely observable squeezing ($\sim$ 2 dB) even for very strong driving. For intermediate widths $\tilde{\sigma}_q = 0.025, 0.05$ (blue, orange), the squeezing suffers at both ends, with dephasing restricting the squeezing at weak driving, and coupling to other centers serving as a limitation at very strong driving. For these widths, an optimum drive strength therefore exists where the metrological gain is maximized, as reflected by the variation of the gain for the four cases of $|\beta|^2$ considered here.

As Fig. 8.3(a) exemplifies, we observe that the TCM (dashed) typically qualitatively reproduces the features seen in the MCM (solid) when studying the effect of momentum width. Except at

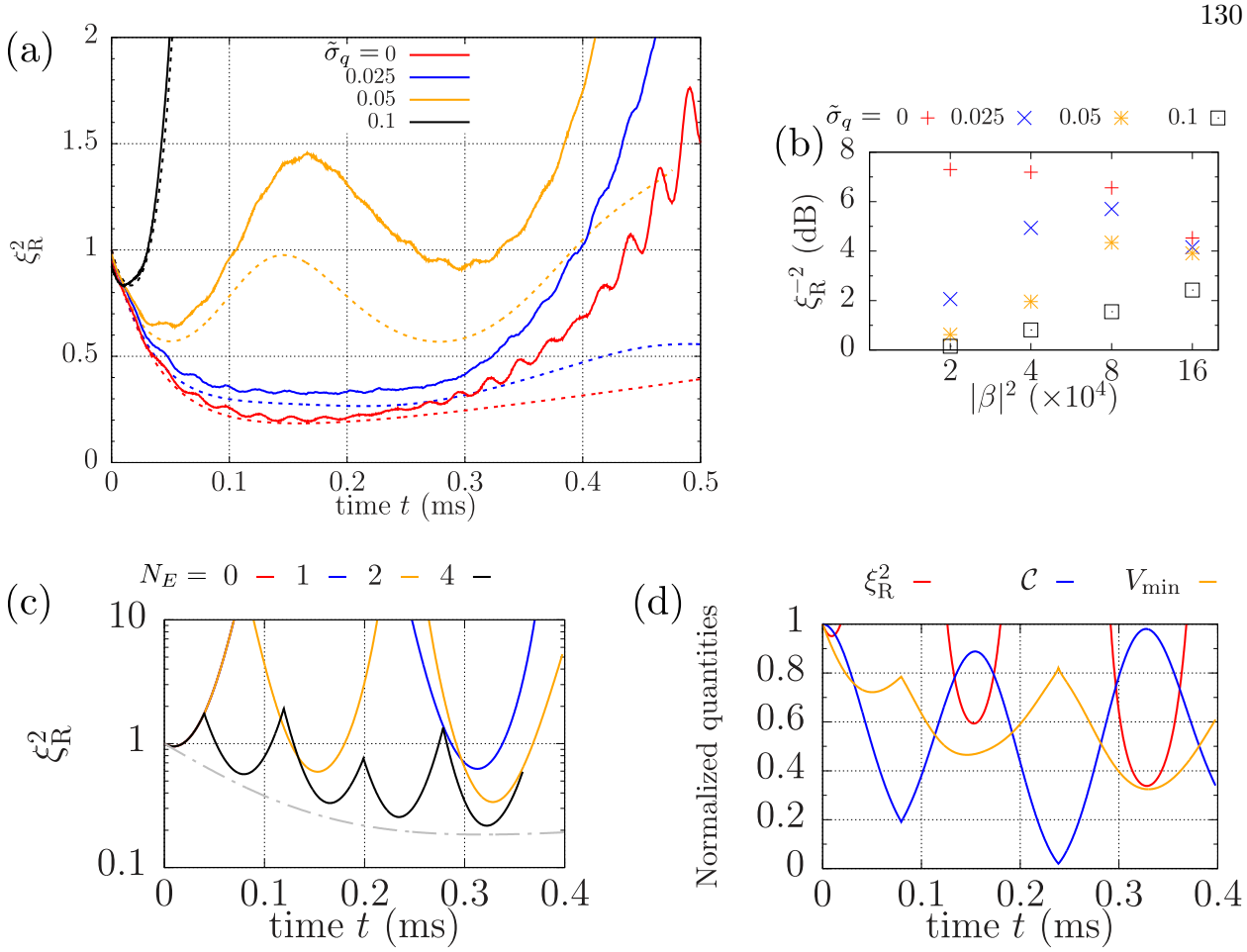

Figure 8.3: Squeezing in the presence of momentum width. (a) Evolution of $\xi^2_{\rm R}$ in the case of $|\beta|^2/10^4 = 4$ for $\tilde{\sigma}_q = 0, 0.025, 0.05, 0.1$. Solid (dashed) lines represent MCM (TCM) results. (b) Maximum metrological gain as a function of drive strength for different $\tilde{\sigma}_q$ values. (c) Evolution of $\xi^2_{\rm R}$ in the TCM for $\tilde{\sigma}_q = 0.1$ and $|\beta|^2/10^4 = 2$ when $N_{\rm E} = 0, 1, 2, 4$ echo pulses are inserted. The $N_{\rm E} = 1, 2, 4$ cases evolve identically to the $N_{\rm E} = 0$ case until the first echo is applied (at different times in the three cases). The gray broken line shows the $\tilde{\sigma}_q = 0$ case with no echoes. (d) Evolution of the constituents, C and $V_{\rm min}$ of $\xi^2_{\rm R}$ in the TCM when $N_{\rm E} = 2$ echo pulses are inserted. Other details are the same as in Fig. 8.2.

very strong driving, the TCM and MCM agree reasonably well in the (T1) cases until the minimum squeezing time, after which the MCM rises very steeply compared to the TCM. In the (T2) cases, both models capture the oscillatory behavior but can be very different quantitatively. Finally, both models agree very well in the (T3) case. The difference in the two models is not only because of the extra momentum centers tracked by the MCM, but also because of the approximations used in solving for the dynamics in these models. In the TCM model, we force all non-trivial three-atom

correlations to zero using a systematic truncation scheme (Section 7.7). However, the MCM is a TWA-style approach that can, in general, capture the build-up of non-trivial three-atom correlations, which should be anticipated in an interacting system such as the one considered here. As an example, the general steep increase of the MCM curves after the minimum squeezing time in the (T1) cases is a manifestation of the effect of three-atom correlations, also visible in the cases plotted in Fig. 8.2(a). On the other hand, the superposed oscillations at frequency $\sim 8\omega_r$ are a result of coupling to the $n_{\pm 1}$ momentum centers.

The dephasing-induced degradation of squeezing can in fact be reversed. To elucidate this point, we consider the case of $|\beta|^2/10^4 = 2$ and $\tilde{\sigma}_q = 0.1$, a situation where achieving squeezing is seemingly hopeless because of weak driving and rapid dephasing (red curve in Fig. 8.3(c)). As a minimal toy model to illustrate our protocol, we consider the TCM and interrupt the squeezing dynamics with a series of 'instantaneous' echo pulses (Appendix B.1.2). In a frame rotating at $4\omega_r$, the axis of rotation for these echoes is the same as that of the initial $\pi/2$-pulse used for preparing the equal superposition of the $n_\downarrow = 0, n_\uparrow = 1$ centers. Figure 8.3(c) shows the evolution of ξ_{R}^2 when $N_{\mathrm{E}} = 0, 1, 2, 4$ echo pulses are inserted during the course of the squeezing dynamics. The gray broken line shows the evolution of ξ_{R}^2 when $\tilde{\sigma}_q = 0$. The timing of the $N_{\mathrm{E}} > 0$ echo pulses are such that they approximately divide the time to achieve the minimum ξ_{R}^2 in the $\tilde{\sigma}_q = 0$ case (~ 0.3 ms) into a sequence of $T, 2T, \ldots, 2T, T$ segments, where the number of $2T$ segments is $N_{\mathrm{E}} - 1$. The insertion of echo pulses leads to a revival of ξ_{R}^2 as it periodically attains minima < 1 as the spins re-phase after an echo pulse is applied. Increasing the number of such echoes prevents ξ_{R}^2 from blowing up to very large values at any point during its evolution and also maintains the periodically attained minima close to the $\tilde{\sigma}_q = 0$ transient.

The applicability of such a protocol to revive the squeezing parameter goes beyond only momentum pseudospins, and is useful on a variety of platforms where squeezing is desired in the presence of unavoidable on-site disorder, for example, in the case of NV centers. For a practical implementation using momentum pseudospins, the non-zero echo pulse duration ($\gtrsim 2\pi/4\omega_r$ to avoid leakage to centers outside $n_\downarrow = 0, n_\uparrow = 1$) and the effect of momentum width on pulse efficiency

[118] have to be considered. Nevertheless, with suitable choice of parameters, we anticipate partial revivals in ξ^2_{R} to be observable despite these deviations from our toy model.

Finally, we investigate the constituent observables of the spin squeezing parameter to better understand this strong revival phenomenon. From Eq. (8.1), ξ^2_{R} comprises of two observables, namely, $\mathcal{C}$ (Eq. (8.2)) and V_{min} (Eq. (8.3)). Figure 8.3(d) plots the evolution of these observables as well as ξ^2_{R} for the case of $N_{\mathrm{E}} = 2$. The re-phasing of the spins after each echo leads to the expected increase of $\mathcal{C}$. However, Fig. 8.3(d) shows that this increase alone is not responsible for the strong revival of ξ^2_{R}. As the spins re-phase, V_{min} also reaches its minima close to the times when $\mathcal{C}$ peaks, thereby leading to sharp dips in ξ^2_{R}.

8.7 Collective physics with a many-body energy gap

Apart from squeezing, yet another type of collective behavior manifests as a result of the cavity mediated atom-atom interactions. We consider the observable $\mathcal{C}_\perp$, defined as the normalized length of the projection of the Bloch vector on to the equatorial plane of the Bloch sphere. Mathematically,

$$\mathcal{C}_\perp = \frac{\sqrt{\langle \hat{\mathcal{J}}^x_{n_\downarrow} \rangle^2 + \langle \hat{\mathcal{J}}^y_{n_\downarrow} \rangle^2}}{N/2}. \tag{8.12}$$

Figure 8.4(a) plots the evolution of $\mathcal{C}_\perp$ in the case $\tilde{\sigma}_q = 0.05$ for different values of $|\beta|^2/10^4 = 2, 4, 8$. The TCM (dashed) and the MCM (solid) are in qualitative agreement in all cases and in quantitative agreement when dephasing dominates, i.e. for weak driving (red). The gray broken line shows the corresponding decay of $\mathcal{C}_\perp$ for freely evolving atoms, i.e. with no interactions, which obeys the analytical expression $\mathcal{C}_\perp(t) = e^{-\mu_d^2 t^2}$, where $\mu_d = 4\sqrt{2}\omega_r \tilde{\sigma}_q$. Clearly, interactions lead to an observably slow decay of contrast compared to the free evolution case.

The effective Hamiltonian, Eq. (7.57), provides insight into the slow decay of $\mathcal{C}_\perp$ in the presence of interactions. We note that for any n,

$$\hat{\mathcal{J}}^-_n \hat{\mathcal{J}}^+_n = \hat{\mathbf{J}}_{\mathbf{n}} \cdot \hat{\mathbf{J}}_{\mathbf{n}} - \hat{\mathcal{J}}^z_n \hat{\mathcal{J}}^z_n - \hat{\mathcal{J}}^z_n. \tag{8.13}$$

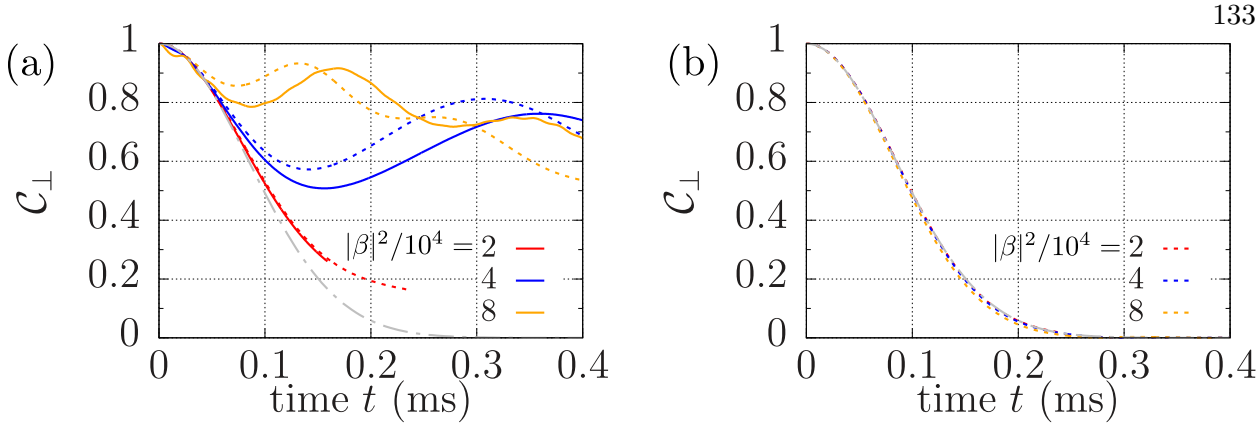

Figure 8.4: Manifestation of a many-body energy gap. (a) Evolution of $\mathcal{C}_\perp$ for $\tilde{\sigma}_q = 0.05$ for different values of $|\beta|^2/10^4 = 2, 4, 8$. (b) TCM results using the same parameters as in (a), but with the gap Hamiltonian $\hat{H}_{\rm G}$ turned off. The gray broken line in each case shows the decay of $\mathcal{C}_\perp$ under free evolution. Solid (dashed) lines represent MCM (TCM) results. Other details are the same as in Fig. 8.2.

We introduce the many-body gap Hamiltonian, $\hat{H}_{\rm G} = \hbar\chi_{n_\downarrow}\hat{\mathbf{J}}_{\mathbf{n}_\downarrow}\cdot\hat{\mathbf{J}}_{\mathbf{n}_\downarrow}$. The initial uncorrelated many-body state can be visualized as a coherent spin state in the equatorial plane of the Bloch sphere corresponding to the maximum quantum number $J_{n_\downarrow} = N/2$ associated with the operator $\hat{\mathbf{J}}_{\mathbf{n}_\downarrow}\cdot\hat{\mathbf{J}}_{\mathbf{n}_\downarrow}$. In other words, this initial state satisfies

$$\langle\hat{\mathbf{J}}_{\mathbf{n}_\downarrow}\cdot\hat{\mathbf{J}}_{\mathbf{n}_\downarrow}(0)\rangle = \frac{N}{2}\left(\frac{N}{2}+1\right),\ \mathcal{C}_\perp(0) = 1. \tag{8.14}$$

The first term of $\hat{H}_{\rm eff}$ in Eq. (7.57) is not collective, causing dephasing of individual spins that leads to shortening of the mean spin length and populates shells of lower $J_{n_\downarrow}$. The presence of $\hat{H}_{\rm G}$ introduces an energy penalty for populating shells of lower $J_{n_\downarrow}$. Specifically, $\hat{H}_{\rm G}$ dictates that

$$\hat{H}_{\rm G}\,|J_{n_\downarrow}, M_{J_{n_\downarrow}}\rangle = \hbar\chi_{n_\downarrow}J_{n_\downarrow}\left(J_{n_\downarrow}+1\right), \tag{8.15}$$

implying that the transition to a lower shell, $J_{n_\downarrow} \to J_{n_\downarrow} - 1$, incurs an energy penalty

$$|\Delta E_{\left(J_{n_\downarrow}\to J_{n_\downarrow}-1\right)}| = 2\hbar\chi_{n_\downarrow}J_{n_\downarrow}. \tag{8.16}$$

As a result, individual atom dephasing is slowed down, leading to slower decay of $\mathcal{C}_\perp$.

We verify this qualitative explanation in Fig. 8.4(b), where we study the dynamics of $\mathcal{C}_\perp$ under the TCM with the gap Hamiltonian $\hat{H}_{\rm G}$ turned off. The decay of $\mathcal{C}_\perp$ is then in excellent

agreement with the free evolution case, although interactions are present through the remaining terms in Eq. (7.57) and the dissipative term of Eq. (7.56).

Investigations with the TCM indicate that the presence of the gap Hamiltonian $\hat{H}_{\mathrm{G}}$ is an advantage from a metrology perspective. The slow decay of contrast leads to a smaller value for the minimum squeezing parameter ξ^2_{R} compared to the case when $\hat{H}_{\mathrm{G}}$ is turned off. Further, the subsequent rise of ξ^2_{R} after the minimum value is attained is slowed down when $\hat{H}_{\mathrm{G}}$ is present. We note that the non-zero momentum spread is an intrinsic source of dephasing in a Bragg interferometer, and the cavity-mediated interactions we engineer naturally provide a many-body gap protection that suppresses this dephasing.

In general, our results are consistent with other examples that confirm that the presence of a many-body gap arising from correlations can supresses adverse effects of single-atom decoherence [88] and potentially contribute to extending the coherence time for precision metrology. This ability to engineer many-body correlations driven either by mediated interactions or particle statistics represents an emerging paradigm for advanced metrology [74].

8.8 Final comments and possible extensions

For studying various aspects of the problem, we have focused on the $^1\mathrm{S}_0 - {}^3\mathrm{P}_1$ transition in ^{88}Sr as an example, working in parameter regimes where < 10 dB of metrological gain is achievable in a few hundred microseconds to a few milliseconds based on the driving strength. While more than sufficient for a proof-of-principle experiment, we expect that with suitable choice of parameters—small momentum width, small ratios of dissipative to dispersive interactions ($R = \kappa/2\delta_{n_\downarrow}$) and moderately strong driving strengths, ~ 10 dB of metrological gain can be achieved. Such parameters are within the reach of current technology: State-of-the-art cooling and velocity selection techniques are able to provide samples with $\tilde{\sigma}_q \lesssim 0.01$ while still ensuring appreciable atom numbers [66, 54]. The R value can be tuned to smaller values by detuning the drive laser farther away from the cavity resonance. Strong driving at large detunings is not a problem since modern lasers are able to deliver orders of magnitude more power than the hundreds of microwatts required in our proof-of-principle

parameter regimes. In addition to squeezing, the same experimental setup can also be used to demonstrate and explore collective physics associated with the opening of a many-body energy gap by measuring a different observable, namely the contrast $\mathcal{C}_\perp$ (Eq. (8.12)).

While in principle the R value can be made arbitrarily small to suppress superradiance and greatly improve the squeezing, with fixed atom number the power required to squeeze at a specified rate Q rapidly increases as $1/R^3$ (Eq. (8.9)), motivating considerations of elegant related schemes that are not as sensitive to superradiance. Recent schemes developed for squeezing on optical clock transitions circumvent this problem by either squeezing faster using a twist and turn mechanism achieved by introducing a resonant drive [53] or by an unconventional choice of initial state that drives the squeezing in a spin component orthogonal to that affected by superradiant decay [72]. The former can be implemented on momentum pseudospins using an additional pair of resonant Bragg lasers injected, for example, one free spectral range away from the cavity mode used for squeezing. The latter scheme requires an initial state with two ensembles pointing along opposite directions in the equatorial plane of the Bloch sphere. It can be implemented by launching two clouds with equal number of atoms which are initially in the $n_\downarrow$ and $n_\uparrow$ states respectively and applying a common $\pi/2$-pulse to rotate them to the equatorial plane. However, in either case, a careful study of the effects of momentum width and potential leakage to other momentum centers has to be performed. The techniques developed here can be readily used to undertake such a study. The latter scheme, combined with differential rotations on the two ensembles [31], can potentially be used to implement an entangled atom Bragg gradiometer.

Since our scheme relies on emission and absorption of a cavity photon, it is only applicable to states separated by $2\hbar k$. Nevertheless, the squeezing can be transferred to higher diffraction orders by subsequently applying large momentum transfer pulses [21, 93]. Finally, our scheme has natural extensions [50] to circumvent situations where the detection noise limits the utility of the prepared spin squeezed states for metrology. By adjusting the frequency of the drive laser, the sign of the squeezing interaction can be reversed, thereby making our scheme amenable to interaction-based readout schemes such as twisting echoes [30] that achieve precision below the standard quantum

limit even in the presence of detection noise [87, 37].

From a modeling standpoint, while simulations with $N = 10^3$ atoms only require modest computational resources, the favorable linear scaling of the multi-center model nevertheless allows a straightforward extension to simulating atomic sources with larger number of atoms. Moreover, our results are directly relevant to potential proof-of-principle experiments with small atomic clouds. The unraveling of the dynamics into phase space trajectories is enabled by considering initial atomic density matrices that have a momentum width but are still diagonal in the momentum basis. The finite spatial extent of realistic atomic sources implies the presence of some degree of initial coherence between the various momentum components. In future work, we will explore possible extensions of our model to study the effects of such initial coherences on the squeezing dynamics, which may be particularly important for sources such as Bose-Einstein condensates launched from strongly confining traps.

In addition to superradiant decay, single atom free-space scattering (FSS) also degrades the squeezing. Superradiance, being collectively enhanced, is the dominant source of degradation in most of the parameter regimes we have considered and therefore we have only focused on this dissipation mechanism. The parameter regime where superradiance dominates FSS is $R^2 \gg 1/NC$ (Appendix B.3), and therefore, FSS is not important when large atom numbers are used such that this inequality is satisfied. Nevertheless, FSS can be straightforwardly included in both the simulation models demonstrated here with very little computational overhead by accounting for the corresponding Lindblad terms. The scaling of the multi-center model remains linear in atom number since FSS occurs independently for each atom.

From a broader perspective, several mature atomic and atom-like platforms are beginning to demonstrate exotic many-body phenomena such as discrete time crystals [135, 22], many-body localization [61, 75] and dynamical phase transitions [59, 114]. Bragg interferometers operating in cavities open avenues for engineering interactions, and the theoretical techniques we have developed here can be used to explore the complex interplay of interactions, losses, disorder and global state rotations in other configurations involving momentum pseudospins.

Chapter 9

Conclusion

In Chapter 1, we listed three focus areas for improved quantum metrology. Accordingly, we first discussed the modeling and successful demonstration of near ground-state cooling of large trapped ion crystals with more than 100 ions. Powered by the robust technique of laser cooling by electromagnetically induced transparency, large ion crystals in Penning traps are now one step closer to becoming improved motion sensors that can potentially aid in future dark matter searches. Second, we presented a new technique to continuously and precisely track the relative phase of a spin superposition. Our scheme was based on atoms interacting with a lossy cavity mode, which was in turn monitored using homodyne detection. Such a scheme is expected to be useful for single-shot tracking of irreproducible signals and for continuous, uninterrupted operation of microwave atomic clocks. Finally, we proposed a scheme to engineer squeezing on momentum pseudospins for use in atomic Bragg interferometers, a platform traditionally operating on single-atom physics and where controllable atom-atom interactions have been hard to engineer till date. Our scheme can help improve the measurement precision of such interferometers and also aid in studies of collective quantum dynamics using momentum pseudospins. We also developed a numerical framework for modeling interacting momentum pseudospins, which can be used to study a range of quantum metrology and simulation protocols that are based on variants of Bragg interferometers. We hope that the tools discussed and demonstrated in this thesis will soon contribute towards improving quantum metrology on atomic platforms.

Bibliography

[1] P A Altin, M T Johnsson, V Negnevitsky, G R Dennis, R P Anderson, J E Debs, S S Szigeti, K S Hardman, S Bennetts, G D McDonald, L D Turner, J D Close, and N P Robins. Precision atomic gravimeter based on bragg diffraction. New Journal of Physics, 15(2):023009, feb 2013.

[2] Michael A. Armen, John K. Au, John K. Stockton, Andrew C. Doherty, and Hideo Mabuchi. Adaptive homodyne measurement of optical phase. Phys. Rev. Lett., 89:133602, Sep 2002.

[3] Frank Arute, Kunal Arya, Ryan Babbush, Dave Bacon, Joseph C. Bardin, Rami Barends, Rupak Biswas, Sergio Boixo, Fernando G. S. L. Brandao, David A. Buell, Brian Burkett, Yu Chen, Zijun Chen, Ben Chiaro, Roberto Collins, William Courtney, Andrew Dunsworth, Edward Farhi, Brooks Foxen, Austin Fowler, Craig Gidney, Marissa Giustina, Rob Graff, Keith Guerin, Steve Habegger, Matthew P. Harrigan, Michael J. Hartmann, Alan Ho, Markus Hoffmann, Trent Huang, Travis S. Humble, Sergei V. Isakov, Evan Jeffrey, Zhang Jiang, Dvir Kafri, Kostyantyn Kechedzhi, Julian Kelly, Paul V. Klimov, Sergey Knysh, Alexander Korotkov, Fedor Kostritsa, David Landhuis, Mike Lindmark, Erik Lucero, Dmitry Lyakh, Salvatore Mandrà, Jarrod R. McClean, Matthew McEwen, Anthony Megrant, Xiao Mi, Kristel Michielsen, Masoud Mohseni, Josh Mutus, Ofer Naaman, Matthew Neeley, Charles Neill, Murphy Yuezhen Niu, Eric Ostby, Andre Petukhov, John C. Platt, Chris Quintana, Eleanor G. Rieffel, Pedram Roushan, Nicholas C. Rubin, Daniel Sank, Kevin J. Satzinger, Vadim Smelyanskiy, Kevin J. Sung, Matthew D. Trevithick, Amit Vainsencher, Benjamin Villalonga, Theodore White, Z. Jamie Yao, Ping Yeh, Adam Zalcman, Hartmut Neven, and John M. Martinis. Quantum supremacy using a programmable superconducting processor. Nature, 574(7779):505–510, 2019.

[4] Peter Asenbaum, Chris Overstreet, Tim Kovachy, Daniel D. Brown, Jason M. Hogan, and Mark A. Kasevich. Phase shift in an atom interferometer due to spacetime curvature across its wave function. Phys. Rev. Lett., 118:183602, May 2017.

[5] H. Ball, Ch. D. Marciniak, R. N. Wolf, A. T.-H. Hung, K. Pyka, and M. J. Biercuk. Site-resolved imaging of beryllium ion crystals in a high-optical-access penning trap with inbore optomechanics. Review of Scientific Instruments, 90(5):053103, 2019.

[6] B. Barrett, A. Bertoldi, and P. Bouyer. Inertial quantum sensors using light and matter. Physica Scripta, 91(5):053006, 2016.

[7] Kristian Baumann, Christine Guerlin, Ferdinand Brennecke, and Tilman Esslinger. Dicke quantum phase transition with a superfluid gas in an optical cavity. Nature, 464:1301, Apr 2010. Article.

[8] Michael J Biercuk, Hermann Uys, Aaron P Vandevender, Nobuyasu Shiga, Wayne M Itano, and John J Bollinger. High-fidelity quantum control using ion crystals in a penning trap. Quantum Information & Computation, 9(11):920–949, 2009.

[9] P.B. Blakie†, A.S. Bradley†, M.J. Davis, R.J. Ballagh, and C.W. Gardiner. Dynamics and statistical mechanics of ultra-cold bose gases using c-field techniques. Advances in Physics, 57(5):363–455, 2008.

[10] R. Blatt and C. F. Roos. Quantum simulations with trapped ions. Nature Physics, 8:277, Apr 2012. Review Article.

[11] J. G. Bohnet, K. C. Cox, M. A. Norcia, J. M. Weiner, Z. Chen, and J. K. Thompson. Reduced spin measurement back-action for a phase sensitivity ten times beyond the standard quantum limit. Nature Photonics, 8:731, Jul 2014. Article.

[12] Justin G. Bohnet, Brian C. Sawyer, Joseph W. Britton, Michael L. Wall, Ana Maria Rey, Michael Foss-Feig, and John J. Bollinger. Quantum spin dynamics and entanglement generation with hundreds of trapped ions. Science, 352(6291):1297–1301, 2016.

[13] J Borregaard, E J Davis, G S Bentsen, M H Schleier-Smith, and A S Sørensen. One- and two-axis squeezing of atomic ensembles in optical cavities. New Journal of Physics, 19(9):093021, sep 2017.

[14] L. Bouten, R. Van Handel, and M. James. An introduction to quantum filtering. SIAM Journal on Control and Optimization, 46(6):2199–2241, 2007.

[15] W.P. Bowen and G.J. Milburn. Quantum Optomechanics. CRC Press, 2015.

[16] Vladimir B. Braginsky, Yuri I. Vorontsov, and Kip S. Thorne. Quantum nondemolition measurements. Science, 209(4456):547–557, 1980.

[17] Joseph W. Britton, Brian C. Sawyer, Adam C. Keith, C. C Joseph Wang, James K. Freericks, Hermann Uys, Michael J. Biercuk, and John J. Bollinger. Engineered two-dimensional ising interactions in a trapped-ion quantum simulator with hundreds of spins. Nature, 484:489, Apr 2012.

[18] A. Camara, R. Kaiser, and G. Labeyrie. Scaling behavior of a very large magneto-optical trap. Phys. Rev. A, 90:063404, Dec 2014.

[19] H.J. Carmichael. Statistical Methods in Quantum Optics 2: Non-Classical Fields. Theoretical and Mathematical Physics. Springer Berlin Heidelberg, 2010.

[20] Yuan Cheng, Ke Zhang, Le-Le Chen, Tao Zhang, Wen-Jie Xu, Xiao-Chun Duan, Min-Kang Zhou, and Zhong-Kun Hu. Momentum-resolved detection for high-precision bragg atom interferometry. Phys. Rev. A, 98:043611, Oct 2018.

[21] Sheng-wey Chiow, Tim Kovachy, Hui-Chun Chien, and Mark A. Kasevich. $102\hbar k$ large area atom interferometers. Phys. Rev. Lett., 107:130403, Sep 2011.

[22] Soonwon Choi, Joonhee Choi, Renate Landig, Georg Kucsko, Hengyun Zhou, Junichi Isoya, Fedor Jelezko, Shinobu Onoda, Hitoshi Sumiya, Vedika Khemani, Curt von Keyserlingk, Norman Y. Yao, Eugene Demler, and Mikhail D. Lukin. Observation of discrete time-crystalline order in a disordered dipolar many-body system. Nature, 543:221, Mar 2017.

[23] A A Clerk, F Marquardt, and K Jacobs. Back-action evasion and squeezing of a mechanical resonator using a cavity detector. New Journal of Physics, 10(9):095010, 2008.

[24] J Cohn, A Safavi-Naini, R J Lewis-Swan, J G Bohnet, M Gärttner, K A Gilmore, J E Jordan, A M Rey, J J Bollinger, and J K Freericks. Bang-bang shortcut to adiabaticity in the dicke model as realized in a penning trap experiment. New Journal of Physics, 20(5):055013, 2018.

[25] Giorgio Colangelo, Ferran Martin Ciurana, Lorena C. Bianchet, Robert J. Sewell, and Morgan W. Mitchell. Simultaneous tracking of spin angle and amplitude beyond classical limits. Nature, 543:525, Mar 2017.

[26] Kevin C. Cox, Graham P. Greve, Joshua M. Weiner, and James K. Thompson. Deterministic squeezed states with collective measurements and feedback. Phys. Rev. Lett., 116:093602, Mar 2016.

[27] Alexander D. Cronin, Jörg Schmiedmayer, and David E. Pritchard. Optics and interferometry with atoms and molecules. Rev. Mod. Phys., 81:1051–1129, Jul 2009.

[28] J Dalibard and C Cohen-Tannoudji. Atomic motion in laser light: connection between semiclassical and quantum descriptions. Journal of Physics B: Atomic and Molecular Physics, 18(8):1661, 1985.

[29] J. Dalibard and C. Cohen-Tannoudji. Laser cooling below the doppler limit by polarization gradients: simple theoretical models. J. Opt. Soc. Am. B, 6(11):2023–2045, Nov 1989.

[30] Emily Davis, Gregory Bentsen, and Monika Schleier-Smith. Approaching the heisenberg limit without single-particle detection. Phys. Rev. Lett., 116:053601, Feb 2016.

[31] R P del Aguila, T Mazzoni, L Hu, L Salvi, G M Tino, and N Poli. Bragg gravity-gradiometer using the 1s0–3p1 intercombination transition of 88sr. New Journal of Physics, 20(4):043002, apr 2018.

[32] F. Dimer, B. Estienne, A. S. Parkins, and H. J. Carmichael. Proposed realization of the dicke-model quantum phase transition in an optical cavity qed system. Phys. Rev. A, 75:013804, Jan 2007.

[33] Daniel H. E. Dubin and T. M. O'Neil. Trapped nonneutral plasmas, liquids, and crystals (the thermal equilibrium states). Rev. Mod. Phys., 71:87–172, Jan 1999.

[34] D. Dylewsky, J. K. Freericks, M. L. Wall, A. M. Rey, and M. Foss-Feig. Nonperturbative calculation of phonon effects on spin squeezing. Phys. Rev. A, 93:013415, Jan 2016.

[35] A. Eddins, S. Schreppler, D. M. Toyli, L. S. Martin, S. Hacohen-Gourgy, L. C. G. Govia, H. Ribeiro, A. A. Clerk, and I. Siddiqi. Stroboscopic qubit measurement with squeezed illumination. Phys. Rev. Lett., 120:040505, Jan 2018.

[36] Jürgen Eschner, Giovanna Morigi, Ferdinand Schmidt-Kaler, and Rainer Blatt. Laser cooling of trapped ions. J. Opt. Soc. Am. B, 20(5):1003–1015, May 2003.

[37] Florian Fröwis, Pavel Sekatski, and Wolfgang Dür. Detecting large quantum fisher information with finite measurement precision. Phys. Rev. Lett., 116:090801, Mar 2016.

[38] M. Galassi, J. Davies, J. Theiler, B. Gough, G. Jungman, P. Alken, M. Booth, F. Rossi, and R. Ulerich. Gnu scientific library reference manual. https://www.gnu.org/software/gsl/, 2018.

[39] Martin Gärttner, Justin G. Bohnet, Arghavan Safavi-Naini, Michael L. Wall, John J. Bollinger, and Ana Maria Rey. Measuring out-of-time-order correlations and multiple quantum spectra in a trapped-ion quantum magnet. Nature Physics, 13:781, May 2017. Article.

[40] JM Geremia, John K. Stockton, Andrew C. Doherty, and Hideo Mabuchi. Quantum kalman filtering and the heisenberg limit in atomic magnetometry. Phys. Rev. Lett., 91:250801, Dec 2003.

[41] C. Gerry and P. Knight. Introductory Quantum Optics. Cambridge University Press, 2004.

[42] K. A. Gilmore, J. G. Bohnet, B. C. Sawyer, J. W. Britton, and J. J. Bollinger. Amplitude sensing below the zero-point fluctuations with a two-dimensional trapped-ion mechanical oscillator. Phys. Rev. Lett., 118:263602, Jun 2017.

[43] Peter W Graham, Jason M Hogan, Mark A Kasevich, and Surjeet Rajendran. New method for gravitational wave detection with atomic sensors. Phys. Rev. Lett., 110(17):171102, 2013.

[44] Gaël Guennebaud, Benoît Jacob, et al. Eigen v3. http://eigen.tuxfamily.org, 2010.

[45] Shay Hacohen-Gourgy, Leigh S. Martin, Emmanuel Flurin, Vinay V. Ramasesh, K. Birgitta Whaley, and Irfan Siddiqi. Quantum dynamics of simultaneously measured non-commuting observables. Nature, 538:491, Oct 2016.

[46] H. Häffner, C.F. Roos, and R. Blatt. Quantum computing with trapped ions. Physics Reports, 469(4):155 – 203, 2008.

[47] Paul Hamilton, Matt Jaffe, Justin M. Brown, Lothar Maisenbacher, Brian Estey, and Holger Müller. Atom interferometry in an optical cavity. Phys. Rev. Lett., 114:100405, Mar 2015.

[48] Paul Hamilton, Matt Jaffe, Philipp Haslinger, Quinn Simmons, Holger Müller, and Justin Khoury. Atom-interferometry constraints on dark energy. Science, 349(6250):849–851, 2015.

[49] N Hinkley, JA Sherman, NB Phillips, M Schioppo, ND Lemke, K Beloy, M Pizzocaro, CW Oates, and AD Ludlow. An atomic clock with 10^{-18} instability. Science, 341(6151):1215–1218, 2013.

[50] O. Hosten, R. Krishnakumar, N. J. Engelsen, and M. A. Kasevich. Quantum phase magnification. Science, 352(6293):1552–1555, 2016.

[51] Onur Hosten, Nils J. Engelsen, Rajiv Krishnakumar, and Mark A. Kasevich. Measurement noise 100 times lower than the quantum-projection limit using entangled atoms. Nature, 529(7587):505, JAN 28 2016.

[52] Onur Hosten, Nils J. Engelsen, Rajiv Krishnakumar, and Mark A. Kasevich. Measurement noise 100 times lower than the quantum-projection limit using entangled atoms. Nature, 529:505, Jan 2016.

[53] Jiazhong Hu, Wenlan Chen, Zachary Vendeiro, Alban Urvoy, Boris Braverman, and Vladan Vuletić. Vacuum spin squeezing. Phys. Rev. A, 96:050301, Nov 2017.

[54] Liang Hu, Nicola Poli, Leonardo Salvi, and Guglielmo M. Tino. Atom interferometry with the sr optical clock transition. Phys. Rev. Lett., 119:263601, 2017.

[55] Matt Jaffe, Victoria Xu, Philipp Haslinger, Holger Müller, and Paul Hamilton. Efficient adiabatic spin-dependent kicks in an atom interferometer. Phys. Rev. Lett., 121:040402, Jul 2018.

[56] D F James and J Jerke. Effective hamiltonian theory and its applications in quantum information. Canadian Journal of Physics, 85(6):625–632, 2007.

[57] G. Janik, W. Nagourney, and H. Dehmelt. Doppler-free optical spectroscopy on the ba+ mono-ion oscillator. J. Opt. Soc. Am. B, 2(8):1251–1257, Aug 1985.

[58] Elena Jordan, Kevin A. Gilmore, Athreya Shankar, Arghavan Safavi-Naini, Murray J. Holland, and John J. Bollinger, 2018. Accompanying paper submitted to Phys. Rev. Lett.

[59] P. Jurcevic, H. Shen, P. Hauke, C. Maier, T. Brydges, C. Hempel, B. P. Lanyon, M. Heyl, R. Blatt, and C. F. Roos. Direct observation of dynamical quantum phase transitions in an interacting many-body system. Phys. Rev. Lett., 119:080501, Aug 2017.

[60] Hidetoshi Katori. Optical lattice clocks and quantum metrology. Nat. Photon., 5(4):203–210, March 2011.

[61] Adam M. Kaufman, M. Eric Tai, Alexander Lukin, Matthew Rispoli, Robert Schittko, Philipp M. Preiss, and Markus Greiner. Quantum thermalization through entanglement in an isolated many-body system. Science, 353(6301):794–800, 2016.

[62] Masahiro Kitagawa and Masahito Ueda. Squeezed spin states. Phys. Rev. A, 47:5138–5143, Jun 1993.

[63] R. Kohlhaas, A. Bertoldi, E. Cantin, A. Aspect, A. Landragin, and P. Bouyer. Phase locking a clock oscillator to a coherent atomic ensemble. Phys. Rev. X, 5:021011, Apr 2015.

[64] T. Kovachy, P. Asenbaum, C. Overstreet, C. A. Donnelly, S. M. Dickerson, A. Sugarbaker, J. M. Hogan, and M. A. Kasevich. Quantum superposition at the half-metre scale. Nature, 528:530, Dec 2015.

[65] Tim Kovachy, Sheng-wey Chiow, and Mark A. Kasevich. Adiabatic-rapid-passage multiphoton bragg atom optics. Phys. Rev. A, 86:011606, Jul 2012.

[66] Tim Kovachy, Jason M. Hogan, Alex Sugarbaker, Susannah M. Dickerson, Christine A. Donnelly, Chris Overstreet, and Mark A. Kasevich. Matter wave lensing to picokelvin temperatures. Phys. Rev. Lett., 114:143004, Apr 2015.

[67] A. Kuzmich, L. Mandel, and N. P. Bigelow. Generation of spin squeezing via continuous quantum nondemolition measurement. Phys. Rev. Lett., 85:1594–1597, Aug 2000.

[68] Regina Lechner, Christine Maier, Cornelius Hempel, Petar Jurcevic, Ben P. Lanyon, Thomas Monz, Michael Brownnutt, Rainer Blatt, and Christian F. Roos. Electromagnetically-induced-transparency ground-state cooling of long ion strings. Phys. Rev. A, 93:053401, May 2016.

[69] D. Leibfried, R. Blatt, C. Monroe, and D. Wineland. Quantum dynamics of single trapped ions. Rev. Mod. Phys., 75:281–324, Mar 2003.

[70] S. Lepoutre, J. Schachenmayer, L. Gabardos, B. Zhu, B. Naylor, E. Maréchal, O. Gorceix, A. M. Rey, L. Vernac, and B. Laburthe-Tolra. Out-of-equilibrium quantum magnetism and thermalization in a spin-3 many-body dipolar lattice system. Nature Communications, 10(1):1714, 2019.

[71] Ian D. Leroux, Monika H. Schleier-Smith, and Vladan Vuletić. Implementation of cavity squeezing of a collective atomic spin. Phys. Rev. Lett., 104:073602, Feb 2010.

[72] Robert J. Lewis-Swan, Matthew A. Norcia, Julia R. K. Cline, James K. Thompson, and Ana Maria Rey. Robust spin squeezing via photon-mediated interactions on an optical clock transition. Phys. Rev. Lett., 121:070403, Aug 2018.

[73] B Lounis and Claude Cohen-Tannoudji. Coherent population trapping and fano profiles. Journal de Physique II, 2(4):579–592, 1992.

[74] Leonardo Lucchesi and Maria Luisa Chiofalo. Many-body entanglement in short-range interacting fermi gases for metrology. Phys. Rev. Lett., 123:060406, Aug 2019.

[75] Alexander Lukin, Matthew Rispoli, Robert Schittko, M. Eric Tai, Adam M. Kaufman, Soonwon Choi, Vedika Khemani, Julian Léonard, and Markus Greiner. Probing entanglement in a many-body–localized system. Science, 364(6437):256–260, 2019.

[76] Jian Ma, Xiaoguang Wang, C.P. Sun, and Franco Nori. Quantum spin squeezing. Physics Reports, 509(2):89 – 165, 2011.

[77] Sandeep Mavadia, Joseph F. Goodwin, Graham Stutter, Shailen Bharadia, Daniel R. Crick, Daniel M. Segal, and Richard C. Thompson. Control of the conformations of ion coulomb crystals in a penning trap. Nature Communications, 4:2571, Oct 2013. Article.

[78] T. Mazzoni, X. Zhang, R. Del Aguila, L. Salvi, N. Poli, and G. M. Tino. Large-momentum-transfer bragg interferometer with strontium atoms. Phys. Rev. A, 92:053619, Nov 2015.

[79] M. McAneny, B. Yoshimura, and J. K. Freericks. Effect of defects on phonons and the effective spin-spin interactions of an ultracold penning-trap quantum simulator. Phys. Rev. A, 88:043434, Oct 2013.

[80] D. Meiser and M. J. Holland. Steady-state superradiance with alkaline-earth-metal atoms. Phys. Rev. A, 81:033847, Mar 2010.

[81] D. Meiser, Jun Ye, D. R. Carlson, and M. J. Holland. Prospects for a millihertz-linewidth laser. Phys. Rev. Lett., 102:163601, Apr 2009.

[82] P. Meystre and M. Sargent. Elements of Quantum Optics. Springer Berlin Heidelberg, 1998.

[83] Giovanna Morigi. Cooling atomic motion with quantum interference. Phys. Rev. A, 67:033402, Mar 2003.

[84] Giovanna Morigi, Jürgen Eschner, and Christoph H. Keitel. Ground state laser cooling using electromagnetically induced transparency. Phys. Rev. Lett., 85:4458–4461, Nov 2000.

[85] Holger Müller, Sheng-wey Chiow, and Steven Chu. Atom-wave diffraction between the raman-nath and the bragg regime: Effective rabi frequency, losses, and phase shifts. Phys. Rev. A, 77:023609, Feb 2008.

[86] TL Nicholson, SL Campbell, RB Hutson, GE Marti, BJ Bloom, RL McNally, W Zhang, MD Barrett, MS Safronova, GF Strouse, et al. Systematic evaluation of an atomic clock at 2×10^{-18} total uncertainty. Nature Communications, 6:6896, 2015.

[87] Samuel P. Nolan, Stuart S. Szigeti, and Simon A. Haine. Optimal and robust quantum metrology using interaction-based readouts. Phys. Rev. Lett., 119:193601, Nov 2017.

[88] Matthew A. Norcia, Robert J. Lewis-Swan, Julia R. K. Cline, Bihui Zhu, Ana M. Rey, and James K. Thompson. Cavity-mediated collective spin-exchange interactions in a strontium superradiant laser. Science, 361(6399):259–262, 2018.

[89] G Pagano, P W Hess, H B Kaplan, W L Tan, P Richerme, P Becker, A Kyprianidis, J Zhang, E Birckelbaw, M R Hernandez, Y Wu, and C Monroe. Cryogenic trapped-ion system for large scale quantum simulation. Quantum Science and Technology, 4(1):014004, 2019.

[90] Richard H. Parker, Chenghui Yu, Weicheng Zhong, Brian Estey, and Holger Müller. Measurement of the fine-structure constant as a test of the standard model. Science, 360(6385):191–195, 2018.

[91] R.K. Pathria and P.D. Beale. Statistical Mechanics. Academic Press. Butterworth-Heinemann, 2011.

[92] Asier Piñeiro Orioli, Arghavan Safavi-Naini, Michael L. Wall, and Ana Maria Rey. Nonequilibrium dynamics of spin-boson models from phase-space methods. Phys. Rev. A, 96:033607, Sep 2017.

[93] Benjamin Plotkin-Swing, Daniel Gochnauer, Katherine E. McAlpine, Eric S. Cooper, Alan O. Jamison, and Subhadeep Gupta. Three-path atom interferometry with large momentum separation. Phys. Rev. Lett., 121:133201, Sep 2018.

[94] Anatoli Polkovnikov. Phase space representation of quantum dynamics. Annals of Physics, 325(8):1790 – 1852, 2010.

[95] Norman F. Ramsey. A molecular beam resonance method with separated oscillating fields. Phys. Rev., 78:695–699, Jun 1950.

[96] Philip Richerme. Two-dimensional ion crystals in radio-frequency traps for quantum simulation. Phys. Rev. A, 94:032320, Sep 2016.

[97] C. Jess Riedel. Direct detection of classically undetectable dark matter through quantum decoherence. Phys. Rev. D, 88:116005, Dec 2013.

[98] AJ Roberts. Modify the improved euler scheme to integrate stochastic differential equations. arXiv preprint arXiv:1210.0933, 2012.

[99] N.P. Robins, P.A. Altin, J.E. Debs, and J.D. Close. Atom lasers: Production, properties and prospects for precision inertial measurement. Physics Reports, 529(3):265 – 296, 2013. Atom lasers: production, properties and prospects for precision inertial measurement.

[100] G. Rosi, F. Sorrentino, L. Cacciapuoti, M. Prevedelli, and G. M. Tino. Precision measurement of the newtonian gravitational constant using cold atoms. Nature, 510(7506):518–521, June 2014.

[101] A. Safavi-Naini, R. J. Lewis-Swan, J. G. Bohnet, M. Gärttner, K. A. Gilmore, J. E. Jordan, J. Cohn, J. K. Freericks, A. M. Rey, and J. J. Bollinger. Verification of a many-ion simulator of the dicke model through slow quenches across a phase transition. Phys. Rev. Lett., 121:040503, Jul 2018.

[102] Arghavan Safavi-Naini. unpublished.

[103] Leonardo Salvi, Nicola Poli, Vladan Vuletić, and Guglielmo M. Tino. Squeezing on momentum states for atom interferometry. Phys. Rev. Lett., 120:033601, 2018.

[104] Brian C. Sawyer, Joseph W. Britton, and John J. Bollinger. Spin dephasing as a probe of mode temperature, motional state distributions, and heating rates in a two-dimensional ion crystal. Phys. Rev. A, 89:033408, Mar 2014.

[105] Brian C. Sawyer, Joseph W. Britton, Adam C. Keith, C.-C. Joseph Wang, James K. Freericks, Hermann Uys, Michael J. Biercuk, and John J. Bollinger. Spectroscopy and thermometry of drumhead modes in a mesoscopic trapped-ion crystal using entanglement. Phys. Rev. Lett., 108:213003, May 2012.

[106] J. Schachenmayer, A. Pikovski, and A. M. Rey. Many-body quantum spin dynamics with monte carlo trajectories on a discrete phase space. Phys. Rev. X, 5:011022, Feb 2015.

[107] Monika H. Schleier-Smith, Ian D. Leroux, and Vladan Vuletić. Squeezing the collective spin of a dilute atomic ensemble by cavity feedback. Phys. Rev. A, 81:021804, Feb 2010.

[108] D. Schlippert, J. Hartwig, H. Albers, L. L. Richardson, C. Schubert, A. Roura, W. P. Schleich, W. Ertmer, and E. M. Rasel. Quantum test of the universality of free fall. Phys. Rev. Lett., 112:203002, May 2014.

[109] Nicolas Schlosser, Georges Reymond, Igor Protsenko, and Philippe Grangier. Sub-poissonian loading of single atoms in a microscopic dipole trap. Nature, 411(6841):1024–1027, 2001.

[110] Athreya Shankar, John Cooper, Justin G. Bohnet, John J. Bollinger, and Murray Holland. Steady-state spin synchronization through the collective motion of trapped ions. Phys. Rev. A, 95:033423, Mar 2017.

[111] Athreya Shankar, Elena Jordan, Kevin A. Gilmore, Arghavan Safavi-Naini, John J. Bollinger, and Murray J. Holland. Modeling near ground-state cooling of two-dimensional ion crystals in a penning trap using electromagnetically induced transparency. Phys. Rev. A, 99:023409, Feb 2019.

[112] N Shiga and M Takeuchi. Locking the local oscillator phase to the atomic phase via weak measurement. New Journal of Physics, 14(2):023034, feb 2012.

[113] Alice Sinatra, Carlos Lobo, and Yvan Castin. The truncated wigner method for bose-condensed gases: limits of validity and applications. Journal of Physics B: Atomic, Molecular and Optical Physics, 35(17):3599–3631, aug 2002.

[114] Scott Smale, Peiru He, Ben A. Olsen, Kenneth G. Jackson, Haille Sharum, Stefan Trotzky, Jamir Marino, Ana Maria Rey, and Joseph H. Thywissen. Observation of a transition between dynamical phases in a quantum degenerate fermi gas. Science Advances, 5(8), 2019.

[115] Anders Søndberg Sørensen and Klaus Mølmer. Entangling atoms in bad cavities. Phys. Rev. A, 66:022314, Aug 2002.

[116] M. J. Steel, M. K. Olsen, L. I. Plimak, P. D. Drummond, S. M. Tan, M. J. Collett, D. F. Walls, and R. Graham. Dynamical quantum noise in trapped bose-einstein condensates. Phys. Rev. A, 58:4824–4835, Dec 1998.

[117] John K. Stockton, J. M. Geremia, Andrew C. Doherty, and Hideo Mabuchi. Robust quantum parameter estimation: Coherent magnetometry with feedback. Phys. Rev. A, 69:032109, Mar 2004.

[118] S. S. Szigeti, J. E. Debs, J. J. Hope, N. P. Robins, and J. D. Close. Why momentum width matters for atom interferometry with bragg pulses. New J. Phys., 14:023009, 2012.

[119] Chen Tang, Dominic Meiser, John J. Bollinger, and Scott E. Parker. First principles simulation of ultracold ion crystals in a penning trap with doppler cooling and a rotating wall potential. Physics of Plasmas, 26(7):073504, 2019.

[120] L K Thomsen, S Mancini, and H M Wiseman. Continuous quantum nondemolition feedback and unconditional atomic spin squeezing. Journal of Physics B: Atomic, Molecular and Optical Physics, 35(23):4937, 2002.

[121] DA Tieri, Minghui Xu, D Meiser, J Cooper, and MJ Holland. Theory of the crossover from lasing to steady state superradiance. arXiv preprint arXiv:1702.04830, 2017.

[122] Thad Walker, David Sesko, and Carl Wieman. Collective behavior of optically trapped neutral atoms. Phys. Rev. Lett., 64:408–411, Jan 1990.

[123] Michael L. Wall, Arghavan Safavi-Naini, and Ana Maria Rey. Simulating generic spin-boson models with matrix product states. Phys. Rev. A, 94:053637, Nov 2016.

[124] C.-C. Joseph Wang, Adam C. Keith, and J. K. Freericks. Phonon-mediated quantum spin simulator employing a planar ionic crystal in a penning trap. Phys. Rev. A, 87:013422, Jan 2013.

[125] W. Wasilewski, K. Jensen, H. Krauter, J. J. Renema, M. V. Balabas, and E. S. Polzik. Quantum noise limited and entanglement-assisted magnetometry. Phys. Rev. Lett., 104:133601, Mar 2010.

[126] D. J. Wineland, C. Monroe, W. M. Itano, D. Leibfried, B. E. King, and D. M. Meekhof. Experimental issues in coherent quantum state manipulation of trapped atomic ions. J. Res. Natl. Inst. Stand. Tech., 103:259, 1998.

[127] H. M. Wiseman. Quantum theory of continuous feedback. Phys. Rev. A, 49:2133–2150, Mar 1994.

[128] H. M. Wiseman. Adaptive phase measurements of optical modes: Going beyond the marginal q distribution. Phys. Rev. Lett., 75:4587–4590, Dec 1995.

[129] H. M. Wiseman and G. J. Milburn. Quantum theory of field-quadrature measurements. Phys. Rev. A, 47:642–662, Jan 1993.

[130] H. M. Wiseman and G. J. Milburn. Quantum theory of optical feedback via homodyne detection. Phys. Rev. Lett., 70:548–551, Feb 1993.

[131] H.M. Wiseman and G.J. Milburn. Quantum Measurement and Control. Cambridge University Press, 2010.

[132] Minghui Xu and M. J. Holland. Conditional ramsey spectroscopy with synchronized atoms. Phys. Rev. Lett., 114:103601, Mar 2015.

[133] Minghui Xu, Simon B. Jäger, S. Schütz, J. Cooper, Giovanna Morigi, and M. J. Holland. Supercooling of atoms in an optical resonator. Phys. Rev. Lett., 116:153002, Apr 2016.

[134] Chenghui Yu, Weicheng Zhong, Brian Estey, Joyce Kwan, Richard H. Parker, and Holger Müller. Atom-interferometry measurement of the fine structure constant. Annalen der Physik, 0(0):1800346, 2019.

[135] J. Zhang, P. W. Hess, A. Kyprianidis, P. Becker, A. Lee, J. Smith, G. Pagano, I.-D. Potirniche, A. C. Potter, A. Vishwanath, N. Y. Yao, and C. Monroe. Observation of a discrete time crystal. Nature, 543:217, Mar 2017.

[136] Zhiqiang Zhang, Chern Hui Lee, Ravi Kumar, K. J. Arnold, Stuart J. Masson, A. L. Grimsmo, A. S. Parkins, and M. D. Barrett. Dicke-model simulation via cavity-assisted raman transitions. Phys. Rev. A, 97:043858, Apr 2018.

Appendix A

Supplementary Material for Chapters 3 and 4

A.1 Equations of motion for first and second order moments

In Table A.1, we introduce a set of "partial sums" that not only simplify the notation, but also speed up the computation time by identifying recurring summations and evaluating them only once per time step. In addition, we split the equations of motion for each moment into three parts that correspond respectively to $\mathcal{L}_0$, $\mathcal{L}_1$ and $\mathcal{L}_2$ contributions from the master equation, Eq. (3.11).

A.1.1 Internal moments

The dynamics of the internal moments are governed by the following equations.

$\mathcal{L}_0$ contribution

$$\frac{d}{dt}\langle\sigma^j_{g_1g_1}\rangle \;=\; -\frac{i}{2}\left(\Omega^*_{1,j}\langle\sigma^j_{g_1e}\rangle - \text{ c.c.}\right) + \Gamma_1\left(1 - \langle\sigma^j_{g_1g_1}\rangle - \langle\sigma^j_{g_2g_2}\rangle\right)$$

Symbol	Definition
$\mathcal{P}^X_{\mu,j}$	$\sum_m \lambda^\mu_{jm}\langle X_m\rangle$
$\mathcal{P}^{XX}_{\mu,j}$	$\sum_{l,m} \lambda^\mu_{jl}\lambda^\mu_{jm}\langle X_l X_m\rangle$
$\mathcal{P}^{bX}_{\mu,jn}$	$\sum_m \lambda^\mu_{jm}\langle b_n X_m\rangle$
$\mathcal{P}^{dX}_{\mu,jn}$	$\sum_m \lambda^\mu_{jm}\langle b^\dagger_n X_m\rangle$
$\mathcal{P}^{X\sigma_\alpha}_{\mu,j}$	$\sum_m \lambda^\mu_{jm}\langle X_m\sigma^j_\alpha\rangle$
$\mathcal{P}^{X\sigma_\alpha}_{\mu,[qj]}$	$\sum_m \lambda^\mu_{qm}\langle X_m\sigma^j_\alpha\rangle$

Table A.1: Definition of partial sums to simplify notation and speed up computation. The symbols X_m and λ^μ_{jm} are defined after Eq. 3.13.

$$\begin{aligned}
\frac{d}{dt}\langle\sigma^j_{g_1g_2}\rangle &= i\left(\Delta_{1,j}(t)-\Delta_{2,j}(t)\right)\langle\sigma^j_{g_1g_2}\rangle + \frac{i\Omega_{1,j}}{2}\langle\sigma^j_{g_2e}\rangle^* - \frac{i\Omega^*_{2,j}}{2}\langle\sigma^j_{g_1e}\rangle \\
\frac{d}{dt}\langle\sigma^j_{g_1e}\rangle &= -\left(\frac{\Gamma}{2}-i\Delta_{1,j}(t)\right)\langle\sigma^j_{g_1e}\rangle - \frac{i\Omega_{1,j}}{2}\left(2\langle\sigma^j_{g_1g_1}\rangle + \langle\sigma^j_{g_2g_2}\rangle - 1\right) - \frac{i\Omega_{2,j}}{2}\langle\sigma^j_{g_1g_2}\rangle \quad \text{(A.1)}
\end{aligned}$$

$\mathcal{L}_1$ contribution

$$\begin{aligned}
\frac{d}{dt}\langle\sigma^j_{g_1g_1}\rangle &+= -\frac{1}{2}\left(\Omega^*_{1,j}\mathcal{P}^{X\sigma_{g_1e}}_{1,j} + \text{ c.c.}\right) \\
\frac{d}{dt}\langle\sigma^j_{g_1g_2}\rangle &+= -\frac{\Omega_{1,j}}{2}\mathcal{P}^{X\sigma_{eg_2}}_{1,j} - \frac{\Omega^*_{2,j}}{2}\mathcal{P}^{X\sigma_{g_1e}}_{2,j} \\
\frac{d}{dt}\langle\sigma^j_{g_1e}\rangle &+= \frac{\Omega_{1,j}}{2}\left(2\mathcal{P}^{X\sigma_{g_1g_1}}_{1,j} + \mathcal{P}^{X\sigma_{g_2g_2}}_{1,j} - \mathcal{P}^{X}_{1,j}\right) + \frac{\Omega_{2,j}}{2}\mathcal{P}^{X\sigma_{g_1g_2}}_{2,j} \quad \text{(A.2)}
\end{aligned}$$

$\mathcal{L}_2$ contribution

$$\begin{aligned}
\frac{d}{dt}\langle\sigma^j_{g_1g_1}\rangle &+= \frac{i}{4}\left\{\Omega^*_{1,j}\left(\mathcal{P}^{XX}_{1,j}\langle\sigma^j_{g_1e}\rangle + 2\mathcal{P}^{X}_{1,j}\mathcal{P}^{X\sigma_{g_1e}}_{1,j} - 2(\mathcal{P}^{X}_{1,j})^2\langle\sigma^j_{g_1e}\rangle\right) - \text{ c.c.}\right\} \\
\frac{d}{dt}\langle\sigma^j_{g_1g_2}\rangle &+= -\frac{i\Omega_{1,j}}{4}\left(\mathcal{P}^{XX}_{1,j}\langle\sigma^j_{g_2e}\rangle^* + 2\mathcal{P}^{X}_{1,j}\mathcal{P}^{X\sigma_{eg_2}}_{1,j} - 2(\mathcal{P}^{X}_{1,j})^2\langle\sigma^j_{g_2e}\rangle^*\right) \\
&\quad + \frac{i\Omega^*_{2,j}}{4}\left(\mathcal{P}^{XX}_{2,j}\langle\sigma^j_{g_1e}\rangle + 2\mathcal{P}^{X}_{2,j}\mathcal{P}^{X\sigma_{g_1e}}_{2,j} - 2(\mathcal{P}^{X}_{2,j})^2\langle\sigma^j_{g_1e}\rangle\right) \\
\frac{d}{dt}\langle\sigma^j_{g_1e}\rangle &+= \frac{i\Omega_{1,j}}{4}\left(\mathcal{P}^{XX}_{1,j}(2\langle\sigma^j_{g_1g_1}\rangle + \langle\sigma^j_{g_2g_2}\rangle - 1) + 2\mathcal{P}^{X}_{1,j}(2\mathcal{P}^{X\sigma_{g_1g_1}}_{1,j} + \mathcal{P}^{X\sigma_{g_2g_2}}_{1,j} - \mathcal{P}^{X}_{1,j})\right. \\
&\quad \left. - 2(\mathcal{P}^{X}_{1,j})^2(2\langle\sigma^j_{g_1g_1}\rangle + \langle\sigma^j_{g_2g_2}\rangle - 1)\right) \\
&\quad + \frac{i\Omega_{2,j}}{4}\left(\mathcal{P}^{XX}_{2,j}\langle\sigma^j_{g_1g_2}\rangle + 2\mathcal{P}^{X}_{2,j}\mathcal{P}^{X\sigma_{g_1g_2}}_{2,j} - 2(\mathcal{P}^{X}_{1,j})^2\langle\sigma^j_{g_1g_2}\rangle\right) \quad \text{(A.3)}
\end{aligned}$$

A.1.2 External moments

In the following equations, the index μ takes on values $1, 2$ to account for the two EIT lasers.

$\mathcal{L}_0$ contribution

$$\begin{aligned}
\frac{d}{dt}\langle b_n\rangle &= -i\omega_n\langle b_n\rangle \\
\frac{d}{dt}\langle b_nb_k\rangle &= -i(\omega_n+\omega_k)\langle b_nb_k\rangle \\
\frac{d}{dt}\langle b^\dagger_nb_k\rangle &= -i(\omega_k-\omega_n)\langle b^\dagger_nb_k\rangle \quad \text{(A.4)}
\end{aligned}$$

$\mathcal{L}_1$ contribution

$$\frac{d}{dt}\langle b_n\rangle \;+= \; -\sum_{\mu,j}\frac{\lambda^\mu_{jn}}{2}\left(\Omega^*_{\mu,j}\langle\sigma^j_{g_\mu e}\rangle - \text{ c.c.}\right)$$

$$
\begin{aligned}
\frac{d}{dt}\langle b_n b_k\rangle &+= -\left\{\sum_{\mu,j}\frac{\lambda^{\mu}_{j,n}}{2}\left(\Omega^{*}_{\mu,j}\langle b_k\sigma^{j}_{g_\mu e}\rangle - \Omega_{\mu,j}\langle b_k\sigma^{j}_{eg_\mu}\rangle\right) + \ n\leftrightarrow k\right\}\\
\frac{d}{dt}\langle b_n^{\dagger} b_k\rangle &+= \sum_{\mu,j}\frac{\lambda^{\mu}_{j,n}}{2}\left(\Omega^{*}_{\mu,j}\langle b_k\sigma^{j}_{g_\mu e}\rangle - \Omega_{\mu,j}\langle b_k\sigma^{j}_{eg_\mu}\rangle\right)\\
&\quad -\sum_{\mu,j}\frac{\lambda^{\mu}_{j,k}}{2}\left(\Omega^{*}_{\mu,j}\langle b_n\sigma^{j}_{eg_\mu}\rangle^{*} - \Omega_{\mu,j}\langle b_n\sigma^{j}_{g_\mu e}\rangle^{*}\right) \qquad \text{(A.5)}
\end{aligned}
$$

$\mathcal{L}_2$ contribution

$$
\begin{aligned}
\frac{d}{dt}\langle b_n\rangle &+= \sum_{\mu,j}\frac{i\lambda^{\mu}_{j,n}}{2}\left(\Omega^{*}_{\mu,j}\mathcal{P}^{X\sigma_{g_\mu e}}_{\mu,j} + \text{ c.c.}\right)\\
\frac{d}{dt}\langle b_n b_k\rangle &+= -\sum_{\mu,j}\Gamma_\mu\langle u^2\rangle_{eg_\mu}\lambda^{\text{sc}}_{\mu,jn}\lambda^{\text{sc}}_{\mu,jk}(1-\langle\sigma^{j}_{g_1g_1}\rangle - \langle\sigma^{j}_{g_2g_2}\rangle)\\
&\quad +\Bigg\{\sum_{\mu,j}\frac{i\lambda^{\mu}_{j,n}}{2}\Big(\Omega^{*}_{\mu,j}\Big\{(\mathcal{P}^{dX}_{\mu,jk})^{*}\langle\sigma^{j}_{g_\mu e}\rangle + \mathcal{P}^{X}_{\mu,j}\langle b_k\sigma^{j}_{g_\mu e}\rangle + \mathcal{P}^{X\sigma_{g_\mu e}}_{\mu,j}\langle b_k\rangle\\
&\quad - \ 2\mathcal{P}^{X}_{\mu,j}\langle\sigma^{j}_{g_\mu e}\rangle\langle b_k\rangle\Big\} + \Omega_{\mu,j}\Big\{g_\mu e\to eg_\mu\Big\}\Big) + \ n\leftrightarrow k\Bigg\}\\
\frac{d}{dt}\langle b_n^{\dagger} b_k\rangle &+= \sum_{\mu,j}\Gamma_\mu\langle u^2\rangle_{eg_\mu}\lambda^{\text{sc}}_{\mu,jn}\lambda^{\text{sc}}_{\mu,jk}(1-\langle\sigma^{j}_{g_1g_1}\rangle - \langle\sigma^{j}_{g_2g_2}\rangle)\\
&\quad -\sum_{\mu,j}\frac{i\lambda^{\mu}_{j,n}}{2}\Big(\Omega^{*}_{\mu,j}\Big\{(\mathcal{P}^{dX}_{\mu,jk})^{*}\langle\sigma^{j}_{g_\mu e}\rangle + \mathcal{P}^{X}_{\mu,j}\langle b_k\sigma^{j}_{g_\mu e}\rangle + \mathcal{P}^{X\sigma_{g_\mu e}}_{\mu,j}\langle b_k\rangle\\
&\quad - \ 2\mathcal{P}^{X}_{\mu,j}\langle\sigma^{j}_{g_\mu e}\rangle\langle b_k\rangle\Big\} + \Omega_{\mu,j}\Big\{g_\mu e\to eg_\mu\Big\}\Big)\\
&\quad +\sum_{\mu,j}\frac{i\lambda^{\mu}_{j,k}}{2}\Big(\Omega^{*}_{\mu,j}\Big\{\mathcal{P}^{dX}_{\mu,jn}\langle\sigma^{j}_{g_\mu e}\rangle + \mathcal{P}^{X}_{\mu,j}\langle b_n\sigma^{j}_{eg_\mu}\rangle^{*} + \mathcal{P}^{X\sigma_{g_\mu e}}_{\mu,j}\langle b_n\rangle^{*}\\
&\quad - \ 2\mathcal{P}^{X}_{\mu,j}\langle\sigma^{j}_{g_\mu e}\rangle\langle b_n\rangle^{*}\Big\} + \Omega_{\mu,j}\Big\{g_\mu e\to eg_\mu\Big\}\Big) \qquad \text{(A.6)}
\end{aligned}
$$

A.1.3 Hybrid moments

Table A.2 introduces some additional partial sums, now over the ions instead of the modes, that will further aid in compact presentation and faster computation by identification of recurring summations.

$\mathcal{L}_0$ contribution

$$
\frac{d}{dt}\langle b_n\sigma^{j}_{g_1g_1}\rangle = -i\omega_n\langle b_n\sigma^{j}_{g_1g_1}\rangle - \frac{i}{2}\left(\Omega^{*}_{1,j}\langle b_n\sigma^{j}_{g_1e}\rangle - \Omega_{1,j}\langle b_n\sigma^{j}_{eg_1}\rangle\right)
$$

Symbol	Definition
$\mathcal{Q}_{jn}^{\mathcal{L}_1}$	$-\sum_{\mu,q\neq j}\frac{\lambda_{q,n}^{\mu}}{2}\left(\Omega_{\mu,q}^{*}\langle\sigma_{g_\mu e}^{q}\rangle - \text{ c.c.}\right)$
$\mathcal{Q}_{jn}^{\mathcal{L}_2(1),\sigma_\alpha}$	$\sum_{\mu,q\neq j}\frac{i\lambda_{qn}^{\mu}}{2}\mathcal{P}_{\mu,[qj]}^{X\sigma_\alpha}\left(\Omega_{\mu,q}^{*}\langle\sigma_{g_\mu e}^{q}\rangle + \text{ c.c.}\right)$
$\mathcal{Q}_{jn}^{\mathcal{L}_2(2)}$	$\sum_{\mu,q\neq j}\frac{i\lambda_{qn}^{\mu}}{2}\left(\Omega_{\mu,q}^{*}\mathcal{P}_{\mu,q}^{X\sigma_{g_\mu e}} + \text{ c.c.}\right)$
$\mathcal{Q}_{jn}^{\mathcal{L}_2(3)}$	$\sum_{\mu,q\neq j}\frac{i\lambda_{qn}^{\mu}}{2}\mathcal{P}_{\mu,q}^{X}\left(\Omega_{\mu,q}^{*}\langle\sigma_{g_\mu e}^{q}\rangle + \text{ c.c.}\right)$

Table A.2: Additional partial sums, over the ions rather than modes, to simplify notation and speed up computation.

$$
\begin{aligned}
& & +\Gamma_1\left(\langle b_n\rangle - \langle b_n\sigma_{g_1g_1}^{j}\rangle - \langle b_n\sigma_{g_2g_2}^{j}\rangle\right)\\
\frac{d}{dt}\langle b_n\sigma_{g_1g_2}^{j}\rangle &=& i\left(\Delta_{1,j}(t)-\Delta_{2,j}(t)-\omega_n\right)\langle b_n\sigma_{g_1g_2}^{j}\rangle\\
& & +\frac{i\Omega_{1,j}}{2}\langle b_n\sigma_{eg_2}^{j}\rangle - \frac{i\Omega_{2,j}^{*}}{2}\langle b_n\sigma_{g_1e}^{j}\rangle\\
\frac{d}{dt}\langle b_n\sigma_{g_1e}^{j}\rangle &=& -\left(\frac{\Gamma}{2}-i\left(\Delta_{1,j}(t)-\omega_n\right)\right)\langle b_n\sigma_{g_1e}^{j}\rangle\\
& & -\frac{i\Omega_{1,j}}{2}\left(2\langle b_n\sigma_{g_1g_1}^{j}\rangle + \langle b_n\sigma_{g_2g_2}^{j}\rangle - \langle b_n\rangle\right) - \frac{i\Omega_{2,j}}{2}\langle b_n\sigma_{g_1g_2}^{j}\rangle\\
\frac{d}{dt}\langle b_n\sigma_{eg_1}^{j}\rangle &=& -\left(\frac{\Gamma}{2}+i\left(\Delta_{1,j}(t)+\omega_n\right)\right)\langle b_n\sigma_{eg_1}^{j}\rangle\\
& & +\frac{i\Omega_{1,j}^{*}}{2}\left(2\langle b_n\sigma_{g_1g_1}^{j}\rangle + \langle b_n\sigma_{g_2g_2}^{j}\rangle - \langle b_n\rangle\right) + \frac{i\Omega_{2,j}^{*}}{2}\langle b_n\sigma_{g_2g_1}^{j}\rangle
\end{aligned}
\tag{A.7}
$$

$\mathcal{L}_1$ contribution

$$
\begin{aligned}
\frac{d}{dt}\langle b_n\sigma_{g_1g_1}^{j}\rangle &+=& -\frac{\Omega_{1,j}^{*}\lambda_{j,n}^{1}}{2}\langle\sigma_{g_1e}^{j}\rangle - \frac{1}{2}\Big\{\Omega_{1,j}^{*}\Big((\mathcal{P}_{1,jn}^{dX})^{*}\langle\sigma_{g_1e}^{j}\rangle + P_{1,j}^{X}\langle b_n\sigma_{g_1e}^{j}\rangle + P_{1,j}^{X\sigma_{g_1e}}\langle b_n\rangle\\
& & - 2P_{1,j}^{X}\langle b_n\rangle\langle\sigma_{g_1e}^{j}\rangle\Big) + \Omega_{1,j}\Big(g_1e\to eg_1\Big)\Big\} + \mathcal{Q}_{jn}^{\mathcal{L}_1}\langle\sigma_{g_1g_1}^{j}\rangle\\
\frac{d}{dt}\langle b_n\sigma_{g_1g_2}^{j}\rangle &+=& -\frac{\Omega_{2,j}^{*}\lambda_{jn}^{2}}{2}\langle\sigma_{g_1e}^{j}\rangle\\
& & -\frac{\Omega_{1,j}}{2}\Big((\mathcal{P}_{1,jn}^{dX})^{*}\langle\sigma_{g_2e}^{j}\rangle^{*} + P_{1,j}^{X}\langle b_n\sigma_{eg_2}^{j}\rangle + P_{1,j}^{X\sigma_{eg_2}}\langle b_n\rangle - 2P_{1,j}^{X}\langle b_n\rangle\langle\sigma_{g_2e}^{j}\rangle^{*}\Big)\\
& & -\frac{\Omega_{2,j}^{*}}{2}\Big((\mathcal{P}_{2,jn}^{dX})^{*}\langle\sigma_{g_1e}^{j}\rangle + P_{2,j}^{X}\langle b_n\sigma_{g_1e}^{j}\rangle + P_{2,j}^{X\sigma_{g_1e}}\langle b_n\rangle - 2P_{2,j}^{X}\langle b_n\rangle\langle\sigma_{g_1e}^{j}\rangle\Big)\\
& & +\mathcal{Q}_{jn}^{\mathcal{L}_1}\langle\sigma_{g_1g_2}^{j}\rangle\\
\frac{d}{dt}\langle b_n\sigma_{g_1e}^{j}\rangle &+=& \frac{\Omega_{1,j}}{2}\Big\{2\Big((\mathcal{P}_{1,jn}^{dX})^{*}\langle\sigma_{g_1g_1}^{j}\rangle + P_{1,j}^{X}\langle b_n\sigma_{g_1g_1}^{j}\rangle + P_{1,j}^{X\sigma_{g_1g_1}}\langle b_n\rangle - 2P_{1,j}^{X}\langle b_n\rangle\langle\sigma_{g_1g_1}^{j}\rangle\Big)\\
& & + \Big(g_1g_1\to g_2g_2\Big) - (\mathcal{P}_{1,jn}^{dX})^{*}\Big\} + \frac{\Omega_{1,j}\lambda_{jn}^{1}}{2}\langle\sigma_{g_1g_1}^{j}\rangle + \frac{\Omega_{2,j}\lambda_{jn}^{2}}{2}\langle\sigma_{g_1g_2}^{j}\rangle
\end{aligned}
$$

$$
\begin{aligned}
&+\frac{\Omega_{2,j}}{2}\left((\mathcal{P}^{dX}_{2,jn})^*\langle\sigma^j_{g_1g_2}\rangle + P^X_{2,j}\langle b_n\sigma^j_{g_1g_2}\rangle + P^{X\sigma_{g_1g_2}}_{2,j}\langle b_n\rangle - 2P^X_{2,j}\langle b_n\rangle\langle\sigma^j_{g_1g_2}\rangle\right)\\
&+\mathcal{Q}^{\mathcal{L}_1}_{jn}\langle\sigma^j_{g_1e}\rangle\\
\frac{d}{dt}\langle b_n\sigma^j_{eg_1}\rangle \;+=\; &\frac{\Omega^*_{1,j}}{2}\left\{2\left((\mathcal{P}^{dX}_{1,jn})^*\langle\sigma^j_{g_1g_1}\rangle + P^X_{1,j}\langle b_n\sigma^j_{g_1g_1}\rangle + P^{X\sigma_{g_1g_1}}_{1,j}\langle b_n\rangle - 2P^X_{1,j}\langle b_n\rangle\langle\sigma^j_{g_1g_1}\rangle\right)\right.\\
&\left.+\left(g_1g_1\to g_2g_2\right) - (\mathcal{P}^{dX}_{1,jn})^*\right\} + \frac{\Omega^*_{1,j}\lambda^1_{jn}}{2}\left(\langle\sigma^j_{g_1g_1}\rangle + \langle\sigma^j_{g_2g_2}\rangle - 1\right)\\
&+\frac{\Omega^*_{2,j}}{2}\left((\mathcal{P}^{dX}_{2,jn})^*\langle\sigma^j_{g_1g_2}\rangle^* + P^X_{2,j}\langle b_n\sigma^j_{g_2g_1}\rangle + P^{X\sigma_{g_2g_1}}_{2,j}\langle b_n\rangle - 2P^X_{2,j}\langle b_n\rangle\langle\sigma^j_{g_1g_2}\rangle^*\right)\\
&+\mathcal{Q}^{\mathcal{L}_1}_{jn}\langle\sigma^j_{g_1e}\rangle^* \qquad\qquad (A.8)
\end{aligned}
$$

$\mathcal{L}_2$ contribution

$$
\begin{aligned}
\frac{d}{dt}\langle b_n\sigma^j_{g_1g_1}\rangle \;+=\; &\frac{i\Omega^*_{1,j}\lambda^1_{jn}}{2}\mathcal{P}^{X\sigma_{g_1e}}_{1,j}\\
&+\frac{i}{4}\left\{\Omega^*_{1,j}\left(\mathcal{P}^{XX}_{1,j}\langle b_n\sigma^j_{g_1e}\rangle + 2(\mathcal{P}^{dX}_{1,jn})^*\mathcal{P}^{X\sigma_{g_1e}}_{1,j} - 2(\mathcal{P}^X_{1,j})^2\langle b_n\rangle\langle\sigma^j_{g_1e}\rangle\right)\right.\\
&\left.-\,\Omega_{1,j}\left(g_1e\to eg_1\right)\right\} + \mathcal{Q}^{\mathcal{L}_2(1),\sigma_{g_1g_1}}_{jn} + \left(\mathcal{Q}^{\mathcal{L}_2(2)}_{jn} - \mathcal{Q}^{\mathcal{L}_2(3)}_{jn}\right)\langle\sigma^j_{g_1g_1}\rangle\\
\frac{d}{dt}\langle b_n\sigma^j_{g_1g_2}\rangle \;+=\; &\frac{i\Omega^*_{2,j}\lambda^2_{jn}}{2}\mathcal{P}^{X\sigma_{g_1e}}_{2,j}\\
&-\frac{i\Omega_{1,j}}{4}\left(\mathcal{P}^{XX}_{1,j}\langle b_n\sigma^j_{eg_2}\rangle + 2(\mathcal{P}^{dX}_{1,jn})^*\mathcal{P}^{X\sigma_{eg_2}}_{1,j} - 2(\mathcal{P}^X_{1,j})^2\langle b_n\rangle\langle\sigma^j_{g_2e}\rangle^*\right)\\
&+\frac{i\Omega^*_{2,j}}{4}\left(\mathcal{P}^{XX}_{2,j}\langle b_n\sigma^j_{g_1e}\rangle + 2(\mathcal{P}^{dX}_{2,jn})^*\mathcal{P}^{X\sigma_{g_1e}}_{2,j} - 2(\mathcal{P}^X_{2,j})^2\langle b_n\rangle\langle\sigma^j_{g_1e}\rangle\right)\\
&+\mathcal{Q}^{\mathcal{L}_2(1),\sigma_{g_1g_2}}_{jn} + \left(\mathcal{Q}^{\mathcal{L}_2(2)}_{jn} - \mathcal{Q}^{\mathcal{L}_2(3)}_{jn}\right)\langle\sigma^j_{g_1g_2}\rangle\\
\frac{d}{dt}\langle b_n\sigma^j_{g_1e}\rangle \;+=\; &\frac{i\Omega_{1,j}}{4}\left\{2\left(\mathcal{P}^{XX}_{1,j}\langle b_n\sigma^j_{g_1g_1}\rangle + 2(\mathcal{P}^{dX}_{1,jn})^*\mathcal{P}^{X\sigma_{g_1g_1}}_{1,j} - 2(\mathcal{P}^X_{1,j})^2\langle b_n\rangle\langle\sigma^j_{g_1g_1}\rangle\right)\right.\\
&\left.+\left(g_1g_1\to g_2g_2\right) - \left(\mathcal{P}^{XX}_{1,j}\langle b_n\rangle + 2(\mathcal{P}^{dX}_{1,jn})^*\mathcal{P}^X_{1,j} - 2(\mathcal{P}^X_{1,j})^2\langle b_n\rangle\right)\right\}\\
&+\frac{i\Omega_{1,j}\lambda^1_{jn}}{2}\mathcal{P}^{X\sigma_{g_1g_1}}_{1,j} + \frac{i\Omega_{2,j}\lambda^2_{jn}}{2}\mathcal{P}^{X\sigma_{g_1g_2}}_{2,j}\\
&+\frac{i\Omega_{2,j}}{4}\left(\mathcal{P}^{XX}_{2,j}\langle b_n\sigma^j_{g_1g_2}\rangle + 2(\mathcal{P}^{dX}_{2,jn})^*\mathcal{P}^{X\sigma_{g_1g_2}}_{2,j} - 2(\mathcal{P}^X_{2,j})^2\langle b_n\rangle\langle\sigma^j_{g_1g_2}\rangle\right)\\
&+\mathcal{Q}^{\mathcal{L}_2(1),\sigma_{g_1e}}_{jn} + \left(\mathcal{Q}^{\mathcal{L}_2(2)}_{jn} - \mathcal{Q}^{\mathcal{L}_2(3)}_{jn}\right)\langle\sigma^j_{g_1e}\rangle\\
\frac{d}{dt}\langle b_n\sigma^j_{eg_1}\rangle \;+=\; &-\frac{i\Omega^*_{1,j}}{4}\left\{2\left(\mathcal{P}^{XX}_{1,j}\langle b_n\sigma^j_{g_1g_1}\rangle + 2(\mathcal{P}^{dX}_{1,jn})^*\mathcal{P}^{X\sigma_{g_1g_1}}_{1,j} - 2(\mathcal{P}^X_{1,j})^2\langle b_n\rangle\langle\sigma^j_{g_1g_1}\rangle\right)\right.\\
&\left.+\left(g_1g_1\to g_2g_2\right) - \left(\mathcal{P}^{XX}_{1,j}\langle b_n\rangle + 2(\mathcal{P}^{dX}_{1,jn})^*\mathcal{P}^X_{1,j} - 2(\mathcal{P}^X_{1,j})^2\langle b_n\rangle\right)\right\}\\
&-\frac{i\Omega^*_{1,j}\lambda^1_{jn}}{2}\left(\mathcal{P}^{X\sigma_{g_1g_1}}_{1,j} + \mathcal{P}^{X\sigma_{g_2g_2}}_{1,j} - \mathcal{P}^X_{1,j}\right)\\
&-\frac{i\Omega^*_{2,j}}{4}\left(\mathcal{P}^{XX}_{2,j}\langle b_n\sigma^j_{g_2g_1}\rangle + 2(\mathcal{P}^{dX}_{2,jn})^*\mathcal{P}^{X\sigma_{g_2g_1}}_{2,j} - 2(\mathcal{P}^X_{2,j})^2\langle b_n\rangle\langle\sigma^j_{g_1g_2}\rangle^*\right)
\end{aligned}
$$

$$+\mathcal{Q}_{jn}^{\mathcal{L}_2(1),\sigma_{eg_1}} + \left(\mathcal{Q}_{jn}^{\mathcal{L}_2(2)} - \mathcal{Q}_{jn}^{\mathcal{L}_2(3)}\right) \langle \sigma_{g_1 e}^{j} \rangle^* \tag{A.9}$$

A.2 Analytic formula for the bright fraction: Derivation outline

The bright-state fraction is $P(|\uparrow\rangle) = 1/N \sum_j 1/2(1+\langle\hat{\sigma}_j^z\rangle)$, where $\langle\hat{\sigma}_j^z\rangle$, the population difference after the final $\pi/2$ pulse, is equal to $-\langle\hat{\sigma}_j^x\rangle$ before that pulse. The problem therefore amounts to computing the quantity $\langle\hat{\sigma}_j^x\rangle$ before the final state rotation. For the Hamiltonian, Eq. (4.3), the propagator $\hat{U}(t)$ factorizes as $\hat{U}(t) = \hat{U}_{\rm SM}(t) \times \hat{U}_{\rm SS}(t)$, where the spin-motion propagator $\hat{U}_{\rm SM}(t)$ and the spin-spin propagator $\hat{U}_{\rm SS}(t)$ are given by [123, 34]

$$\begin{aligned}
\hat{U}_{\rm SM}(t) &= \prod_n \exp\left[\sum_j \left(\alpha_{nj}(t)\hat{a}_n^\dagger - \alpha_{nj}^*(t)\hat{a}_n\right)\hat{\sigma}_j^z\right], \\
\hat{U}_{\rm SS}(t) &= \exp\left[-i\sum_{i\neq j} J_{ij}(t)\hat{\sigma}_i^z\hat{\sigma}_j^z\right].
\end{aligned} \tag{A.10}$$

Before detailing the coupling constants, we note that these propagators have to be adapted to the thermometry sequence depicted in Fig. 4.2. For the purpose of computing the bright fraction, the effect of the spin-echo pulse can simply be viewed as a change in the sign of F in the second arm of the ODF sequence. Further, an arbitrary phase offset ϕ_0 can be introduced in the second-arm of the ODF sequence, which modifies the lineshape. These features can be accounted for by the replacement $\cos(\mu_r t) \to g(t)$ in Eq. (4.3), where

$$g(t) = \begin{cases} \cos(\mu_r t), & t < \tau \\ 0, & \tau < t < \tau + t_\pi \\ -\cos(\mu_r t + \phi_0), & \tau + t_\pi < t < 2\tau + t_\pi. \end{cases} \tag{A.11}$$

With this adaptation, the coupling constants in Eq. (A.10) are given by

$$\begin{aligned}
\alpha_{nj}(t) &= -i\frac{F}{\hbar}\mathcal{M}_{jn}\sqrt{\frac{\hbar}{2M\omega_n}}\int_0^t dt' g(t') e^{i\omega_n t'}, \\
J_{ij}(t) &= \mathrm{Im}\sum_n \frac{F^2}{\hbar^2}\mathcal{M}_{in}\mathcal{M}_{jn}\frac{\hbar}{2M\omega_n}\int_0^t dt_1 \int_0^{t_1} dt_2 g(t_1) g(t_2) e^{i\omega_n(t_2-t_1)}.
\end{aligned} \tag{A.12}$$

We evaluate these expressions within the rotating-wave approximation that $|\delta_n| = |\mu_r - \omega_n| \ll \mu_r, \mu_r + \omega_n$, where the frequency $\delta_n = \mu_r - \omega_n$ is the detuning of the ODF difference frequency from mode n. Specifically, at time $2\tau + t_\pi$, the expressions evaluate to

$$\begin{aligned}
\alpha_{nj}(2\tau + t_\pi) &= \frac{F\mathcal{M}_{jn}}{2\hbar\delta_n}\sqrt{\frac{\hbar}{2M\omega_n}}\left(e^{-i\delta_n\tau} + e^{-i\phi_0}e^{-i\delta_n(\tau+t_\pi)} - e^{-i\phi_0}e^{-i\delta_n(2\tau+t_\pi)} - 1\right) \\
J_{ij}(2\tau + t_\pi) &= \sum_n \frac{F^2\mathcal{M}_{in}\mathcal{M}_{jn}}{4\hbar^2\delta_n^2}\frac{\hbar}{2M\omega_n}\left(2\delta_n\tau + \sin(\delta_n(2\tau + t_\pi) + \phi_0) + \sin(\delta_n t_\pi + \phi_0)\right. \\
&\qquad \left. -2\sin(\delta_n\tau) - 2\sin(\delta_n(\tau + t_\pi) + \phi_0)\right). \qquad \text{(A.13)}
\end{aligned}$$

For μ_r close to the COM mode ($n = 1$) frequency, here denoted ω_1, the contribution of the other modes is negligible because of the large detunings δ_n for $n \neq 1$. As a result, $\alpha_{nj} \approx 0$ for $n \neq 1$ and the symmetric coupling of the c.m. mode to all the ions results in $\alpha_{1j}(2\tau + t_\pi) \equiv \alpha$ and $J_{ij}(2\tau + t_\pi) \equiv J$, independent of the ion numbers i, j, with expressions

$$\begin{aligned}
\alpha &= \frac{F}{2\hbar\sqrt{N}\delta_1}\sqrt{\frac{\hbar}{2M\omega_z}}\left(e^{-i\delta_1\tau} + e^{-i\phi_0}e^{-i\delta_1(\tau+t_\pi)} - e^{-i\phi_0}e^{-i\delta_1(2\tau+t_\pi)} - 1\right) \\
J &= \frac{F^2}{4\hbar^2 N\delta_1^2}\frac{\hbar}{2M\omega_z}\left(2\delta_1\tau + \sin(\delta_1(2\tau + t_\pi) + \phi_0) + \sin(\delta_1 t_\pi + \phi_0)\right. \\
&\qquad \left. -2\sin(\delta_1\tau) - 2\sin(\delta_1(\tau + t_\pi) + \phi_0)\right). \qquad \text{(A.14)}
\end{aligned}$$

The lineshapes in Fig. 4.3 are obtained with a phase offset of $\phi_0 = 0$.

With the modes initially in thermal states characterized by mean occupations $\bar{n}_n$, and the spins initialized along the x direction, the evolution of any observable can be computed using the propagator $\hat{U}(t)$ whose form is detailed in Eq. (A.10). Specifically, the expression for $\langle\hat{\sigma}_j^x\rangle$ evaluates to [102]

$$\langle\hat{\sigma}_j^x\rangle = \left\{\prod_{i\neq j}\cos(4J_{jk})\right\}\exp\left[-2\sum_n|\alpha_{nj}|^2\left(2\bar{n}_n + 1\right)\right]. \qquad \text{(A.15)}$$

A convenient way to account for thermal motional states is to first compute $\langle\hat{\sigma}_j^x\rangle$ for initial Fock states of the modes and then sum over these initial states with appropriate coefficients.

For μ_r close to the COM mode $\langle\hat{\sigma}_x^j\rangle$ becomes independent of j and reduces to

$$\langle\hat{\sigma}^x\rangle = \left(\cos(4J)\right)^{N-1}\exp\left[-2|\alpha|^2\left(2\bar{n}_1 + 1\right)\right]. \qquad \text{(A.16)}$$

The ODF lasers also lead to free-space scattering that results in decoherence at rate Γ. This results in an additional factor of $\exp(-2\Gamma\tau)$ in Eq. (A.15) and Eq. (A.16) that decreases the value of $\langle\hat{\sigma}_j^x\rangle$.

Appendix B

Supplementary Material for Chapters 7 and 8

B.1 Implementing instantaneous state rotations

B.1.1 Multi-center model

In the multi-center model, we implement an instantaneous rotation in order to initialize the c-numbers in accordance with the initial state being in an equal superposition of the $n_\downarrow, n_\uparrow$ centers. We adopt a pragmatic approach to implement such a rotation: In the lab frame, we consider a fictitious Hamiltonian

$$\hat{H} = \frac{\hbar\Omega}{2} \sum_{j=1}^{N} \left(\hat{\sigma}^j_{n_\downarrow, n_\uparrow} e^{-i\theta} + \hat{\sigma}^j_{n_\uparrow, n_\downarrow} e^{i\theta} \right) \tag{B.1}$$

to act on the collection of atoms for a time $T = \pi/2\Omega$ so that the pulse area is $A = \pi/2$. Here θ specifies the orientation of the axis of rotation on the equatorial plane of the Bloch sphere. By ignoring the energy difference $\hbar(\omega^j_m - \omega^j_n)$ between any pair of states n, m, we are making the assumption that the pulse is 'instantaneous'. While in practice any state preparation pulse requires a finite amount of time, here we assume such instantaneous pulses for simplicity and to avoid complications associated with pulse efficiencies and momentum widths [118].

B.1.2 Two-center model

In the two-center model, instantaneous state rotations are used for state initialization and for probing the effect of echo pulses on the evolution of the squeezing parameter. To implement perfect, instantaneous rotations, we consider a Bloch sphere for each $\tilde{q}$ value with the North and

South poles represented by the states $|n_\uparrow, \tilde{q}\rangle$ and $|n_\downarrow, \tilde{q}\rangle$ respectively. The perfect rotation pulses are assumed to not couple states with different $\tilde{q}$. The transformation of this pair of states under a rotation with axis $\hat{\mathbf{n}}$ and pulse area A ($\in [0, 2\pi]$) is,

$$\begin{pmatrix} |n_\uparrow, \tilde{q}\rangle' \\ \\ |n_\downarrow, \tilde{q}\rangle' \end{pmatrix} = U(\hat{\mathbf{n}}, A) \begin{pmatrix} |n_\uparrow, \tilde{q}\rangle \\ \\ |n_\downarrow, \tilde{q}\rangle \end{pmatrix}, \tag{B.2}$$

where the matrix $U(\hat{\mathbf{n}}, A)$ is given by

$$U(\hat{\mathbf{n}}, A) = \begin{pmatrix} \cos\frac{A}{2} - in^z \sin\frac{A}{2} & -i(n^x + in^y)\sin\frac{A}{2} \\ \\ -i(n^x - in^y)\sin\frac{A}{2} & \cos\frac{A}{2} + in^z \sin\frac{A}{2} \end{pmatrix}. \tag{B.3}$$

Since we track expectation values, we need to recast this transformation in terms of the means of one and two-atom operators. In what follows, we label $n_\uparrow, n_\downarrow$ using binary digits, i.e. $n_\uparrow \equiv 0$ and $n_\downarrow \equiv 1$. For one-atom operators, we define $\mathbf{v}_1^{\tilde{q}}$ with elements $v_1^{\tilde{q},j} = \langle \hat{\sigma}^{1,\tilde{q}}_{n_j,m_j} \rangle$, where $j = 0, \ldots, 3$ and n_j (m_j) is the second (first) digit from the right in the binary decomposition of j. The vector $\mathbf{v}_1^{\tilde{q}}$ transforms under the Bragg pulse to $\bar{\mathbf{v}}_1^{\tilde{q}} = M_1(\hat{\mathbf{n}}, A)\mathbf{v}_1^{\tilde{q}}$, where

$$M_1(\hat{\mathbf{n}}, A) = \begin{pmatrix} |U_{11}|^2 & U_{11}^* U_{21} & U_{21}^* U_{11} & |U_{21}|^2 \\ \\ U_{11}^* U_{12} & U_{11}^* U_{22} & U_{21}^* U_{12} & U_{21}^* U_{22} \\ \\ U_{12}^* U_{11} & U_{12}^* U_{21} & U_{22}^* U_{11} & U_{22}^* U_{21} \\ \\ |U_{12}|^2 & U_{12}^* U_{22} & U_{22}^* U_{12} & |U_{22}|^2 \end{pmatrix}. \tag{B.4}$$

For two-atom operators, we similarly define $\mathbf{v}_2^{\tilde{q},\tilde{q}'}$ with elements $v_2^{\tilde{q},\tilde{q}',j} = \langle \hat{\sigma}^{1,\tilde{q}}_{n_j,m_j} \hat{\sigma}^{2,\tilde{q}}_{r_j,s_j} \rangle$, where $j = 0, \ldots, 15$ and n_j, m_j, r_j, s_j are respectively the fourth, third, second and first digits from the right in the binary decomposition of j. This vector transforms as $\bar{\mathbf{v}}_2^{\tilde{q},\tilde{q}',j} = M_2(\hat{\mathbf{n}}, A)\mathbf{v}_2^{\tilde{q},\tilde{q}',j}$ where $M_2(\hat{\mathbf{n}}, A) = M_1(\hat{\mathbf{n}}, A) \otimes M_1(\hat{\mathbf{n}}, A)$ is a 16×16 matrix obtained as the Kronecker product of M_1 with itself.

B.2 Rabi oscillation model for population leakage

We consider the case when $\tilde{\sigma}_q \approx 0$. The two spin states correspond to $|n_\downarrow\rangle = |0\hbar k\rangle$ and $n_\uparrow = |2\hbar k\rangle$. We assume that mode 2 is dominantly sourced by the coherence between $n_\downarrow$ and $n_\uparrow$

and neglect the fluctuating terms to simplify the equation for ζ (Eq. 7.25) to

$$\frac{d}{dt}\zeta = -\left(\frac{\kappa}{2} - i\Delta_{cl}\right)\zeta + i\frac{g_{\text{eff}}}{2}\sum_j s^j_{n_\uparrow,n_\downarrow}. \tag{B.5}$$

We transform to the rotating frame $s^j_{n_\uparrow,n_\downarrow} = \tilde{s}^j_{n_\uparrow,n_\downarrow}e^{4i\omega_r t}$, $\zeta = \tilde{\zeta}e^{4i\omega_r t}$. At short times ($N\Gamma_{n_\downarrow}t \ll 1$), assuming that the state is prepared along the x-axis of the Bloch sphere in the $n_\downarrow, n_\uparrow$ manifold, $\tilde{s}^j_{n_\uparrow,n_\downarrow} \approx 1/2$ for all j. Then, using the fact that $|\kappa/2 - i\delta_{n_\downarrow}| \gg N\chi_{n_\downarrow}$, we can adiabatically eliminate $\tilde{\zeta}$ as

$$\tilde{\zeta} \approx \frac{ig_{\text{eff}}/2}{\kappa/2 - i\delta_{n_\downarrow}}\sum_j \tilde{s}^j_{n_\uparrow,n_\downarrow} \approx -\frac{g_{\text{eff}}}{\delta_{n_\downarrow}}\frac{N}{4}, \tag{B.6}$$

where in the last approximation we have assumed that $R = \kappa/2\delta_{n_\downarrow} \ll 1$. As an example of population leakage, we consider the $n_\uparrow \leftrightarrow n_{+1}$ transition. By symmetry, the same arguments hold true for the $n_\downarrow \leftrightarrow n_{-1}$ transition. Assuming $s_{n_{+1},n_{+1}}$ is negligible, $s_{n_\uparrow,n_\uparrow} \approx 1/2$, and zero populations and coherences associated with n_{+2}, the equation for the coherence $s_{n_{+1},n_\uparrow}$ reads

$$\frac{d}{dt}s^j_{n_{+1},n_\uparrow} = 12i\omega_r s_{n_{+1},n_\uparrow} + i\frac{N}{4\delta_{n_\downarrow}}\left(\frac{g_{\text{eff}}}{2}\right)^2 e^{4i\omega_r t}, \tag{B.7}$$

where we have used the expression for ζ from Eq. (B.6). From Eq. (7.55), the combination $g^2_{\text{eff}}/4\delta_{n_\downarrow}$ can be immediately identified as $\chi_{n_\downarrow}$ for $R \ll 1$. Solving for $s^j_{n+1,n_\uparrow}$ gives

$$s^j_{n_{+1},n_\uparrow} = -\frac{N\chi_{n_\downarrow}}{32\omega_r}\left(e^{4i\omega_r t} - e^{12i\omega_r t}\right). \tag{B.8}$$

Further, still neglecting the n_{+2} center, we can arrive at an equation for the dynamics of the population in n_{+1} as

$$\frac{d}{dt}s^j_{n_{+1},n_{+1}} = i\frac{g_{\text{eff}}}{2}\left(\zeta^* s_{n_{+1},n_\uparrow} - \zeta s_{n_\uparrow,n_{+1}}\right), \tag{B.9}$$

which can be solved using Eq. (B.6) and Eq. (B.8) to give

$$s^j_{n_{+1},n_{+1}} \approx \frac{1}{4}\left(\frac{N\chi_{n_\downarrow}}{8\omega_r}\right)^2(1 - \cos 8\omega_r t). \tag{B.10}$$

This expression explains the oscillations at frequency $\sim 8\omega_r$ that can be seen in the populations at the $n_{\pm1}$ centers in Fig. 8.2(c-d), while the peak value scaled to the number of atoms gives the analytic expression for $P^{\max}_{n_{\pm1}}$ (Eq. (8.11)) plotted in Fig. 8.2(e).

From Eq. (B.8), the maximum magnitude of the coherence $s^j_{n_{+1},n_\uparrow}$ is $N\chi_{n_\downarrow}/16\omega_r$. In estimating the intracavity field, we assumed that it is sourced only by the $s_{n_\uparrow,n_\downarrow}$ coherence. This approximation is valid as long as

$$\left|\frac{s_{n_{+1},n_\uparrow}}{s_{n_\uparrow,n_\downarrow}}\right| \ll 1 \implies N\chi_{n_\downarrow} \ll 8\omega_r. \tag{B.11}$$

The breakdown of the approximation, Eq. (B.11), signals the strong driving regime, i.e. it is the regime where the squeezing rate $N\chi_{n_\downarrow}$ becomes comparable to the relative detuning $8\omega_r$ between the $n_\downarrow \leftrightarrow n_\uparrow$ and $n_\uparrow \leftrightarrow n_{+1}$, $n_{-1} \leftrightarrow n_\downarrow$ transitions.

B.3 Relative importance of free-space scattering

Here, we analyze the relative importance of single-atom free-space scattering and collective superradiant decay in increasing the variance $V_{\min}$ that enters Eq. (8.1). Since the squeezing is driven by a term $\sim \hat{J}^z\hat{J}^z$, the axis corresponding to the minimum variance orients towards the z-axis over time [76]. As a result, we can estimate the degrading effect of various diffusive processes by estimating the corresponding increase in $(\Delta J^z)^2$.

Free-space scattering: We assume that once a photon is scattered into free-space, the atom recoils in a random direction and is lost from the atomic cloud. The rate of emission for a single atom is $\gamma\left(g^2|\beta|^2/4\Delta_c^2\right)$, where the term in parenthesis is the effective population in $|e\rangle$ as a result of the drive laser. Starting with an equal superposition of $|g,n_\downarrow\rangle$ and $|g,n_\uparrow\rangle$, each such photon could have been scattered equally likely from these two states, and so we have (assuming $\gamma t \ll 1$)

$$\dot{N}_{n_\downarrow}/N = \dot{N}_{n_\uparrow}/N = -\frac{\gamma}{2}\left(\frac{g^2|\beta|^2}{4\Delta_c^2}\right). \tag{B.12}$$

Scattering from the $n_\downarrow$ ($n_\uparrow$) state of any single atom increases (decreases) J^z by $1/2$, therefore, the increase in variance in a time t is

$$\begin{aligned}\frac{(\Delta J^z)^2}{N/4} &= \frac{4}{N}N\left(\frac{\gamma t}{2}\left(\frac{g^2|\beta|^2}{4\Delta_c^2}\right)\left((-1/2)^2+(1/2)^2\right)\right.\\ &\quad\left.-\left(\frac{\gamma t}{2}\left(\frac{g^2|\beta|^2}{4\Delta_c^2}\right)(-1/2+1/2)\right)^2\right)\\ &= \gamma t\left(\frac{g^2|\beta|^2}{4\Delta_c^2}\right).\end{aligned} \tag{B.13}$$

Superradiant decay: The Lindblad term $\propto \Gamma_{n_\downarrow}$ in Eq. (7.53) contributes the following time evolution for $\langle \hat{J}^z \rangle$:

$$\frac{d}{dt}\langle \hat{J}^z \rangle = 2\Gamma_{n_\downarrow}\langle \hat{J}^- \hat{J}^+ \rangle = 2\Gamma_{n_\downarrow}\left(\langle \hat{\mathbf{J}} \cdot \hat{\mathbf{J}} \rangle - \langle \hat{J}^z \hat{J}^z \rangle - \langle \hat{J}^z \rangle\right), \tag{B.14}$$

where we have used Eq. (7.4). For our initial state, we have $\langle \hat{\mathbf{J}} \cdot \hat{\mathbf{J}} \rangle = N/2(N/2+1)$, $\langle \hat{J}^z \hat{J}^z \rangle = N/4$ and $\langle \hat{J}^z \rangle = 0$, so that,

$$\dot{N}_{n_\uparrow} = -\dot{N}_{n_\downarrow} = \Gamma_{n_\downarrow} N^2/2, \tag{B.15}$$

where $N_{n_\uparrow} \approx N/2 + \langle \hat{J}^z \rangle$ and $N_{n_\downarrow} \approx N/2 - \langle \hat{J}^z \rangle$. The above rates are valid for times such that $N\Gamma_{n_\downarrow} t \ll 1$. We can identify a per-atom rate of emission as $\Gamma_{n_\downarrow} N/2$. Each such photon increases J^z by 1, therefore, the increase in variance in a time t is

$$\frac{(\Delta J^z)^2}{N/4} = \frac{4}{N} N \left(\frac{N\Gamma_{n_\downarrow} t}{2} (+1)^2 - \left(\frac{N\Gamma_{n_\downarrow} t}{2} \right)^2 \right) \approx 2N\Gamma_{n_\downarrow} t. \tag{B.16}$$

From Eq. (B.13) and Eq. (B.16), the contribution of free-space scattering can be neglected compared to that of superradiant decay when

$$\gamma t \left(\frac{g^2 |\beta|^2}{4\Delta_c^2} \right) \ll 2N\Gamma_{n_\downarrow} t \implies R^2 \gg \frac{1}{NC}. \tag{B.17}$$

Here, $R = \kappa/2\delta_{n_\downarrow}$ is assumed to be $\ll 1$. As a result, when R^2 becomes comparable to the inverse collective cooperativity, free-space scattering can no longer be neglected. In the simulations presented in this paper, $N = 10^3$, $C = 1, 10$, giving $NC = 10^3, 10^4$. As a result, $R \gg 0.032, 0.01$ respectively for the two values of C. The values of R we consider are in the range $0.025 - 0.2$, and therefore some of our parameter regimes (e.g. $R = 0.025, C = 1$) do not satisfy the preceding requirement. A more precise estimate of the squeezing parameter for such regimes requires the inclusion of free-space scattering. Nevertheless, in an experiment, increasing the total number of atoms leads to a larger product NC and reduces the relative importance of free-space scattering at fixed R.